

# **Ion Frictional Heating in the High-Latitude Ionosphere**

Thesis submitted for the degree of  
Doctor of Philosophy  
at the University of Leicester

by

**Jacqueline Anne Davies**  
Department of Physics and Astronomy  
University of Leicester

September, 1996

UMI Number: U084860

All rights reserved

INFORMATION TO ALL USERS

The quality of this reproduction is dependent upon the quality of the copy submitted.

In the unlikely event that the author did not send a complete manuscript and there are missing pages, these will be noted. Also, if material had to be removed, a note will indicate the deletion.



UMI U084860

Published by ProQuest LLC 2015. Copyright in the Dissertation held by the Author.  
Microform Edition © ProQuest LLC.

All rights reserved. This work is protected against  
unauthorized copying under Title 17, United States Code.



ProQuest LLC  
789 East Eisenhower Parkway  
P.O. Box 1346  
Ann Arbor, MI 48106-1346



# **ION FRICTIONAL HEATING IN THE HIGH-LATITUDE IONOSPHERE**

**Jacqueline Anne Davies**

## **Abstract**

At auroral latitudes, large electric fields drive the F-region plasma of the ionosphere through the thermosphere, heating the ion population through frictional contact with the neutral gas. Ion frictional heating, which can double the unperturbed ion temperature, is an important manifestation of both magnetosphere-ionosphere and ionosphere-thermosphere interaction and provides a significant contribution to the energy budget of the ionosphere and neutral atmosphere at high-latitudes. Perhaps the single most powerful technique for ground based remote sensing of the ionosphere is incoherent scatter. The EISCAT radar facility, located in northern Scandinavia, employs this technique to investigate the highly dynamic nature of the high-latitude ionosphere. This thesis documents a study of ion frictional heating in the high-latitude ionosphere, principally employing common programme observations by the tristatic EISCAT UHF system. In excess of 3200 hours of EISCAT observations, taken during a six year period, were employed to study, on a statistical basis, ion frictional heating in the high-latitude F-region. The diurnal distribution of frictional heating was established and its dependence on such factors as geomagnetic activity and solar cycle was investigated; the distributions were interpreted with reference to corresponding distributions of enhanced ion velocity. A prolonged and intense interval of ion frictional heating was observed by EISCAT postnoon on 04/03/1992: this interval was modelled, using the Sheffield University plasmasphere and ionosphere model, and the model results compared with the observations. This study highlights the importance of ionospheric effects in determining neutral dynamics, particularly on the dayside. Furthermore, during this interval, the altitude dependence of the effect of enhanced electric fields on the velocity and temperature of the ion population was studied and, moreover, employed to provide first-order estimates of the normalised ion-neutral collision frequency and the neutral wind at E-region altitudes.

## Contents

### Acknowledgements

### Glossary

### Chapter 1: The solar-terrestrial environment

1.1	Introduction	1
1.2	The solar environment	1
1.2.1	The sun	1
1.2.2	The solar wind	1
1.2.3	The interplanetary magnetic field	1
1.3	The near Earth environment	2
1.3.1	The magnetosphere	2
1.3.2	The neutral atmosphere	2
1.3.3	The ionosphere	3
1.3.4	The high-latitude ionosphere	4
1.3.5	Radar studies of the ionosphere and upper atmosphere	6
1.4	Aims of the present study	6
1.5	Summary	7

### Chapter 2: Review of ion frictional heating

2.1	Introduction	8
2.2	Review of ion frictional heating	8
2.3	Phenomena associated with ion frictional heating	13
2.3.1	Non-Maxwellian ion thermal velocity distributions	13
2.3.2	Anisotropic ion temperatures	16
2.3.3	Neutral winds and ion drag	18
2.3.4	Ion composition modification	20
2.3.5	Large field-aligned plasma flows	22
2.3.6	Electron density depletion	24
2.3.7	Auroral precipitation and micropulsations	26
2.4	Summary	27

### Chapter 3: Incoherent scatter and the EISCAT system

3.1	Introduction	28
3.2	Theory of incoherent scatter	28
3.2.1	Incoherent scatter	28
3.2.2	Calculation of parameters from incoherent scatter	31
3.3	Development of incoherent scatter radar	33
3.4	The European incoherent scatter (EISCAT) facility	35

3.4.1	Operational characteristics of EISCAT	35
3.4.2	Measurement techniques	36
3.4.3	EISCAT common programmes	39
3.4.4	Incoherent scatter data analysis	40
3.4.5	Errors in incoherent scatter measurements	42
3.5	Summary	44

#### **Chapter 4: Statistical study of ion frictional heating**

4.1	Introduction	45
4.2	Experimental arrangement	45
4.3	Selection criterion for the identification of ion frictional heating	46
4.4	Statistical study of ion frictional heating	49
4.4.1	Diurnal distribution of ion frictional heating	49
4.4.2	Variation with interplanetary magnetic field orientation	54
4.4.3	Variation with geomagnetic activity	58
4.4.4	Variation with solar activity	59
4.4.5	Variation with season	61
4.5	Summary and conclusions	63

#### **Chapter 5: Dayside ion frictional heating: EISCAT observations and comparison with model results**

5.1	Introduction	64
5.2	EISCAT observations of an interval of dayside ion frictional heating	64
5.2.1	EISCAT CP-1-J	64
5.2.2	Observations of an interval of dayside ion frictional heating	65
5.3	Modelling the interval of dayside ion frictional heating with the Sheffield University plasmasphere and ionosphere model (SUPIM)	71
5.3.1	SUPIM - An overview of the model	71
5.3.2	Modelling the interval of dayside ion frictional heating	72
5.3.3	Comparison of EISCAT observations with model results	74
5.3.4	Inclusion of a calculated neutral wind in SUPIM	78
5.3.5	Comparison of EISCAT observations with results of the amended model	79
5.4	Summary and conclusions	81

#### **Chapter 6: E-region ion-neutral coupling during intervals of enhanced electric field**

6.1	Introduction	83
6.2	A new method for the estimation of the normalised ion-neutral collision frequency during intervals of enhanced electric field	83

6.3	Derivation of the normalised ion-neutral collision frequency from EISCAT CP-1-J observations	87
6.3.1	Experimental arrangement	87
6.3.2	EISCAT CP-1-J observations of E- and F-region ion velocity	87
6.3.3	Derivation of the normalised ion-neutral collision frequency	89
6.3.4	Estimation of the neutral wind	93
6.3.5	Revised estimate of the normalised ion-neutral collision frequency	98
6.4	Summary and conclusions	100

#### **Chapter 7: Summary and further work**

7.1	Introduction	101
7.2	Summary of the principal results	101
7.3	Suggestions for further work	103

#### **References**

## **Acknowledgements**

I wish to sincerely thank the following for their contributions during my course of study:

Professor Tudor Jones for his supervision and, with Professor Ken Pounds, for allowing me the opportunity to work in the Physics and Astronomy department at the University of Leicester.

Dr. Mark Lester, for outstanding encouragement and support.

Dr. Terry Robinson and Dr. Ian McCrea for invaluable advice.

Prof. Roy Moffett, Dr. Barbara Jenkins and Linda Wilkinson for their modelling work with the Sheffield University plasmasphere and ionosphere model.

Nigel Wade for his EISCAT expertise and, with Dr Chris Thomas and Andrew Stone, for maintaining the computer system.

Everyone else in the Radio and Space Plasma Physics group, past and present, for their support and assistance, especially Dr. Stephen Milan.

The Director and the staff of the EISCAT scientific association and all of the EISCAT group at Rutherford Appleton Laboratory. EISCAT is an association of the scientific agencies of Finland, France, Germany, Japan, Norway, Sweden and the United Kingdom.

The staff at the World Data Centre, for supplying the geomagnetic indices and the interplanetary magnetic field data.

The Science and Engineering Research Council for funding me through my postgraduate studies.

Special thanks to Matthew Orme and Bagheera for seeing me through to the end of this thesis.

Finally I wish to thank, though he will probably never see this thesis, Ian Johnson.

*This thesis is  
dedicated to  
Dad, Mum and  
Wendy*

## Glossary of terms and symbols

All symbols and abbreviations are defined where they first occur in the text. In addition, those used most frequently are listed below.

ACF	Autocorrelation function	b	Signal bandwidth
<b>B</b>	Magnetic field	$B_y$	y component of the IMF
$B_z$	z component of the IMF	c	Speed of light
CP	Common programme	D	Debye length
$D'$	Ion mach number	e	Electronic charge
<b>E</b>	Applied electric field	$E_{\text{eff}}$	Effective electric field
EISCAT	European incoherent scatter radar	h	Altitude
$k_B$	Boltzmann constant	IMF	Interplanetary magnetic field
$m_e$	Electron mass	$k_p$	Planetary geomagnetic activity index
$m_i$	Ion mass	$m_n$	Neutral mass
$\langle m_n \rangle$	Mean neutral mass	$N_e$	Electron number density
$N_i$	Ion number density	$N_n$	Neutral number density
$P_s$	Signal power	snr	Signal to noise ratio
t	Time	$T_e$	Electron temperature
$T_i$	3-dimensional ion temperature	$T_{ir}$	Line-of-sight ion temperature
$T_{i\parallel}$	Field-parallel ion temperature	$T_{i\perp}$	Field-perpendicular ion temperature
$T_n$	Neutral temperature	$v_e$	Electron vector velocity
UT	Universal time	$v_n$	Neutral vector velocity
$v_i$	Ion vector velocity	$\beta_{\perp}$	Field-perpendicular ion temperature partition coefficient
$\beta_{\parallel}$	Field-parallel ion temperature partition coefficient	$\lambda$	Radar wavelength
$\gamma$	Polarisation angle	$v_{in}$	Ion-neutral momentum transfer collision frequency
$v_{ie}$	Ion-electron momentum transfer collision frequency	$\tau$	Radar pulse length
$\sigma_e$	Direct backscattering cross section of an electron	$\tau_{ni}$	Ion drag time constant
$\phi_{in}/\psi_{in}$	Velocity dependant collision corrections	$\Omega_i$	Ion gyrofrequency

## Chapter 1

### The solar-terrestrial environment

#### 1.1 Introduction

The solar and terrestrial environments couple through the action of radiation, particles and magnetic fields. The aim of the present chapter is to summarise, albeit briefly, solar-terrestrial relations with particular reference to the high-latitude ionosphere and the investigation of this region using ground based radar techniques. An outline of the research documented in this thesis is then presented.

#### 1.2 The solar environment

##### 1.2.1 The sun

The emission of hard and soft X-rays and extreme ultraviolet (EUV) radiation from the solar photosphere is of particular importance in the interaction of the sun with the terrestrial atmosphere, for the reasons discussed in section 1.3.3. Radiation at these wavelengths exhibits, on average, an 11 year periodicity although individual cycles may last from 8 to 14 years. Emission in the ultraviolet varies in flux by a factor of two over a solar cycle and X-radiation by a factor approaching five.

##### 1.2.2 The solar wind

The plasma of the solar atmosphere, the corona, expands under great thermal pressure. Thus a stream of coronal particles, predominantly protons and electrons, flows into interplanetary space. This is the solar wind. At a distance of one astronomical unit (AU), the solar wind velocity is generally within the range 300 to 600 km s<sup>-1</sup> and its concentration is typically between 1x10<sup>6</sup> and 1x10<sup>7</sup> m<sup>-3</sup>, although the occurrence of coronal holes and solar flares causes shocks and plasma density enhancements which can raise the solar wind velocity to more than 1000 km s<sup>-1</sup> and its density to values around 5x10<sup>7</sup> m<sup>-3</sup> (e.g. Gosling *et al.*, 1976; 1978).

##### 1.2.3 The interplanetary magnetic field

The solar wind has, embedded within it, a magnetic field of solar origin, the interplanetary magnetic field (IMF). Close to the sun the interplanetary magnetic field co-rotates with the sun, further out it assumes a spiral form which, at one AU, is typically at an angle of 45° to the radial direction. The interplanetary magnetic field often has a sector structure dividing the ecliptic plane into sunward and antisunward directed field. Figure 1.1 is a schematic representation of the solar wind and the spiral and sector structure of the interplanetary magnetic field. The interplanetary magnetic field configuration typically exhibits two or, as illustrated, four sectors, although at solar maximum there are intervals when the sector structure becomes more complex. Indeed, a study by Hapgood *et al.* (1991), based on satellite observations taken over two complete solar cycles, revealed a

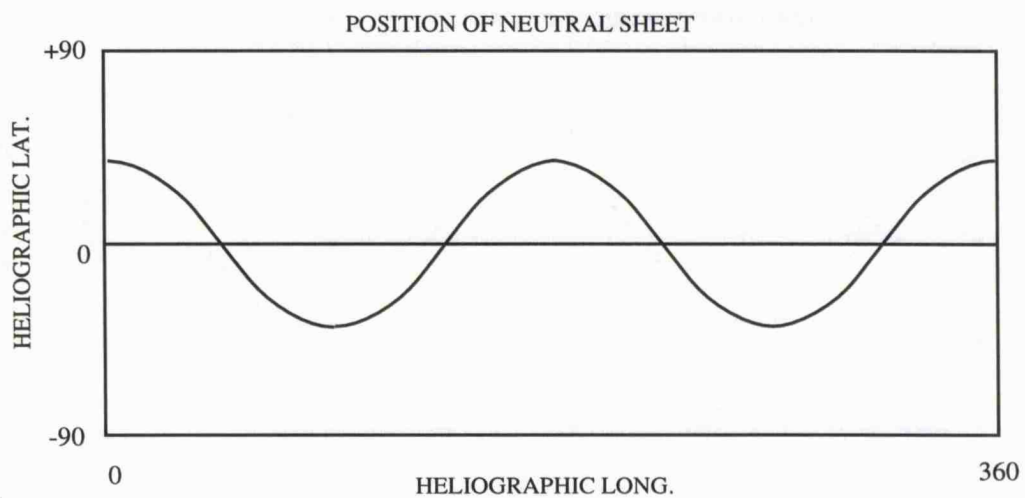
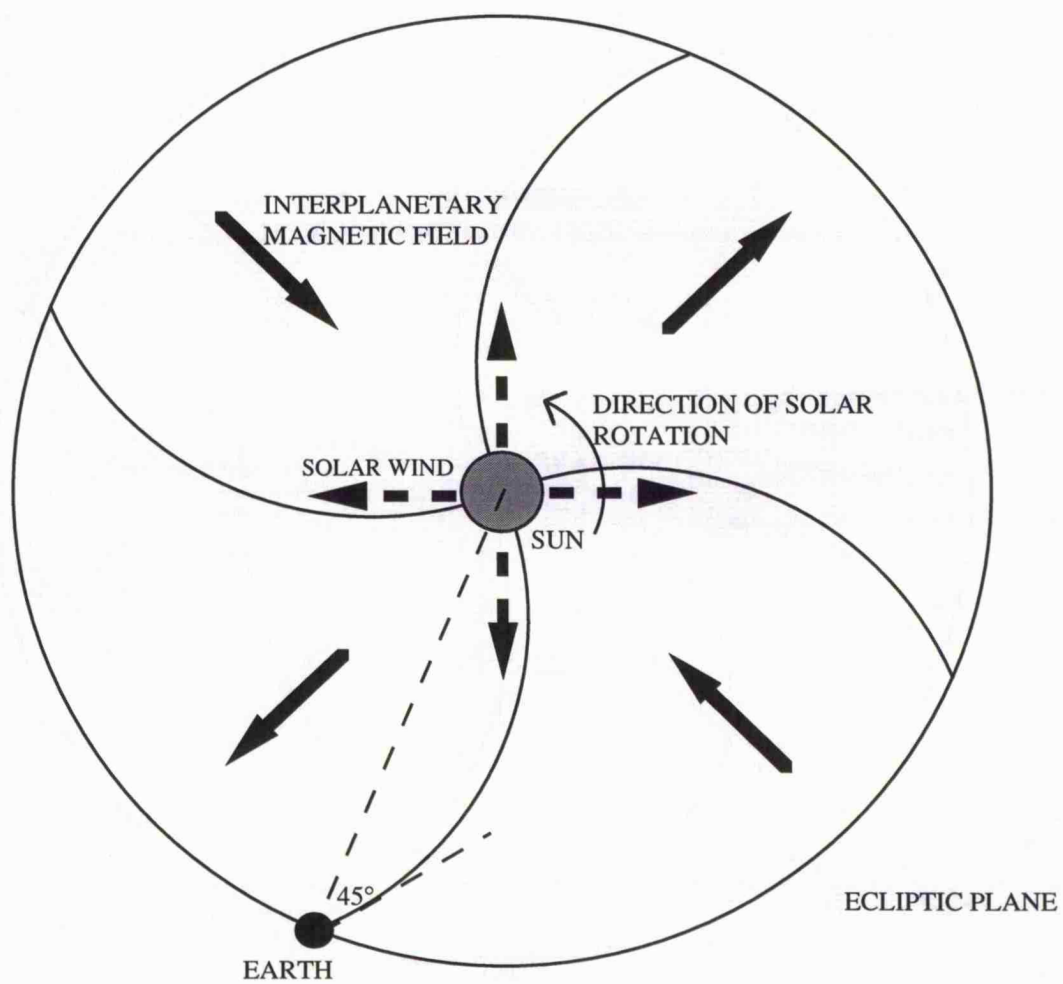


**FIGURE 1.1** Schematic representation of the solar wind and the spiral and sector structure of the interplanetary magnetic field

distinct solar cycle variation in both the IMF and solar wind. The orientation of the component of the interplanetary magnetic field perpendicular to the ecliptic, the z component, has a profound effect on the extent of coupling of solar wind energy into the magnetosphere/ ionosphere system.

### **1.3 The near earth environment**

#### **1.3.1 The magnetosphere**

The Earth has an intrinsic magnetic field, the axis of which is inclined at an angle of some  $12^\circ$  to the Earth's rotational axis. The magnetised plasma of the solar wind impinges on the geomagnetic field, which is compressed but is strong enough to divert the flow thus creating a geomagnetic cavity in the solar wind. This cavity is termed the magnetosphere and at its boundary there exists a current sheet, the magnetopause. The supersonic and super Alfvénic nature of the solar wind results in the formation of the bow shock, a shock wave, upstream of the magnetosphere. The region between the bow shock and magnetopause, the magnetosheath, contains slowed, heated solar wind plasma. On the nightside the magnetic field is drawn into a tail, the magnetotail, the presence of which has been observed out to distances of 1000 Earth radii (*Villante, 1975*). Strictly speaking, the magnetosphere is defined as that region of geospace in which the energy density of the magnetic field exceeds that of the plasma but, as this definition places much of the topside ionosphere within the magnetosphere, the magnetosphere is usually taken as extending outwards from some 1000 km altitude (*e.g. Ratcliffe, 1972*). Figure 1.2 presents a cross-section through the geomagnetic field illustrating the aforementioned regions. The structure of the magnetosphere, and the physical processes which occur within this region of geospace are reviewed by, for example, *Hargreaves (1979)*.

Transfer of energy from the solar wind drives magnetospheric convection by a combination of both viscous interaction (*Axford and Hines, 1961*) and reconnection effects (*Dungey, 1961*), although the relative importance of these processes depends upon the orientation of the z component of the interplanetary magnetic field. The release of energy of solar wind origin in the magnetotail, associated with tailside reconnection, in the so-called substorm expansion phase has a dramatic effect on the behaviour of the nightside ionosphere particularly at high-latitudes (*e.g. McPherron, 1979*).

#### **1.3.2 The neutral atmosphere**

The Earth's neutral atmosphere can be classified according to several schemes. The regions of the neutral atmosphere, classified according to its temperature structure, are illustrated as a function of altitude in figure 1.3. These regions are called the troposphere, stratosphere, mesosphere and thermosphere. The upper altitude boundaries of the troposphere, stratosphere and mesosphere are termed the tropopause, stratopause and mesopause, respectively. Of particular relevance to the present work is the region of the neutral atmosphere above some 90 km altitude, the thermosphere. In the thermosphere the

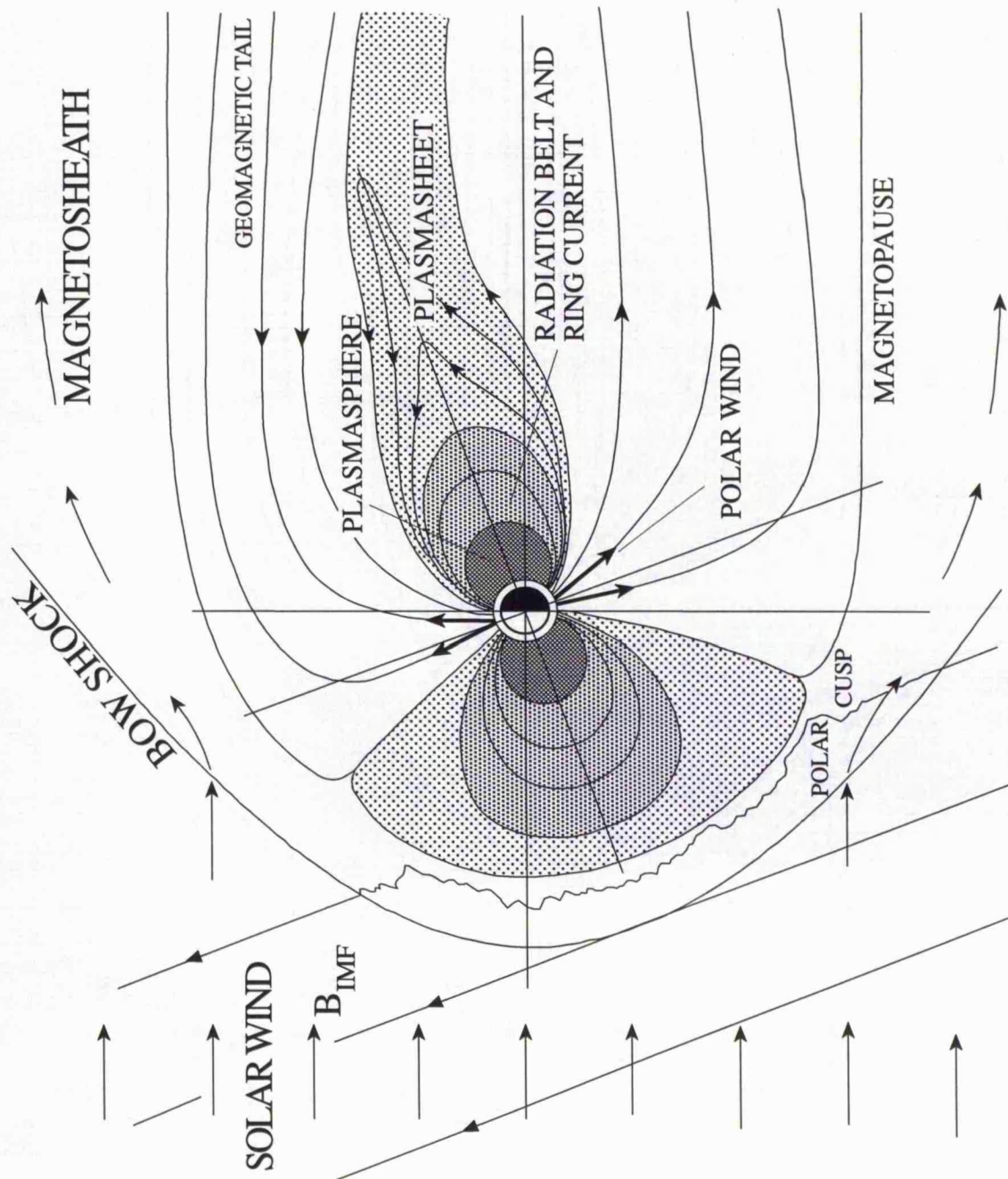


**FIGURE 1.2** Illustration of various regions of the geomagnetic field

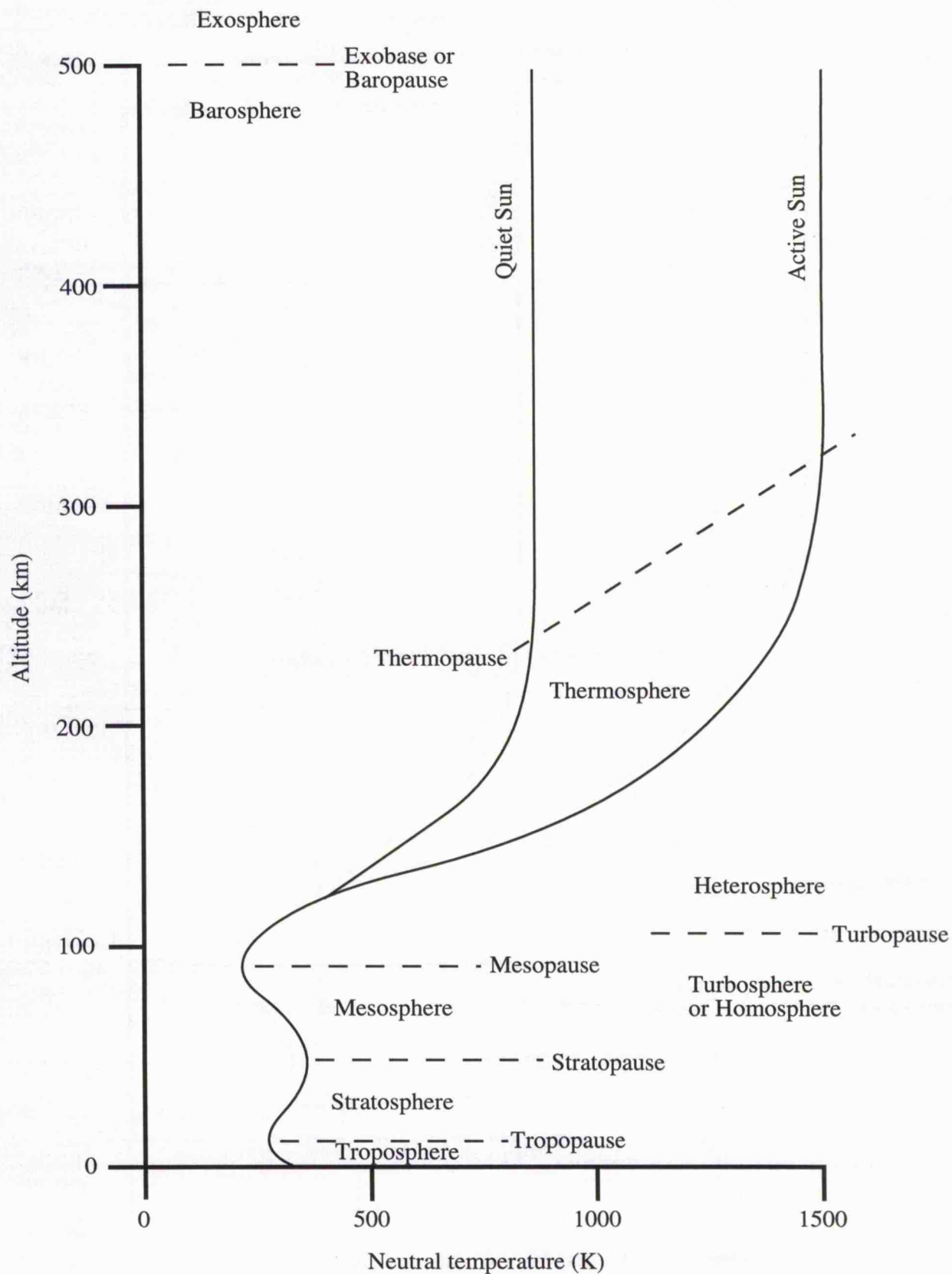


**FIGURE 1.3** Vertical structure of the neutral atmosphere for high and low solar activity

neutral temperature increases rapidly with altitude due to solar heating, principally by the dissociation of molecular oxygen into atomic oxygen, and ionisation, to an approximately constant value at the thermopause. Although the primary source of energy in the thermosphere is the absorption of solar radiation, other mechanisms, such as Joule heating and tidal dissipation, also heat the neutral atmosphere, particularly at high-latitudes. The altitude of the thermopause and its limiting neutral temperature vary diurnally, seasonally and with solar cycle as well as with geographical location.

The major constituents of the neutral atmosphere and their distribution with altitude are presented in figure 1.4 (*Richmond, 1982*). Below the turbopause, which is at an altitude around 110 km, within a region termed the homosphere or turbosphere (see figure 1.3), the constituents are mixed by turbulence and the composition of the neutral atmosphere remains relatively constant with height. Above the turbopause, in the heterosphere, the different species take up a distribution according to their relative masses due to diffusive separation, as the increase in the neutral temperature with altitude makes the atmosphere stable to vertical motion. This gravitational separation causes lighter neutral species to dominate at higher altitudes. Photo-dissociation of molecular oxygen, the rate of which maximises near 100 km altitude, accounts for atomic oxygen constituting the major neutral species between about 200 and 600 km altitude. The distribution of the minor components, such as carbon dioxide and water vapour, is largely controlled by chemical reaction.

The density and pressure of the neutral atmosphere decrease with altitude such that at 50 km they are only about 0.1% of their values at ground level. Below some 500 km altitude, within a region called the barosphere (see figure 1.3), the density of the neutral atmosphere is high enough to provide sufficient collisions to prevent gaseous escape. Above the baropause or exobase, in the exosphere, particles, particularly atomic hydrogen and, to a lesser extent, atomic helium which predominate at exospheric heights, can be lost from the Earth's environment.

The neutral atmosphere is subject to tidal oscillations and is affected by ionospheric motion, particularly in the high-latitude F-region.

### 1.3.3 The ionosphere

Solar electromagnetic radiation is incident on the Earth's neutral atmosphere. Radiation of sufficient energy, specifically the X-ray and EUV part of the solar spectrum, photo-ionises the atmospheric gas, producing a region of ionisation, i.e. free electrons and atomic and molecular ions. The ionosphere is defined as that altitude region containing sufficient free electrons to significantly influence the propagation of radio waves and, for practical purposes, is regarded as extending from 60 to 1000 km. Despite the significant effects of the ionosphere on radio propagation, the charge carriers rarely constitute more than a thousandth of the total concentration at any given altitude. The Earth's ionosphere is reviewed in some detail by such authors as *Schunk (1983)* and *Rishbeth (1988)*.

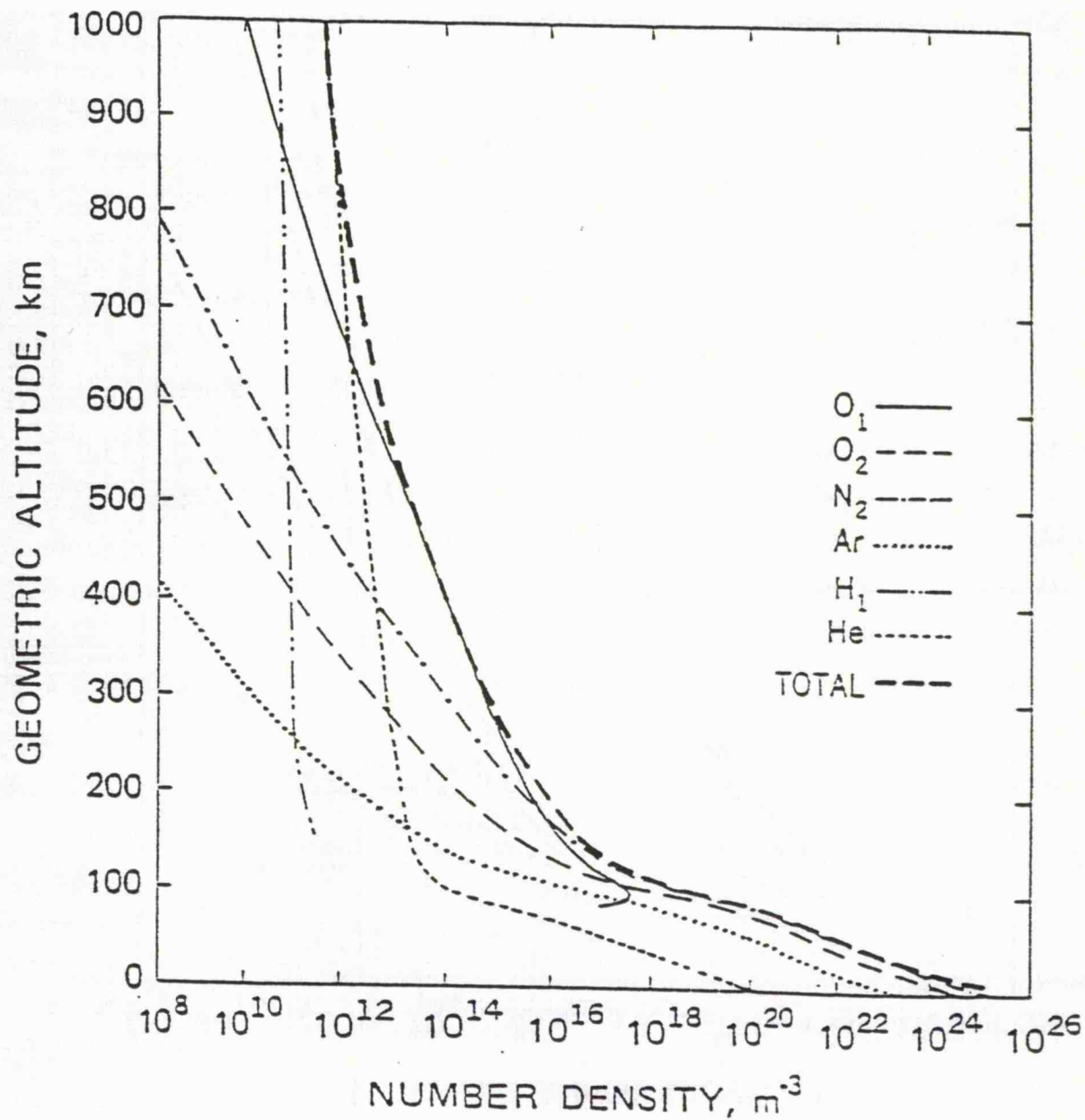


**FIGURE 1.4** Density and composition of the neutral atmosphere as a function of altitude (Richmond, 1982)

Early studies of the ionosphere revealed that it is stratified into distinct layers. There are three main ionospheric layers: the D-, E- and F-regions, although by day the F-region may comprise an F1- and an F2-layer. Idealised electron density profiles through both the day and night-time ionosphere are illustrated in figure 1.5, in which the ionising radiation and principal ion species for each layer are indicated. In addition to the diurnal variation evident from figure 1.5, the plasma concentration exhibits a solar cycle dependence as a consequence of variation in emission in the X-ray and UV portion of the solar spectrum; between solar minimum and solar maximum the peak electron density can vary by a factor exceeding two. Although there is a seasonal variation in the ionospheric electron concentration, at F-region altitudes this is contrary to what might be expected due to solar control; the electron density is greater on the dayside during the winter than in summer. This so-called seasonal anomaly is a consequence of retarded recombination in the winter months. Although the ion species  $N_2^+$ ,  $N^+$ ,  $O_2^+$ ,  $O^+$ ,  $He^+$  and  $H^+$  are the direct products of photo-ionisation, the chemical composition of the ionosphere is dictated by a variety of subsequent ion-ion and ion-neutral reactions along with transport mechanisms such as diffusion. The chemical and physical processes which govern the ionospheric ion composition are discussed more fully by *Rees (1989)*.

The E- and F-regions of the ionosphere are of particular relevance to the present thesis. The E-region is formed mainly by EUV radiation, although, near solar maximum, soft X-rays become significant. The majority of EUV absorption, however, occurs between 160 and 180 km altitude. The principal ion species in the E-region and, if present, the F1-layer are  $O_2^+$  and  $NO^+$ ; the latter is created by chemical reaction rather than direct photo-ionisation. The behaviour of these ionospheric regions is governed by solar production and loss by recombination. In the F2-region, where  $O^+$  is the principal ion species, transport effects become important and are dominant above the F-region peak. Above about 700 km altitude in the topside ionosphere,  $O^+$  is progressively replaced by the light ions,  $H^+$  and  $He^+$ , as a consequence of gravitational separation.

Some striking deviations from normal ionospheric behaviour are found at high- and low-latitudes. To a large extent these arise from the orientation of the geomagnetic field in these regions. At equatorial latitudes the magnetic field lies in a near horizontal direction leading to the equatorial anomaly, a minimum in electron density at the equator caused by the electrodynamic lift of plasma which diffuses under gravity down field lines to higher and lower latitudes where secondary maxima in electron density consequently arise. The behaviour of the high-latitude ionosphere is described in the following section.

#### **1.3.4 The high-latitude ionosphere**

The magnetic field lines which thread the high-latitude ionosphere extend far out into the magnetosphere or even, within the polar cap, open directly into interplanetary space, thus allowing exchange of energy and particles between these regions. In addition to the ionospheric processes described in the previous section, magnetospheric processes

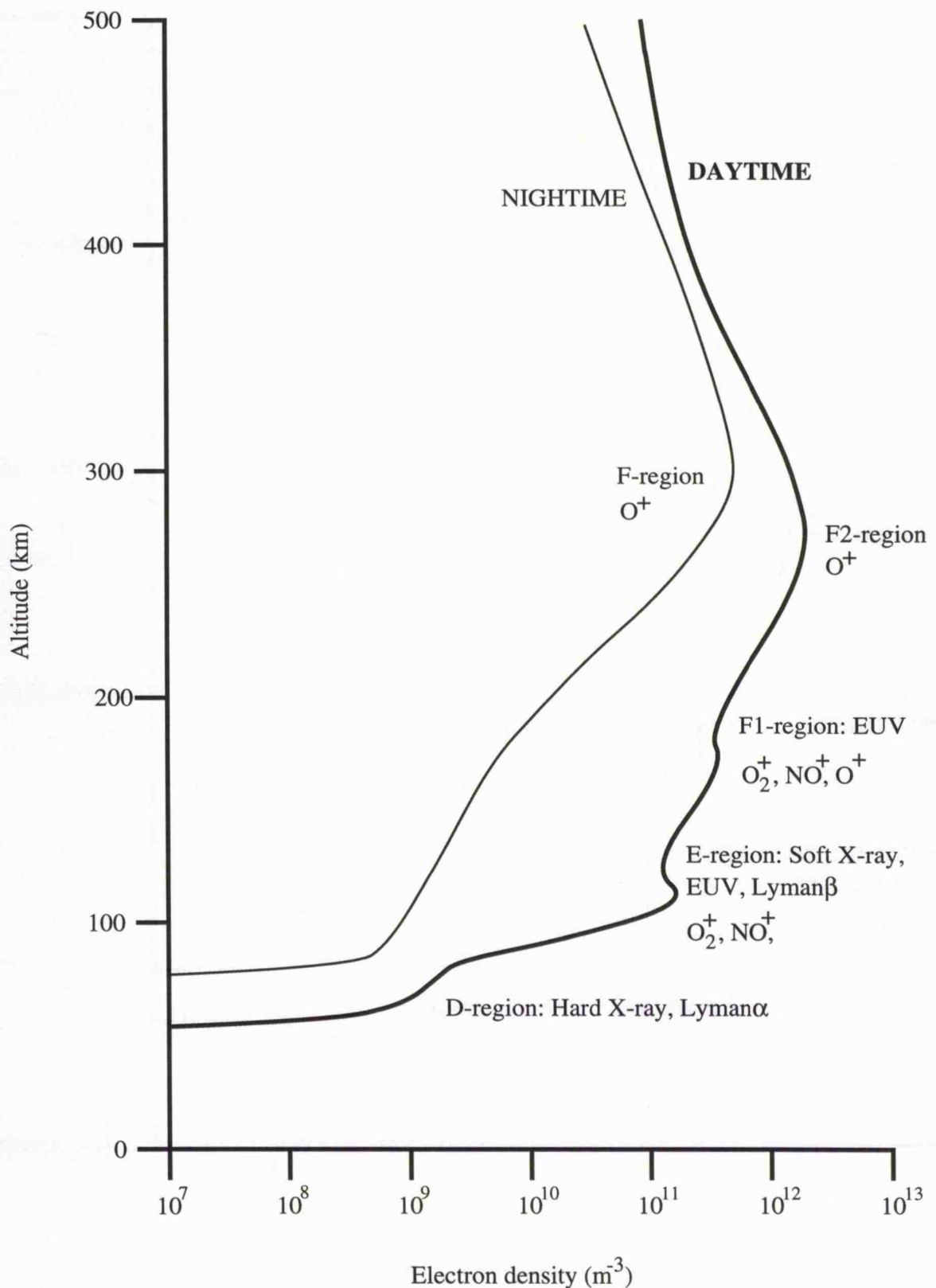


**FIGURE 1.5** Typical mid-latitude electron density profiles for moderate solar activity

will, therefore, have an important effect on the morphology of the high-latitude ionosphere. The morphological regions of the high-latitude ionosphere, described below, are illustrated in figure 1.6.

Open field lines enable the direct entry of solar wind particles into the ionosphere at the polar cap and also the loss of light ions, predominantly  $H^+$  and  $He^+$ , from the exosphere. These processes are termed the polar rain and polar wind, respectively.

The precipitation of highly energetic (1-100 keV) particles from the magnetospheric plasma sheet into the atmosphere at high-latitudes excites neutral species into metastable states. The mechanism by which these precipitating particles, principally electrons and protons, are accelerated to such energies is not yet fully understood. The excited neutrals decay with the emission of photons producing optical aurora. Auroral precipitation is, in general, confined to an irregular high-latitude zone centred on the magnetic pole. This is termed the auroral oval, which extends to lower latitudes on the nightside than on the dayside. The oval expands and its equatorward boundary penetrates to lower latitudes with increasing geomagnetic activity (*Feldstein and Galperin, 1985*).

The main ionospheric trough is a region of depleted F-region electron density, which lies at the equatorward boundary of the nightside auroral oval. Its formation is attributed to, amongst other mechanisms, plasma stagnation and enhanced recombination.

The electric fields set up by magnetospheric convection (see section 1.3.1) map down highly conducting field lines driving high-latitude ionospheric plasma convection, which normally comprises two cells, with antisunward flow over the polar cap and sunward return flow around the flanks (see figure 1.6). Ionospheric convection and its excitation is reviewed by *Lockwood (1991)*. In the F-region, the ion and electron gyrofrequencies greatly exceed their respective collision frequencies with the neutral population and, therefore, under the conditions of an externally applied electric field ( $\mathbf{E}$ ), both ions and electrons move with the  $\mathbf{E} \times \mathbf{B}$  drift velocity, where  $\mathbf{B}$  represents the geomagnetic field. In the upper E-region, however, the electrons move with the  $\mathbf{E} \times \mathbf{B}$  velocity but the ions are collisionally constrained, to some extent, by the neutrals. Magnetospheric electric fields drive the F-region ions at velocities of typically 500 to 1000  $m s^{-1}$  but which frequently exceed 3  $km s^{-1}$ . The response time of the neutral atmosphere in the F-region is of the order of hours, consequently relative ion-neutral velocities can arise. A relative velocity between the ions and the neutral atmosphere causes frictional heating of the ion population (*Rees and Walker, 1968*). Ion frictional heating can double the unperturbed ion temperature and may result in ion composition modification, electron density depletion and is associated with the development of non-Maxwellian ion velocity distributions and anisotropic ion temperatures. Ion frictional heating constitutes a significant mechanism through which magnetospheric energy, originating in the solar wind, may be deposited into the high-latitude ionosphere and ultimately the Earth's neutral atmosphere. Frictional heating is reviewed in detail, in chapter 2.

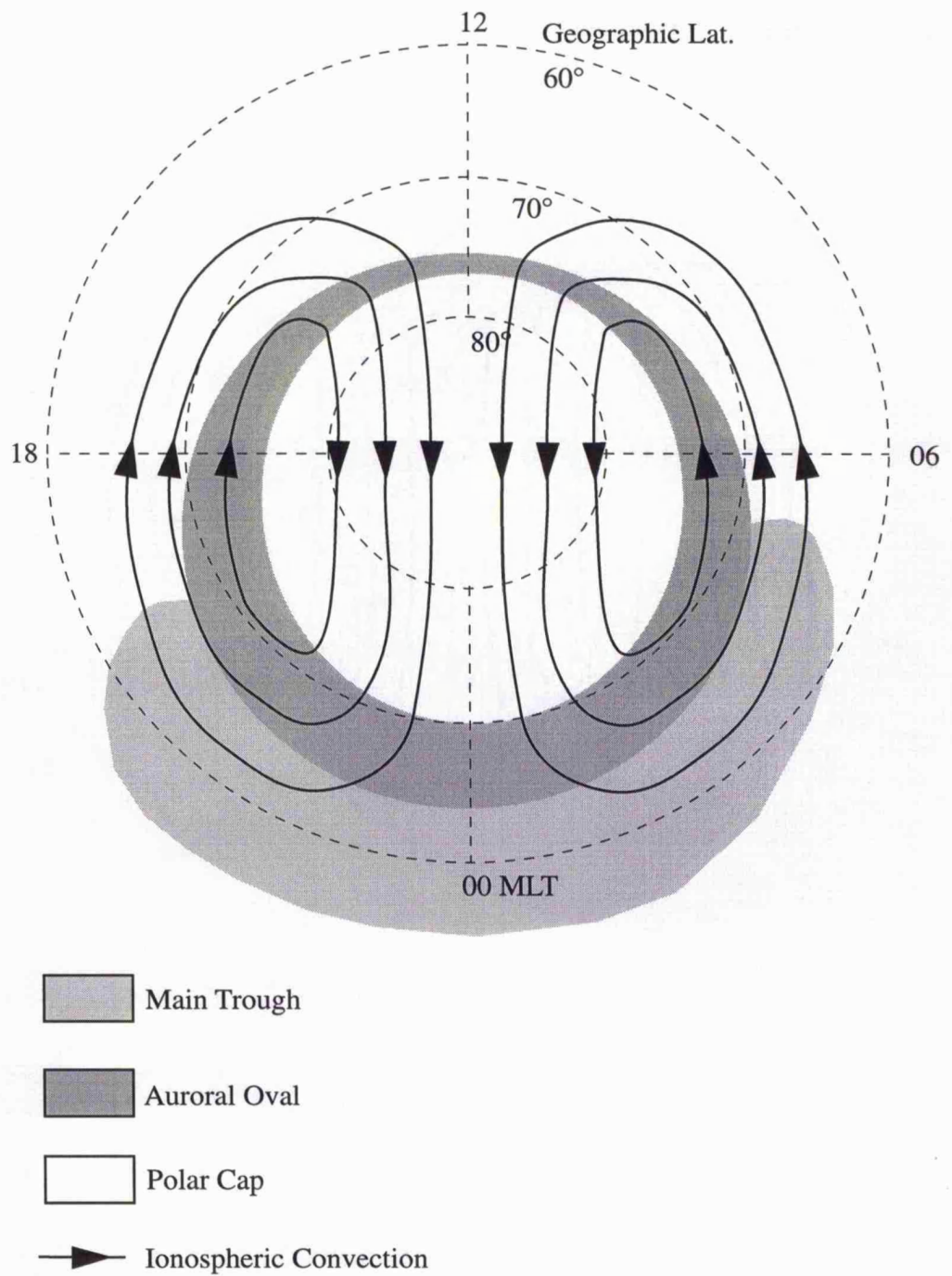


**FIGURE 1.6** Morphology of the high-latitude ionosphere

### 1.3.5 Radar studies of the ionosphere and upper atmosphere

There are two basic techniques employed in the study of the ionosphere and neutral upper atmosphere. The first is the deployment of equipment, such as mass spectrometers and retarding potential analysers, on rockets and man-made satellites to perform *in-situ* measurements. *In-situ* investigation may also be performed by probes, such as magnetometers. Experimental methods of the other type involve remote sensing of the ionosphere and atmosphere by mainly ground based instrumentation, for example optical equipment and radars.

There are various methods of studying the ionosphere and upper atmosphere using radar techniques, each utilising different physical processes and enabling the measurement of different parameters. One of the main distinctions between these methods is the radio frequency required for the physical process involved to be detected. Examples of ground based radar techniques employed for study of the ionosphere and upper atmosphere are total reflection, Faraday rotation, coherent backscatter and incoherent scatter.

Incoherent scatter is possibly the single most important technique for ground based remote study of the ionosphere and upper atmosphere. Transmitted high-powered radio waves scatter off electron- and ion-acoustic waves which, due to the general thermal motion of the plasma, exist naturally in the ionosphere. Analysis of the returned spectrum enables many parameters including electron density, electron and ion temperatures and line-of-sight ion velocity to be directly determined and a variety of others, such as neutral density and temperature, may be derived indirectly. UHF and VHF radio waves provide the optimum frequencies for ionospheric incoherent scatter.

There are currently seven incoherent scatter radar facilities in operation. The principal experimental facility utilised in the present investigation is the European Incoherent Scatter (EISCAT) system, situated in northern Scandinavia (*Rishbeth and Williams, 1985*). This facility comprises both a monostatic VHF and a tristatic UHF radar, and commenced operation in August 1982. The UHF radar of the EISCAT facility is the only tristatic incoherent scatter radar presently in operation. The tristatic nature of the UHF radar enables the full vector ion velocity to be calculated in the volume of intersection of the three receiver beams, and, in addition, permits investigation of anisotropic ion temperatures which exist in the ionospheric plasma during geomagnetically disturbed conditions. An extension to the EISCAT facility, a monostatic UHF radar on the island of Spitsbergen in the Svalbard archipelago, several hundreds of miles North of the Norwegian mainland, has been constructed and is, at present, being tested.

The theory of incoherent scatter and operational characteristics and capabilities of the EISCAT radar facility are discussed in detail in chapter 3.

### 1.4 Aims of the present study

This thesis documents an investigation into various aspects of ion frictional heating

in the high-latitude ionosphere based on observations from the EISCAT radar facility. Ion frictional heating is an important process in the coupling of the solar and terrestrial environments.

A data set comprising nearly 3500 hours of field-aligned EISCAT UHF common programme F-region observations from 1985 to 1990 is employed in a synoptic study of ion frictional heating, documented in chapter 4. Such an extensive data set, covering that part of solar cycle 22 characterised by a general increase in solar activity, is sufficient to enable an investigation into the solar cycle dependence of ion frictional heating to be undertaken, in addition to the determination of any diurnal and seasonal variation.

EISCAT observations during a single interval of ion frictional heating are discussed in detail in chapter 5. The interval is unusual in that it exceeds 4 hours in duration and occurs in the postnoon sector of the dayside ionosphere. The observations of the behaviour of the F-region ionospheric plasma are, in addition, compared with results from the Sheffield University plasmasphere and ionosphere model (SUPIM).

Chapter 6 presents an alternative method by which the ion-neutral collision frequency in the high-latitude E-region may be derived from EISCAT observations under conditions of enhanced electric fields. This technique is illustrated by means of observations from the interval presented in the previous chapter.

## **1.5 Summary**

A brief overview of the interaction of the solar and terrestrial environments has been presented. The chemistry and dynamics of the ionosphere, particularly at high-latitudes, have been discussed as has the investigation of the ionospheric plasma by radar techniques. Finally, the research presented in the remainder of the thesis has been outlined.

## Chapter 2

### Review of ion frictional heating

#### 2.1 Introduction

Relative motion between the ion and neutral populations of the ionosphere results in an enhancement in the temperature of the ions through frictional contact with the neutral atmosphere. This mechanism is termed ion frictional heating and, at auroral latitudes where its occurrence was first indicated by satellite observations, is a manifestation of the coupling between the ionosphere and the magnetosphere. The present chapter describes the phenomenon of ion frictional heating from both a theoretical and observational perspective, and offers a detailed discussion of other physical processes associated with the occurrence of ion frictional heating, such as the deviation of the ion temperature from isotropy and modification of the ion composition. Attempts to model these effects, both locally and globally, are discussed.

#### 2.2 Review of ion frictional heating

The 13 moment approximation of the ion energy balance equation has been discussed extensively by authors including *Schunk (1975, 1977)* and *Banks (1980)* and can be expressed in the following form

$$\begin{aligned} \nabla \cdot \mathbf{q}_i + \boldsymbol{\tau}_i : \nabla \mathbf{v}_i + \frac{5}{2} p_i (\nabla \cdot \mathbf{v}_i) + \frac{D}{Dt} \left( \frac{3}{2} p_i \right) = \\ \sum_n \frac{N_i m_i v_{in}}{m_i + m_n} \left[ 3k_B (T_n - T_i) \Psi_{in} + m_n (\mathbf{v}_i - \mathbf{v}_n)^2 \Phi_{in} \right] + \\ N_i v_{ie} 3k_B (T_e - T_i) + N_i v_{ie} m_e (\mathbf{v}_i - \mathbf{v}_e)^2 \end{aligned} \quad (2.1)$$

in which	$k_B$ = Boltzmann constant $m_n$ = neutral mass $p_i$ = ion pressure $t$ = time $T_i$ = ion temperature $\mathbf{v}_e$ = electron vector velocity $\mathbf{v}_n$ = neutral vector velocity $v_{ie}$ = ion-electron momentum transfer collision frequency $v_{in}$ = ion-neutral momentum transfer collision frequency $\Psi_{in}, \Phi_{in}$ = velocity dependent collision corrections	$m_i$ = ion mass $N_i$ = ion number density $\mathbf{q}_i$ = ion heat flow vector $T_e$ = electron temperature $T_n$ = neutral temperature $\mathbf{v}_i$ = ion vector velocity $\boldsymbol{\tau}_i$ = ion stress tensor
----------	--	---

The terms on the left-hand side of the equation, respectively, represent heat conduction, viscous heating, energy transport due to divergence of the ion flow (adiabatic heating) and convective heating, which comprises both advective and time derivative terms

$$\frac{D}{Dt} \left( \frac{3}{2} p_i \right) = \mathbf{v}_i \cdot \nabla \left( \frac{3}{2} p_i \right) + \frac{\partial}{\partial t} \left( \frac{3}{2} p_i \right) \quad (2.2)$$

The right-hand side of the ion energy balance equation describes thermal energy exchange and frictional heating of the ion population through collisional interaction of the ions with both the neutral atmosphere and the electron gas.

The ion population of the ionosphere generally remains in thermal equilibrium with the neutral atmosphere up to some 250 km altitude. At higher altitudes, ion-neutral collisions become infrequent and significant electron-ion energy exchange, due to the high electron temperature, enhances the temperature of the ions above that of the neutrals (*e.g.* Banks, 1967). Figure 2.1 illustrates typical altitude profiles of neutral, ion and electron temperature during undisturbed summertime conditions for solar maximum (upper panel) and solar minimum (lower panel). Ion temperatures have been derived by the Utah State model, from an ion energy balance equation including the effects of ion-neutral and ion-electron thermal energy exchange, thermal conduction and convective heating (Schunk and Sojka, 1982a). The neutral temperatures presented in figure 2.1 are also taken from this model and the electron temperatures from measurements by the Millstone Hill incoherent scatter radar (Evans, 1971). Modelled profiles are determined for a location within the polar cap, under steady state conditions at local noon.

As suggested by the form of equation 2.1, however, a relative velocity between the ion and neutral populations of the ionosphere results in heating of the ions through frictional contact with the neutral atmosphere, a mechanism which is termed ion frictional heating. The ions are heated in a characteristic time which is the inverse of the ion-neutral collision frequency, of the order of several seconds in the F-region, and, since the ion and neutral masses are comparable, both populations are heated at roughly the same rate although the resultant increase in the neutral temperature is far less than that of the ions due to the much higher concentration of neutral particles. At high-latitudes, ion-neutral relative motion is generated in the ionosphere by the action of ionospheric electric fields. Electric fields, perpendicular to the geomagnetic field, arise as a consequence of the mapping down along highly conducting field lines of magnetospheric convection electric fields. Perpendicular electric fields in the high-latitude ionosphere may also be associated with auroral features and pulsation events, as discussed in section 3.7 of this chapter.

Ion frictional heating in the high-latitude ionosphere has been described extensively in the literature, by such authors as Rees and Walker (1968), Roble and Dickinson (1972), Watkins and Banks (1974), Schunk *et al.* (1975), Kelley and Wickwar (1981), St-Maurice and Hanson (1982) and Killeen *et al.* (1984), and may result in the enhancement of the ion temperature by more than 1000 K. Ion frictional heating constitutes one of the principal mechanisms through which magnetospheric energy, originating in the solar wind, may be deposited into the high-latitude ionosphere. Indeed, under disturbed conditions, up to a quarter of the total power extracted from the solar wind

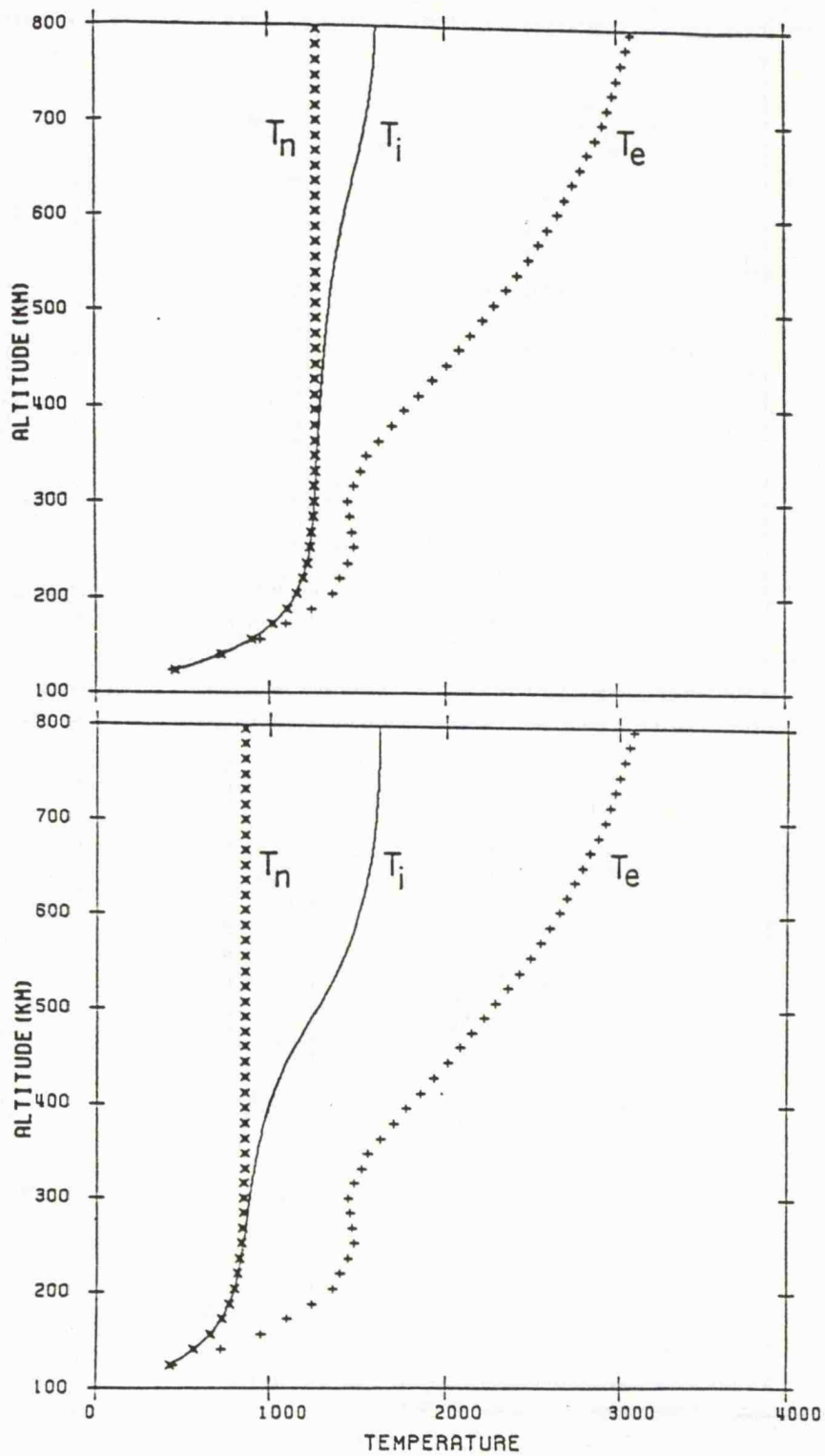


FIGURE 2.1 Typical profiles of ion, neutral and electron temperature for conditions of solar maximum (upper panel) and solar minimum (lower panel) (Schunk and Sojka, 1982a).

by the magnetosphere-ionosphere system, some  $10^{12}$  Watts, is deposited in the high-latitude ionosphere by ion frictional heating (*e.g. Weiss et al., 1992*). This is equivalent to the power produced by 10000 major power stations.

The response of the velocity of the ionospheric ion population to an applied electric field,  $\mathbf{E}$ , depends greatly on altitude (*e.g. Fedder and Banks, 1972*). The relative velocity between the ions and the neutral atmosphere at a given altitude, resulting from an electric field applied perpendicular to the magnetic field  $\mathbf{B}$ , may be expressed in the form of equation 2.3 below.

$$\mathbf{v}_i - \mathbf{v}_n = \frac{1}{1 + (\mathbf{v}_n/\Omega_i)^2} \left[ \frac{\mathbf{E}_{\text{eff}} \times \mathbf{B}}{B^2} + \frac{\mathbf{v}_n \mathbf{E}_{\text{eff}}}{\Omega_i B} \right] \quad (2.3)$$

where  $\mathbf{E}_{\text{eff}}$  is the effective electric field, the electric field in the frame of the neutral atmosphere, at that altitude and can be written in the form

$$\mathbf{E}_{\text{eff}} = \mathbf{E} + \mathbf{v}_n \times \mathbf{B} \quad (2.4)$$

The ion gyrofrequency,  $\Omega_i$ , is given by the standard formula

$$\Omega_i = \frac{eB}{m_i} \quad (2.5)$$

in which  $e$  represents the electronic charge. Above about 150 km altitude, where the ion gyrofrequency greatly exceeds the ion-neutral collision frequency, the ions move, in the frame of reference of the geomagnetic field, approximately with the  $\mathbf{E} \times \mathbf{B}$  drift in the field-perpendicular direction; in the absence of an applied electric field F-region plasma motion is confined to the magnetic field direction. With decreasing altitude through the lower F- and E-regions, the increasing effect of ion-neutral collisions rotates the relative ion-neutral velocity vector towards the direction of the effective electric field and, furthermore, leads to a reduction in the magnitude of the differential ion-neutral velocity; the lower E-region ions being collisionally constrained to move with the neutral wind. Large electric fields can, however, drive the F-region ions through the neutral atmosphere at speeds which may exceed several  $\text{km s}^{-1}$  (*e.g. Schunk and Walker, 1972*).

The occurrence of ion frictional heating was first indicated by the observation of structured and enhanced ion temperatures in the high-latitude F-region by satellite borne probes, reported by *Harris et al. (1967)* and *Knudsen and Sharp (1967)*. Figure 2.2 illustrates satellite observations of ion temperature as a function of latitude from the Explorer 2 satellite, as presented by *Harris et al. (1967)*. Measurements made with the Chatanika incoherent scatter radar confirmed observationally the role of elevated ion velocities in the enhancement of the ion temperature through frictional heating, as illustrated in figure 2.3 (*Watkins and Banks, 1974*). The first truly quantitative studies of the relationship between ion temperature and ion velocity employed high-latitude

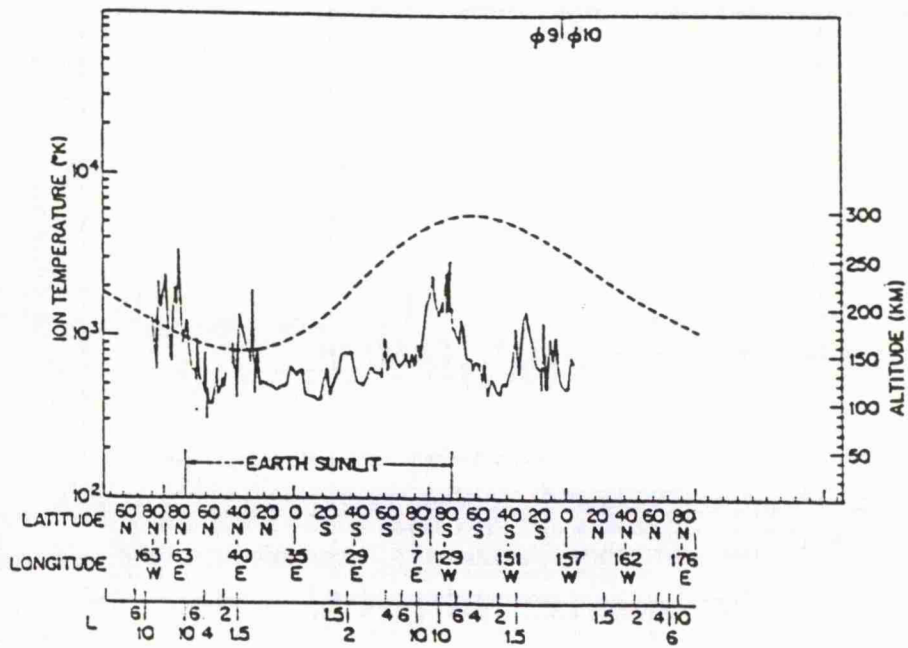


FIGURE 2.2 Ion temperature as a function of latitude during an orbit of the Explorer 2 satellite (*Harris et al., 1967*). The dotted line represents the altitude of the satellite.

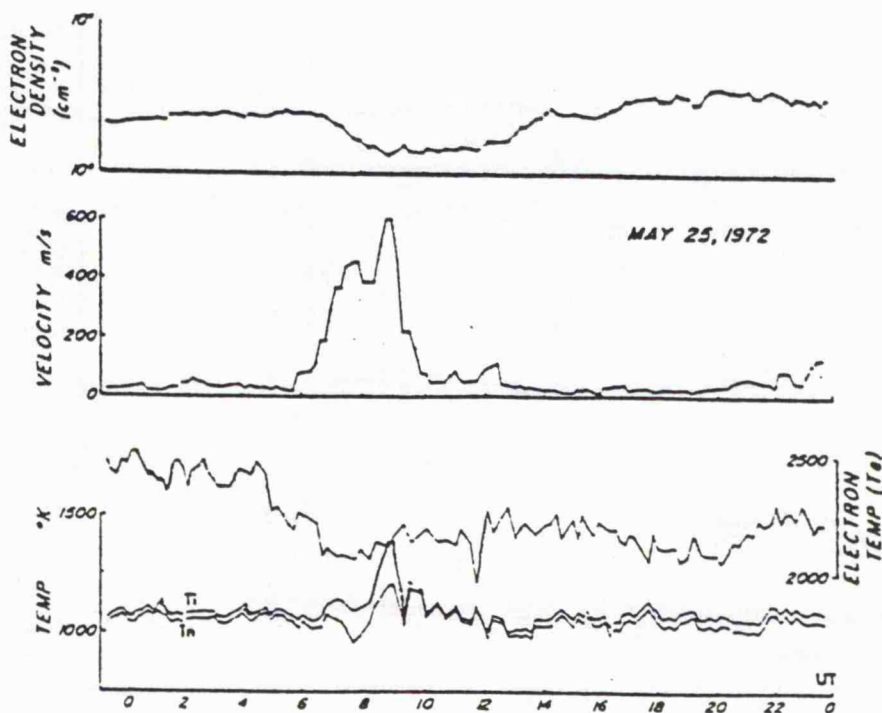


FIGURE 2.3 Plasma parameters measured by the Chatanika radar during an interval of ion frictional heating (*Watkins and Banks, 1974*).

observations by the Atmospheric Explorer-C satellite. Observations from two orbits of the Atmospheric Explorer satellite-C are illustrated in figure 2.4 (*St-Maurice and Hanson, 1982*). For each high-latitude pass, the perpendicular ion velocity vector along the track of the satellite is illustrated, as is the velocity magnitude and the ion temperature. The work presented by *St-Maurice and Hanson (1982)* revealed a high-degree of correlation between the ion velocity and temperature indicating a first-order balance between frictional heating and cooling rates. Although ion frictional heating is generally associated with enhancements in the ion velocity, a small frictional heating effect has been observed at mid-latitudes due to the action of neutral winds (*Stubbe and Chandra, 1971*).

The generalised ion energy balance equation, equation 2.1, can be greatly simplified for F-region conditions of strong ion frictional heating (*e.g. St-Maurice and Hanson, 1982*). Above approximately 150 km altitude in the F-region, under the influence of an imposed electric field, both ion and electron populations drift together with the  $\mathbf{ExB}$  drift and, assuming no ion-electron relative drift occurs in the field-parallel direction, the term on the right hand side of equation 2.1 containing the differential ion-electron velocity can be neglected. In addition, all of the terms on the left hand side of equation 2.1 can normally be discounted at F-region altitudes in the presence of strong electric fields. Viscous heating is small for phenomena occurring on spatial scale lengths longer than a few kilometres in the F-region and the time derivative term of convective heating is negligible for time scales longer than a few seconds (*Schunk, 1975*). The divergence of the ion velocity can be ignored as the flow is essentially incompressible (*Rishbeth and Hanson 1974*). *Schunk and Sojka (1982a)* studied the effect of advection and heat conduction on ion energy balance and concluded that these terms are usually unimportant at altitudes below some 500 km. Under these simplifying assumptions the ion energy balance equation becomes

$$\sum_n \left( \frac{m_i v_{in}}{m_n + m_i} \right) 3k_B (T_i - T_n) \psi_{in} \approx \sum_n \left( \frac{m_i v_{in} m_n}{m_n + m_i} \right) (\mathbf{v}_i - \mathbf{v}_n)^2 \phi_{in} + v_{ie} 3k_B (T_e - T_i) \quad (2.6)$$

Equation 2.6 represents the ion energy balance equation for a thermosphere comprising a number of neutral species; for a neutral atmosphere dominated by a single species, the energy balance equation may be further simplified

$$3k_B (T_i - T_n) \psi_{in} \approx m_n (\mathbf{v}_i - \mathbf{v}_n)^2 \phi_{in} + \left( \frac{m_n + m_i}{m_i} \right) \frac{v_{ie}}{v_{in}} 3k_B (T_e - T_i) \quad (2.7)$$

The quantities  $\phi_{in}$  and  $\psi_{in}$  are corrections for the velocity dependence of the ion-neutral collision cross-section which remain, to a good degree of approximation, unity for all ion-

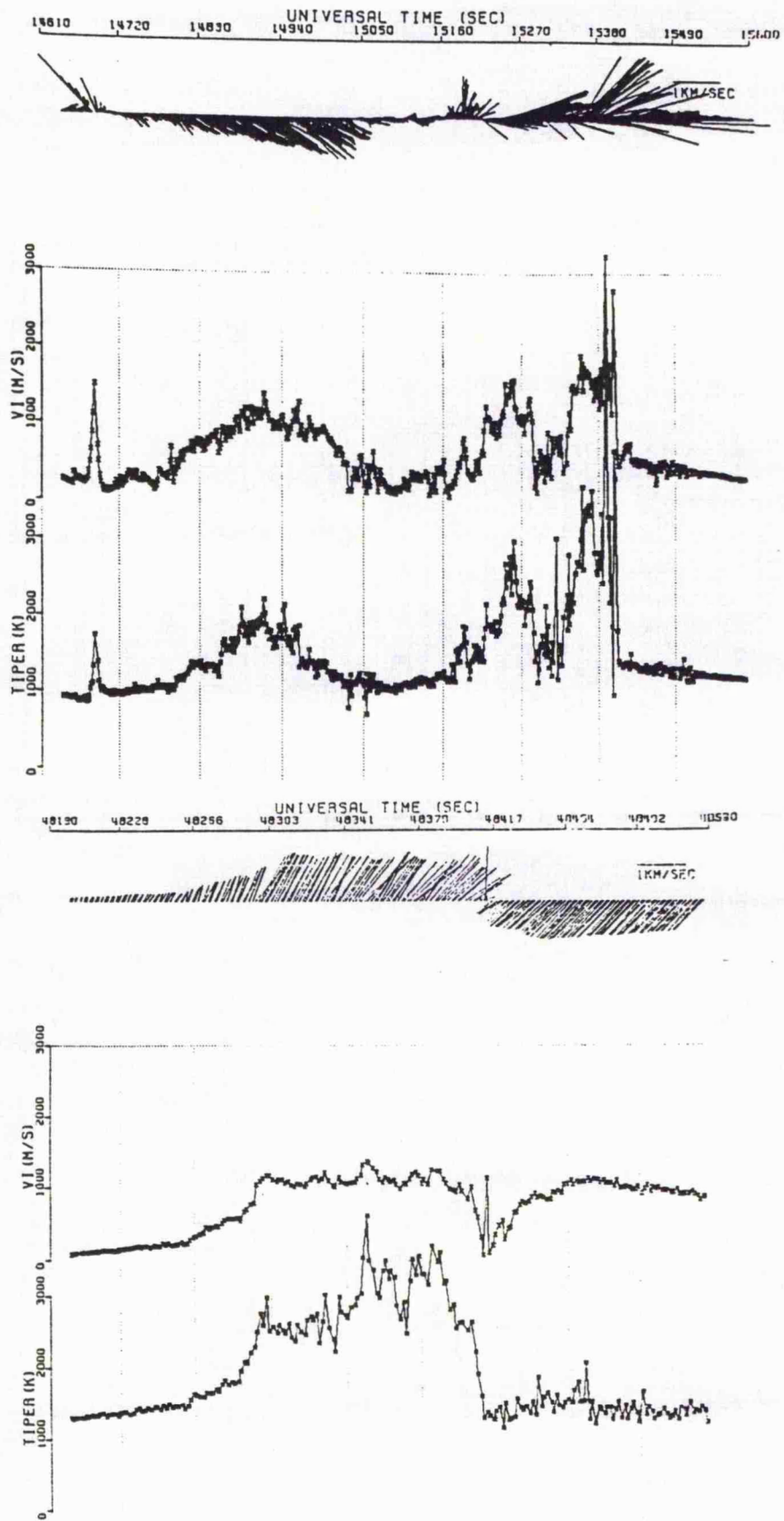


FIGURE 2.4 High-latitude ion velocity and ion temperature measurements by the Atmospheric Explorer satellite during two orbits (*St-Maurice and Hanson, 1982*).

neutral interactions (*St-Maurice and Hanson, 1982*). The second term on the right hand side of equation 2.4 describes electron-ion thermal energy exchange, which is usually of the order of several tens of degrees. The equation describes steady state conditions implying that the energy acquired by the ions through frictional heating is instantaneously redistributed locally to the neutral gas. The direct frictional heating of the neutral gas plus the ion-neutral heat exchange is referred to as Joule heating, most of which energy is deposited at E-region altitudes (*e.g. Cole, 1961; 1962; Banks, 1980*). Joule heating is an important source of energy deposition into the high-latitude neutral atmosphere and, for large electric fields, the magnitude of the Joule heating rate can exceed that due to solar heating.

The response of the ionospheric plasma to an external perpendicular electric field was modelled, using the Utah State model, by *Schunk and Sojka (1982a)*. Figure 2.5 illustrates modelled ion temperature profiles under steady state conditions at local noon for an effective electric field of  $100 \text{ mV m}^{-1}$  for low (L) and high (H) magnetic activity in both summer (crosses) and wintertime (full line). The upper panel represents solar maximum and the lower panel, solar minimum conditions. An elevation in the ion temperature at all altitudes, but particularly in the lower F-region, was predicted, the magnitude of which was found to be dependent on both solar and geomagnetic conditions. Furthermore, the global response of the ion temperature to enhancements in the convection electric field was modelled, again with the Utah State model, by *Schunk and Sojka (1982b)*. The authors predicted the formation of single or double 'hot spots' in F-region ion temperature, depending on whether the ion drift velocity was enhanced in one or both convection cells. Ion temperature predictions for 340 km altitude at successive instants during the modelled storm of *Sojka and Schunk (1984)* are presented in figure 2.6, in which the shaded areas correspond to ion temperatures exceeding 1600 K. The figure indicates highly elevated ion temperatures in the enhanced dusk convection cell. The work of *Sojka and Schunk (1984)* does not, however, include a self-consistent neutral wind. Indeed, modelling work with coupled ionosphere-thermosphere models indicated, contrary to the work of *Sojka and Schunk (1984)*, that enhanced ion temperatures were more likely to be observed in the dawn sector (*e.g. Lockwood and Fuller-Rowell, 1987a; 1987b*). The action of neutral wind tends to suppress ion frictional heating preferentially in the pre-midnight hours (see section 2.3.3).

The occurrence of ion-neutral relative velocities and elevated ion temperatures, in response to enhancements in the ionospheric electric fields, further modifies the ionospheric plasma. Subsequent sections detail effects such as the distortion of the ion thermal velocity distribution from an isotropic Maxwellian, the modification of the ion composition and the depletion of electron concentration which may be associated with the occurrence of ion frictional heating.

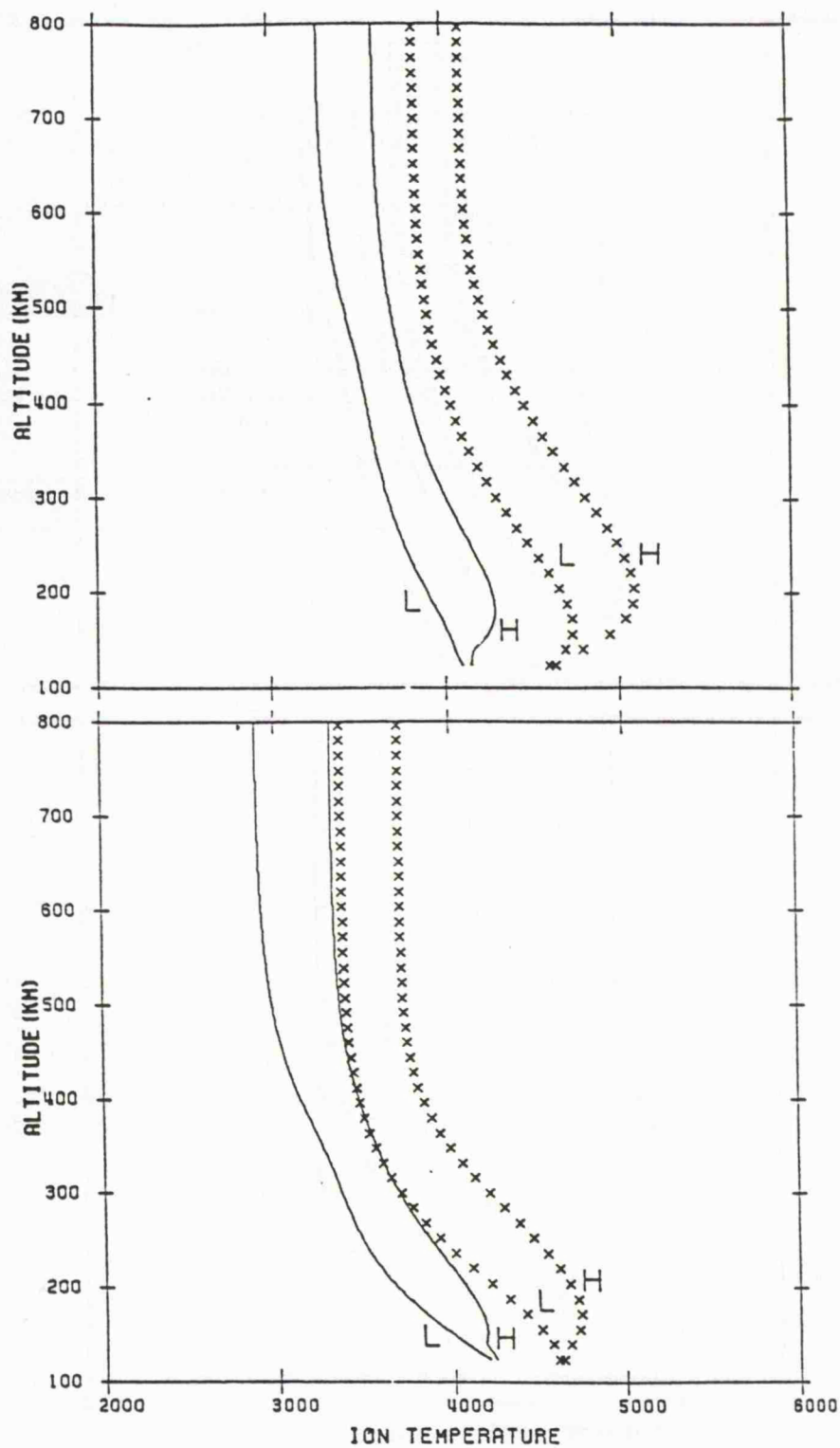


FIGURE 2.5 Modelled profiles of ion temperature for a meridional electric field of  $100 \text{ mV m}^{-1}$  under conditions of high (H) and low (L) geomagnetic activity for solar maximum (upper panel) and solar minimum (lower panel) (Shunk and Sojka, 1982a). The crossed and solid lines represent summer and wintertime profiles, respectively.

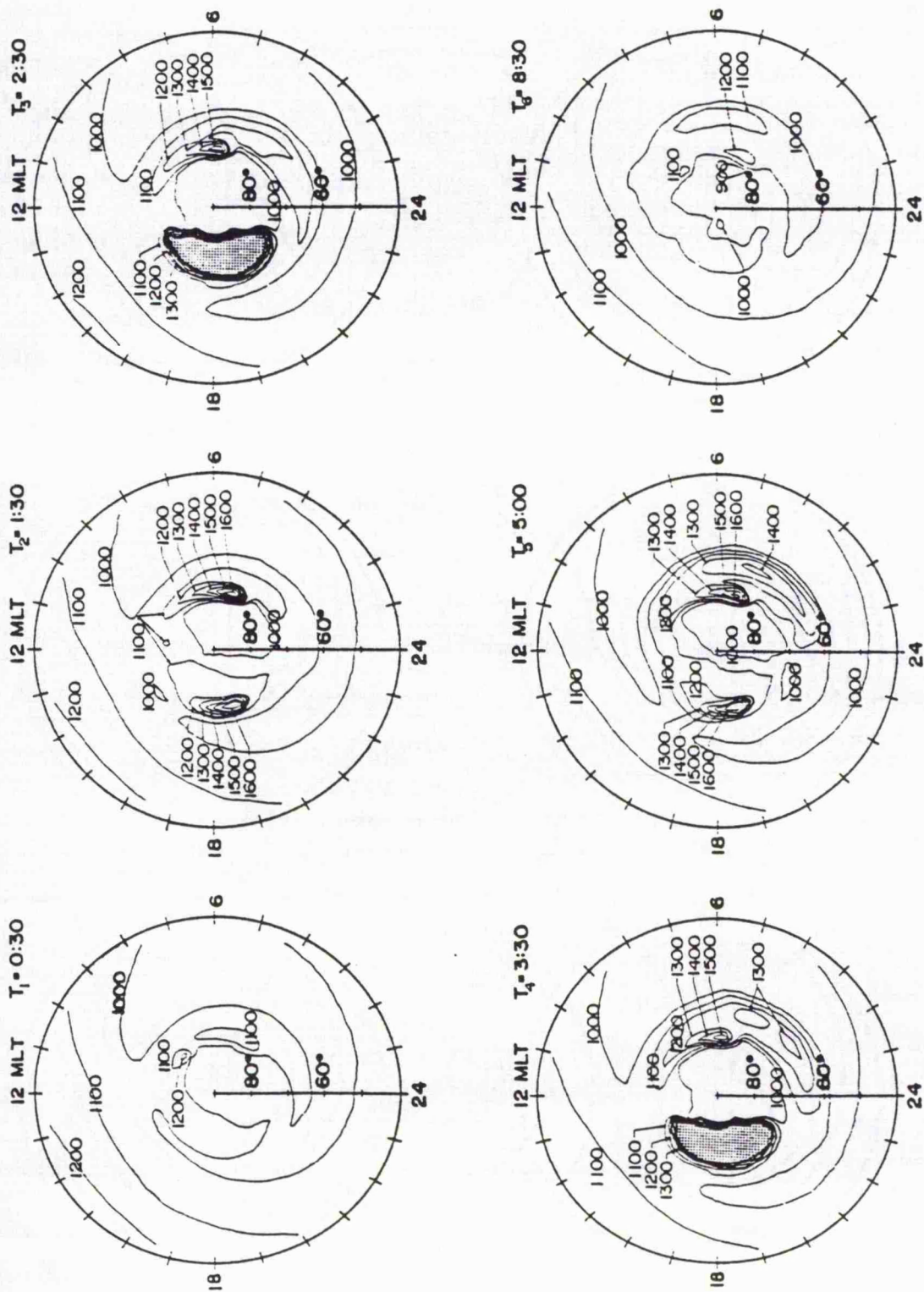


FIGURE 2.6 Global F-region ion temperature predictions at 6 successive times during a modelled magnetic storm (Sojka and Schunk, 1984).

## 2.3 Phenomena associated with ion frictional heating

### 2.3.1 Non-Maxwellian ion thermal velocity distributions

In the unperturbed ionosphere the 3-dimensional ion thermal velocity distribution takes the form of an isotropic Maxwellian. *Cole (1971)* first predicted theoretically that a large relative velocity between the ion and neutral populations of the ionosphere would result in significant distortion of the ion thermal velocity distribution from an isotropic Maxwellian. As discussed in the previous section, such ion-neutral relative velocities arise in the high-latitude ionosphere, through the action of electric fields of magnetospheric origin. The form of the ion thermal velocity distribution under the influence of enhanced electric fields has since been the subject of much theoretical work, including that of *Schunk and Walker (1972)*, *St-Maurice and Schunk (1973, 1974, 1977, 1979)*, *Hubert (1982, 1983, 1984)*, *Bakar et al. (1983)*, *Hubert and Kinzelin (1992)* and *Winkler et al. (1992)*.

The existence of a relative velocity between the ions and neutrals causes the thermal distribution functions of the two populations to diverge, although constantly occurring ion-neutral collisions allow a steady state ion velocity distribution to form in a time inversely proportional to the ion-neutral collision frequency. The degree of distortion of the ion thermal velocity distribution from a Maxwellian depends upon both the type and frequency of ion-neutral collisions and the direction relative to the magnetic field, as discussed by *Hubert and Kinzelin (1992)*, amongst others. In the ionosphere, resonant charge exchange and polarisation interactions comprise the dominant collisional mechanisms at E- and F-region altitudes where non-Maxwellian distributions can form; these types of interaction are addressed below. When an ion collides with a neutral atom or molecule, the resultant interaction consists of long range polarisation attraction combined with short-range repulsion. Such collisions constitute non-resonant interactions. However, for collisions involving an ion and its parent neutral, for example  $O^+-O$  collisions, in addition to a polarisation type interaction, resonant charge exchange can occur and will, indeed, dominate the collision frequency at temperatures over a minimum value dependent on the species involved, 235 K for the above interaction. A detailed review of the collision processes governing many ion-neutral interactions is given by *Banks (1966)*.

*St-Maurice and Schunk (1973, 1974)* theoretically determined the form of the ion thermal velocity distribution for a collision model which comprised direct backscatter, the so-called relaxation collision model. Although the relaxation collision model constitutes only an idealised collision mechanism, it proved useful in illustrating the effects of collisions on the ion velocity distribution. Subsequent work by *St-Maurice and Schunk (1977)* and *Hubert (1982, 1983)*, however, employed more physically realistic collision models, corresponding to polarisation and resonant charge exchange type interactions in

situations where the ion gyrofrequency greatly exceeds the ion-neutral collision frequency, appropriate to F-region altitudes. For small electric fields, the authors demonstrated that the 3-dimensional ion thermal distribution could be well described by a bi-Maxwellian, a combination of two different Maxwellians, one in the direction parallel to the magnetic field, the other in the field-perpendicular direction. With increasing electric field, however, the 3-dimensional ion velocity distribution was shown to assume a toroidal form. Figure 2.7 demonstrates the deviation of the ion thermal velocity distribution from a bi-Maxwellian for both polarisation and resonant charge exchange types of collision for values of  $D'$  of 0.5, 1.0 and 1.5 where  $D'$  is the so-called ion Mach number, the ratio of the relative ion-neutral drift to the two-dimensional neutral thermal speed (*St-Maurice and Schunk, 1977*).  $D'$ , which as a ratio of two speeds is dimensionless, takes the form

$$D' = \left( \frac{\langle m_n \rangle}{2k_B T_n} \right)^{\frac{1}{2}} (|\mathbf{v}_i - \mathbf{v}_n|) \quad (2.8)$$

in which  $\langle m_n \rangle$  is the mean neutral mass which may be represented (*e.g. Schunk and Walker, 1972*)

$$\langle m_n \rangle = \frac{\sum_n v_{in} m_n / (m_i + m_n)}{\sum_n v_{in} / (m_i + m_n)} \quad (2.9)$$

For a neutral population dominated by a single species the mean neutral mass is simply equivalent to the mass of that species. Figure 2.7 illustrates the distortion from a bi-Maxwellian in both the magnetic field-parallel and Hall ( $\mathbf{E} \times \mathbf{B}$ ) direction, the latter representative of the deviation in both field-perpendicular directions (contours represent the ratio of the actual distribution to a bi-Maxwellian, axes are the random ion velocities in the parallel and Hall directions, represented by  $C_{\parallel}$  and  $C_H$  respectively, normalised by the two-dimensional ion thermal speed,  $V_{Ti}$ ). For values of  $D'$  greater than unity, corresponding to a perpendicular electric field of some  $50 \text{ mV m}^{-1}$ , the velocity distribution significantly deviates from a bi-Maxwellian, although the perturbation from a line-of-sight Maxwellian is far greater in the direction perpendicular to the field than in the field-parallel direction. Furthermore, the 3-dimensional ion thermal velocity distribution is more distorted for resonant charge exchange interactions than for polarisation type collisions, although, for a given electric field, departures from a bi-Maxwellian distribution increase for polarisation collisions with increasing ion to neutral mass ratio; the lower panel of figure 2.7 represents an ion to neutral mass ratio of unity.

Although the ion thermal velocity distribution remains gyrotropic (symmetric with respect to the magnetic field) in the F-region where the ions are magnetised, at altitudes in the E-region where the ion-neutral collision frequency is comparable to the ion gyrofrequency the ion thermal velocity distributions in the Hall and Pedersen ( $\mathbf{E}$ )

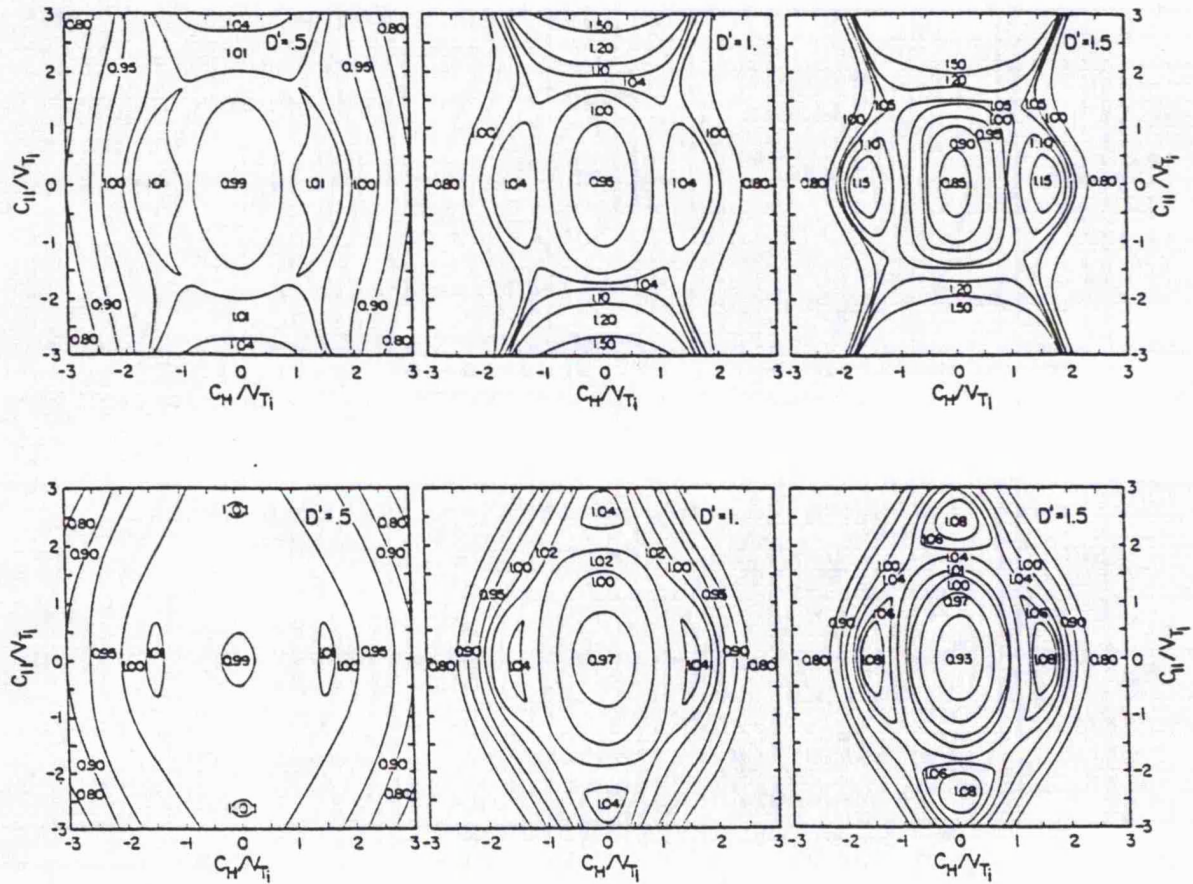


FIGURE 2.7 Deviation of the ion thermal velocity distribution function from a bi-Maxwellian for  $D'$  of 0.5, 1.0 and 1.5 for resonant charge exchange collisions (upper panel) and polarisation collisions (lower panel) (*St-Maurice and Schunk, 1977*).

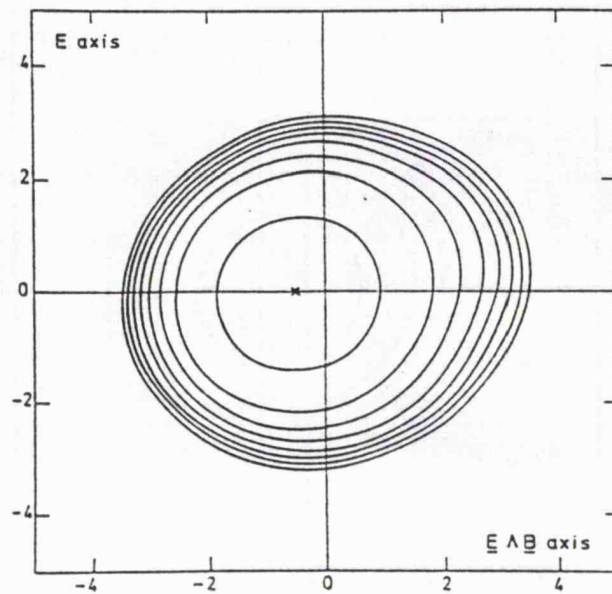


FIGURE 2.8 Predicted deviation of the ion velocity distribution function in the field-perpendicular plane from a Maxwellian for equal ion-neutral collision and ion gyro frequencies and polarisation collisions (*Hubert, 1984*).

directions diverge somewhat (*e.g. St-Maurice and Schunk, 1973; 1974; Hubert, 1984*). This feature is illustrated in figure 2.8, taken from the work of *Hubert (1984)*. Figure 2.8 presents the predicted deviation of the ion velocity distribution in the field-perpendicular plane from a Maxwellian for equal ion-neutral collision and ion gyrofrequencies and for a value of  $D'$  of 3. The collision model adopted is that appropriate to polarisation collisions for an ion to neutral mass ratio of unity. Contour levels decrease by a factor  $e^{1/2}$  from the maximum shown by the cross, and are plotted against the normalised random ion velocities in the Hall and Pedersen directions. The 3-dimensional ion thermal velocity distribution can be well represented by a tri-Maxwellian even for intense electric fields. At lower altitudes where the collision to gyrofrequency ratio greatly exceeds unity, the two field-perpendicular distributions reconverge.

In addition to the effect of ion-neutral collisions, Coulomb (ion-ion and ion-electron) interactions can have a significant effect on the ion thermal velocity distribution, especially in the upper F-region where ion-neutral collisions become more infrequent. Ion-ion and ion-electron collisions act to stabilise the ion velocity distribution, as discussed theoretically by such authors as *St-Maurice and Hanson (1982)*, *Løvhaug and Flå (1986)* and, more recently, *Tereshchenko et al. (1991)*.

The first experimental evidence of non-Maxwellian ion thermal velocity distributions in the ionospheric plasma, reported by *Swift (1975)*, was provided by observations from the Chatanika incoherent scatter radar. Later authors, for example *Raman et al. (1981)*, have, however, largely discredited Swift's interpretation that these observations indicated the presence of non-Maxwellian velocity distributions; the observations were at E-region altitudes with very poor spatial resolution. The occurrence of non-Maxwellian velocity distributions in the ionosphere was subsequently confirmed by F-region observations from the Atmospheric Explorer-C satellite, documented by *St-Maurice et al. (1976)*; the authors noted that the velocity distribution perpendicular to the magnetic field diverged significantly from a Maxwellian form during periods of high ion-neutral relative velocities, the latter identified by large ion temperatures. *Yau et al. (1983)* presented observations from sounding rockets which also highlighted the occurrence of distinctly non-Maxwellian F-region ion thermal velocity distributions, although their formation was attributed to ion-cyclotron waves in a region of accelerating ions during the expansive phase of a substorm rather than the presence of large electric fields. Observations by the EISCAT incoherent scatter radar have also indicated non-Maxwellian line-of-sight ion thermal velocity distributions, particularly at large aspect angles (*e.g. Lockwood et al., 1987; Winser et al., 1987; 1989; Moorcroft and Schlegel, 1988*). EISCAT observations implying non-Maxwellian ion velocity distributions, with particular reference to their significance with respect to the interpretation of incoherent scatter data, are discussed in the following chapter.

Modelling of the distribution of non-thermal plasma in the ionospheric F-region (*Lockwood and Fuller-Rowell, 1987a; 1987b; Farmer et al., 1988*) predicted the

occurrence of non-Maxwellian ion velocity distributions under disturbed geomagnetic conditions, but particularly in the morning sector as confirmed observationally by, for example, *Moorcroft and Schlegel (1988)*, where there is a tendency towards the generation of larger ion-neutral relative velocities (see section 2.3.3).

### 2.3.2 Anisotropic ion temperatures

The deviation of the 3-dimensional ion thermal velocity distribution from an isotropic Maxwellian, under the influence of an external electric field, will result in anisotropy of the ion temperature, as discussed by, for example *Schunk and Walker (1972)* and *St-Maurice and Schunk (1973, 1974, 1977, 1979)*. *St-Maurice and Schunk (1977)* replaced the conventional definition of a single ion temperature with two components of ion temperature, one parallel and one perpendicular to the magnetic field. For a gyrotropic ion thermal velocity distribution, *St-Maurice and Schunk (1977)* derived a first-order expression for the behaviour of the field-parallel ion temperature,  $T_{i\parallel}$ , and the field-perpendicular ion temperature,  $T_{i\perp}$

$$T_{i\parallel} = T_n(1 + \beta_{\parallel}D'^2) \quad (2.10a)$$

$$T_{i\perp} = T_n(1 + \beta_{\perp}D'^2) \quad (2.10b)$$

in which  $\beta_{\parallel}$  = field-parallel ion temperature partition coefficient  
 $\beta_{\perp}$  = field-perpendicular ion temperature partition coefficient

The field-parallel and field-perpendicular ion temperature partition coefficients are dimensionless numbers and may be represented by the following expressions (*e.g. Løvhaug and Flå, 1986; McCrea et al., 1993*)

$$\beta_{\parallel} = \frac{2}{3} - \frac{A_1}{15A_2} \quad (2.11a)$$

$$\beta_{\perp} = \frac{2}{3} + \frac{A_1}{30A_2} \quad (2.11b)$$

in which  $A_1$  and  $A_2$  are given by the expressions

$$A_1 = 10 \sum_n \frac{m_i m_n v_{in}}{(m_i + m_n)} \left(1 - 3 \frac{\alpha_{in}}{4}\right) \sum_n \frac{m_i v_{in}}{(m_i + m_n)} \quad (2.11c)$$

$$A_2 = \sum_n \frac{m_i v_{in}}{(m_i + m_n)} \left(1 + \frac{3 m_n \alpha_{in}}{4 m_i}\right) \sum_n \frac{m_i m_n v_{in}}{(m_i + m_n)} \quad (2.11d)$$

$\alpha_{in}$  is a numerical constant, the value of which has been presented by *St-Maurice and Schunk (1977)* for various collision mechanisms and ranges of temperatures, and is given

by

$$\alpha_{\text{in}} = \frac{Q_{\text{in}}^{(2)}}{Q_{\text{in}}^{(1)}} \quad (2.12)$$

where  $Q_{\text{in}}^{(1)}$  and  $Q_{\text{in}}^{(2)}$  are generalised transport cross sections (*e.g.* Schunk, 1977). As noted in the previous section, Coulomb collisions act to stabilise the thermal velocity distribution of the ion population, and, consequently, reduce the anisotropy in the ion temperature (*e.g.* St-Maurice and Hanson, 1982). The effect of such collisions can be incorporated into the definitions of the ion temperature partition coefficients (*St-Maurice and Hanson, 1982; Løvhaug and Flå, 1986; McCrea et al., 1993*).

The ion temperature partition coefficients are related through the expression

$$\beta_{\parallel} + 2\beta_{\perp} = 2 \quad (2.13)$$

This equation is, however, only strictly valid for Maxwell molecules, whose neutral collision cross-section is inversely proportional to the ion-neutral relative velocity; pure polarisation attraction constitutes such an interaction. More importantly, perhaps, the definition of the ion temperature partition coefficients is based on equations 2.10a and 2.10b above, equations which assume a first-order balance between frictional heating of the ion population and cooling by ion-neutral thermal energy transfer. Thus, in the derivation of equation 2.13 there is an implicit assumption that all other terms in the ion energy balance equation, such as ion-electron thermal energy exchange and heat conduction, can be neglected: equation 2.13 is, therefore, only really an approximation.

Theoretical values of the field-parallel and field-perpendicular ion temperature partition coefficients for resonant charge exchange and polarisation collisions (of varying ion to neutral mass ratio) derived by *St-Maurice and Schunk (1977)* are tabulated in table 2.1, although for larger values of electric field *Bakarati et al. (1983)*, through Monte-Carlo type simulations, found that the partition coefficients were slowly varying functions of  $D'$ . Since the field-parallel ion temperature partition coefficient remains consistently lower than the perpendicular coefficient for both types of interaction, it follows that the field-perpendicular component of the ion temperature should exceed the parallel component in the F-region in the presence of an electric field. Table 2.2 contains values of the field-parallel and field-perpendicular ion temperatures, assuming a neutral temperature of 1000 K, for resonant charge exchange and polarisation collisions (of equal ion and neutral masses) for varying values of  $D'$  (*St-Maurice and Schunk, 1977*).

For any gyrotropic ion thermal velocity distribution, the 3-dimensional ion temperature,  $T_i$ , may be related to its parallel and perpendicular components via the equation

$$T_i = \frac{T_{i\parallel} + 2T_{i\perp}}{3} \quad (2.14)$$

Model	$\beta_{\parallel}$	$\beta_{\perp}$
Relaxation	0	1
Resonant charge exchange	0.3364	0.8318
Polarisation ( $m_i/m_n \Rightarrow 0$ )	0.6666	0.6666
Polarisation ( $m_i/m_n = 0.5$ )	0.5876	0.7062
Polarisation ( $m_i/m_n = 1$ )	0.5547	0.7226
Polarisation ( $m_i/m_n = 2$ )	0.5253	0.7373
Polarisation ( $m_i/m_n \Rightarrow \infty$ )	0.4750	0.7625

**TABLE 2.1** Theoretically derived ion frictional heating partition coefficients for resonant charge exchange and polarisation collision models (*St-Maurice and Schunk, 1977*).

$D'$	Relaxation		Resonant charge exchange		Polarisation ( $m_i/m_n = 1$ )	
	$T_{i\parallel}$	$T_{i\perp}$	$T_{i\parallel}$	$T_{i\perp}$	$T_{i\parallel}$	$T_{i\perp}$
<b>0.5</b>	1000	1250	1084	1208	1139	1181
<b>1.0</b>	1000	2000	1336	1832	1555	1723
<b>1.5</b>	1000	3250	1757	2871	2248	2626
<b>2.0</b>	1000	5000	2346	4327	3219	3890

**TABLE 2.2** Theoretically derived field-parallel and perpendicular ion temperatures for relaxation, resonant charge exchange and polarisation collision models for a neutral temperature,  $T_n$ , of 1000 K (*St-Maurice and Schunk, 1977*).

and the temperature in the direction at an angle  $\phi$  to the magnetic field,  $T_{ir}$ , is given as

$$T_{ir} = T_{i\parallel} \cos^2 \phi + T_{i\perp} \sin^2 \phi \quad (2.15)$$

If  $\phi$  is  $54.7^\circ$  the line of sight ion temperature equals the 3-dimensional ion temperature irrespective of the form of the velocity distribution. Equation 2.15 does, however, assume a symmetry in the ion thermal velocity distribution along the magnetic field direction.

Observations of anisotropic F-region ion temperatures by the EISCAT UHF incoherent scatter radar during intervals of ion frictional heating have been reported by *Perraut et al. (1984)*, *Løvhaug and Flå (1986)*, *Glatthor and Hernández (1990)*, *Lathuillère et al. (1991)* and *McCrea et al. (1993)*. Each of these investigations demonstrated a distinct aspect angle dependence of the ion temperature such that the parallel and perpendicular ion temperatures were significantly different. The ion temperature partition coefficients derived from the observations were broadly consistent with those predicted from the presence of resonant charge exchange interactions. Furthermore, the decrease in the ion temperature anisotropy with increasing altitude observed by *McCrea et al. (1993)* was attributed to an increase in the frequency of ion-ion collisions relative to that of ion-neutral collisions.

### 2.3.3 Neutral winds and ion drag

Neutral winds are directed principally anti-sunward in response to pressure gradients set up by solar heating, although this is modified to some extent by the effect of the Earth's rotation upon the neutral atmosphere. Thermospheric winds, particularly at F-region altitudes, have been reviewed in detail by *Rishbeth (1972)*. In the high-latitude ionosphere, however, the occurrence of large ion flows driven by electric fields may significantly influence the pattern of neutral velocities. The neutrals are coupled to the ions via collisions which tend to equalise the velocities of the two populations, a mechanism referred to as ion drag (*Rishbeth, 1972; Fedder and Banks, 1972*).

A simplified momentum equation for the neutral gas, neglecting horizontal viscosity, may be presented in the following form (*e.g. Baron and Wand, 1983*).

$$m_n N_n \frac{\delta \mathbf{v}_n}{\delta t} \approx \frac{\delta}{\delta h} \left( \mu \frac{\delta \mathbf{v}_n}{\delta h} \right) + m_i N_i \mathbf{v}_i (\mathbf{v}_i - \mathbf{v}_n) - 2m_n N_n \boldsymbol{\Omega} \times \mathbf{v}_n - \nabla p_n \quad (2.16)$$

in which  $p_n$  = neutral gas pressure  
 $N_n$  = neutral number density  
 $\mu$  = coefficient of viscosity of the neutral gas  
 $\boldsymbol{\Omega}$  = angular frequency of the Earth's rotation

The terms on the right hand side represent momentum change in the neutral atmosphere due to vertical viscosity, ion drag, the Coriolis force and pressure gradients, respectively.

If ion drag comprises the dominant force governing neutral dynamics, the neutral

velocity will approach the ion velocity exponentially with a time constant given by  $\tau_{ni}$ , given by the inverse of the neutral-ion collision frequency,  $\nu_{ni}$  (*Baron and Wand, 1983*). An expression for the so-called ion drag time constant derived by *Baron and Wand (1983)* is reproduced below.

$$\tau_{ni} = \frac{1}{\nu_{ni}} = \frac{m_n N_n}{m_i N_i \nu_{in}} \quad (2.17)$$

Furthermore, from the above expression, the authors derived an ion drag time constant for an ion population dominated by atomic oxygen ions which is valid to within 10% under a wide variety of geophysical conditions.

$$\tau_{ni} \approx \frac{0.226 \times 10^{16}}{N_i} \quad (2.18)$$

The time constant of the neutral atmosphere to respond to ion drag is a function of the plasma density and, as such, is highly variable. Equation 2.18 yields response time constants of some 40 and 400 minutes for ion densities of  $10^{12} \text{ m}^{-3}$  and  $10^{11} \text{ m}^{-3}$ , respectively.

Ion drag progressively reduces the relative velocity between the ions and the neutral atmosphere and, in consequence, acts to suppress ion frictional heating. However, the depletion in electron density which tends to accompany ion frictional heating (see section 2.3.6) acts as a feedback mechanism, prolonging the response time of the neutral atmosphere and reducing the effect of ion drag (*Killeen et al., 1984; Alcayd e et al., 1984*).

The effect of ion drag on ion frictional heating in the high-latitude F-region is dramatically illustrated in the case of a moving convection shear, a feature indicated by the satellite observations presented in the lower panel of figure 2.4. This figure, which has been previously discussed in section 2.2, presents simultaneous observations of ion velocity and ion temperature by the Atmospheric Explorer-C satellite. As the neutral wind is slow to respond, frictional heating is intense on the trailing edge of the moving shear: in front of the feature, however, the neutrals have had sufficient time to be accelerated through the process of ion drag to a velocity comparable to that to the ions, thereby virtually totally suppressing frictional heating.

The F-region electron density is generally lower in the morning sector than during the afternoon and evening hours, due to the decay of solar produced ionisation, thus the ion drag force on the neutral atmosphere will tend to be less. The weaker coupling between the ions and the neutral population post midnight, results in larger ion-neutral relative velocities and, in consequence, more intense ion frictional heating during these hours. Another factor which determines the extent to which the neutral wind can be accelerated by ion drag is the length of time for which it is resident in the region of large auroral ion flows. In the dusk sector, the Coriolis and centrifugal accelerations of a packet

of neutral air tend to cancel and its motion largely westward; air which remains within the region of strong auroral ion flows acquire a large westward velocity. Conversely, in the dawn convection cell both centrifugal and Coriolis forces act in the same direction, moving the packet of neutral air equatorward out of the oval thus preventing it from acquiring a large momentum from the ions (*e.g. Lockwood and Fuller-Rowell, 1987a; 1987b*). Both of these factors account for the observations of *Baron and Wand (1983)* and *Moorcroft and Schlegel (1988)*, amongst others, of larger ion temperatures in the post midnight sector. Figure 2.9 illustrates the dawn-dusk asymmetry in ion temperature derived from simultaneous observations by the Chatanika and Millstone Hill incoherent scatter radars (*Baron and Wand, 1983*).

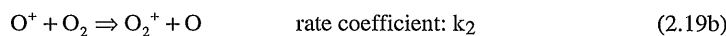
*Alcaydé et al. (1984)* proposed an additional mechanism which would contribute to this effect; a mechanism also relating to the role of the Coriolis force on the neutral atmosphere. The authors pointed out that the strongly developed southward neutral winds which exist on the nightside under both disturbed and quiet conditions, a feature of global thermospheric circulation, would induce a Coriolis force which opposes the ion drag force arising from eastward plasma flow during the post-midnight hours whereas in the evening sector these two forces would act in the same direction.

From observations by the Atmospheric Explorer satellite *St-Maurice and Hanson (1984)* deduced that for ion velocities exceeding  $1 \text{ km s}^{-1}$ , ion drag constitutes the controlling factor governing neutral atmospheric motion.

#### 2.3.4 Ion composition modification

The ion composition in the E-region comprises predominantly  $\text{NO}^+$  and  $\text{O}_2^+$  (see figure 1.5). With increasing altitude, molecular ions are progressively replaced by atomic oxygen ions, which dominate above some 200 km. Above an altitude of around 1000 km, the proportion of the light ions,  $\text{He}^+$  and  $\text{H}^+$ , becomes significant although the exact height at which they become the dominant ion species is highly dependent on the thermospheric temperature (*e.g. Banks and Kockarts, 1973*).

Atomic oxygen ions do not readily recombine directly with electrons, in preference undergoing reactions with molecular neutrals to produce molecular ions. In the F-region, where the dominant molecular neutral species are  $\text{N}_2$  and  $\text{O}_2$ , the following reactions occur



The reaction of atomic oxygen ions with molecular oxygen, reaction 2.19b, constitutes a charge exchange reaction, whereas reaction 2.19a is an example of ion-atom interchange. The rates of reactions 2.19a and 2.19b are given by  $k_1 N_{[\text{O}^+]} N_{[\text{N}_2]}$  and  $k_2 N_{[\text{O}^+]} N_{[\text{O}_2]}$ , where  $N_{[\text{O}^+]}$ ,  $N_{[\text{N}_2]}$  and  $N_{[\text{O}_2]}$ , represent the concentrations of  $\text{O}^+$ ,  $\text{N}_2$  and  $\text{O}_2$ ,

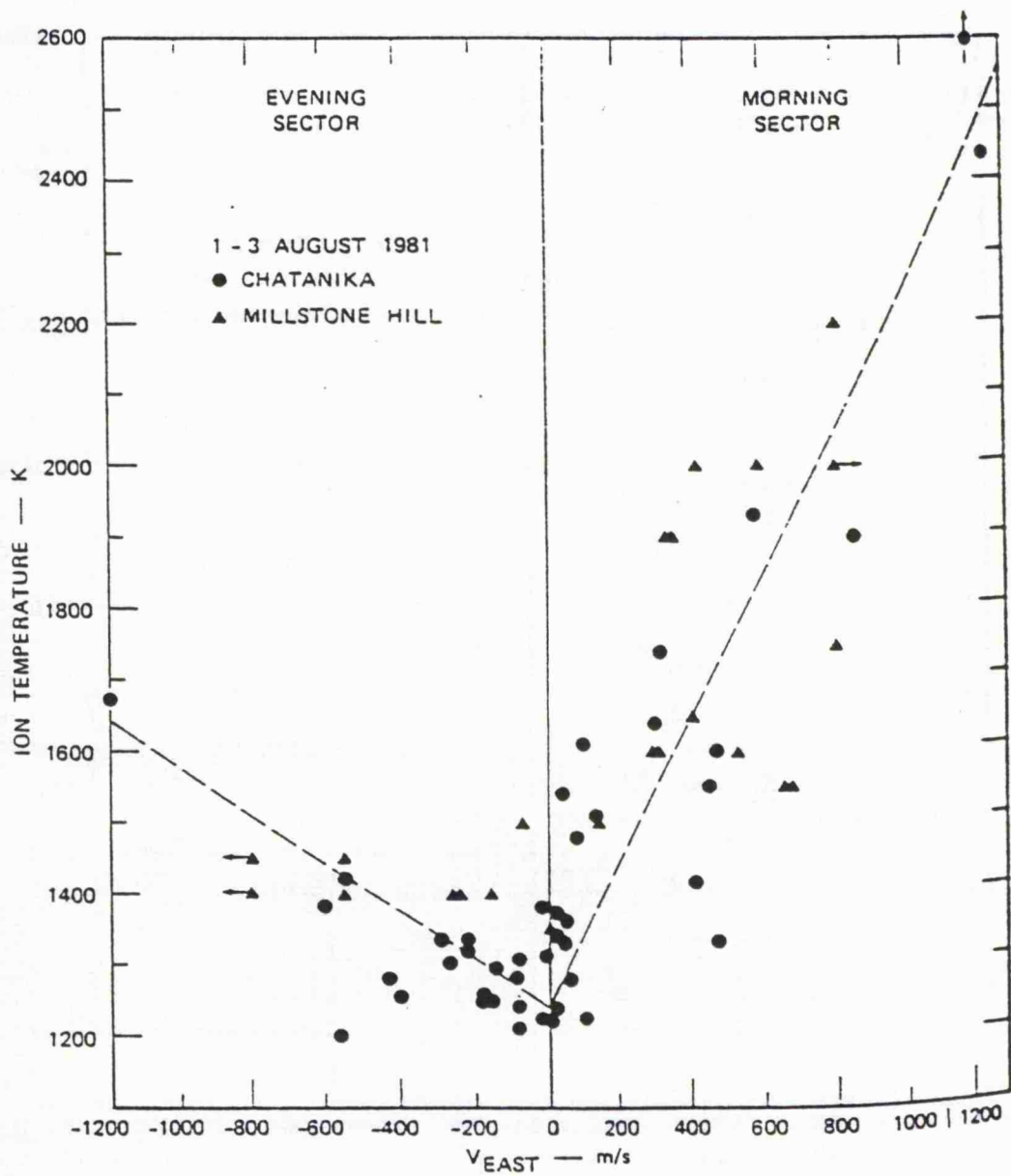


FIGURE 2.9 Variation of ion temperature with zonal ion velocity, derived from observations by the Chatanika and Millstone Hill incoherent scatter radars (Baron and Wand, 1983).

respectively. The rates of the above reactions are highly energy dependent (*e.g.* McFarland *et al.*, 1973; Schunk *et al.*, 1975; St-Maurice and Torr, 1978; Torr and Torr, 1978). St-Maurice and Torr (1978) derived expressions for the rate coefficients for the above reactions in the ionosphere, employing cross sections obtained by laboratory experiment (Albritton *et al.*, 1977). The rate coefficients, expressed in units of  $\text{m}^3 \text{s}^{-1}$ , take the form

$$k_1 = 1.533 \times 10^{-6} - 5.92 \times 10^{-7} \left( \frac{T_{\text{eff}}}{300} \right) + 8.6 \times 10^{-8} \left( \frac{T_{\text{eff}}}{300} \right)^2 \quad 300 \leq T_{\text{eff}} \leq 700 \text{ K} \quad (2.20a)$$

$$k_1 = 2.73 \times 10^{-6} - 1.155 \times 10^{-6} \left( \frac{T_{\text{eff}}}{300} \right) + 1.483 \times 10^{-7} \left( \frac{T_{\text{eff}}}{300} \right)^2 \quad 1700 < T_{\text{eff}} < 6000 \quad (2.20b)$$

$$k_2 = 2.82 \times 10^{-5} - 57.74 \times 10^{-6} \left( \frac{T_{\text{eff}}}{300} \right) + 1.073 \times 10^{-6} \left( \frac{T_{\text{eff}}}{300} \right)^2 - 5.17 \times 10^{-8} \left( \frac{T_{\text{eff}}}{300} \right)^3 + 9.65 \times 10^{-10} \left( \frac{T_{\text{eff}}}{300} \right)^4 \quad 300 < T_{\text{eff}} \leq 6000 \text{ K} \quad (2.20c)$$

$T_{\text{eff}}$ , the effective temperature, is a measure of the total energy of collision and can be represented in the form

$$T_{\text{eff}} = \frac{2\text{KE}_{\text{cm}}}{3k_B} = T_n + \frac{m_n}{m_i + m_n} \left( \frac{m_i + < m_n}{3k_B} \right) (\mathbf{v}_i - \mathbf{v}_n)^2 \quad (2.21)$$

where the subscript *i* refers specifically to the  $\text{O}^+$  ion and *n* to the reactant neutral species.  $\text{KE}_{\text{cm}}$  is the mean relative energy in the centre of mass system.

Enhanced electric fields in the high-latitude ionosphere increase the rate of reactions 2.19a and 2.19b through the dependence of the effective temperature on the relative flow speed between the ion and neutral gases. Figure 2.10 presents the predicted ion composition for effective perpendicular electric fields of 0, 50, 100 and 200  $\text{mV m}^{-1}$  (Schunk *et al.*, 1975), derived from the Utah state model, illustrating the increased production of molecular ions, principally  $\text{NO}^+$ , in the F-region due to the enhanced reaction rate coefficients; the reaction rate coefficients employed are those of McFarland *et al.* (1973). Unlike those derived by previous workers (*e.g.* McFarland *et al.*, 1973; Albritton *et al.*, 1977), the reaction rate coefficients of St-Maurice and Torr (1978) are applicable under situations of a nonthermal plasma, although the authors found that the coefficients were essentially coincidental with the thermal distribution values of Albritton *et al.* (1977). The rate coefficients of St-Maurice and Torr (1978) were also found to be in good agreement with ionospheric values, determined from *in-situ* observations by the Atmospheric Explorer satellite (Torr *et al.*, 1977). Upwelling of the lower atmosphere rich in reactant neutrals, in response to Joule heating during intervals of enhanced electric field, further increases the reaction rates (*e.g.* Raitt *et al.*, 1975; Schunk *et al.*, 1975).

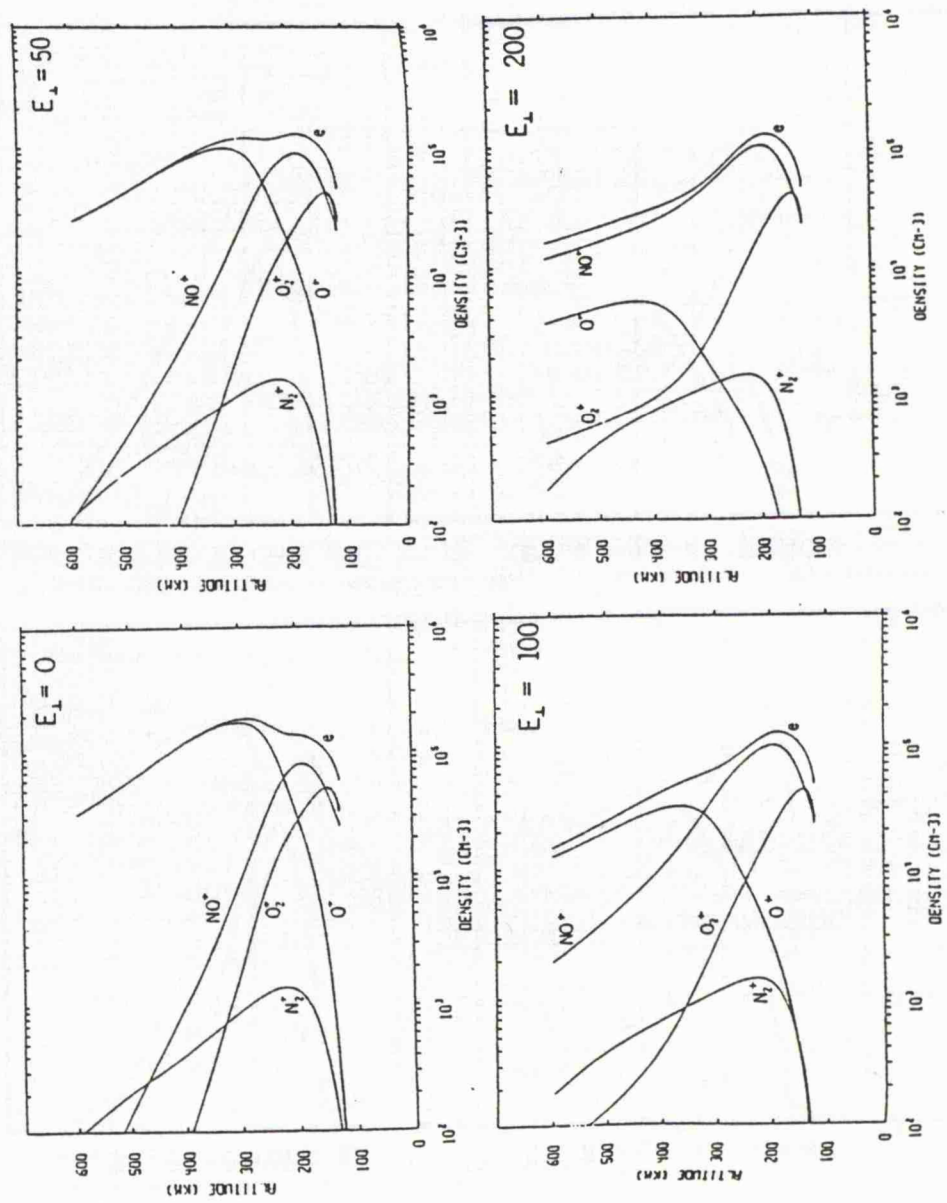


**FIGURE 2.10** Variation of the modelled profile of ion composition with increasing effective electric field (*Schunk et al., 1975*).

Ionised species can undergo a complex, and poorly understood, series of reactions which may result in the formation of electronically and vibrationally excited neutrals, such as  $N(^2D)$ ,  $N(^4S)$  and vibrationally excited  $N_2$  and  $O_2$  (e.g. *Torr and Torr, 1978*). Workers have found that vibrational and kinetic energies exhibit a near equivalent effect in raising reaction rate coefficients (*Schmeltekopf et al., 1968*). Consequently, in addition to those factors discussed above, the formation of vibrationally excited molecular neutrals at ionospheric altitudes can significantly increase the rate of production of molecular ions. The chemistry of the thermosphere and ionosphere is reviewed in detail by *Torr and Torr (1978)*.

A direct correlation between enhancements in the density of  $NO^+$  and the occurrence of elevated ion velocities was revealed by the Atmospheric Explorer satellite at high-latitude in the southern hemisphere, as presented in figure 2.11 (*Brinton, 1975*). Smaller enhancements in the  $O_2^+$  concentration were also detected in conjunction with high ion flows. Similarly, observations by the Chatanika incoherent scatter radar revealed an increased molecular ion content in the F-region during enhanced electric fields (*Kelley and Wickwar, 1981*). *Lathuillère et al. (1983a)* and *Lathuillère and Brekke (1985)* subsequently presented measurements of ion composition by the EISCAT radar which indicated increased proportions of molecular ions during such intervals, although averaging over periods of order of an hour was necessary to produce reasonable values. More recently, *Hägström and Collis (1990)*, *Winser et al. (1990)* and *Glatthor (1993)* employed EISCAT observations of ion temperature and plasma flow to investigate changes in the ion composition in response to enhancements in the convection electric field via a simplified form of the ion energy balance equation. Results presented by *Hägström and Collis (1990)* indicated a dominance of molecular ions up to an altitude of 400 km in response to an electric field of some  $80 \text{ mV m}^{-1}$  (figure 2.12), although the authors made no allowance for ion temperature anisotropy in their calculations (*Lockwood et al., 1993*). Indeed, *Lockwood et al. (1993)* demonstrated that, by taking no account of ion temperature anisotropy, *Hägström and Collis (1990)* had significantly overestimated the fractional content of molecular ions in the F-region plasma.

Contours of the molecular-atomic transition altitude, in temporal sequence during the modelled storm of *Sojka and Schunk (1984)* are presented in figure 2.13, illustrating an increase in the altitude of the molecular to atomic ion species transition corresponding to an enhanced dusk convection cell and coincident with the occurrence of high ion temperatures (see figure 2.5).

### 2.3.5 Large field-aligned plasma flows

Large ionospheric electric fields can lead to the substantial upflow of F-region plasma along the magnetic field direction due to a combination of various physical processes, which are discussed by such authors as *Winser et al. (1986)*, *Jones et al. (1988)* and *Rodger et al. (1992)*. The principal factors influencing the field-aligned plasma

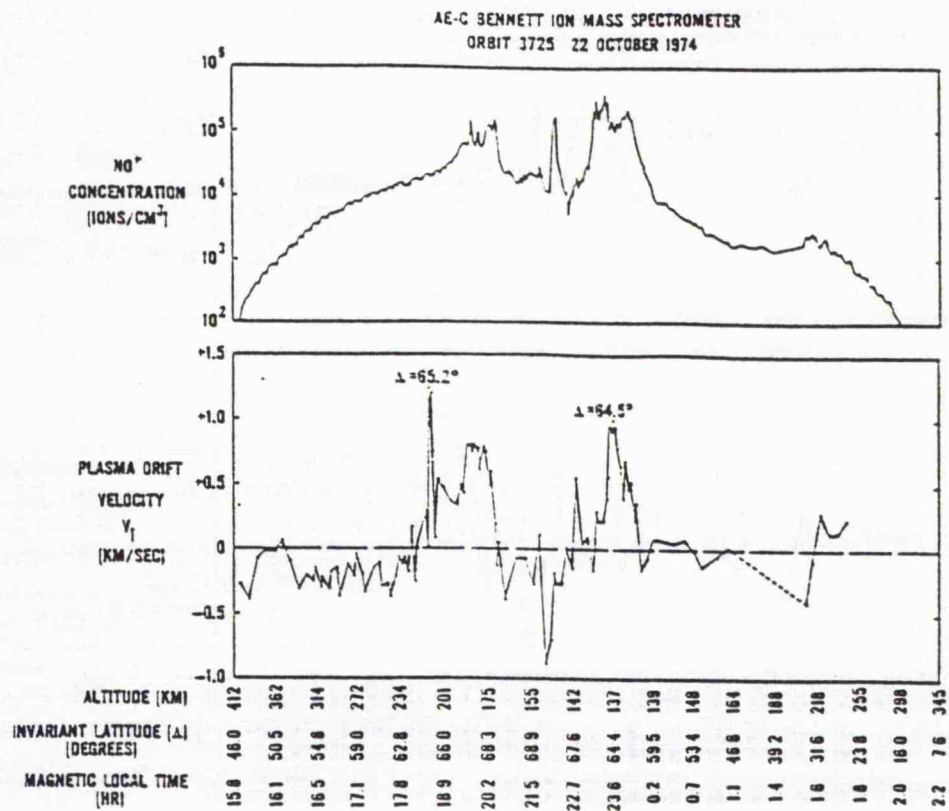


FIGURE 2.11 Mass spectrometer measurements of  $\text{NO}^+$  concentration and plasma drift velocity during a high-latitude southern hemisphere pass of the Atmospheric Explorer satellite (Brinton, 1975).

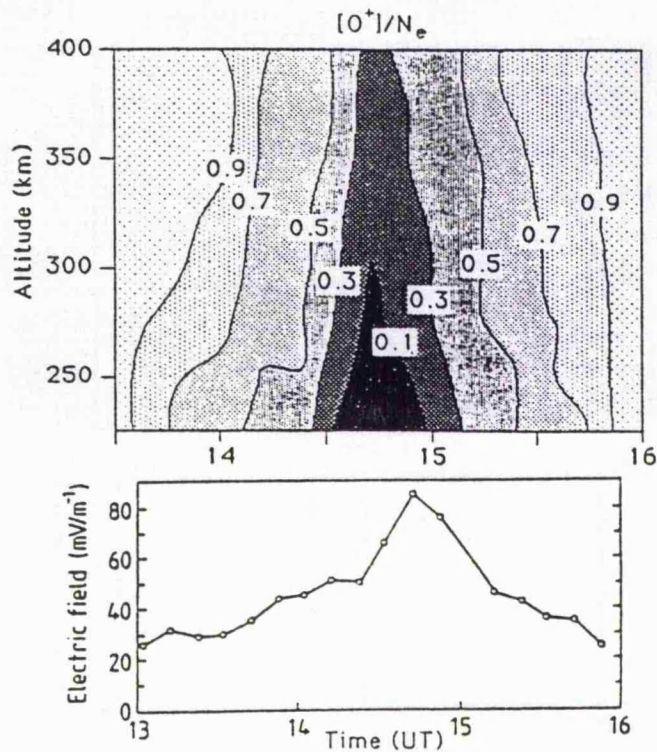


FIGURE 2.12 Variation with altitude and time of the proportion of the total ion density comprised by  $\text{O}^+$  (top panel) derived from observations by the EISCAT incoherent scatter radar during an interval of enhanced electric field (lower panel) (Häggström and Collis, 1990).

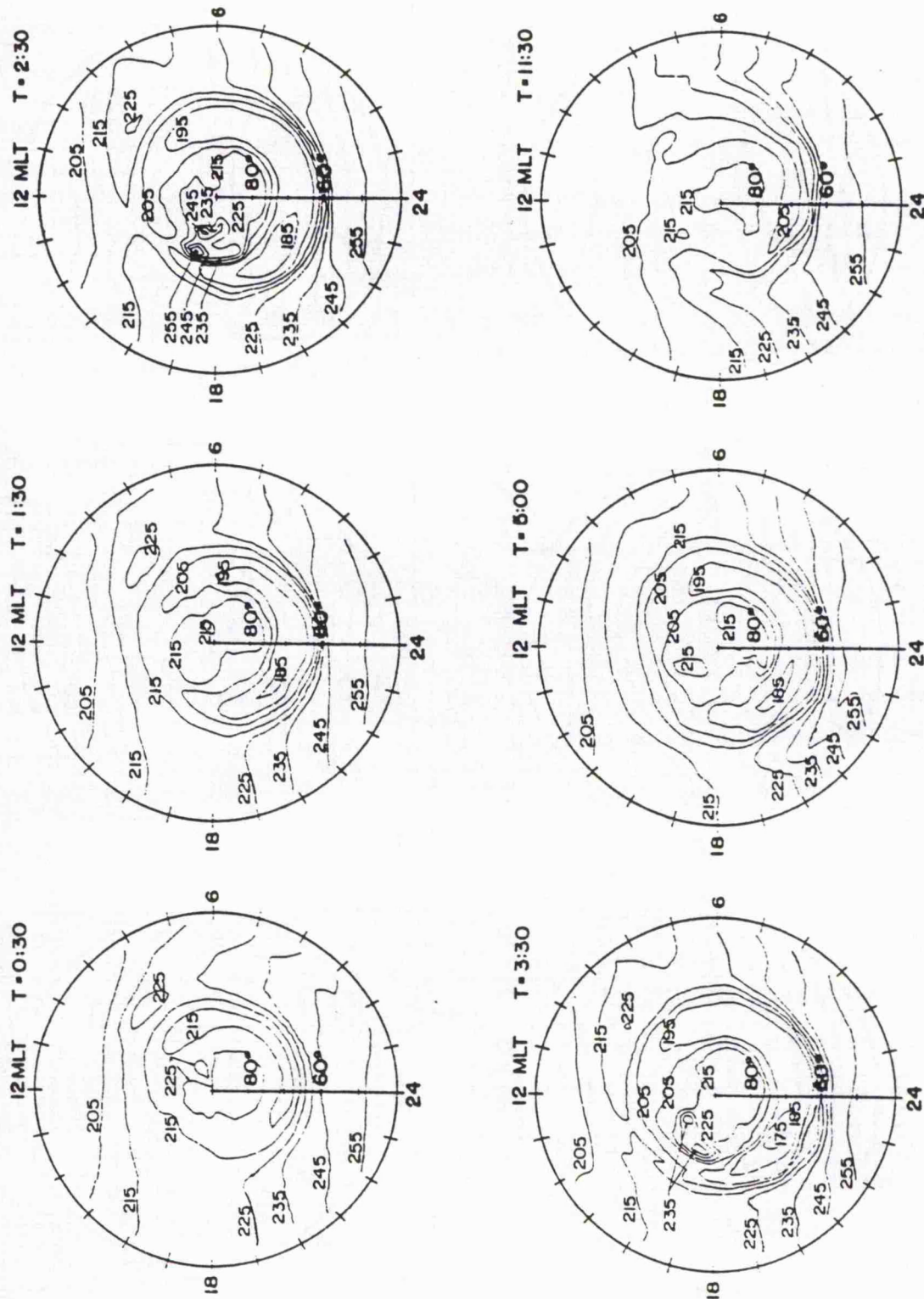


FIGURE 2.13 Global F-region ion composition predictions at 6 successive times during a modelled magnetic storm (Sojka and Schunk, 1984).

velocity in the presence of electric fields are represented schematically in figure 2.14, adapted from an illustration of *Rodger et al. (1992)*, and are discussed below.

Ion frictional heating sets up a steep gradient in ion temperature between the F-region and the topside, as evident from figure 2.5, which leads to an enhanced rate of ambipolar diffusion, driving F-region plasma upwards along the magnetic field lines. The diffusion velocity of the plasma along the magnetic field direction,  $v_d$ , due to a change in the parallel ion temperature,  $\Delta T_{i||}$ , at altitude  $h$  is given by (e.g. *Williams and Jain, 1986*)

$$v_d = -\frac{k_B}{m_i v_{in}} \frac{\partial(\Delta T_{i||})}{\partial h} \quad (2.22)$$

The field-parallel plasma velocity resulting from enhanced diffusion in response to the imposition of a perpendicular velocity spike, has been modelled by *Sellek et al. (1991)* using the Sheffield University plasmasphere and ionosphere model (SUPIM) (*Bailey and Sellek, 1990*), as illustrated in figure 2.15. Upward velocities of hundreds of  $m\ s^{-1}$  may be generated by this mechanism, substantially depleting the F-region ionisation (*Rodger et al., 1992*).

Electric fields result in Joule heating of the thermosphere, much of the energy of which is deposited at E-region altitudes. Upwelling of the lower neutral atmosphere, a consequence of thermal expansion in response to Joule heating, lifts the ionosphere above the level of heating, driving field-aligned outflows of F-region plasma. The velocity of the neutral air due to Joule heating of the lower thermosphere has been investigated computationally by, amongst others, *Wu and Cole (1976)* and *Fuller-Rowell (1984)*, the latter predicting that vertical neutral velocities approaching  $40\ m\ s^{-1}$  may result from an electric field of  $100\ mV\ m^{-1}$ , and it has been estimated that, under typical conditions, upwelling of the atmosphere drives the plasma up the field lines with a velocity of  $50\text{-}100\ m\ s^{-1}$  (*Winser et al., 1988a*).

A further mechanism suggested to enhance field-parallel plasma flow in the presence of applied electric fields is the hydromagnetic mirror force caused by diverging field lines which causes acceleration of upward flowing plasma in the topside, particularly in the presence of electric fields when the ion thermal velocity distribution is anisotropic (e.g. *Suvanto et al., 1989a*). *Lockwood and Fuller-Rowell (1987a)*, however, concluded that even with strong convection this force is unlikely to exceed the equivalent of 0.1 times the opposing effect of gravity.

Although the aforementioned factors contribute to the generation of large field-aligned outflows of F-region plasma in the presence of perpendicular electric fields, this will be further modulated by the component of the ambient neutral wind along the magnetic meridian which induces field-aligned plasma velocities of typically  $30\ m\ s^{-1}$ , but which may exceed  $70\ m\ s^{-1}$ . On the dayside, solar heating tends to produce a poleward meridional neutral wind component which drives plasma downwards along the magnetic

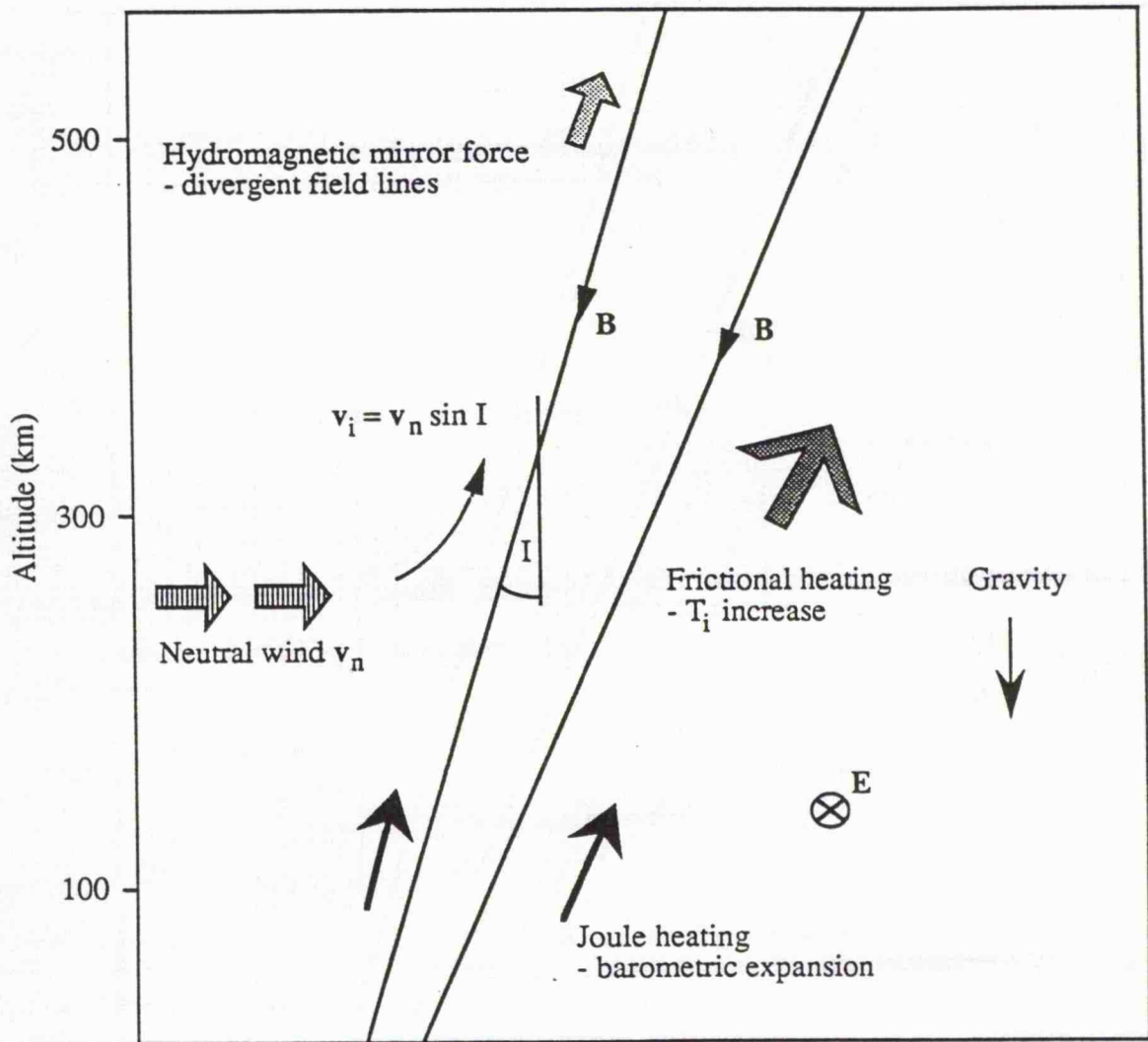


**FIGURE 2.14** Schematic of the principal factors affecting field-aligned plasma flow under conditions of a perpendicular electric field.

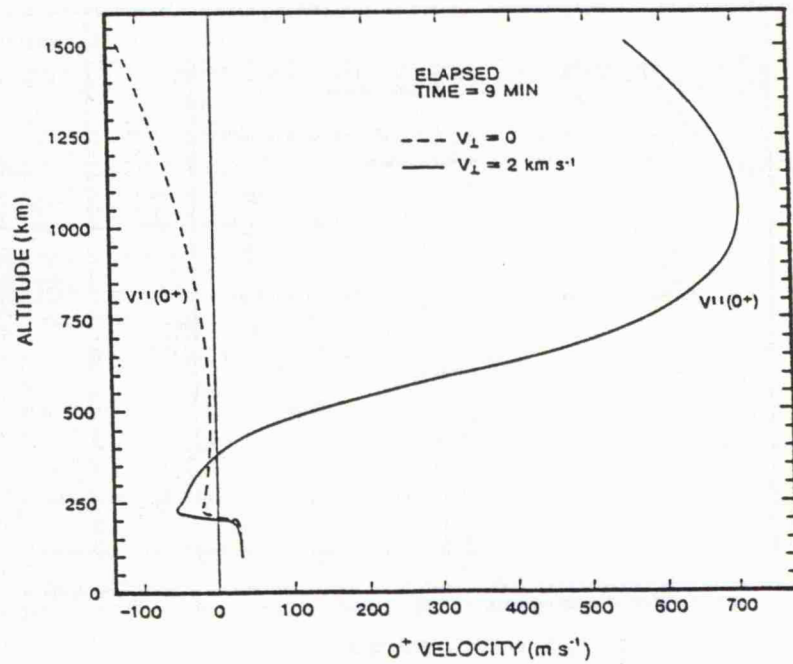


FIGURE 2.15 Modelled field-aligned plasma velocity prior to (dashed line) and during (full line) the imposition of a velocity spike of maximum value  $2 \text{ km s}^{-1}$  (Rodger *et al.*, 1992).

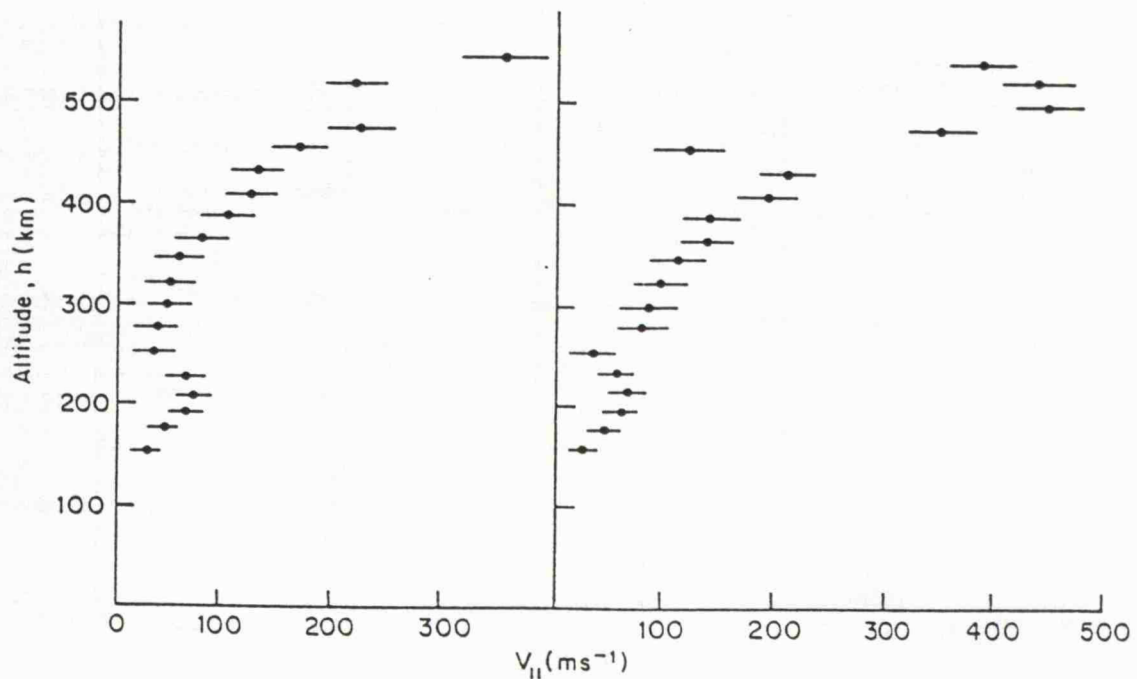


FIGURE 2.16 EISCAT observations of enhanced field-parallel ion outflows driven by large perpendicular electric fields (Jones *et al.*, 1988).

field direction while, conversely, upward field-aligned plasma motion arises on the nightside where the neutral wind tends to be equatorward due to both solar and auroral processes.

The occurrence of large field-aligned plasma outflows under conditions of large electric fields has been noted in radar and satellite observations of the high-latitude F-region and topside, predominantly on the nightside where upward plasma flow is enhanced due to the action of an equatorward neutral wind. *Bates (1973, 1984)* reported measurements by the Chatanika incoherent scatter radar of upward field-aligned plasma velocities around the F-region peak exceeding  $100 \text{ m s}^{-1}$  and large field-aligned plasma outflows have been observed with the EISCAT radar facility by *Winser et al. (1986, 1988a, 1988b)*, *Williams and Jain (1986)* and *Jones et al. (1988)*. Figure 2.16 presents EISCAT measurements of plasma velocity parallel to the magnetic field line corresponding to perpendicular electric fields of  $45 \text{ mV m}^{-1}$  and  $55 \text{ mV m}^{-1}$ , respectively, illustrating field-parallel flows exceeding  $200 \text{ m s}^{-1}$  at 500 km altitude (*Jones et al., 1988*). A statistical analysis of field-aligned flows performed by *Keating et al. (1990)*, employing EISCAT observations taken over a three year period, indicated that almost half of the outflows observed corresponded to intervals of elevated ion temperature.

Various other physical mechanisms have been proposed to account for the generation of large field-aligned plasma flows in the absence of enhanced perpendicular electric fields. *Bakar and Schunk (1983)* suggested that enhanced plasma diffusion could arise as a consequence of the enhanced electron temperature gradients due to the precipitation of energetic particles to ionospheric altitudes. Furthermore, observations of plasma outflows have been attributed to field-aligned currents associated with auroral arcs (*Block and Fälthammar, 1968*) and transverse acceleration of ions due to heating by ion cyclotron waves (*e.g. Ungstrup et al., 1979; Lockwood, 1982*).

The role of large outflows of plasma along magnetic field lines in the formation of ionisation troughs in the ionospheric F-region is discussed in the following section.

### 2.3.6 Electron density depletion

Chemical loss of ionospheric electrons occurs principally through dissociative recombination, thus enabling momentum to be more easily conserved. Examples of such reactions are



Atomic oxygen ions do not readily directly recombine but, preferentially, undergo reactions which, in the F-region, predominantly produce the molecular ion species  $\text{NO}^+$  and  $\text{O}_2^+$  (see section 2.3.4). These ion species recombine via reactions 2.23a and 2.23b above, the rates of which are given by  $\alpha_1 N_{[\text{NO}^+]} N_e$  and  $\alpha_2 N_{[\text{O}_2^+]} N_e$  respectively;  $N_{[\text{NO}^+]}$

represents the concentrations of  $\text{NO}^+$  and  $\text{N}_{[\text{O}_2^+]}$ , that of  $\text{O}_2^+$ .  $\alpha_1$  and  $\alpha_2$ , the recombination coefficients of reactions 2.23a and 2.23b respectively, can be presented in the following form (*Torr and Torr, 1978*)

$$\alpha_1 = 4.2 \times 10^{-1} \left( \frac{300}{T_e} \right)^{0.85} \quad (2.24a)$$

$$\alpha_2 = 1.6 \times 10^{-1} \left( \frac{300}{T_e} \right)^{0.55} \quad (2.24b)$$

The rate coefficients given above are expressed in units of  $\text{m}^3 \text{s}^{-1}$ .

The occurrence of large electric fields enhances the rate of production of the molecular ion species  $\text{NO}^+$  and  $\text{O}_2^+$ , via the mechanisms discussed in section 2.3.4, thus increasing the rate of the dissociative recombination reactions 2.24a and 2.24b which leads to a reduction in electron density. The predicted effect of large electric fields on ionospheric electron concentration due to enhanced chemical recombination is evident in figure 2.10, which illustrates the correlation of F-region electron density depletion with enhancements in the concentration of molecular ion species (*Schunk et al., 1975*).

Observations and the theoretical foundation for the occurrence of large field-aligned outflows of plasma in the F-region and topside ionosphere in the presence of strong electric fields are discussed in the previous section of the present chapter. Plasma loss by this mechanism further depletes the electron population. In fact, the observed depletion in electron density during such conditions could not be explained without invoking transport effects due to field-aligned plasma flows in addition to those chemical effects described above (*Williams and Jain, 1986; Winser et al., 1986*). Although both chemical and transport effects act to reduce the electron concentration, each dominates over a distinct altitude regime, with recombination being the principal plasma loss mechanism below the F-region peak and field-aligned outflows accounting for the majority of plasma depletion in the topside. Figure 2.17 illustrates diagrammatically the geophysical mechanisms whereby electron density depletions or troughs are formed in regions of strong electric fields in the high-latitude F-region (*Rodger et al., 1992*).

Electron density depletion in response to convection electric fields is suggested to be a contributory factor in the formation of the main or mid-latitude F-region trough, the other proposed mechanisms being stagnation of plasma caught between the regimes of corotation and high-latitude convection and convection of low density plasma from the nightside (*e.g. Moffett and Quegan, 1983*). *Rodger et al. (1992)* presents a comprehensive review of the role of ion drift in the formation of ionisation troughs in the mid- and high-latitude ionosphere.

Electron density depletion in regions of enhanced electric fields at high-latitudes has been observed by satellites, including the Atmospheric Explorer-C (*Brinton et al.,*

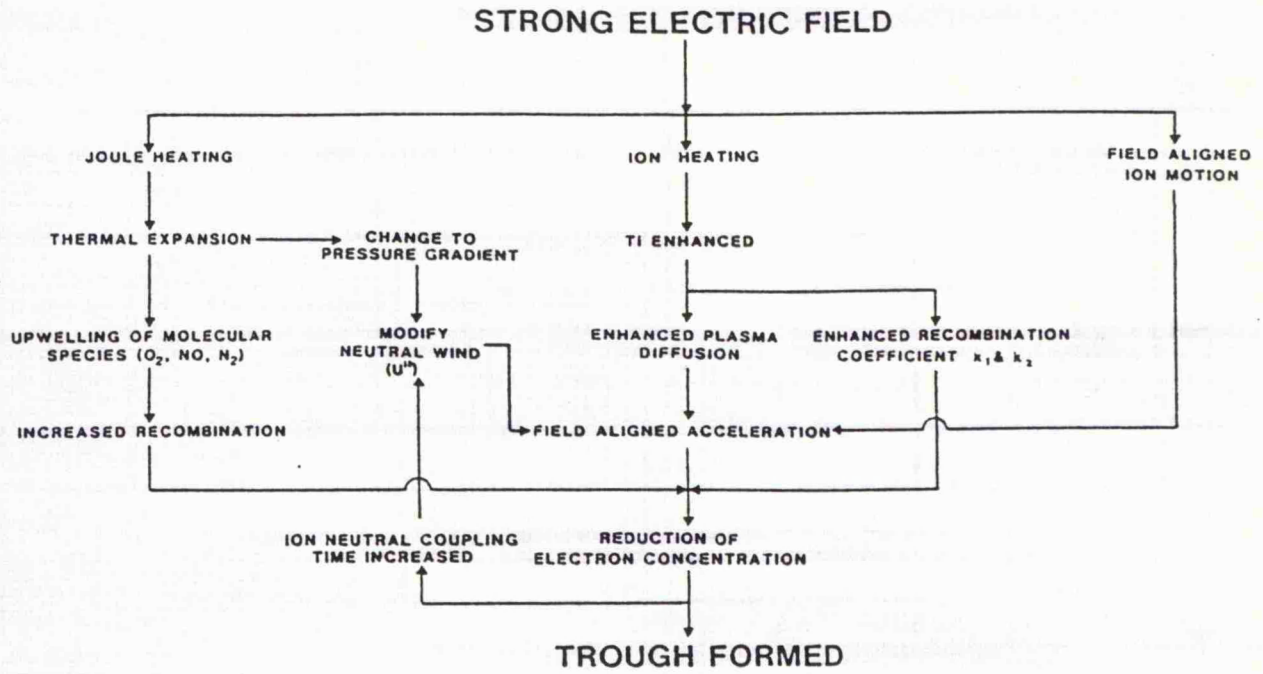


**FIGURE 2.17** Schematic representation of the role of enhanced electric fields in the formation of ionization troughs in the high-latitude F-region (Rodger *et al.*, 1992).

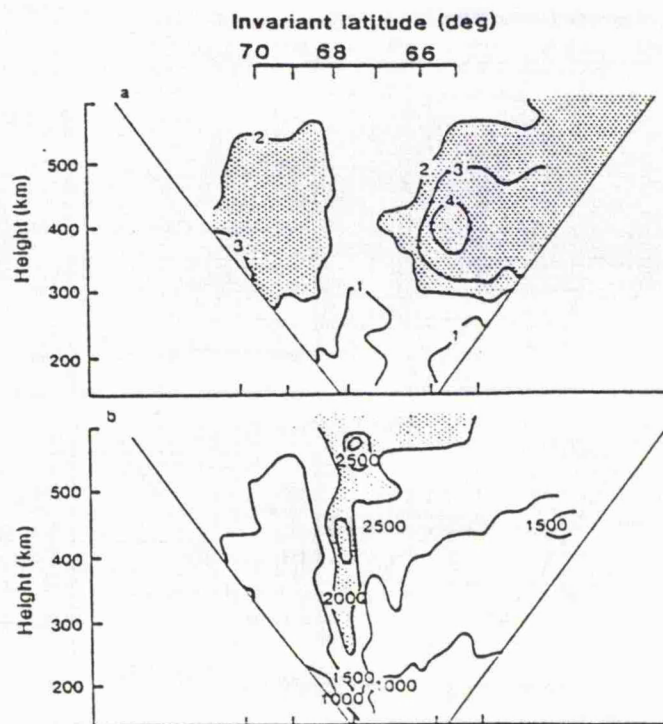


**FIGURE 2.18** EISCAT common programme observations illustrating enhanced ion temperatures (panel b) in the vicinity of a high-latitude electron density trough (panel a) (Williams and Jain, 1986).

1978) and the Dynamics Explorer-2 (Killeen *et al.*, 1984). Such features have also been observed by incoherent scatter radar; EISCAT observations of trough features have been reported by such authors as Williams and Jain (1986). Figures 2.18 illustrates the correlation between the occurrence of ion frictional heating and electron density depletions in the high-latitude F-region during intervals of strong electric fields, as observed with the EISCAT radar (Williams and Jain, 1986). Furthermore, steady state trough features have been reproduced by modelling the ionospheric response to a global convection electric field (*e.g.* Quegan *et al.*, 1982; Sojka and Schunk, 1989).

### 2.3.7 Auroral precipitation and micropulsations

The precipitation of energetic plasma from the magnetosphere into the upper atmosphere is a distinctive feature at high-latitudes. Most precipitation can be classified into two broad categories: structureless and continuous precipitation produces diffuse aurora whereas discrete auroral forms, such as arcs, are produced by highly structured precipitation at slightly higher geomagnetic latitudes. Precipitation of the latter type is associated with the occurrence of substorms and is principally confined to the nightside. A review of particle precipitation and auroral luminosity structure in the high-latitude upper atmosphere and their relationship to large-scale magnetospheric structure is presented by Feldstein and Galperin (1985). In addition to a characteristic optical signature, particle precipitation can result in substantial enhancement of the ionospheric electron concentration, particularly at E-region altitudes, through collisional ionisation.

The electrodynamic structure of discrete auroral features has been the subject of much work, by such authors as de la Beaujardière *et al.* (1977, 1981), Marklund *et al.* (1982), Marklund (1984), Timofeev *et al.* (1987), Opgenoorth *et al.* (1990), Aikio *et al.* (1993) and Lewis *et al.* (1994). By collating previous observations of auroral arcs and their associated electric field patterns, including rocket observations by Cahill *et al.* (1980) and Marklund *et al.* (1982) and radar observations by de la Beaujardière *et al.* (1977, 1981), Marklund (1984) classified such features according to the method by which current continuity was maintained across them. The author classified arcs into those in which current continuity was maintained by means of (a) polarisation electric fields (polarisation arcs), (b) field-aligned or Birkeland currents (Birkeland current arcs) or (c) a combination of polarisation electric fields and field-aligned currents (combination arcs).

Following this, Opgenoorth *et al.* (1990) stated that two general types of auroral arc should be considered. The first type is characterised by a polarisation electric field across the arc which is oriented in the opposite sense to any background convection electric field such that the total electric field within the arc is reduced. Arcs of this type, referred to as anti-correlation arcs by Marklund (1984), have no associated field-aligned currents bar those associated with the particle precipitation that creates the feature itself. Observations by the Chatanika incoherent scatter radar illustrating the reduction of the total electric field within an anti-correlation type arc were presented by de la Beaujardière

*et al. (1977)*. An extensive investigation of the relationship between ion frictional heating and auroral precipitation, employing a substantial database of EISCAT observations, is documented by *McCrea et al. (1991)*. The authors noted regions of enhanced E-region electron density above which ion frictional heating was suppressed, consistent with the behaviour of an anti-correlation type auroral arc.

Many authors, including *de la Beaujardière et al. (1981)*, *Marklund et al. (1982)*, *Timofeev et al. (1987)*, *Opgenoorth et al. (1990)* and *Lewis et al. (1994)*, have presented observations which reveal the presence of enhanced electric fields directly adjacent to auroral arcs. Such enhanced fields, which tend to be in the same direction as the underlying convection electric field and can exceed  $100 \text{ mV m}^{-1}$ , are located on the equatorward edge of arcs in the pre-midnight sector and poleward of arcs in the post-midnight sector. Auroral features with such an electric field signature represent the second of the two general types of arc isolated by *Opgenoorth et al. (1990)*. *Timofeev et al. (1987)* found, on examination of the signatures of many such asymmetric arcs in radar and optical observations, the region of electric field enhancement to have a characteristic width of several tens of kilometres, similar to that of the arc itself. *Marklund (1984)* explained the electrodynamics of such features by a gradual decrease in the meridional convection electric field towards the convection reversal modified by a combination of both polarisation electric fields and Birkeland currents. *Opgenoorth et al. (1990)*, however, proposed an alternative explanation; the authors stated that an intensification of the electric field is necessary to close the circuit between the downward and upward directed field-aligned currents. *McCrea et al. (1991)* observed many instances of substantially enhanced ion temperatures coincident with sharp gradients in E-region electron density although not within the features themselves, a signature consistent with the passage of an asymmetric arc through the EISCAT beam (see figure 2.19).

In addition to the effects of auroral precipitation, geomagnetic micropulsations act to modify the underlying convection electric field in the ionosphere. Geomagnetic micropulsations comprise fluctuations on the Earth's magnetic field of periods between a few seconds and several minutes. The oscillations of the magnetic field lines are reproduced as fluctuations in the magnetic field-perpendicular ion velocity in the ionospheric F-region. EISCAT observations, reported by *Crowley et al. (1985)*, illustrate periodic ion frictional heating associated with a Pc5 micropulsation.

## 2.4 Summary

In this chapter, an overview of ion frictional heating and the phenomena related to its occurrence, approached from both theoretical and observational standpoints, has been presented. The research documented in the present thesis centres principally upon the investigation of ion frictional heating using the EISCAT facility, an incoherent scatter radar system located in Northern Scandinavia. The following chapter describes, in some detail, the EISCAT facility, with particular reference to the EISCAT UHF radar.

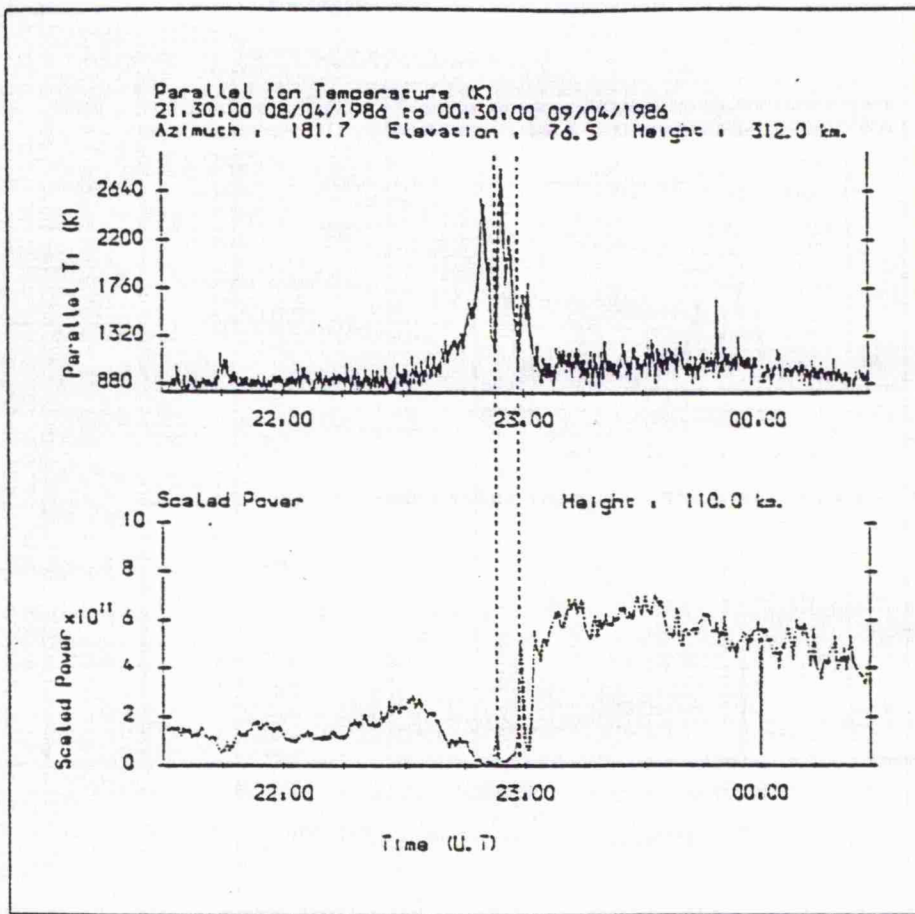


**FIGURE 2.19** Simultaneous EISCAT observations of F-region ion temperature and E-region electron density (*McCrea et al., 1991*).

## Chapter 3

### Incoherent scatter and the EISCAT system

#### 3.1 Introduction

Incoherent scatter of radio waves from the acoustic waves generated in a plasma by random thermal motion, enables the measurement of a variety of plasma parameters such as the electron density and ion and electron temperatures. Application of this technique to ground based remote study of the upper atmosphere enables the investigation of the ionospheric plasma and, to some extent, the neutral atmosphere. Perhaps the most advanced incoherent scatter radar facility in operation is the European Incoherent Scatter (EISCAT) facility in northern Scandinavia, which comprises two radars: a monostatic VHF radar and a tristatic UHF system. In this chapter the mechanism of incoherent scatter is discussed, as is the development of incoherent scatter radar. The EISCAT facility is described in detail, with particular reference to the UHF system. The procedure by which the returned incoherent scatter signal is analysed is outlined, highlighting some possible causes of uncertainty in the resulting parameters.

#### 3.2 Theory of incoherent scatter

##### 3.2.1 Incoherent scatter

In 1906, J. J. Thomson demonstrated that a single free electron is capable of scattering electromagnetic radiation in a particular direction with a scattering cross-section,  $\sigma$ , given by (*Thomson, 1906*)

$$\sigma = 4\pi(r_e \sin \gamma)^2 \quad (3.1)$$

in which  $r_e$  is the classical radius of an electron and  $\gamma$  is the polarisation angle (the angle between the direction of electric field in the incident radiation and direction of observer). For direct backscatter a free electron would consequently have a scattering cross section,  $\sigma_e$ , of some  $10^{-28} \text{ m}^2$ .

*Fabry (1928)* first proposed that Thomson or incoherent scatter might be used to probe the ionospheric plasma and suggested that the returned frequency spectrum of a monochromatic radar beam scattered from the free electrons of the ionosphere would take the form of a Gaussian, centred on the transmitted frequency, with a Doppler broadening corresponding to the random thermal motion of the electrons. Theory predicts a returned power proportional to  $\sigma_e N_e$ , where  $\sigma_e N_e$  equals the total electron backscatter cross section.

*Gordon (1958)* predicted that the half power half-width of the spectrum would equal  $0.7\Delta F_e$ , where  $\Delta F_e$  is the Doppler shift of an electron approaching the radar at the electron thermal speed and is given by

$$\Delta F_e = \left( \frac{8k_B T_e}{m_e \lambda^2} \right)^{\frac{1}{2}} \quad (3.2)$$

in which  $\lambda$  signifies the radar wavelength.

The existence of small-scale forces within a plasma results in the formation of a ‘shielding’ layer around each electron. The radius of this layer, determined by the balance between electrostatic potential energy and random thermal energy, is termed the Debye length,  $D$ , and is given by

$$D = \left( \frac{\epsilon_0 k_B T_e}{e^2 N_e} \right)^{\frac{1}{2}} \approx 69 \left( \frac{T_e}{N_e} \right)^{\frac{1}{2}} \quad (3.3)$$

in which  $\epsilon_0$  represents the permittivity of free space. The dependence of the Debye length of the ionospheric plasma on electron temperature and density, results in its variation with altitude, being longer in the upper F-region and topside than at E-region altitudes. Furthermore, the Debye length in the ionosphere varies with factors such as season, solar cycle and geographic location, typical values ranging from some 0.3 to 6.0 cm. On scales shorter than the Debye length the electrons may be considered as free, since organised motion cannot be sustained in the plasma whereas, at larger scales, random thermal motion of the electrons generates longitudinal fluctuations in the plasma due to electrostatic coupling, known as ion-acoustic and electron-acoustic waves. Acoustic modes in a plasma propagate isotropically and over a wide and continuous range of frequencies, and have been studied theoretically by, amongst others, *Fejer (1960)*, *Dougherty and Farley (1960)* and *Hagfors (1961)*.

A transmitted radio wave of wavelength less than or comparable to the Debye length will undergo true incoherent scatter off the ionospheric plasma and its backscattered frequency spectrum will be as predicted by Fabry. However, transmitted wavelengths which greatly exceed the Debye length undergo quasi-coherent scatter off those ion- and electron-acoustic waves which satisfy the Bragg criterion for the investigating radar wavelength. The resulting frequency spectrum consists of four components corresponding to the ion- and electron-acoustic waves propagating towards and away from the radar. Theory predicts that the Doppler shifts arising from ion- and electron-acoustic modes,  $F_i(\lambda)$  and  $F_e(\lambda)$  respectively, are given by

$$F_i(\lambda) = \pm \frac{2}{\lambda} \left[ \left( \frac{k_B T_i}{m_i} \right) \left( 1 + \frac{T_e}{T_i} \right) \right]^{\frac{1}{2}} \quad (3.4a)$$

$$F_e(\lambda) = \pm f_p \left( 1 + \frac{12\pi^2 D^2}{\lambda^2} \right)^{\frac{1}{2}} \quad (3.4b)$$

in which  $f_p$ , the plasma frequency, is given by

$$f_p = \left( \frac{e^2 N_e}{4\pi^2 \epsilon_0 m_e} \right)^{\frac{1}{2}} \quad (3.5)$$

The radio wave will scatter off acoustic waves whose phase front is normal to the mirror direction: the mirror direction is that along the bisector of the angle between the transmitter and receiver beams. For a monostatic system, a system in which the transmitter and receiver are co-located, the radar is sensitive to acoustic waves with phase fronts which are normal to the wave vector, i.e. along the direction of the beam.

A charged particle in a plasma, moving in the direction of an electrostatic wave but with a slightly slower speed, will be accelerated due to the transfer of energy from the wave. This results in attenuation of the wave, termed Landau damping. Conversely, particles moving slightly faster than the wave will result in its enhancement. The ion-acoustic velocity lies well within the velocity distribution of the thermal ion population, as illustrated in figure 3.1. More ions travel slightly slower than the ion-acoustic wave than travel slightly faster than the wave leading to significant attenuation of the wave by Landau damping and, hence, substantial broadening of the ion-acoustic lines of the backscattered spectrum. The ion lines broaden to such an extent that they merge. The total width of the backscattered ion line spectrum from the ionospheric plasma varies between 10 kHz (E-region) and 50 kHz (F-region). Electron-acoustic waves propagate at far greater velocity than the majority of thermal electrons (see figure 3.1), thus the electron-acoustic (or plasma) lines will remain sharp. Figure 3.2 presents a representation of a typical returned frequency spectrum for a radar wavelength greatly exceeding the Debye length and for equal ion and electron temperatures, illustrating both the ion and plasma lines.

The spectral shape varies as a function of the sounding wavelength, particularly for transmitted frequencies which do not exceed significantly the Debye length. This factor is illustrated by figure 3.3, which presents the variation of the ion line spectrum as a function of a parameter  $\alpha$ , where  $\alpha$  is given by

$$\alpha = \frac{4\pi D}{\lambda} \quad (3.6)$$

In addition to those discussed above, other factors which determine the spectral shape are the electron to ion temperature ratio, ion composition and collisional effects.

For transmission of a radio wave with a wavelength significantly longer than the Debye length, scatter is quasi-coherent rather than truly incoherent. Nevertheless, in the absence of more appropriate nomenclature, this process is still universally referred to as incoherent scatter.

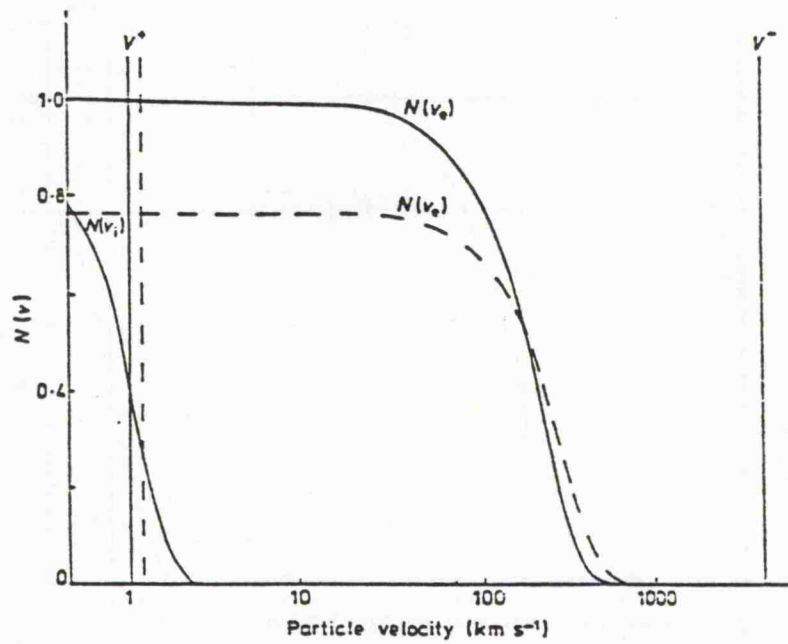


**FIGURE 3.1** Typical velocity distribution of thermal electrons  $N(v_e)$  and thermal ions  $N(v_i)$  and the phase velocity of electron-acoustic ( $V^-$ ) and ion-acoustic ( $V^+$ ) waves (Beynon and Williams, 1978). Solid line:  $T_e = 3500$ , Dashed line:  $T_e = 2500$

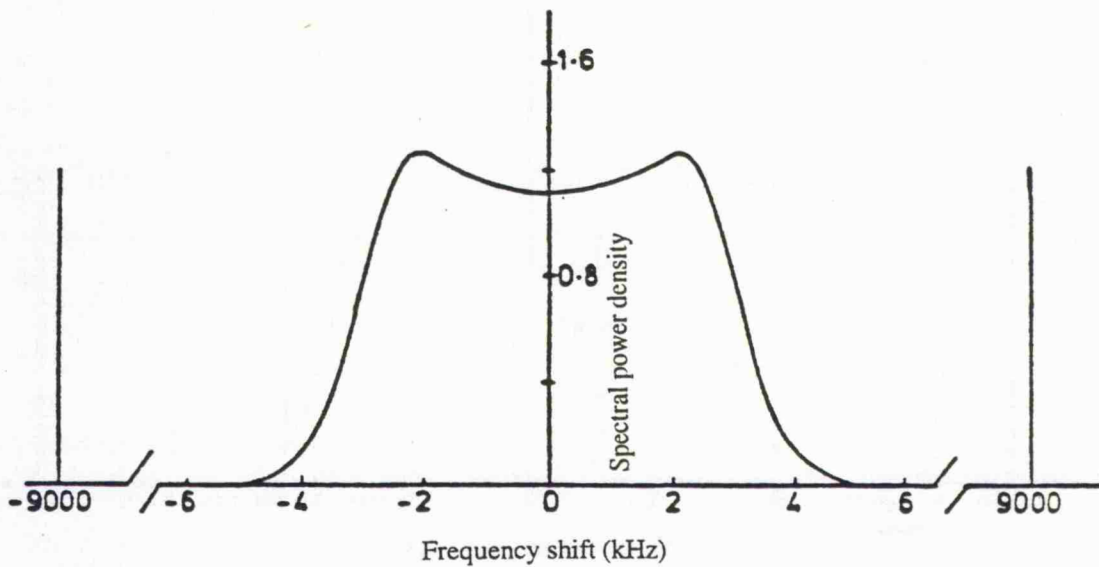


**FIGURE 3.2** Typical incoherent scatter spectrum (Beynon and Williams, 1978).

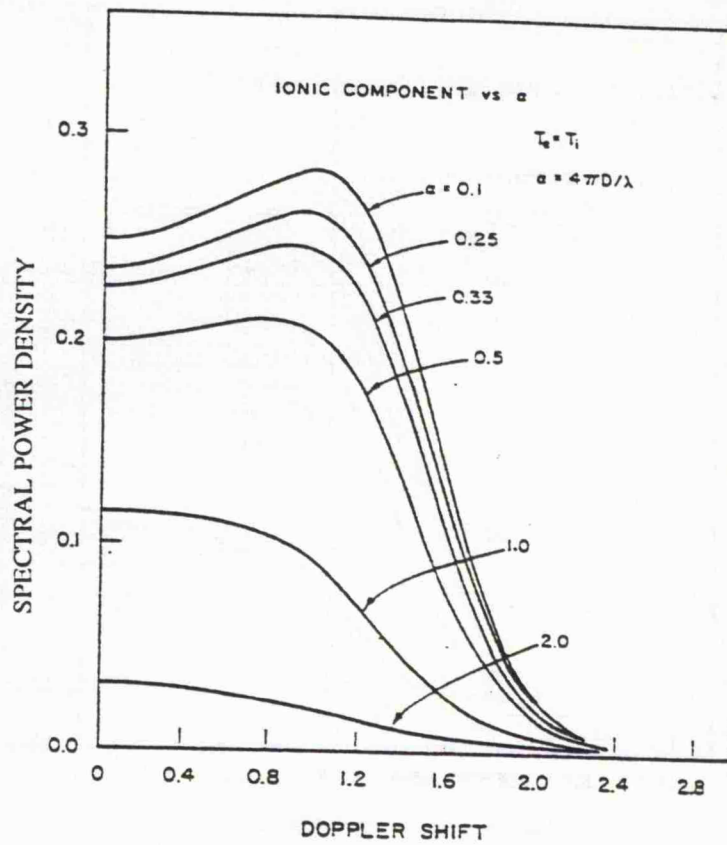


FIGURE 3.3 Variation of the spectrum of the ionic component of the scattered signal with the parameter  $\alpha$  (Evans, 1969).

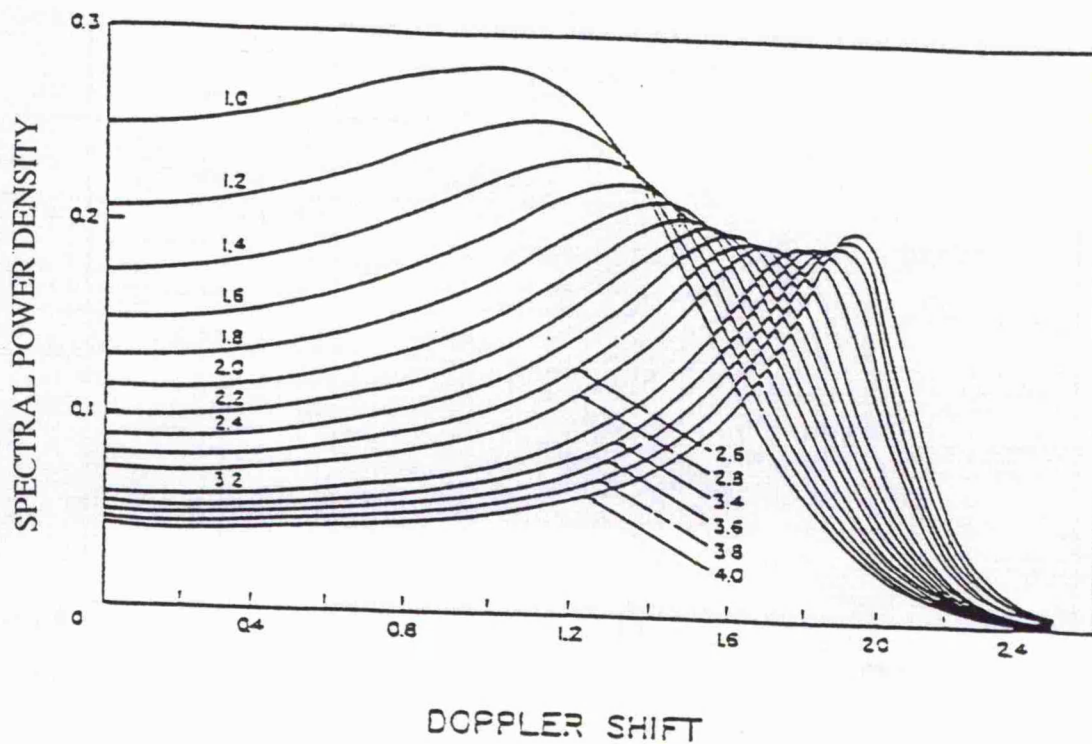


FIGURE 3.4 Variation of the ion line spectral shape for a range of plasma temperature ratios,  $T_e/T_i$  (Evans, 1969).

### 3.2.2 Calculation of parameters from incoherent scatter

A variety of parameters, both of the ionospheric plasma and the neutral atmosphere, may be measured or derived indirectly from incoherent scatter. These are discussed below.

**Electron density** The ionospheric electron density profile may be determined from the total power,  $P_s$ , of the returned signal which, for radars of wavelength greatly exceeding the Debye length, if scattered from an altitude  $h$  is given by

$$P_s(h) = \frac{K\sigma_e N_e(h)}{[1 + (T_e/T_i)]h^2} \quad (3.7)$$

in which  $K$  is a system constant proportional to both the transmitted power and the effective collecting area of the receiver. The system constant can be established by calibration of the measured density with an independent diagnostic and the ratio of the electron and ion temperatures, derived from the shape of the incoherent scatter spectrum. The majority of power scattered by acoustic modes in a plasma is contained within the ion line spectrum. Alternative, but rather more difficult, methods of determining the electron density are by the measurement of the Faraday rotation of the signal (the rotation of its plane of polarisation) and from the offset of the plasma lines of the incoherent scatter spectrum.

**Plasma temperatures and ion composition** The ion lines of an incoherent scatter spectrum are broadened by Landau damping, the degree of which depends on the ratio of the electron and ion temperatures. If the electron temperature is raised relative to the ion temperature the ion-acoustic velocity moves into a region of the thermal ion velocity distribution where the gradient is no longer as steep such that less attenuation of the wave, and hence less broadening of the spectral ion lines, occurs (see figure 3.1). The variation of the ion line spectrum as a function of the electron to ion temperature ratio is shown in figure 3.4. The temperature ratio is thus a controlling factor in determining the sharpness of the ion lines, and can be obtained from the ratio of the peak spectral power density of the ion line spectrum to that at its central minimum.

The separation of the two ion lines is approximately twice the ion-acoustic frequency; the latter may be expressed in the form of equation 3.4a. Given the electron to ion temperature ratio, derived from the spectral shape, the ratio of the ion temperature to the ion mass can be determined from the separation of the two maxima. Furthermore, if an ion mass is assumed the absolute value of the ion temperature and hence the electron temperature can be established. The adoption of a standard ion composition provides the basis for the majority of incoherent scatter analysis, however difficulty in recovering accurate plasma temperatures occurs at altitudes where the ion composition is not well modelled or during disturbed conditions when the ion composition may be significantly modified.

The spectrum of the scattered signal for a multi-ion plasma is not simply that corresponding to the mean ion mass, rather a superposition of the spectra of the individual ion species. The slope of the half-power point is particularly affected by the composition of a plasma containing species of substantially different mass, as demonstrated theoretically by *Moorcroft (1964)* for the transition region between  $O^+$  and the light ions of the topside (see figure 3.5) and by *Lathuillère et al. (1983a)* for the transition region between molecular and atomic species. Thus, provided the measured spectrum is of sufficient signal-to-noise ratio, the ion composition may be measured directly.

**Ion and electron velocities** Bulk motion of the ion population produces a Doppler shift in the frequency of the ion line spectrum corresponding to the component of the mirror velocity along the line-of-sight of the radar. The mirror velocity is that along the mirror direction, as represented diagrammatically in figure 3.6, which for a monostatic system is along the direction of the radar beam. The Doppler shift,  $\Delta F_d$ , due to a ion velocity  $v_m$  along the mirror direction is given by

$$\Delta F_d = \frac{2v_m}{\lambda} \cos\left(\frac{\gamma}{2}\right) \quad (3.8)$$

and, although small compared to the width of the ion line spectrum (as illustrated in figure 3.7), will provide an estimate of the mirror velocity of the ion gas given measurements of sufficient accuracy: figure 3.7 indicates the frequency shift in the ion line spectrum for a plasma velocity of  $100 \text{ m s}^{-1}$  along the mirror direction, and for a transmitted radio wavelength of 1 m.

The plasma lines of the incoherent scatter spectrum will, correspondingly, be Doppler shifted by any bulk motion of the electron gas, although, in the relatively collisionless plasma of the F-region ionosphere, the electrons can realistically be assumed to move with the ion population.

**Ion-neutral collision frequency** In the lower E-region, where the ion-neutral collision frequency greatly exceeds the ion-acoustic frequency, ion-acoustic waves no longer propagate. The returned ion line spectrum thus loses its double-humped appearance and becomes narrower. The influence of ion-neutral collisions on the ion line spectrum for equal ion and electron temperatures is demonstrated in figure 3.8, which illustrates the dependence of the spectral shape on a parameter  $\psi_i$  where

$$\psi_i = \frac{\lambda v_{in}}{4\pi} \left[ \frac{m_i}{2k_B T_i} \right]^{\frac{1}{2}} \quad (3.9)$$

If the ion and electron temperatures are assumed equal, the ion-neutral collision frequency can thus be retrieved directly from the returned spectrum, although fitting of this type is restricted to altitudes below some 120 km altitude and electric fields of less than  $25 \text{ mV m}^{-1}$  (e.g. *Wickwar et al., 1981; Huuskonen et al., 1986*).

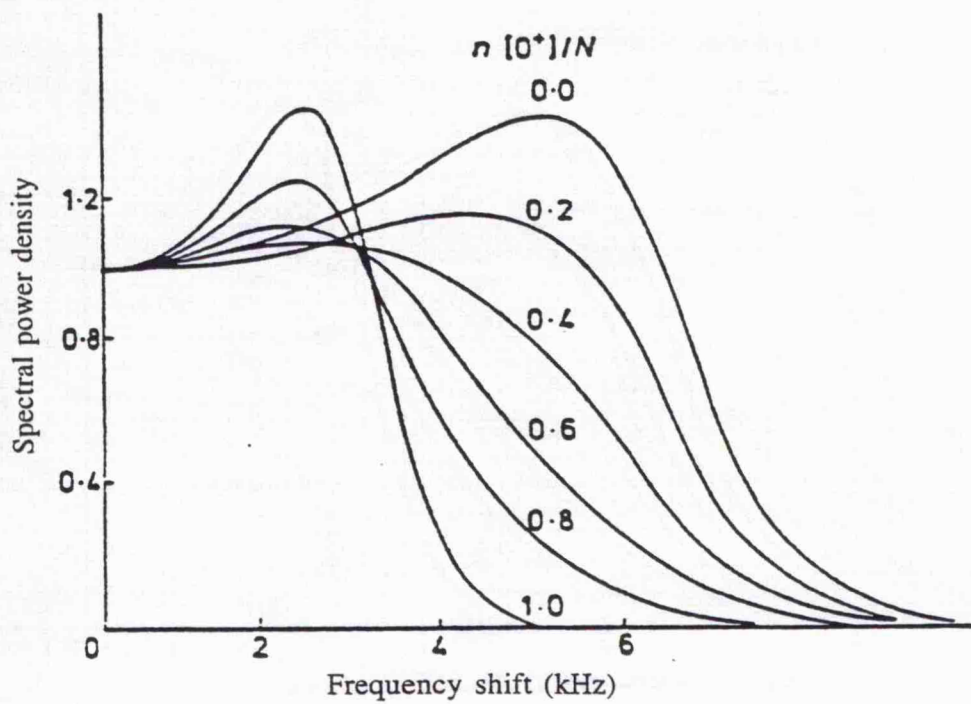


FIGURE 3.5 Variation of the ion spectrum for different mixtures of  $O^+$  and  $He^+$  (Moorcroft, 1964).

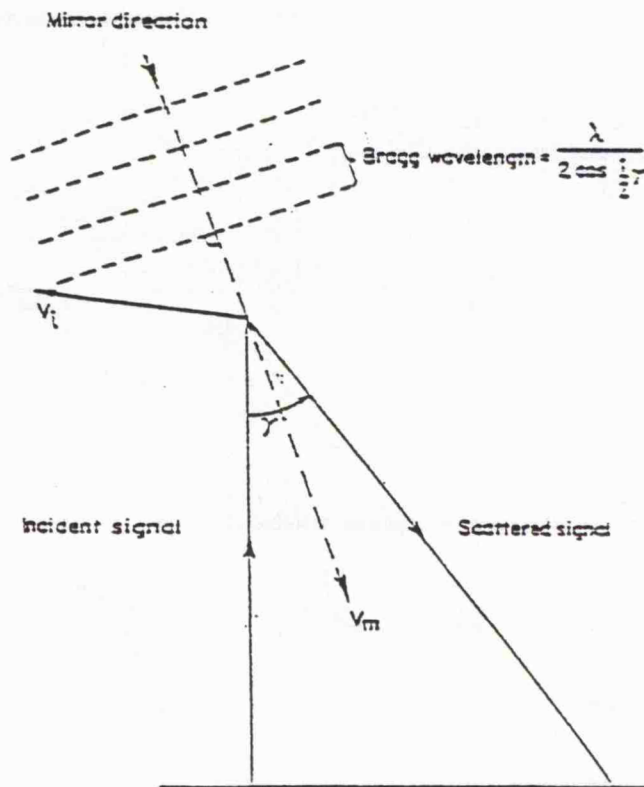


FIGURE 3.6 Mirror geometry for a bistatic radar system (Rishbeth and Williams, 1985).

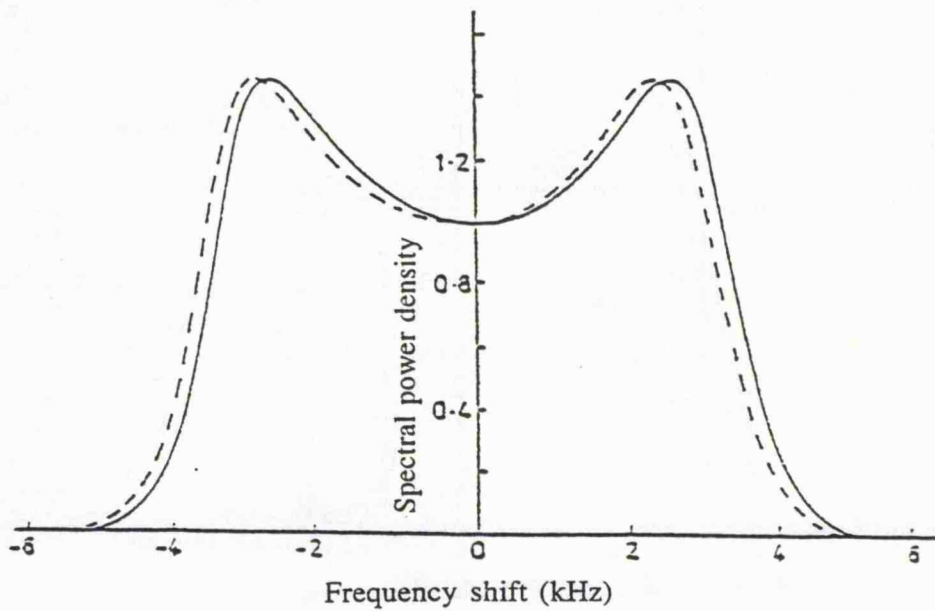


FIGURE 3.7 Frequency shift of the ion line spectrum due to a plasma velocity of  $100 \text{ m s}^{-1}$  away from the radar (dotted line) compared to an unshifted ion line spectrum (solid line) (Beynon and Williams, 1978).

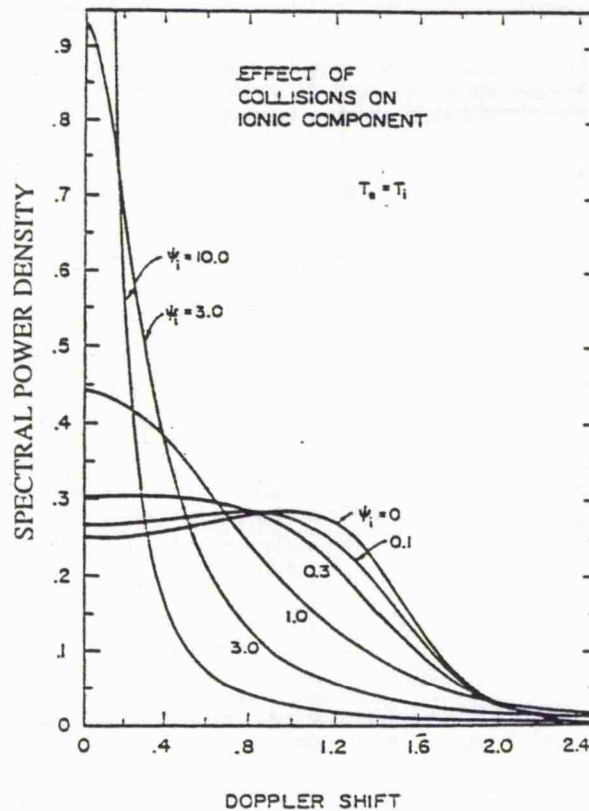


FIGURE 3.8 The effect of collisions on the ionic component of the incoherent scatter spectrum (Evans, 1969).

**Other parameters** In addition to those already discussed, two other parameters may be determined directly from the returned incoherent scatter spectrum under favourable conditions or over a limited altitude range. These are the spectra of suprathermal electrons, which can significantly enhance the plasma lines of the returned spectrum, and the electric current density which, it has been suggested, would be directly measurable from any differential Doppler shift between the ion and electron lines of the returned spectrum. From those ionospheric parameters which can be directly measured others may be estimated; including the electric field and the Hall and Pedersen conductivities. In addition, by making certain assumptions several parameters of the neutral atmosphere may be derived.

All of the parameters which can be measured directly or derived by incoherent scatter are listed in table 3.1. Those parameters in table 3.1 which are denoted by an asterisk can not be fully described by measurements from a single receiver station, rather it is only the component along the line-of-sight of the radar which is resolved. The tristatic nature of the EISCAT UHF radar enables the full vector velocity to be established and, moreover, permits investigation of ion temperature anisotropy, both of which are of considerable importance to the present work.

The mechanism of incoherent scatter and the derivation of ionospheric parameters thereby are extensively reviewed in the literature (*e.g. Beynon and Williams, 1978; Evans, 1969*).

### 3.3 Development of incoherent scatter radar

Very high-power radar facilities, developed for use in World War II, were suggested to be capable of detecting the small returned signal from Thomson scatter off the ionospheric electrons (*Gordon, 1958*). *Gordon (1958)* predicted that the half-width of the returned Gaussian frequency spectrum would be some 200 kHz at typical ionospheric electron temperatures for a transmitted radio wave of wavelength 1.5 m, and, consequently, a very large antenna system would be required for detection of such signals.

The first experimental measurements of ionospheric backscatter were performed by *Bowles (1958)*, by means of a 6 MW, 41 MHz transmitter at Long Branch, Illinois. Although the power of the returned frequency spectrum was consistent with that which would be expected from Thomson scatter, the bandwidth was considerably narrower. *Bowles (1958)* surmised that the ions influence the scattering characteristics of the plasma. Later authors confirmed theoretically that for a transmitted wavelength significantly greater than the Debye length it is inappropriate to consider scatter off free electrons in the ionosphere (see section 3.2.1).

One of the earliest facilities constructed specifically for incoherent scatter studies, and still one of the highest powered, is the dipole array, covering an area exceeding 80,000 square metres, constructed at Jicamarca, Peru (*Bowles, 1963*). This facility was situated within 2° of the geomagnetic equator, ideally located to study such phenomena as the

Directly measured	Derived indirectly
Electron density, $N_e$	Electric field, $E$
Electron temperature, $T_e$	Hall conductivity, $\sigma_H$
Ion temperature, $T_i$ *	Pedersen conductivity, $\sigma_P$
Ion composition, $m_i$	Exospheric heat flux, $\phi$
Ion velocity, $v_i$ *	Neutral density, $N_n$
Electron velocity, $v_e$ *	Neutral temperature, $T_n$
Ion-neutral collision frequency, $\nu_{in}$	Neutral velocity, $v_n$
Photoelectron flux	
Electric current density, $J=N_e(v_e-v_i)$ *	

**TABLE 3.1** Parameters measured and derived from incoherent scatter.

equatorial anomaly and equatorial electrojet, and began observations in 1961. The following year, the 305 m diameter spherical reflector at Arecibo, Puerto Rico, commenced operation (*Gordon, 1964*). These were joined, in 1963, by an incoherent scatter radar facility at Millstone Hill, Massachusetts, comprising one, and later two, parabolic antennas, a 68 m diameter fixed vertical pointing dish and a fully steerable 25 m dish.

In 1965 an incoherent scatter radar commenced operation at Stanford, California, employing a 27 m parabolic dish. In 1971, this system was moved to Chatanika, Alaska, following developing interest in the investigation of the high-latitude ionosphere, where it provided seminal observations of auroral phenomena (*Leadabrand et al., 1972*). The radar was subsequently moved to a position closer to the geomagnetic pole at Sondrestromfjörd in Greenland. The installation in 1972, at the Kharkov Polytechnic in the former USSR, of a 100 m parabolic dish enabled further, albeit not generally available, incoherent scatter ionospheric observations.

The first incoherent scatter radar facility in Europe was constructed at St. Santin, France, and became operational in 1965 (*du Castel et al., 1966*). An existing radio-telescope at Nancay was employed as a remote receiver establishing the first bistatic incoherent scatter radar and by 1973 two further receivers, at St. Cassien and Mende, were incorporated to resolve several limitations identified in the initial system. An incoherent scatter radar facility at Malvern in the United Kingdom was upgraded, after three years of monostatic operation from 1968 (*Hey et al., 1968*), with the addition of remote receiver sites at Wardle, Chilbolton and Aberystwyth. Both the French and British facilities ceased operation in the late seventies.

Since 1985, the Japanese Middle and Upper atmosphere (MU) radar, at Shigaraki, has been performing incoherent scatter measurements (*e.g. Oliver et al., 1988, Sato et al., 1989*). The MU radar is a monostatic radar with an active phased-array system, the antenna of which comprises a circular array of 475 crossed Yagi elements, having a total diameter of 103 m. The major detriment for incoherent scatter operation with the MU radar is the significant galactic background noise encountered at its operating frequency of 46.5 MHz.

The operating characteristics of all of the aforementioned incoherent scatter radars are contained in table 3.2, based on that presented by *Beynon and Williams (1978)*.

The idea for a high-latitude incoherent scatter radar facility, far more sophisticated than any then in operation, was advanced at an URSI meeting in 1969. Negotiations culminated in the signing, in 1975, of an agreement between the research councils of six European countries, Finland, France, Norway, Sweden, the United Kingdom and Germany (then West Germany), to construct the European Incoherent Scatter radar facility (EISCAT). Moreover, the Japanese have, within the last year, become the seventh member of the EISCAT Scientific Association. The following sections discuss the operational characteristics and capabilities of the EISCAT radar facility, specifically with

Station	Geographic Location	Antenna	Frequency (MHz)	Power	
				Peak (MW)	Mean (MW)
Jicamarca (1962)	11.9° S 76.9° W	290x290 m dipole array	49.9	4.0	0.4
Arecibo (1962)	18.3° N 66.8° W	305 m spherical reflector	430.0	2.0	0.1
Millstone Hill (1963)	42.6° N 71.5° W	68 m parabola	440.0	3.0	0.12
Millstone Hill (1963)	42.6° N 71.5° W	25 m parabola	1295.0	4.0	0.12
Stanford (1965-71)	37.4° N 122.2° W	27 m parabola	1300.0	5.0	0.12
Chatanika (1971-1982)	64.9° N 147.7° W	27 m parabola	1300.0	5.0	0.12
Sondrestrom- fjörd (1982)	67.0° N 51.0° W	27 m parabola	1300.0	5.0	0.12
Kharkov (1972)	48.5° N 36.9° E	100 m parabola	150.0	2.0	
St Santin (1965-87)	44.6° N 2.2° E	20x100 m reflector	935.0		0.15 (cw)
Nancay (1965-87)	47.4° N 2.2° E	40x200 m reflector		Receiver station	
St Cassien (1973-87)	44.7° N 0.8° E	25 m parabola		Receiver station	
Mende (1973-87)	44.5° N 3.5° E	25 m parabola		Receiver station	
Malvern (1968-75)	52.1° N 2.3° W	43 m parabola		400.5	8.0
Wardle (1971-75)	53.1° N 2.6° W	25x36 m parabola		Receiver station	
Chilbolton (1971-75)	51.1° N 1.4° W	25 m parabola		Receiver station	
Aberystwyth (1972-75)	52.4° N 4.0° W	Two 12x25 m parabolic troughs		Receiver station	
MU (1985)	34.9° N 136.1° W	103 m circular array of 475 crossed Yagis	46.5	1.0	0.05

TABLE 3.2 Operational characteristics of incoherent scatter radars (Beynon and Williams, 1978).

reference to the EISCAT UHF radar.

### **3.4 The European incoherent scatter (EISCAT) facility**

#### **3.4.1 Operational characteristics of EISCAT**

The European Incoherent Scatter (EISCAT) facility comprises three radars, a tristatic UHF radar, which commenced full operation in late 1981, a monostatic VHF system and the recently constructed EISCAT Svalbard radar (ESR) which is presently undergoing preliminary testing. The VHF radar, from which reliable observations are available since 1985, has both transmitter and receiver co-located in Tromsø, Northern Norway. The transmitter of the UHF radar system is located at Tromsø and receivers are sited at Tromsø, Kiruna in Sweden and Sodankylä in Finland: the UHF radar of the EISCAT facility is currently the only tristatic incoherent scatter radar in operation. The ESR is a monostatic UHF radar sited at Longyearbyen the island of Spitsbergen in the Svalbard archipelago, several hundreds of miles north of mainland Norway. The ESR is seen as an essential ground based tool for the study of the cleft/cusp region of the magnetosphere. Some general characteristics of the three radars are tabulated in table 3.3 and figure 3.9 illustrates the geographic position of the three mainland EISCAT sites. Further discussion will be limited to the UHF system of the EISCAT facility, observations from which provide the majority of data employed in the research documented in this thesis, although a detailed description of the characteristics of the EISCAT VHF radar may be found in, for example, *Hagfors et al. (1982)* and *Folkestad et al. (1983)* and details of the ESR will be available in many future publications.

The UHF system comprises three parabolic antennas, each of 32 m diameter providing an effective collecting area of 570 m<sup>2</sup>. Each antenna has a half-power beam width of 0.6° and is fully steerable independently in both azimuth (270° either side of geographic north) and elevation (from 2° to 100°), at a maximum rate of 80° per minute. The UHF transmitter, powered by a single klystron, is capable of providing a peak power of 2 MW and, on a maximum duty cycle of 12.5 %, an average power of some 250 kW. The transmitter can operate on any of 16 frequencies, spaced at 0.5 MHz intervals around a central frequency which is currently 931.5 MHz (initially 933.5 MHz, but recently adjusted due to interference from mobile telephone systems), and can switch between frequencies on a time scale of microseconds, although sampling is limited to eight tuneable receiver channels. The wavelength of UHF transmission, some 30 cm, is conducive to probing of the ionospheric plasma by incoherent scatter at altitudes typically between 80 km and 1500 km, although the longest range from which observations are available is constrained by power considerations. Circular polarisation is transmitted, corresponding to the reception of circular polarisation by the receiver at Tromsø and elliptically polarised signals at the remote sites.

Primary receivers comprise GaAs-FET amplifiers (helium cooled at the remote

Station	Geographic	Antenna	Frequency (MHz)	Power	
	Location			Peak (MW)	Mean (MW)
Tromsø VHF	69.6° N 19.2° E	120x40 m parabolic trough ( Tx /Rx )	224.0	5.0	0.62
Tromsø UHF	69.6° N 19.2° E	32 m parabola ( Tx / Rx )	933.5	2.0	0.25
Kiruna UHF	67.9° N 20.4° E	32 m parabola		Receiver station	
Sodankylä UHF	67.4° N 26.7° E	32 m parabola		Receiver station	
Longyearbyen ESR	78.2° N 16.1° E	32 m parabola	500.0	0.5	0.125

**TABLE 3.3** Operating characteristics of the EISCAT radars.



sites, uncooled at Tromsø) giving a noise temperature of the order 90 K and 30 K at Tromsø and the remote sites, respectively. These replaced the original helium cooled parametric amplifiers installed at each receiver site. The preamplified received incoherent scatter signal is mixed, using a 1051.5 MHz local oscillator, down to  $120 \pm 4$  MHz. The signal is then attenuated by between 0 and 63 dB and divided between the eight receiver channels. The signal from each channel is further downconverted, to an intermediate frequency of 30 MHz, and bandpass filtered. The resulting signal enters a hybrid detector, fed by a 30 MHz reference signal, to produce two outputs in quadrature. These signals, after further baseband filtering and amplification, deliver cosine and sine inputs to an analogue/digital converter (ADC) where they are sampled at a rate compliant with communication theory (*Shannon, 1948*). The width of the baseband filter must be sufficient to accommodate the backscattered ion line spectrum, taking also into consideration possible Doppler shift due to bulk plasma flow along the line-of-sight. The output from each ADC is passed to a correlator which comprises a 'ping-pong' type buffer memory. The correlator reads from one half of the buffer memory while the ADC simultaneously writes to the other half, this process reversing every pulse repetition period. The correlator computes autocorrelation functions (ACFs), Fourier transforms of the incoherent scatter power spectra, from which the ionospheric parameters are retrieved. The results of these computations, containing both the real and imaginary parts of the ACF, are written to the result memory from where they are dumped to disc from which they are subsequently copied to magnetic tape or digital audio tape.

Each EISCAT site is controlled by means of a NORD ND-500 computer, interfaced to the hardware devices. The three site computers are linked by telephone lines and inter-site communication, which was previously controlled by a NORD ND-10 at Kiruna, is now via the internet. All high-precision timing signals are generated by a radar controller, programmed in a language known as TARLAN (transmitter and receiver language). Lower level commands, such as antenna pointing and data handling, are specified using EROS (EISCAT real time operating system). The RTGRAPH (real time graphics) system enables real time monitoring of the returned signal, ACFs and spectra.

A comprehensive description of the technical characteristics and operational capabilities of the EISCAT radar facility has been documented by, amongst others, *Folkestad et al. (1983)*.

### 3.4.2 Measurement techniques

In the simple case of single pulse transmission, the pulse is sampled at a discrete set of intervals during its passage through the ionosphere, each being multiples of a basic lag increment (*Farley, 1969*). An estimate of the ACF is formed from the cross-products of these samples. The time delay between the two samples in a cross-product constitutes a lag of a given interval. Multiple estimates of each lag are obtained and the  $k$ th lag of the ACF,  $A_k$ , is given by their average.

$$A_k = \frac{1}{(m-k)} \sum_1^{m-k} S_i S_{i+k}^* \quad (0 \leq k \leq m-1) \quad (3.10)$$

in which  $m$  = total number of samples  
 $m-k$  = number of estimates of  $k$ th lag  
 $S_i^{(*)}$  = (complex conjugate of)  $i$ th sample

Figure 3.10 illustrates the range-time diagram for a single pulse of length  $\tau$  indicating the manner in which various lags of the ACF are calculated from measured samples. The receiver is 'gated' over a length  $\tau$  such that returned signals are received from the scattering volume centred at range  $R$ , although contributions are present between  $R-c\tau/2$  and  $R+c\tau/2$ , where  $c$  is the speed of light. The technique of calculating an ACF from a closed set of samples corresponds to the method by which ACFs were calculated in early EISCAT observations. The number of estimates of each lag of the ACF and the spatial extent over which lags are correlated decrease with increasing lag number, the longest lag being derived from a single estimate at the central range. These factors introduce a reduction in the effective signal-to-noise ratio for the longer lags and an uneven spatial distribution for the different lags of the ACF. These problems were resolved by the implementation, in 1984, of the GEN system of correlator programs (*Turunen, 1986*) which introduced the idea of gating after the evaluation of cross-products.

There are other, often conflicting, constraints on the form of the transmitted pulse. The signal-to-noise ratio (snr) for EISCAT UHF measurements over a bandwidth limited by the width of the ion line spectrum is given by (*Rishbeth and Williams, 1985*)

$$\text{snr} = \frac{P_s}{P_n} \propto \frac{\hat{P}\tau N_e}{R^2 [1 + (T_e/T_i)]} \quad (3.10)$$

in which  $P_n$  = noise power  
 $\hat{P}$  = peak transmitter power

The accuracy of the received signal power of a pulsed radar,  $\Delta P_s/P_s$ , is related to the signal-to-noise ratio via the following expression (*du Castel and Vasseur, 1972*).

$$\frac{\Delta P_s}{P_s} = \frac{1 + \text{snr}^{-1}}{(b\tau N)^2} \quad (3.11)$$

in which  $b$  represents the signal bandwidth and  $N$ , the number of pulses integrated.

The accuracy of the deduced ionospheric parameters is related to that of the backscattered signal power, given in equation 3.11, via empirical relationships. Both equations 3.10 and 3.11 illustrate the need to maximise the pulse length for increased signal-to-noise ratio and accuracy of observations.

Other limitations on pulse length are imposed by ionospheric conditions. The height resolution of the radar measurements should be shorter than the scale height,  $H$ , of the ionospheric plasma, which varies between several km in the E-region and 50 km in the F-region, in order to describe adequately its altitude variation. For vertical transmission the maximum pulse length should, therefore, be  $2H/c$ , although much higher spatial resolution may be necessary for the study of small scale features, such as sporadic E. To attain maximum spectral resolution from the backscattered signal the maximum correlation time of the pulse must exceed that of the ionosphere ( $\tau_i$ ), which is given by the reciprocal of the ion line bandwidth. The need for both adequate range resolution and spectral resolution imposes contradictory constraints on the length of the transmitted pulse, which, for the EISCAT UHF system is unattainable for altitudes below some 200 km (see figure 3.11). The time-of-flight of the radar pulse is given by  $2h/c$ ; this determines the length of the longest pulse which can be transmitted, since simultaneous transmission and reception is not possible. The problem is resolved by the transmission of multi-pulse or alternating code pulse schemes which enable measurements to be obtained at altitudes where a single long pulse is unsuitable.

The multi-pulse technique is described, in detail, by *Farley (1969, 1972)* and involves the transmission of a series of sub-pulses, each short enough to provide adequate altitude resolution, at variable spacings within an envelope of sufficient duration to provide adequate spectral resolution. Figure 3.12 presents the range-time diagram for one of the simplest multi-pulse schemes, that comprising four pulses each of length  $\tau$  transmitted at times 0, 1, 4 and 6 units; the correlated signals are represented as dark cells. This multi-pulse allows the formation of estimates of lags 1 to 6 of an ACF with an altitude resolution corresponding to  $\tau$ . Multi-pulse schemes do not provide a true zero lag although this is overcome by transmitting a single pulse of length  $\tau$  at a slightly different frequency, often termed a power profile. The use of multi-pulse transmission by EISCAT is discussed by *la Hoz (1982)*. One basic disadvantage of multi-pulse schemes is their relatively low signal-to-noise ratio, due to a combination of self-clutter (the simultaneous reception of echoes from different sub-pulses indicated by shaded cells) and the small proportion of the duty cycle employed. The latter is partially offset by exploiting the frequency agility of EISCAT to nest together several multi-pulse sequences.

A more recent technique of achieving measurements of improved spectral and spatial resolution by EISCAT is by the transmission of alternating codes (*Lehtinen and Haggström, 1987*). An alternating code is a series of pulses, each comprising a continuous sequence of either 8 or 16 phase coded sub-pulses of length  $\tau$ . There are two types of alternating code, strong and weak condition. For strong condition alternating codes the phase coding within each pulse is such that, on decoding the backscattered signal, all but a single lag of the ACF at a single range, with resolution corresponding to  $\tau$ , totally cancels out. Varying the sequence of decoding enables the formation of any predetermined lag at any specified range. Although for strong condition alternating codes all clutter from

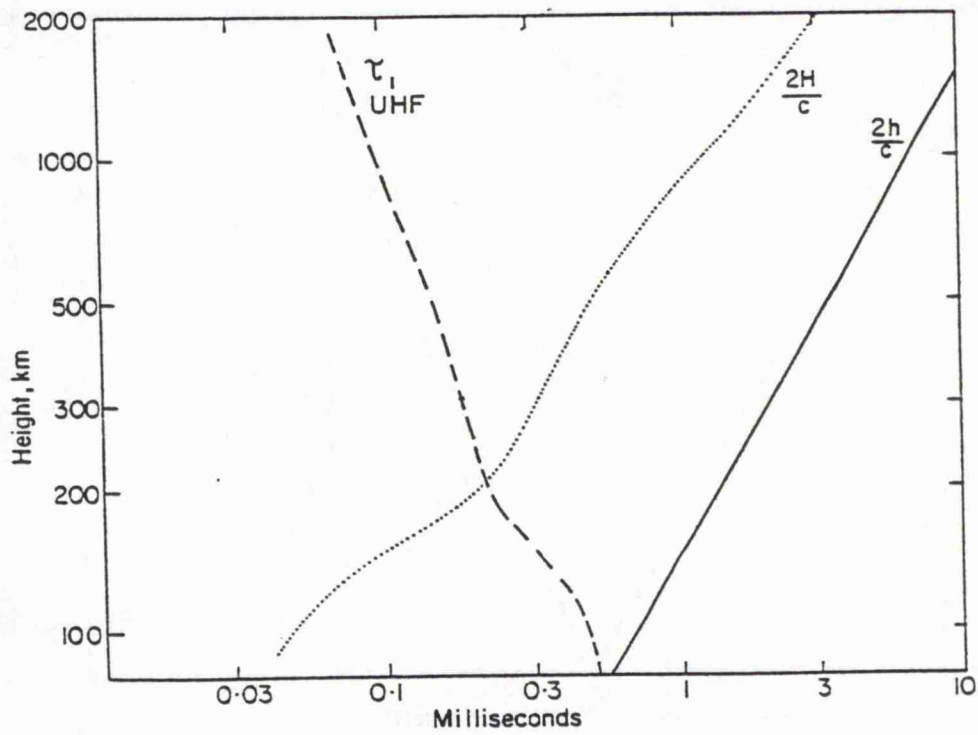


**FIGURE 3.11** Some constraining factors for incoherent scatter experiments (*Rishbeth and Williams, 1985*).

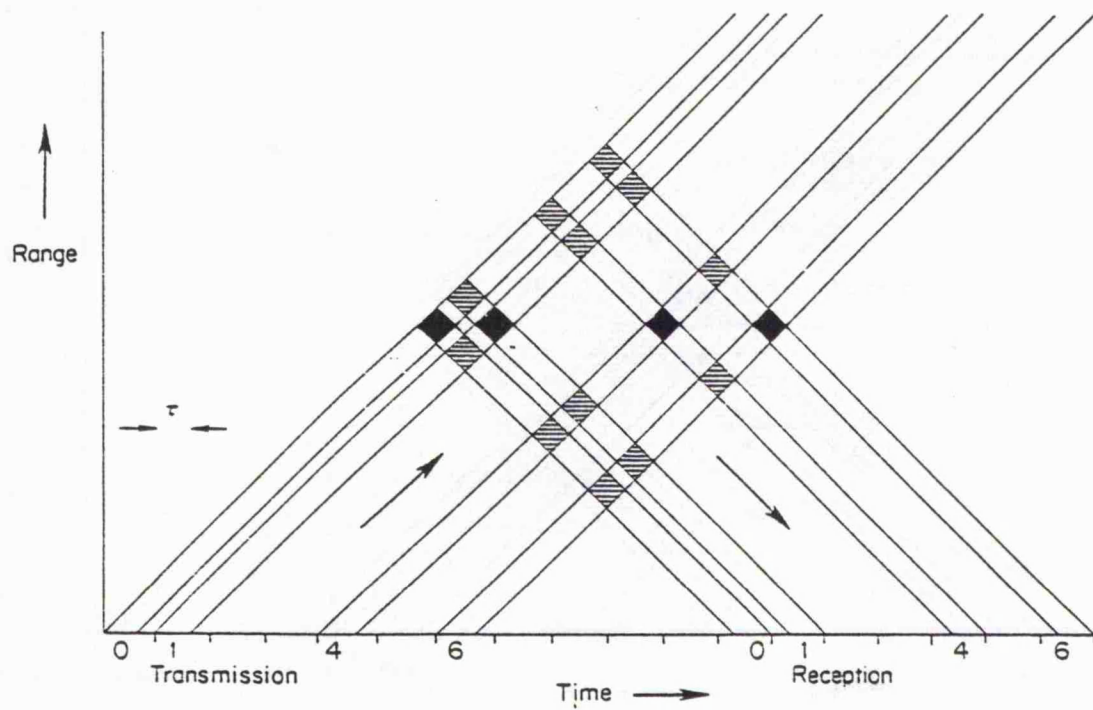


**FIGURE 3.12** Range time diagram for a four pulse multi-pulse pattern (*Rishbeth and Williams, 1985*).

adjacent pulses cancels out, this is not so for weak condition alternating codes. To resolve this, the sub-pulses of weak condition alternating codes may themselves be coded or transmitted at two frequencies. Alternating code pulse schemes do not provide a true zero lag, although this may be overcome, as it is for multi-pulse transmission, by the transmission of a power profile of pulse length  $\tau$ . Alternating codes employ a large proportion of the available duty cycle, and, at least for strong condition codes, there is no contamination by self-clutter thus good signal-to-noise levels are attainable.

### 3.4.3 EISCAT common programmes

50% of the observing time of the EISCAT facility, some 1000 hours annually, is designated to the operation of so-called 'special programmes' and the other half to running 'common programmes'. Common programmes are operated routinely whereas special experiments are designed and run by scientists of individual associate member countries. There are presently seven EISCAT common programmes, three for the VHF radar (common programmes 4, 6 and 7) and four for the UHF system (common programmes 1, 2, 3 and 5). Although each common programme has, since its introduction, subsequently been refined and modified, the basic idea is retained to provide substantial data sets, enabling long-term studies to be performed. The observing geometry of each of the UHF common programmes is as follows (*Rishbeth and Williams, 1985; Röttger, 1991*).

**Common programme 1 (CP-1)** The CP-1 experiment was designed for high time resolution studies of dynamic phenomena, such as substorms. Indeed, the CP-1 and CP-2 UHF experimental modes, the latter of which is discussed below, provide the majority of observations employed in the analysis documented in the present thesis. In CP-1, and its forerunners CP-M1 and CP-0, the transmitter is aligned along the local magnetic field direction near the F-region peak, which, at Tromsø, is approximately southwards at an elevation of some  $77^\circ$ . In the current version of CP-1, CP-1-K, the remote site antenna beams intersect the transmitter beam at the F-region altitude of 278 km, although in previous versions of this common programme the remote site UHF receivers observed in both the E- and F-regions. Long pulse, two power profiles and an alternating code pulse scheme are transmitted, the latter being a recent replacement for multi-pulse transmission in earlier versions.

**Common programme 2 (CP-2)** In the present version of CP-2 the transmitter performs a four position scan, one position of which is field-aligned and another vertical. The remaining two pointing directions are south and south-east of the vertical position. The remote site antennas follow the scan, intersecting the transmitter beam at a fixed altitude in the F-region, 278 km in the current version. The dwell time for each position of the scan is 1.5 minutes, giving a cycle time of 6.0 minutes. As in the CP-1 experiment, long pulse, power profile and alternating code pulse schemes are transmitted, the latter, again, a recent inclusion. The CP-2 experiment was designed to incorporate both the adequate spatial and temporal resolution necessary to study wave-like phenomena such as

atmospheric gravity waves.

**Common programme 3 (CP-3)** CP-3 performs a sixteen position latitude scan in a meridian passing over both Tromsø and Kiruna and covering some 64 to 74° in geographic latitudinal extent. The remote site antennas follow the scan, observing at 278 km altitude. An additional position, 20° to the north-east of the scan trajectory enables velocity determinations in the far north of the viewing area by a beam-swinging technique. The duration of a scan is some 26 minutes and scans are synchronised to begin on 30 minute boundaries. Long pulse and power profile pulse schemes are transmitted. CP-3 enables the investigation of latitudinally elongated features, such as troughs, and allows mapping of the convection pattern over a large latitude range albeit at a reduced temporal resolution.

**Common programme 5 (CP-5)** CP-5 is a little run common programme and is a compromise between the CP-1 and CP-3 experiments, intended to remove the spatial/temporal ambiguity inherent in these programmes. A ten position scan, comprising the central positions of the CP-3 scan, is performed with a cycle time of 30 minutes. Each scan includes an extended (10 minutes) field-aligned dwell. The remote site antennas follow the scan at 278 km altitude, although in the field-aligned position the remotes cycle between this altitude and four E-region intersection altitudes. Long pulse, multi-pulse and two power profiles are transmitted.

In addition to the standard UHF common programmes discussed above there are three so-called 'unusual programmes (UP)', designed for the study of particular geophysical phenomena such as auroral events and sporadic E-layers. These unusual programmes can be started on very short notice when the appropriate geophysical conditions arise.

#### 3.4.4 Incoherent scatter data analysis

The dependence of the incoherent scatter ion line spectrum on a variety of geophysical parameters has been detailed in section 3.2.2. The technique for analysis of the spectra, or equally the ACFs, to provide estimates of these parameters is summarised in figure 3.13, for various forms of radar data.

If identical measurements are made on different frequencies, the ACFs from each channel may be integrated. Successive dumps of data from the correlator may also be added together. Such post-integration over frequency and time reduces uncorrelated noise. In alternating code and multi-pulse data the power profile may be used to create a zero lag for the ACF, although the zero lag can be obtained by interpolation. Other preliminary corrections may be necessary depending on the pulse code or the form of the correlator program.

The three main instrumental effects on the ACF arise from the form of the transmitted pulse, the response of the receiver and the weighting of the lags due to the method of correlation. The modification in the appearance of the incoherent scatter ACF

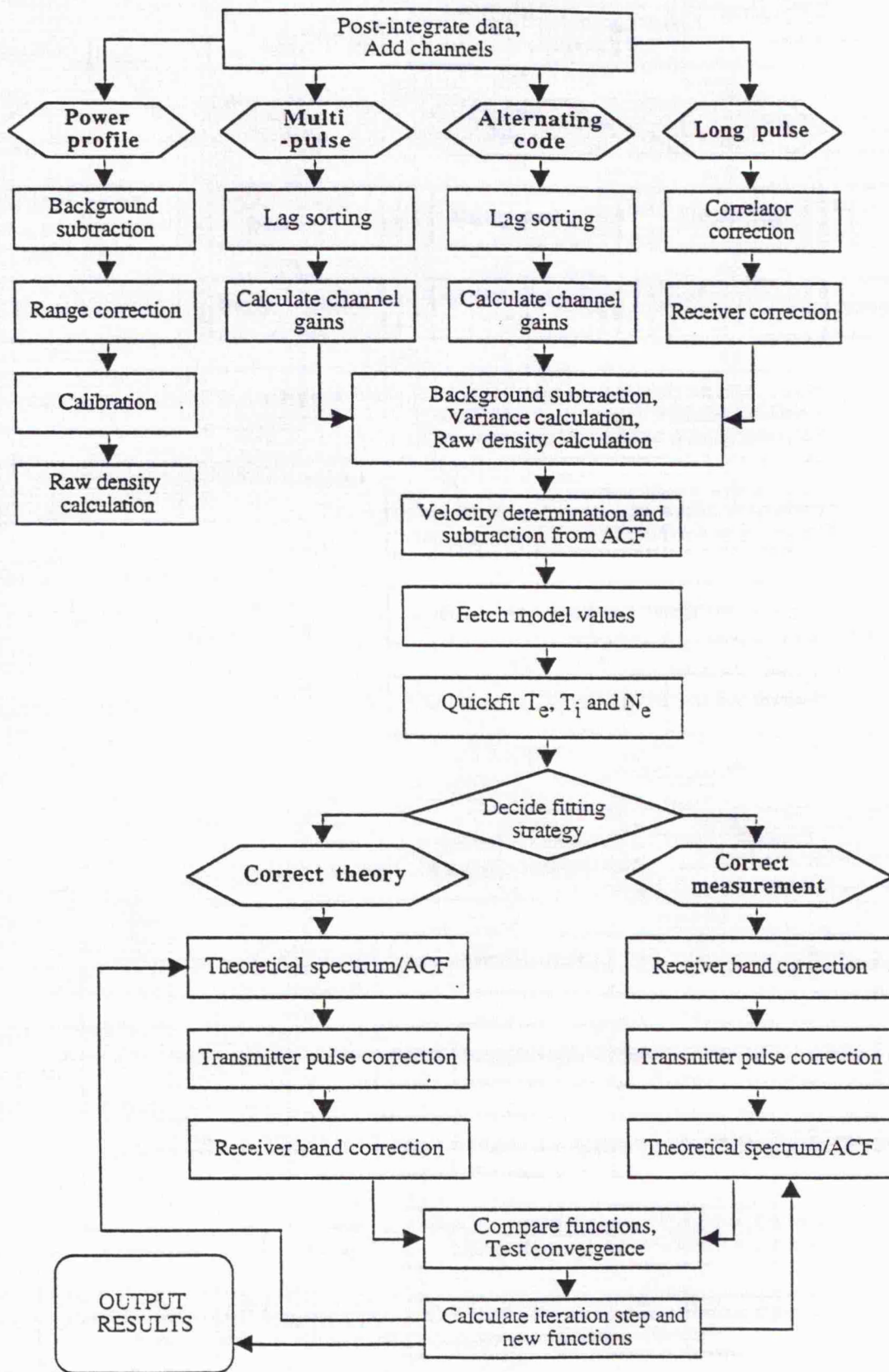


**FIGURE 3.13** Block diagram illustrating the principal features of the UK incoherent scatter analysis program.

due to these effects is illustrated in figure 3.14. The ACF of a pulse incoherently scattered from the ionospheric plasma,  $A_S(t)$ , is the product of the ACF of the transmitted pulse,  $A_T(t)$ , and the incoherent scatter ACF,  $A_I(t)$ . This is equivalent to the convolution of the appropriate spectra. The ACF is subsequently modified during its passage through the receiver, where a noise spike at the zero lag (not visible in the figure) is also introduced. The ACF output by the receiver, given by  $A_R(t)$ , is equal to the convolution of the ACF of the received pulse and that of the baseband filter. The ACF output by the correlator,  $A_F(t)$ , incorporates any weighting due to gating of the samples prior to determining their cross-products, although this is now largely avoided with the advent of the GEN system of forming correlator products. A more detailed discussion of instrumental effects on the ACF measured by the incoherent scatter technique is presented by *Rishbeth and Williams (1985)*.

After correction to remove instrumental effects has been performed, the background noise level, an estimate of which is deduced by sampling beyond the last signal gate, is subtracted from the signal in each gate. After such pre-processing the derivation of ionospheric parameters can proceed.

A preliminary estimation of the raw electron density, based on the backscattered signal power (the zero lag of the ACF (see figure 3.15)), is calculated via equation 3.6 in which the ion and electron temperatures are assumed equal and the system constant is neglected. If the plasma has a bulk motion the spectrum will be Doppler shifted and the ACF produced in the correlator will have both real and imaginary components. Using a matched filter technique the drift velocity may be determined and its effect removed from the ACF.

The ACF can then be used to determine the other parameters. This is done by minimising the variance between the measured ACF and a theoretical ACF corresponding to known plasma parameters. To do this efficiently it is necessary to adopt reasonable initial values for each of the parameters to be derived. These are obtained from the principal features of the unshifted ACF by a 'quick-fitting' method. Approximate values of the ion and electron temperatures are determined from the first cross-over point and the first minimum of the ACF (see figure 3.15) and are then employed to correct the raw electron density. From these quick-fit estimates of electron density and plasma temperature, an empirically produced ion line spectral function is computed. Alternatively, the parameters from the previous fit can be used as initial estimates. The theoretical spectrum is continuously corrected and compared, transformed into the time domain, with the measured ACF employing a multi-variant least squares fit. Iteration proceeds until the variance between the theoretical and measured ACFs is less than a specified threshold and gives an optimum set of parameters: if, however, convergence is not attained within a pre-set maximum number of iterations, the fit is deemed a failure and a 'bad fit' flag is set.

Although, in general, analysis is performed to provide estimates of the ion drift

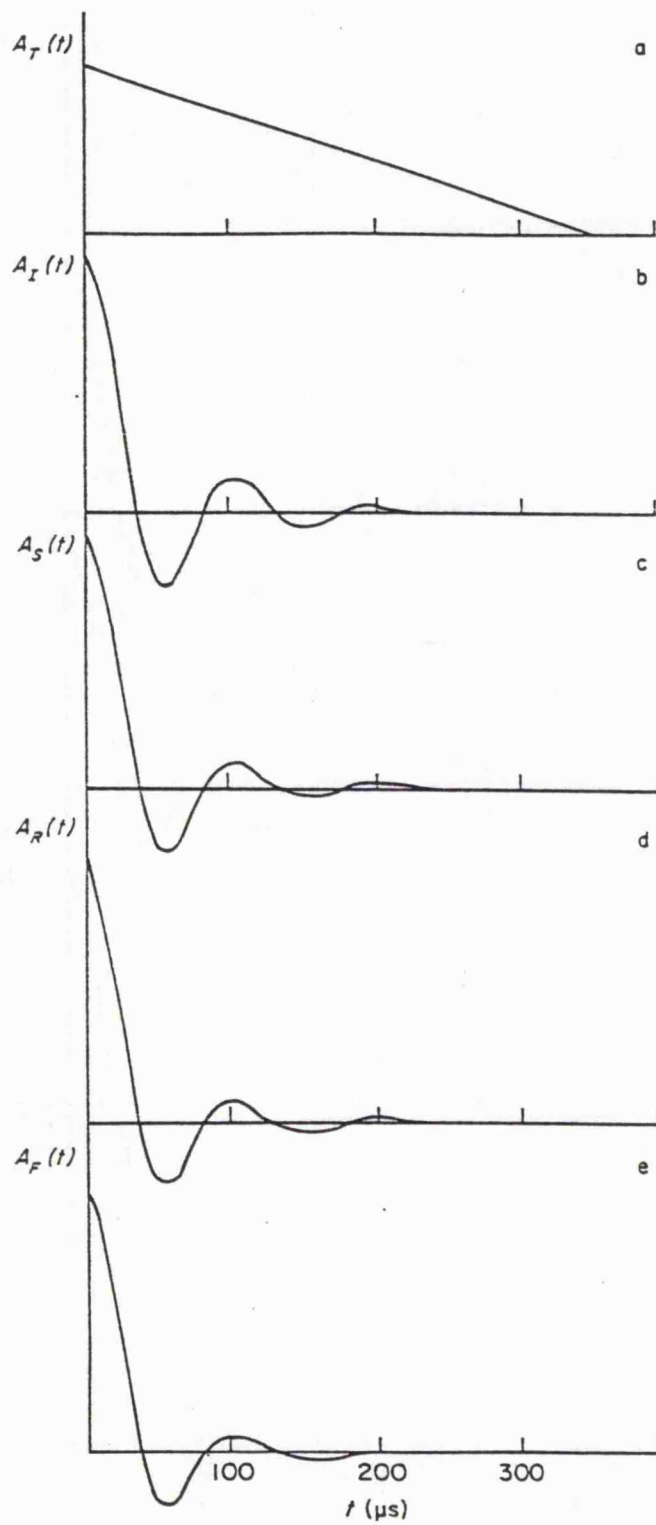


**FIGURE 3.14** ACFs illustrating the effects of the system on the incoherent scatter signal (Rishbeth and Williams, 1985).

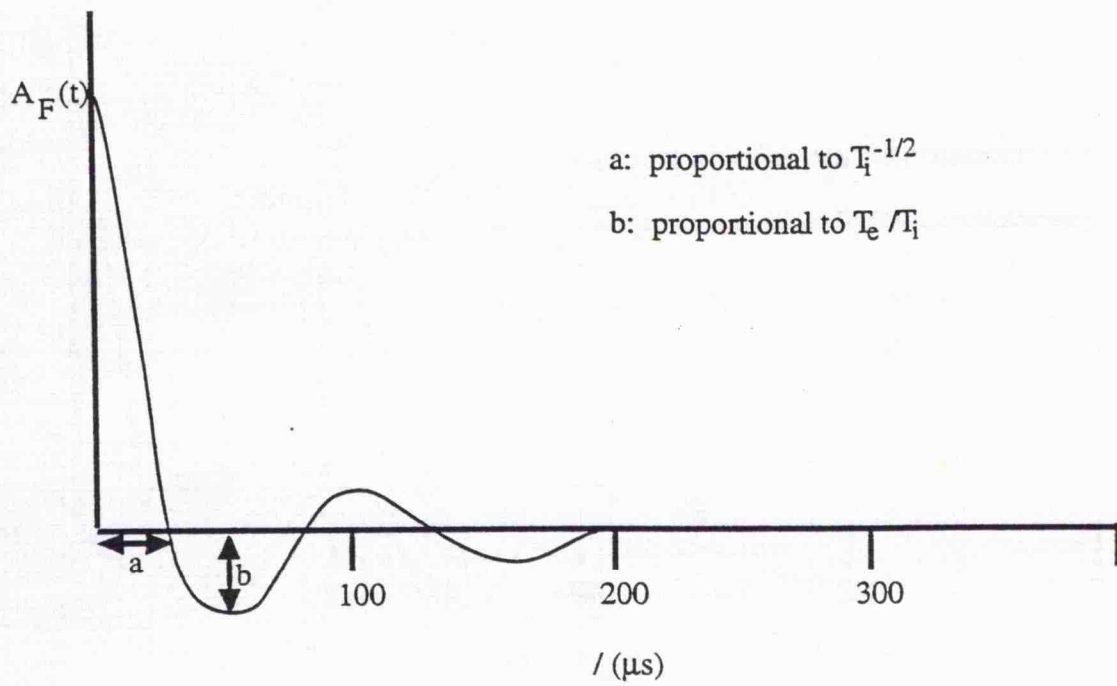


**FIGURE 3.15** Correlated ACF indicating the derivation of parameters for initial quickfit analysis

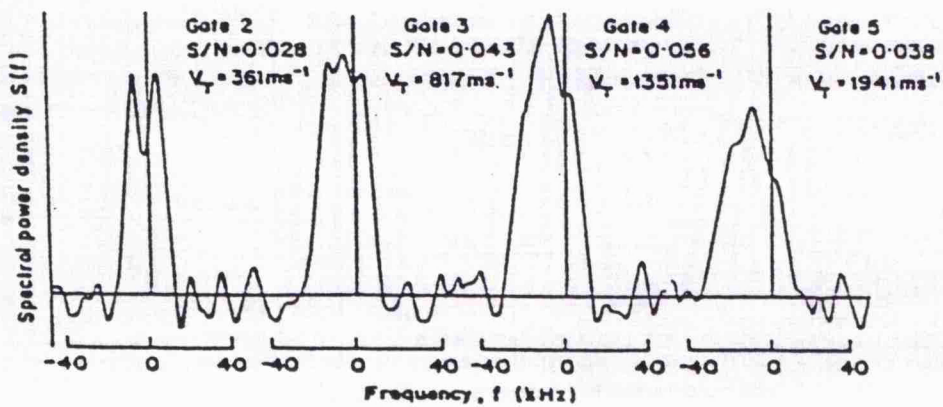


**FIGURE 3.16** Non-Maxwellian spectra observed by the EISCAT radar (Lockwood *et al.*, 1987).

velocity, ion and electron temperatures and electron density other parameters, such as the ion composition and ion-neutral collision frequency, may be retrieved from analysis under certain conditions (see section 3.2.2.).

### 3.4.5 Errors in incoherent scatter measurements

An awareness of the possible sources of uncertainty in incoherent scatter measurements is necessary for their unambiguous interpretation. Some of the more important sources of error, in both the collection and analysis of EISCAT observations, are discussed below.

**Random error** The significance of incoherent scatter measurements can be established from empirical relationships between the uncertainty in a given parameter and the signal-to-noise ratio. The accuracy of the received signal power of a pulsed radar,  $\Delta P_s/P_s$ , is given by equation 3.11 (*du Castel and Vasseur, 1972*). The authors concluded that the accuracy of measurement of the electron density ( $\Delta N_e/N_e$ ), electron temperature ( $\Delta T_e/T_e$ ) and ion temperature ( $\Delta T_i/T_i$ ) are related to that of the signal power by the formulae

$$\frac{\Delta P_s}{P_s} \approx \frac{\Delta N_e}{N_e} \approx \frac{\Delta T_e}{2T_e} \approx \frac{\Delta T_i}{2T_i} \quad (3.12)$$

and the random error in the line-of-sight ion velocity is given by

$$\Delta v_i = (0.5 + \text{snr}^{-1}) \frac{\lambda}{2} \frac{\Delta F_i}{(b\tau N)^{\frac{1}{2}}} \quad (3.13)$$

in which  $\Delta F_i$  signifies the ion line half-width. Similar analysis by *Murdin (1979)*, based on computationally simulated data, corresponding to the procedure by which EISCAT autocorrelation functions are formed, yielded similar formulae with the exception that the error in the electron density was twice that predicted by *du Castel and Vasseur (1972)*.

**Fit error** As described in the previous section, the plasma parameters are retrieved in EISCAT analysis by minimising the variance between the measured autocorrelation function and a theoretical one. The sum of the residuals between the measured and theoretical autocorrelation functions is further used to calculate an error in each parameter due to the fitting procedure. This error is referred to as the fit error for a given parameter.

**Uncertainty due to plasma velocity distribution** In EISCAT common program analysis the ion and electron thermal velocity distributions along the direction of measurement are assumed to be Maxwellian. This removes the requirement to fit for the ion temperature and the form of the ion velocity distribution function simultaneously. During intervals of high ion-neutral relative flow the form of the line-of-sight ion thermal velocity distribution may depart significantly from Maxwellian, especially at large aspect angles (*e.g. Hubert and Kinzelin, 1992*). The degree of distortion depends upon the type of collision, but tends to be more for atomic  $O^+$  than molecular ions. The characteristic effect of a non-

Maxwellian ion velocity distribution on an F-region incoherent scatter spectrum is to produce a maximum, or less depressed minimum, at the central frequency, predicted by *Raman et al. (1981)* and identified in EISCAT observations by *Lockwood et al. (1987)* and *Winser et al. (1987)*. This is accompanied by an increase in backscattered power, possibly due to the presence of coherent irregularities (*Lockwood et al., 1988*). Figure 3.16 illustrates non-Maxwellian spectra observed by EISCAT at an aspect angle of  $73^\circ$ , during an interval of enhanced ion flow (*Lockwood et al., 1987*). Analysis of EISCAT incoherent scatter signals where the line-of-sight ion thermal velocity distribution is actually non-Maxwellian has been found to lead to erroneous temperature measurements; an overestimate of the ion temperature and an underestimate of the electron temperature (*e.g. Lockwood et al., 1993; Moorcroft and Schlegel, 1988*), confirmed by analysis of simulated spectra by *Lathuillère and Hubert (1989)*. Attempts to fit the incoherent scatter spectra observed by *Winser et al. (1987)* to the non-Maxwellian velocity distribution function produced by a simple relaxation collision model were found to produce credible results for aspect angles greater than  $30^\circ$  (*Suvanto et al., 1989b*). It has also been suggested that the F-region electron thermal velocity distribution may become non-Maxwellian in regions of field-aligned current (*Maehlum et al., 1984*).

**Uncertainty due to ion composition** Standard analysis of EISCAT data proceeds by means of a time invariant ion composition profile which specifies the relative proportions of atomic and molecular ions, although attempts have been made to fit for ion composition directly from EISCAT measurements (*e.g. Lathuillère et al., 1983a; Lathuillère and Brekke, 1985*). The molecular ion species assumed present in the composition model for standard EISCAT analysis are  $\text{NO}^+$  and  $\text{O}_2^+$  in the proportion 3:1 and the atomic population comprises  $\text{O}^+$ , at least below an altitude of some 800 km. Figure 3.17 illustrates how the adopted ion composition, specifically the proportion of molecular ions, varies as a function of altitude. Accuracy in the determination of the plasma temperatures from the incoherent scatter autocorrelation function relies on the adoption of a realistic model of ion composition (*e.g. McCrea et al., 1995*). The adopted composition profile is reasonably representative of the true ion composition during undisturbed conditions. However, as has been discussed in detail in the previous chapter of the present thesis, ion frictional heating can result in substantial modification of the ion composition, particularly in the lower F-region where significant production of molecular ions takes place (*e.g. Lathuillère, 1987*). An underestimate in the fraction of molecular ions present results in an underestimate in the ion and electron temperatures, as apparent from equation 3.4a; the ratios of the real to derived plasma temperatures is reasonably well approximated as equal to that between the real and assumed ion masses (*Lockwood et al., 1993*). The adoption of a time-invariant ion composition model places an important constraint on the accuracy to which both ion and electron temperatures can be determined during such intervals, a problem considered further in later chapters.

**Errors due to single temperature analysis** Standard EISCAT analysis assumes that, for

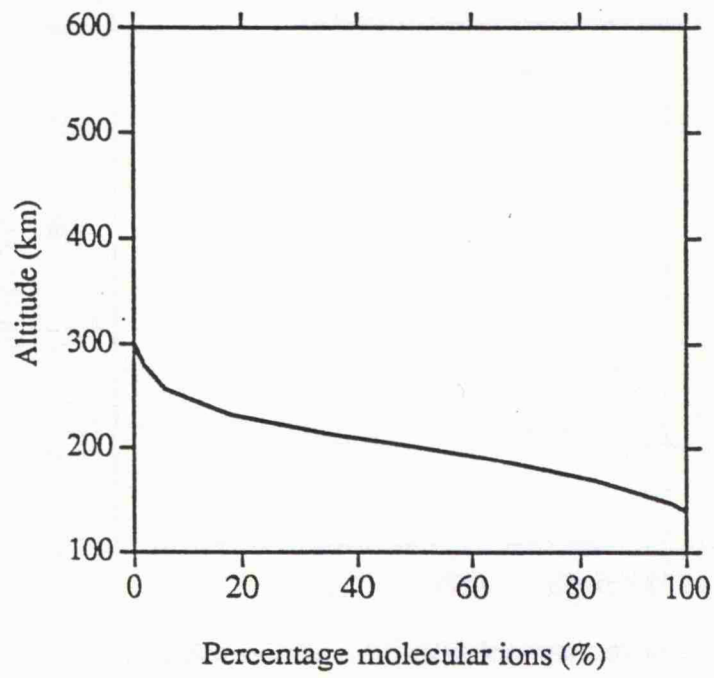


**FIGURE 3.17** The ion composition model adopted for standard E- and F-region EISCAT analysis

a multi-ion plasma, the line-of sight ion temperatures of all species are equal. In single temperature EISCAT analysis for a multi-ion plasma, the derived temperature is not simply a weighted mean of the temperature of each ion species due to the non-linearity of the incoherent scatter spectrum. As each ion species is subject to different collisional mechanisms, a relative velocity between the ion and neutral populations causes the ion temperatures to diverge, particularly those of atomic and molecular species (*Lathuillère and Hubert, 1989*). The temperature difference between the species varies as a function of ion-neutral relative velocity and also aspect angle, with the greatest deviation being in the direction of the magnetic field (*Lathuillère and Hubert, 1989*). Caution must therefore be exercised in the interpretation of ion temperatures derived from single temperature EISCAT analysis during intervals when relative ion-neutral flows exist. A detailed discussion of all of the limitations of EISCAT analysis during intervals of high ion-neutral relative flow, particularly to provide estimates of ion temperature, is contained in *McCrea et al. (1995)*.

### **3.5 Summary**

An overview of the process of incoherent scatter of radio waves from the acoustic waves present in a plasma has been presented. The application of this technique to ground based investigation of the ionospheric plasma through the development of incoherent scatter radar has been discussed, with particular reference to the European incoherent scatter (EISCAT) facility in northern Scandinavia. The analysis of the scattered signal has been detailed, including possible causes of uncertainty in the derived parameters.

## Chapter 4

### Statistical study of ion frictional heating

#### 4.1 Introduction

This chapter presents the results of a statistical study of F-region ion frictional heating based on in excess of 3200 hours of field-aligned common programme observations taken between January 1985 and December 1990 by the EISCAT UHF radar facility. The criterion adopted in the present study for the identification of ion frictional heating is that defined by *McCrea et al. (1991)*, which is based on a selection criterion for frictional heating derived by *St-Maurice and Hanson (1982)* for the study of high-latitude F-region ion temperature observations from the Atmospheric Explorer-C satellite. The diurnal distribution of ion frictional heating observed by EISCAT is established and, furthermore, its dependence on such factors as solar cycle and the orientation of the interplanetary magnetic field is investigated. The occurrence distributions of ion frictional heating are interpreted with reference to corresponding distributions of enhanced ion velocity, again derived from the extended set of EISCAT UHF common programme observations.

#### 4.2 Experimental arrangement

The following investigation is based on F-region observations taken by the EISCAT UHF radar in versions F, H and I of the common programme 1 (CP-1) mode of operation and versions C and D of common programme 2 (CP-2). The basic geometry of each common programme, noted in section 4.3 of chapter 3, is retained to enable long term studies of the type documented in the present chapter to be performed, although subsequent versions of each programme are updated and refined. The geometrical arrangement and measurement techniques adopted in each experiment are discussed below and any relevant difference between successive versions of each programme is highlighted.

In the EISCAT CP-1 mode, the beam from the UHF transmitter is aligned along the local magnetic field direction in the F-region which, for a radar located at Tromsø, is at an elevation of around  $77.5^\circ$  and an azimuth of  $182.5^\circ$ . In the versions of CP-1 employed in the present study, the remote site radars, at Kiruna and Sodankylä, alternated between E- and F-region observation with a scan of 10 minutes duration. In version F of the CP-1 programme (CP-1-F) the remote site radars performed a five position scan intersecting the transmitter beam at four E-region altitudes and at 312 km in the F-region. In the subsequent version, CP-1-H, the remote site scan was slightly modified in that the F-region intersection volume was reduced in altitude to 278 km. In both the CP-1-F and CP-1-H experimental modes, the effective dwell time at the F-region intersection altitude was some 90 seconds. In CP-1-I, however, the remote site radars performed an eight position scan intersecting the transmitter beam at six different E-region altitudes and at 278 km altitude in the F-region, the latter being repeated twice within each scan with a dwell time of approximately 60 seconds.

In the earlier version of the CP-1 mode, CP-1-F, four pulse schemes were

transmitted: long pulse, multi-pulse, and two power profiles. A long pulse scheme of pulse length 360  $\mu\text{s}$  yielded an altitude resolution of some 22 km along the radar beam direction, with observations extending from approximately 150 to 590 km altitude. The 5 pulse multi-pulse transmission scheme, with an elementary pulse length of 20  $\mu\text{s}$ , was employed for high resolution E-region observations, affording an altitude resolution of approximately 4.5 km. A power profile pulse scheme, of pulse length 20  $\mu\text{s}$ , was included for the determination of raw electron density in the D- and E-regions at high altitude resolution, providing, moreover, a zero lag for the multi-pulse scheme. A further power profile of pulse length 60  $\mu\text{s}$  provides a more coarse determination of the electron density at higher altitudes. In the two later versions, CP-1-H and CP-1-I, the same pulse schemes as in CP-1-F were transmitted although the pulse lengths of the long pulse, the elementary pulse length of the multi-pulse scheme and lengths of the high and low resolution power profile pulses were adjusted to 350  $\mu\text{s}$ , 14  $\mu\text{s}$ , 14  $\mu\text{s}$  and 29  $\mu\text{s}$ , respectively.

In CP-2, the transmitter performs a four position scan, one position of which is vertical and another, field-aligned. In the remaining two positions, the transmitter points geomagnetically eastward of the zenith. The dwell time for each position of the scan is 1.5 minutes, giving a total cycle time of 6 minutes. The remote site radars follow the transmitter beam scan, observing at a fixed F-region altitude, 312 km for CP-2-C and 278 km in the subsequent version, CP-2-D. For CP-2-C, the transmission schemes were as for CP-1-F, although no multi-pulse scheme was included. The pulse schemes transmitted in CP-2-D were identical to those for the CP-1-H and CP-1-I experimental modes described above.

For the present study, CP-1 observations from Tromsø were post-integrated at a temporal resolution of 5 minutes and the remote site data over the dwell time at each scan position. CP-2 observations from all sites were post-integrated over the dwell time at each scan position. Data were analysed by assuming the standard, time-invariant ion composition profile illustrated in figure 18 of the previous chapter. Individual experiment runs included in the extended data set are listed in table 4.1, which notes start and end times (in UT) of each run and the experiment mode. Tables 4.1a, 4.1b and 4.1c include experimental runs from 1985 and 1986, 1987 and 1988 and 1989 and 1990, respectively; providing a total of 3237 hours of EISCAT common programme observations.

It is accepted that the analysis of incoherent scatter spectra to provide estimates of ion temperature is limited by three factors when the ion-neutral relative velocity is high. These factors are the occurrence of non-Maxwellian line-of-sight ion thermal velocity distributions, modification of the ion composition and the divergence of the temperatures of the different ion species. The effect of these limitations is briefly discussed with respect to the present observations at salient points in the text, although a more detailed discussion is contained in chapter 3.

### 4.3 Selection criterion for the identification of ion frictional heating

The current study extends that documented by *McCrea (1989)* and *McCrea et al.*

Start date	Start time	End date	End time	Mode
28/01/85	12:00 UT	29/01/85	12:00 UT	CP-1-F
14/02/85	12:00	15/02/85	12:00	CP-1-F
19/02/85	14:00	20/02/85	14:00	CP-2-C
10/04/85	13:00	11/04/85	13:00	CP-2-C
16/04/85	11:00	17/04/85	11:00	CP-1-F
07/05/85	07:00	08/05/85	07:00	CP-2-C
14/05/85	08:00	15/05/85	08:00	CP-1-F
21/05/85	08:00	22/05/85	12:00	CP-1-F
25/06/85	12:00	26/06/85	12:00	CP-1-F
02/07/85	08:00	03/07/85	08:00	CP-2-C
06/08/85	08:00	07/08/85	08:00	CP-1-F
13/08/85	08:00	14/08/85	13:45	CP-1-F
03/09/85	08:00	03/09/85	22:00	CP-1-F
10/09/85	08:00	11/09/85	22:00	CP-1-F
14/10/85	23:00	18/10/85	12:00	CP-2-C
29/10/85	09:00	30/10/85	09:00	CP-1-F
05/11/85	09:00	06/11/85	09:00	CP-1-F
12/11/85	09:00	13/11/85	23:00	CP-1-F
03/12/85	09:00	04/12/85	23:00	CP-1-F
18/02/86	09:00	19/02/86	09:00	CP-1-F
25/02/86	09:00	26/02/86	09:00	CP-1-F
25/03/86	09:00	26/03/86	09:00	CP-1-F
08/04/86	08:00	09/04/86	08:00	CP-1-F
22/04/86	08:30	23/04/86	08:00	CP-2-C
21/05/86	08:00	22/05/86	08:00	CP-2-C
27/05/86	08:00	28/05/86	08:00	CP-1-F
15/07/86	12:30	16/07/86	12:30	CP-1-F
22/07/86	08:00	23/07/86	08:00	CP-1-F
29/07/86	08:00	30/08/86	22:00	CP-1-F
05/08/86	08:00	06/08/86	08:00	CP-1-F
12/08/86	08:00	13/08/86	08:00	CP-1-F
02/09/86	08:00	03/09/86	11:00	CP-1-F
30/09/86	09:00	01/10/86	17:00	CP-2-C
21/10/86	09:00	22/10/86	23:00	CP-2-C
11/11/86	14:00	12/11/86	23:00	CP-2-D
19/11/86	14:00	20/11/86	23:00	CP-2-D
10/12/86	09:00	11/12/86	23:00	CP-1-F

TABLE 4.1a EISCAT experiment runs included in statistical study (1985 and 1896).

<b>Start date</b>	<b>Start time</b>	<b>End date</b>	<b>End time</b>	<b>Mode</b>
13/01/87	14:00	14/01/87	23:00	CP-1-H
20/01/87	09:00	21/01/87	23:00	CP-2-D
10/02/87	10:00	11/02/87	23:00	CP-1-H
17/02/87	09:00	18/02/87	09:00	CP-2-D
24/02/87	09:00	25/02/87	09:20	CP-1-H
17/03/87	09:00	18/03/87	21:45	CP-2-D
24/03/87	09:00	25/03/87	23:00	CP-1-H
14/04/87	08:00	15/04/87	22:00	CP-1-H
05/05/87	08:00	06/05/87	22:00	CP-2-D
12/05/87	08:00	13/05/87	22:00	CP-1-H
16/06/87	08:00	17/06/87	08:00	CP-1-H
23/06/87	08:00	24/06/87	08:00	CP-2-D
28/07/87	08:00	29/07/87	08:00	CP-1-H
21/09/87	08:00	25/09/87	08:00	CP-1-H
20/10/87	09:00	22/10/87	11:00	CP-2-D
10/11/87	08:00	12/11/87	23:00	CP-1-H
17/11/87	09:00	19/11/87	23:00	CP-1-H
16/03/88	09:00	20/03/88	09:00	CP-1-H
05/04/88	08:00	06/04/88	08:00	CP-1-H
06/04/88	18:00	07/04/88	06:15	CP-1-H
11/04/88	08:00	13/04/88	08:00	CP-2-D
03/05/88	08:00	04/05/88	08:00	CP-1-H
13/06/88	08:00	15/06/88	08:00	CP-2-D
26/07/88	08:00	27/07/88	22:00	CP-1-H
09/08/88	08:00	10/08/88	08:00	CP-2-D
16/08/88	08:00	18/08/88	22:00	CP-2-D
30/08/88	08:00	01/09/88	22:00	CP-1-H
06/09/88	08:00	07/09/88	22:00	CP-1-H
27/10/88	15:30	27/10/88	23:00	CP-1-H
15/11/88	09:00	17/11/88	07:00	CP-2-D

TABLE 4.1b EISCAT experiment runs (1987 and 1988).

Start date	Start time	End date	End time	Mode
10/01/89	09:00	11/01/89	23:00	CP-1-I
07/02/89	09:00	08/02/89	09:30	CP-1-I
14/02/89	08:30	15/02/89	17:00	CP-2-D
28/03/89	08:00	29/03/89	22:00	CP-1-I
25/04/89	08:00	26/04/89	20:30	CP-2-D
02/05/89	08:00	03/05/89	08:00	CP-1-I
01/08/89	13:00	03/08/89	16:00	CP-1-I
05/09/89	10:00	06/09/89	13:00	CP-1-I
28/08/89	12:00	01/09/89	16:00	CP-2-D
23/10/89	18:00	25/10/89	14:40	CP-2-D
14/11/89	10:00	16/11/89	16:00	CP-1-I
24/01/90	10:00	25/01/90	16:00	CP-1-I
20/03/90	15:30	22/03/90	16:00	CP-2-D
09/04/90	10:00	10/04/90	16:00	CP-1-I
21/05/90	10:00	22/05/90	16:00	CP-2-D
05/06/90	10:00	06/06/90	16:00	CP-1-I
12/06/90	08:00	13/06/90	13:45	CP-1-I
02/07/90	10:30	03/07/90	16:00	CP-1-I
30/07/90	18:00	01/08/90	04:00	CP-1-I
25/09/90	10:00	27/09/90	22:00	CP-1-I
09/10/90	09:00	09/10/90	21:00	CP-1-I
10/10/90	11:30	11/10/90	16:00	CP-1-I
24/10/90	10:00	25/10/90	16:00	CP-2-D
13/11/90	11:20	15/11/90	16:00	CP-2-D
20/11/90	15:30	21/11/90	16:00	CP-2-D
27/11/90	10:00	28/11/90	16:00	CP-1-I

TABLE 4.1c EISCAT experiment runs (1989 and 1990).

(1991) in which the authors present the diurnal distribution of ion frictional heating, along with that of the related phenomena of enhanced ion velocity, derived statistically from F-region EISCAT CP-1 and CP-2 observations taken during 1985 and 1986. The criterion employed in the present study for the identification of ion frictional heating is that adopted by *McCrea et al. (1991)*, itself based on a condition derived by *St-Maurice and Hanson (1982)* for the examination of high-latitude field-perpendicular ion temperature measurements taken by the retarding potential analyser on board the Atmosphere Explorer-C satellite. The selection criterion of *St-Maurice and Hanson (1982)* for the identification of ion frictional heating required an enhancement in the field-perpendicular ion temperature of at least 200 K over the values measured in the absence of strong electric fields. The authors concluded that this threshold would exclude enhancements in ion temperature arising from other physical processes, such as heat conduction and thermal energy transfer from the electron population, as well as significantly exceeding the uncertainty in their measurements. *St-Maurice and Hanson (1982)* quoted a relative ion-neutral drift of between 400 and 600 m s<sup>-1</sup> as necessary to produce such an enhancement in the field-perpendicular ion temperature.

Under conditions of a large relative velocity between the ion and neutral populations, the 3-dimensional ion thermal velocity distribution will become distorted from an isotropic Maxwellian. The deviation of the ion velocity distribution from a Maxwellian form is discussed in detail in section 3.1 of chapter 2. In EISCAT common programme analysis the ion temperature is derived by assuming that the ion velocity distribution along the direction of observation is Maxwellian; an assumption which has been demonstrated theoretically to lead to an overestimate in the ion temperature in situations where the velocity distribution is non-Maxwellian (*e.g. Lockwood et al., 1993*). Theoretical predictions, however, indicate that along the field-parallel direction the departure of the ion velocity distribution from a Maxwellian is small and that the line-of-sight ion temperature derived by assuming a Maxwellian velocity distribution is accurate to within 5% for field-perpendicular ion velocities of up to some 4 km s<sup>-1</sup> (*Lathuillère and Hubert, 1989*). For this reason, *McCrea et al. (1991)* constrained their analysis to that of EISCAT observations taken along the magnetic field direction, from CP-1 and the field aligned position of CP-2. Since the satellite observations for which *St-Maurice and Hanson (1982)* derived their threshold for the identification of ion frictional heating were restricted to a direction orthogonal to the geomagnetic field, *McCrea et al. (1991)* suggested that the threshold should be adapted for studies based on measurements taken along the magnetic field direction. The latter authors stated that in the ionospheric F-region, for O<sup>+</sup>-O interactions constituting the dominant collision mechanism, a field-perpendicular ion temperature enhancement of 200 K would be accompanied by an enhancement in the field-parallel ion temperature of less than 100 K, due to the unequal partition of energy into the field-parallel and field-perpendicular ion populations. *McCrea et al. (1991)* thus adopted 100 K as the enhancement in the field-parallel ion temperature necessary for the identification of ion frictional heating.

Under conditions of a large ion-neutral relative velocity, the proportion of molecular

ions in the F-region, particularly  $\text{NO}^+$ , increases as a consequence of enhancements in both the reaction rate coefficients and the concentration of reactant neutrals (*e.g. St-Maurice and Torr, 1978*). The modification of the ion composition due to the existence of differential flow between the ion and neutral populations is discussed more fully in section 3.4 of chapter 2 and can result in substantial underestimation of the ion temperature derived from standard analysis of incoherent scatter data (see chapter 3, section 4.5). Moreover, under such conditions the field-parallel ion temperature components for the atomic and molecular ion species can diverge significantly; in the parallel direction the temperature of  $\text{NO}^+$  has been predicted theoretically to exceed that of  $\text{O}^+$  by almost 500 K for a value of  $D'$  of unity and a neutral atmosphere dominated by atomic oxygen (*Lathuillère and Hubert, 1989*). Standard analysis of EISCAT data assumes, however, that the ion population can be described by a single ion temperature, which, for a multi-ion plasma, is a non-linear combination of the temperatures of the individual ion species present. *McCrea et al. (1991)* concentrated on observations from the range gate centred at the altitude of 312 km to perform their study, which corresponded to the F-region tristatic altitude for the CP-1 and CP-2 observations employed. At this altitude, the authors stated that it would be unlikely that significant proportions of molecular ions would be produced for the majority of intervals of ion frictional heating.

Furthermore, *McCrea et al. (1991)* imposed the criterion that the field-parallel ion temperature must be enhanced by more than 100 K for two or more consecutive integration periods to exclude anomalous spikes in the ion temperature data. The authors noted that such spikes, which did not correlate with enhancements in the ion velocity, were a regular feature of the ion temperature data and considered them unlikely to be associated with actual physical structures but speculated that they arose from contamination of the radar data due to the presence of a satellite in the sidelobes of the radar beam or due to a system fault. It has, however, been observed that the electric field in the auroral F-region can fluctuate over time scales of the order of a minute (*e.g. Williams et al., 1990a; Lanchester et al., 1996*) and the addition of this condition unfortunately had the effect of eliminating some ion temperature enhancements which corresponded to instances of ion frictional heating occurring on time scales shorter than a single 5 minute integration period.

Implementation of the selection criterion for the identification of intervals of ion frictional heating relies on the calculation of an ambient value of ion temperature, defined as that in the absence of a relative velocity between the ion and neutral populations. *St-Maurice and Hanson (1982)*, for their study of ion data from the Atmospheric Explorer-C satellite, chose as their baseline temperature the ion temperature from nearby positions of the orbit where no, or very weak, electric fields were found. *McCrea et al. (1991)* suggested that the modal value would be an appropriate estimate of the equilibrium ion temperature; as the ion temperature at a given altitude exhibits little diurnal variation the mode would remain a valid description of the ambient ion temperature regardless of time of day. The authors calculated the ambient ion temperature, for each run of EISCAT observations, as the central

temperature of the modal bin of the ion temperature distribution, calculated with a bin size of 10 K.

In addition to the derivation of the diurnal distribution of ion frictional heating, *McCrea (1989)* deduced the distribution with universal time of the occurrence of enhanced ion velocities from their two year set of UHF EISCAT common programme observations. The author applied the criterion that the magnitude of the ion velocity, calculated at the F-region tristatic altitude, should exceed  $500 \text{ m s}^{-1}$ ; this threshold was selected as it is approximately the ion velocity required to produce an enhancement in the F-region field-parallel ion temperature of 100 K, although this assumes a stationary neutral atmosphere. In order to eliminate unreliable estimates of ion velocity, any velocity estimates for which the signal-to-noise ratio at any of the three UHF receiver sites was less than 2% were excluded.

#### 4.4 Statistical study of ion frictional heating

##### 4.4.1 Diurnal distribution of ion frictional heating

The selection criterion described in the previous section for the identification of ion frictional heating was applied to the present extended data set of CP-1 and field-aligned CP-2 observations of field-parallel ion temperature at 312 km altitude. The modal value of the ion temperature, calculated at that altitude for each experiment run, was employed as an estimate of the unperturbed ion temperature, as used by *McCrea et al. (1991)*. The variation of this calculated ambient ion temperature at 312 km altitude over the six year set of observations, is presented in figure 4.1 (full line). Also illustrated in the figure, represented by a dotted line, is the temperature of the neutral atmosphere calculated for the same altitude and at the location of EISCAT, using the MSIS-86 model (*Hedin, 1987*). The value of neutral temperature presented is the mode calculated for the first day of each month, and, as for ion temperature, the diurnal variation of the neutral temperature is only of the order of several tens of Kelvin. The values of the  $A_p$  index and the 10.7 cm solar flux ( $F_{10.7}$ ), input parameters required by the MSIS-86 model to characterise geomagnetic and solar conditions, were those appropriate to the days for which the model was run. The neutral and ion temperatures exhibit a similar trend, both seasonally and with solar cycle, tending to be highest in summer and towards the peak of the solar cycle, corresponding to increased solar UV and X-ray photon flux. In general, the ambient temperature of the ion population tends to exceed slightly the neutral temperature, indicative of energy transfer to the ions from the hotter electron gas. The difference in the unperturbed ion temperature between conditions of solar minimum (1986) and solar maximum (1991) is some 500 K; the annual variation in the ambient ion temperature is less than 300 K. Solar cycle and seasonal effects are far less pronounced than the enhancement in the field-parallel ion temperature which may be observed during intervals of frictional heating, illustrating the importance of ion frictional heating as a source of energy deposition into the high-latitude ionosphere and thermosphere.

A total of 879 intervals of frictional heating were identified from the 3237 hour set of

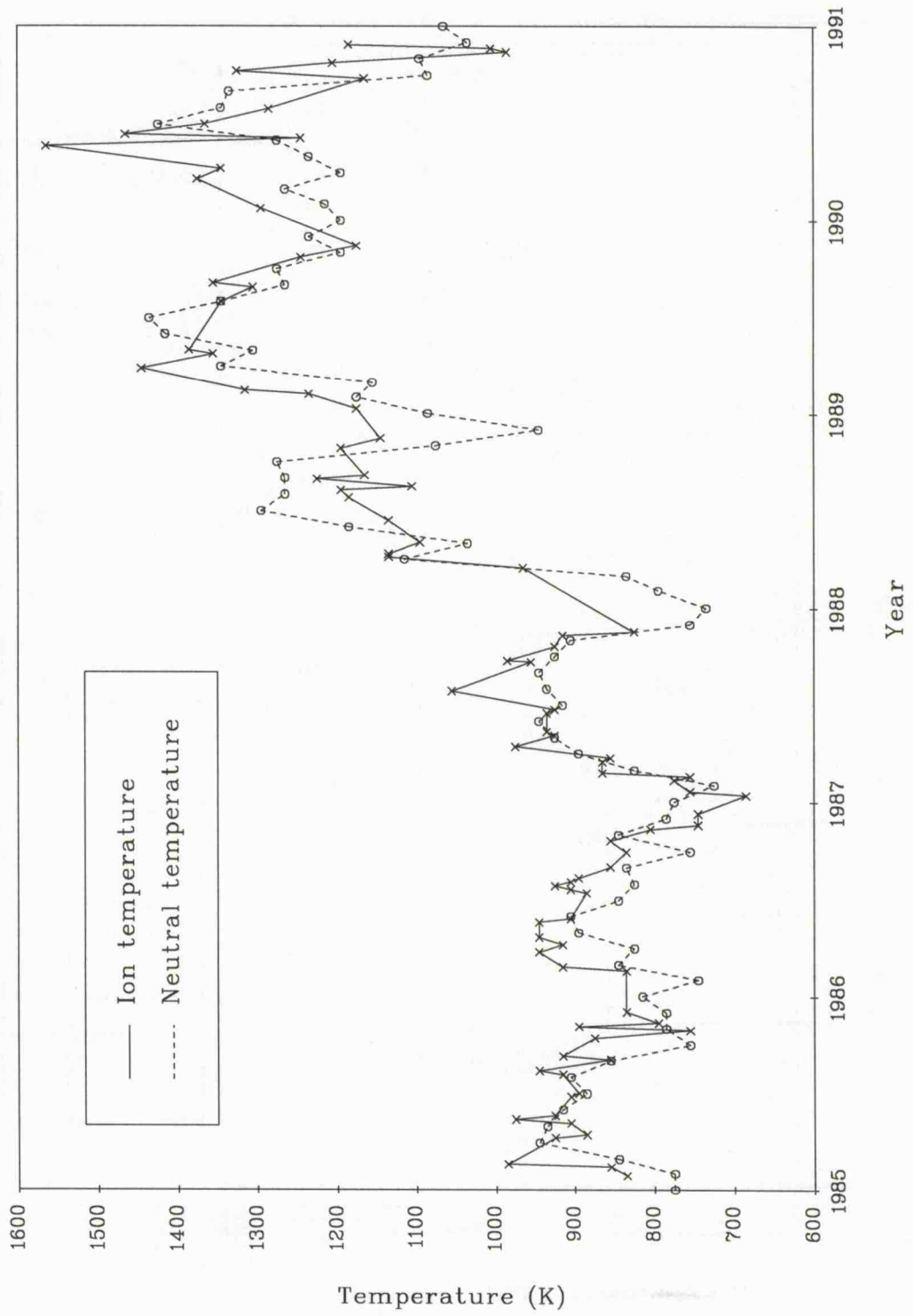


FIGURE 4.1: Variation of modal ion and neutral temperatures

field-parallel ion temperature observations, ranging in duration from the minimum of 2 integration periods, 10 and 12 minutes for CP-1 and CP-2, respectively, to several hours. Ion frictional heating was observed to some extent during the vast majority of the EISCAT common programme runs incorporated in the present study.

As in the study of *McCrea et al (1991)*, the diurnal distribution of ion frictional heating was constructed by dividing the day into 30 minute bins and summing the number of occasions on which heating occurs in each. Events which span 30 minute boundaries contribute in each time bin in which they were observed. The observational coverage, however, is not uniform throughout the day, with a minimum in the number of observations between 22:00 UT and 08:00 UT; the number of observations of each 30 minute bin lies between some 100 and 160. To negate the effect of non-uniform sampling the diurnal distribution of ion frictional heating was derived as a percentage of the number of observations of each half hour bin. The diurnal distribution of ion frictional heating derived from EISCAT UHF field-parallel CP-1 and CP-2 observations at 312 km altitude is presented as a function of universal time in figure 4.2. The histogram represents the percentage occurrence of ion frictional heating as a function of universal time (left hand scale) and the line plot illustrates the number of observations of each 30 minutes bin (right hand scale).

The diurnal distribution of F-region ion frictional heating observed by EISCAT at 312 km altitude exhibits a broad peak in the night-time sector with relatively few events occurring between 06:00 and 13:00 UT on the dayside. The distribution is centred at approximately 20:00 UT about which it is asymmetric, with a propensity for ion frictional heating in the early morning sector, some 50% maximum occurrence, and a somewhat smaller peak in occurrence, approximately 35%, around 17:00 UT. Between 18:00 and 21:00 UT on the nightside there is a slight reduction in the occurrence of ion frictional heating; the percentage occurrence of frictional heating during this interval is around 30%. A physical interpretation of the diurnal variation in the occurrence of F-region ion frictional heating observed by EISCAT is detailed later in the present section, particularly with reference to the observed distribution of enhanced ion flow.

The variation of the enhancement in the field-parallel ion temperature at 312 km altitude, during identified intervals of ion frictional heating, is illustrated as a function of universal time in figure 4.3. The solid line represents the median value of the field-parallel ion temperature enhancement in each half hour bin during recognised intervals of frictional heating (left hand scale); the vertical lines encompass the range of parallel temperature enhancements bounded by the upper and lower quartiles. The number of estimates of the field-parallel ion temperature enhancement in each 30 minute bin is signified by a dotted line (right hand scale). The criterion for the identification of ion frictional heating that the enhancement in the parallel ion temperature should exceed 100 K, imposes that threshold as a lower limit on the median enhancement observed. The median field-parallel temperature enhancement during recognised intervals of ion frictional heating exhibits a distinct

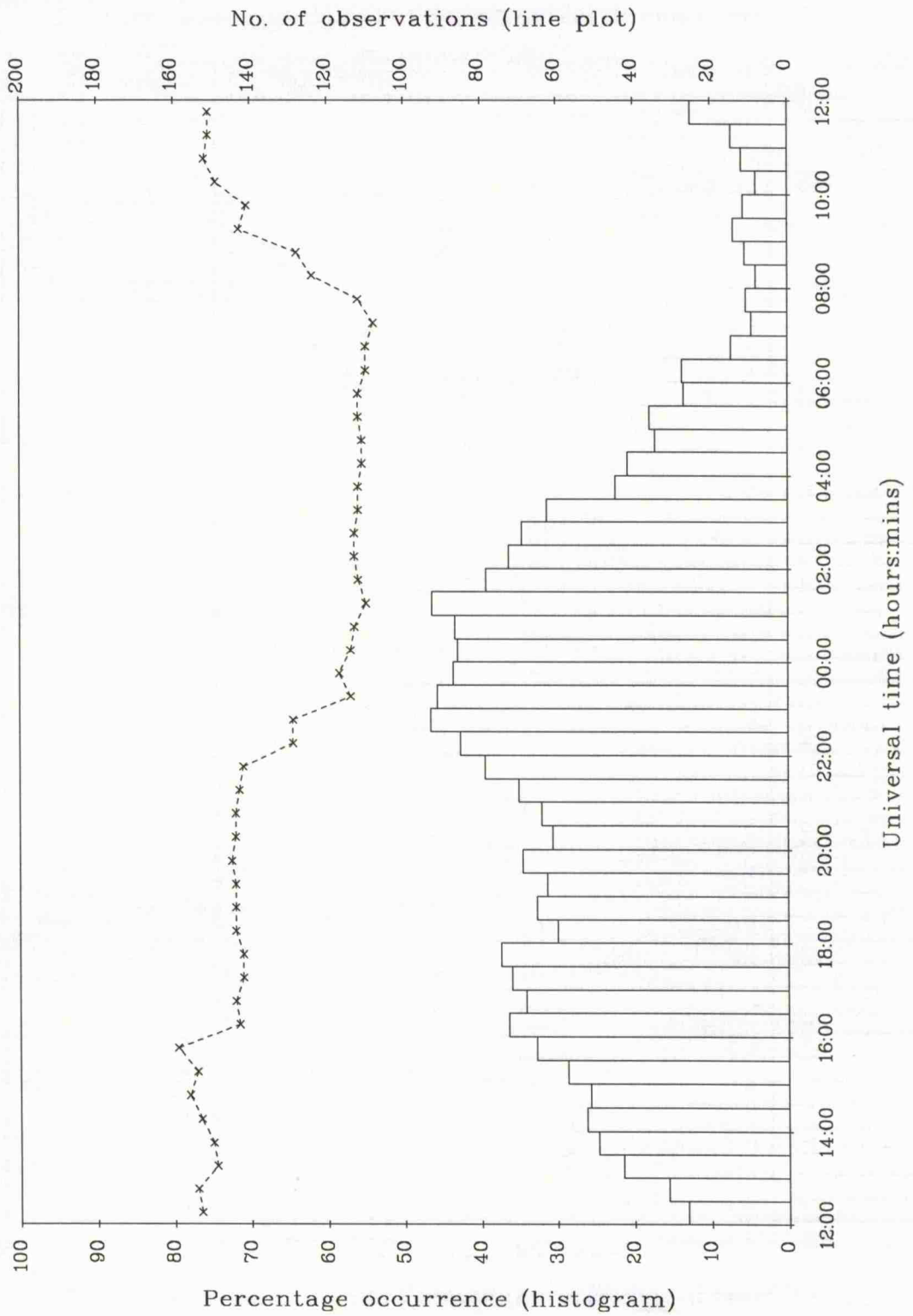


FIGURE 4.2: Diurnal distribution of ion frictional heating

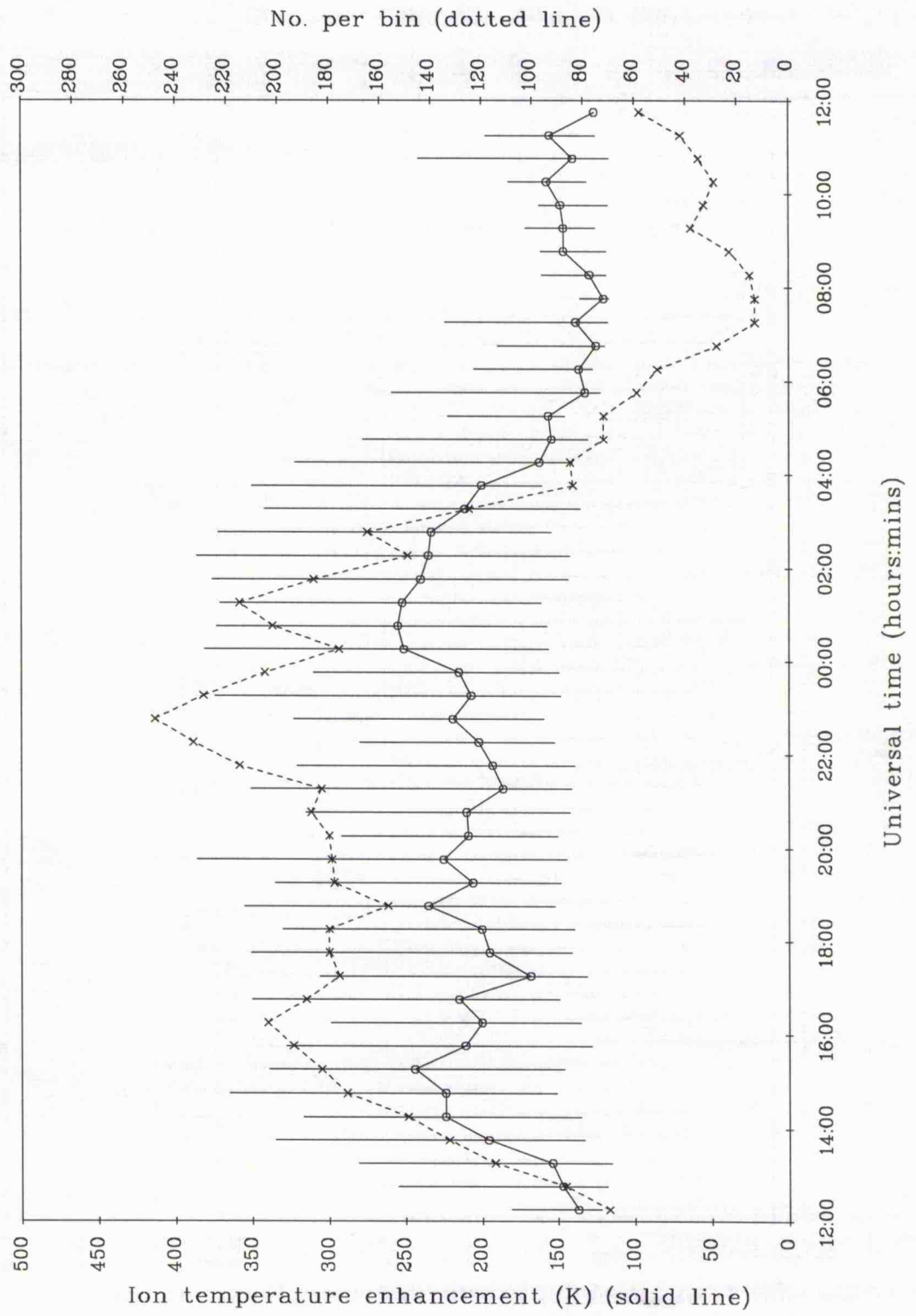


FIGURE 4.3: Enhancement in field-parallel ion temperature

dependence with universal time, ranging from a maximum approaching 300 K at 00:00 UT to little over 100 K between 06:00 and 13:00 UT on the dayside. Furthermore, the spread of observed parallel ion temperature enhancements tends to be far greater after 14:00 UT and prior to 04:00 UT on the nightside, during which time a quarter exceed some 350 K. The median enhancement in the field-parallel ion temperature tends to be greater over those range of universal times where the probability of occurrence of ion frictional heating is high. Indeed, the asymmetry in the observation occurrence of ion frictional heating between the post and pre-magnetic midnight hours evident from figure 4.2 is reflected to some degree in the enhancement in the parallel ion temperature during those hours.

The duration of each interval of ion frictional heating, identified from the extended data set of common programme observations, was also noted. Figure 4.4 presents the diurnal variation of the duration of ion frictional heating, identified by the selection criterion discussed in the previous section. The format of this illustration is similar to that of the previous figure. The solid line (corresponding to the left hand scale) represents the median value of the duration of identified intervals of ion frictional heating in each half hour bin; the vertical lines span the range of durations bounded the upper and lower quartiles. The dotted line (right hand scale) corresponds to the number of estimates of the duration of frictional heating in each 30 minute bin. The duration of intervals of ion frictional heating which span 30 minute boundaries contribute in each bin in which the event was observed. The minimum duration of intervals of frictional heating is set by the selection criterion, two integration periods corresponding to 10 minutes and 12 minutes for CP-1 and CP-2, respectively.

The duration of identified intervals of ion frictional heating exhibits an obvious diurnal variation; frictional heating events characterised by a long duration tend to occur on the nightside. The median duration of identified intervals of ion frictional heating exceeds 60 minutes between 00:00 and 02:00 UT, reducing to between 20 and 30 minutes between 06:00 and 12:00 UT on the dayside. Frictional heating of prolonged duration corresponds, in general, to periods where the probability of observing such heating is higher, and those which are observed are characterised by larger temperature enhancements. Between 16:00 and 22:00 UT a distinct reduction in event duration is noted; between these hours the duration of frictional heating events reduces to similar values to those observed in the dayside hours. The minimum in the duration of frictional heating between 16:00 and 22:00 UT on the nightside is rather more marked than the corresponding minima in the percentage occurrence of frictional heating and the enhancement in the field-parallel ion temperature during such intervals.

The observed absence of ion frictional heating, by EISCAT, on the dayside is a consequence of the equatorward edge of the ionospheric convection pattern typically being situated far poleward of the radar during these hours, a result of the displacement of the convection pattern as a whole in the antisunward direction. More interesting, however, is the observed asymmetry between the occurrence of ion frictional heating prior to magnetic

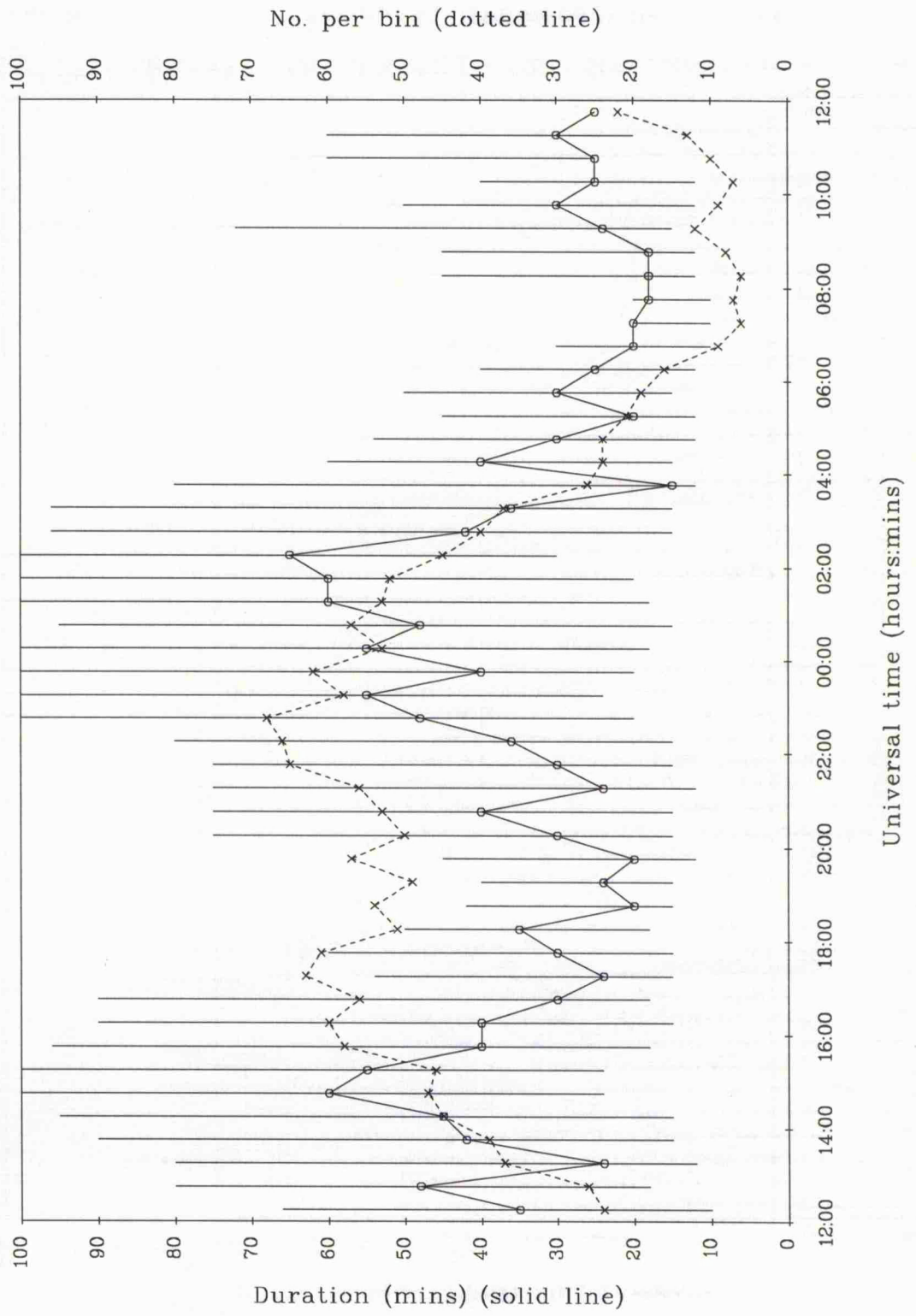


FIGURE 4.4: Duration of ion frictional heating

midnight and that in the post-midnight sector. These observations are consistent with those of *Baron and Wand (1983)*, *Alcaydé et al. (1984)*, *Alcaydé and Fontanari (1986)* and *Moorcroft and Schlegel (1988)* in that these authors also noticed a propensity for the occurrence of ion frictional heating during the hours post magnetic midnight. These previous observations are detailed in section 3.3 of chapter 2. It has been suggested that the dawn-dusk asymmetry in the occurrence of ion frictional heating results from a weaker coupling between the ions and the neutral population during the post-midnight sector than prior to magnetic midnight. During the morning sector the F-region plasma density tends to be lower than during the afternoon and evening hours, due to the decay of solar produced ionisation. Consequently, the ion drag force on the neutral atmosphere, which is inversely proportional to the electron density, is less after magnetic midnight permitting the generation of larger ion-neutral difference velocities and hence greater frictional heating of the ion population (*e.g. Baron and Wand, 1983*). Moreover, the residence time of the neutral atmosphere within the region of strong auroral ion drifts tends to be longer during the pre-midnight hours than after midnight, such that the thermosphere can be accelerated to larger velocities in the dusk sector, preferentially suppressing frictional heating during those hours (*e.g. Lockwood and Fuller-Rowell, 1987a; 1987b*). *Alcaydé et al. (1984)* proposed an additional factor which would contribute to this effect; the Coriolis force produced by southward neutral winds in the midnight sector opposes the ion drag force arising from eastward plasma flow, whereas in the evening sector these two forces act in the same direction.

To aid the interpretation of the diurnal distribution of ion frictional heating it is instructive to construct a similar distribution with universal time of enhanced ion velocity. The selection criterion adopted was used by *McCrea (1989)* for the identification of intervals of enhanced ion flow; the magnitude of the ion velocity should exceed  $500 \text{ m s}^{-1}$ , the velocity necessary to produce an enhancement of 100 K in the ion temperature component parallel to the geomagnetic field. To excluded unreliable estimates of velocity, the condition was implemented that the signal-to-noise ratio at each receiver site should exceed 2%; a threshold applied by the previous authors. Figure 4.5 presents the diurnal distribution of ion velocities exceeding  $500 \text{ m s}^{-1}$ , derived from the common programme 1 and 2 observations taken over the six year period, 1985 to 1990 inclusive. As for figure 4.2, the histogram represents the percentage occurrence of enhanced ion velocity (left hand scale) and the line plot, the number of observations of each 30 minute bin (right hand side). Moreover, velocities have been subdivided according to the orientation of the zonal flow; ion velocities in which the zonal component is westward are represented as light shading whereas darker shading illustrates ion velocities with an associated eastward component. The number of observations of each 30 minute bin in figure 4.5 tends to be less than that in figure 4.2, the former ranging from 80 to 140 and the latter from 100 to 160; it is necessary to have line-of-sight ion velocity measurements from all UHF receiver sites in order to estimate the magnitude of the ion velocity and the returns from which these velocities are

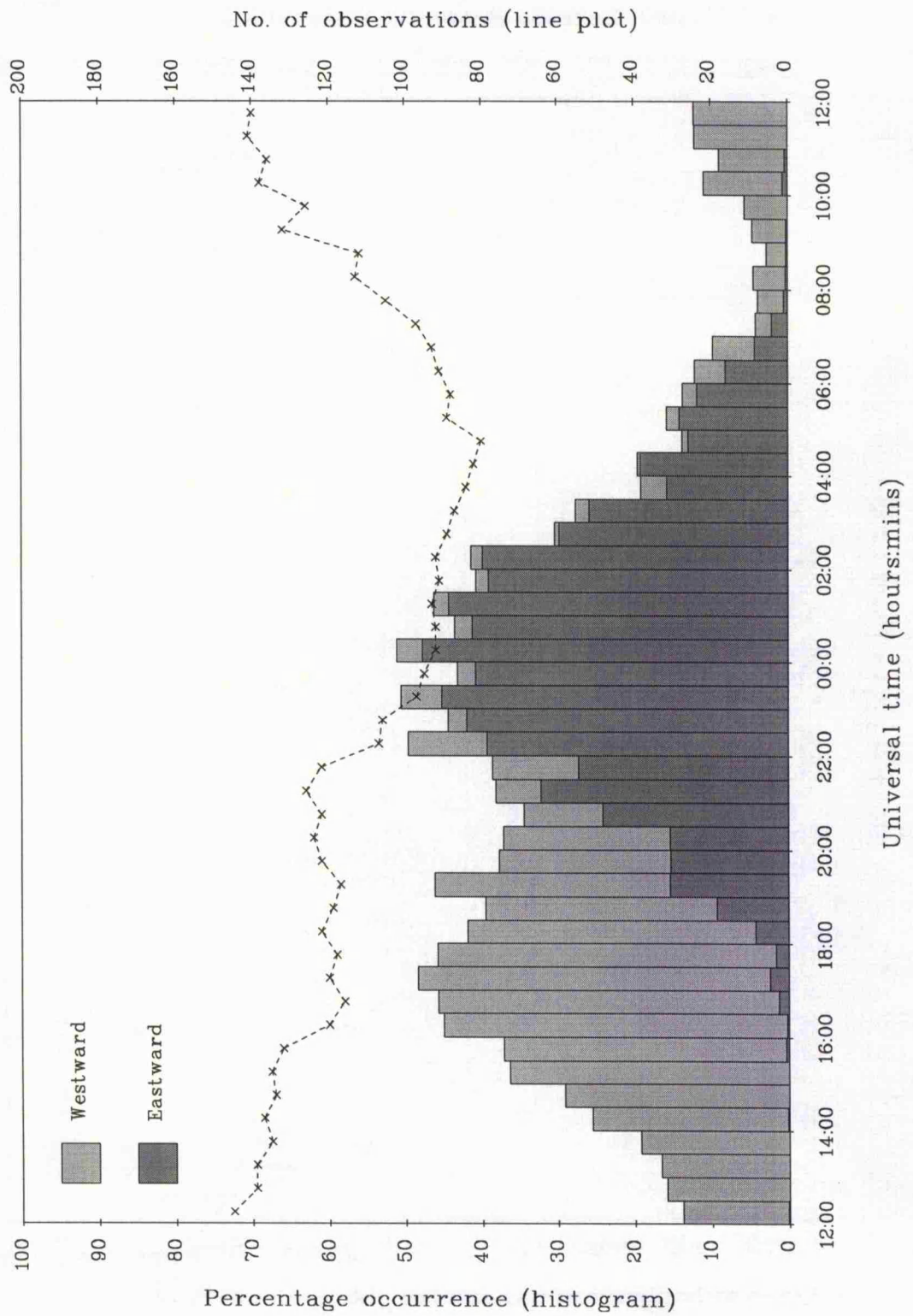


FIGURE 4.5: Diurnal distribution of enhanced ion velocity

obtained are, moreover, subject to a 2% signal-to-noise threshold.

An exact correspondence between the ion velocity magnitude and the enhancement in the parallel ion temperature, and consequently their diurnal distributions, is not expected since it is the relative ion-neutral velocity that determines the extent of frictional heating of the ion population and not simply the magnitude of the ion velocity. The distribution of enhanced ion velocities exhibits a similar form to that of ion frictional heating, a broad peak about midnight with a central minimum corresponding to the location of the nightside convection reversal which is characterised by lower velocities. Ion velocities exceeding  $500 \text{ m s}^{-1}$  are seldom observed by EISCAT between 06:00 and 12:00 UT due to the antisunward displacement of the convection pattern. The nightside convection reversal, corresponding to a change from eastwards to westward flow, is generally located temporally between 18:00 and 22:00 UT at the latitude of EISCAT. The occurrence of enhanced ion velocities appears symmetric about the nightside reversal, implying the equal occurrence of enhanced ion velocities in the dawn (westward) and dusk (eastward) convection cells, although the tendency for lower neutral atmosphere response times and the opposition of the ion drag and Coriolis forces during the early morning hours gives rise to asymmetry in the distribution of ion frictional heating between these two regimes. Within the convection reversal, intervals of ion frictional heating are characteristically of very short duration - comparable to that of intervals observed by EISCAT on the dayside. This highlights the highly dynamic nature of this region of plasma flow.

The asymmetric response of the F-region ion temperature to enhancements in the dawn and dusk convection cells can be investigated more fully using simultaneous observations of the ion vector velocity determined at the tristatic altitude and the enhancement in the field-parallel ion temperature during intervals of ion frictional heating. Figure 4.6 presents the variation in the median enhancement in the field-parallel ion temperature at 312 km altitude during identified intervals of ion frictional heating as a function of the simultaneously observed ion velocity magnitude, derived from the entire six year set of EISCAT CP-1 and CP-2 observations. The ion velocity observations have, moreover, been classified according to the orientation of their field-orthogonal zonal component. The left hand side of figure 4.6 illustrates the variation of field-parallel temperature enhancement with ion velocity magnitude where the field-perpendicular zonal component of the ion velocity is eastward; the right hand side of the figure shows the functional response of the ion temperature enhancement with velocity magnitude where the associated zonal velocity component is westward. The ion temperature enhancement has been binned according to ion velocity with a bin width in velocity of  $100 \text{ m s}^{-1}$ . For both orientations of the zonal velocity component, vertical bars join the upper and lower quartiles of the temperature enhancement in each velocity bin, and the dotted line indicates the number of estimates of the parallel ion temperature enhancement in each velocity bin.

The response of the field-parallel ion temperature with ion velocity magnitude is clearly asymmetric with respect to the zonal velocity component; in the dusk convection cell

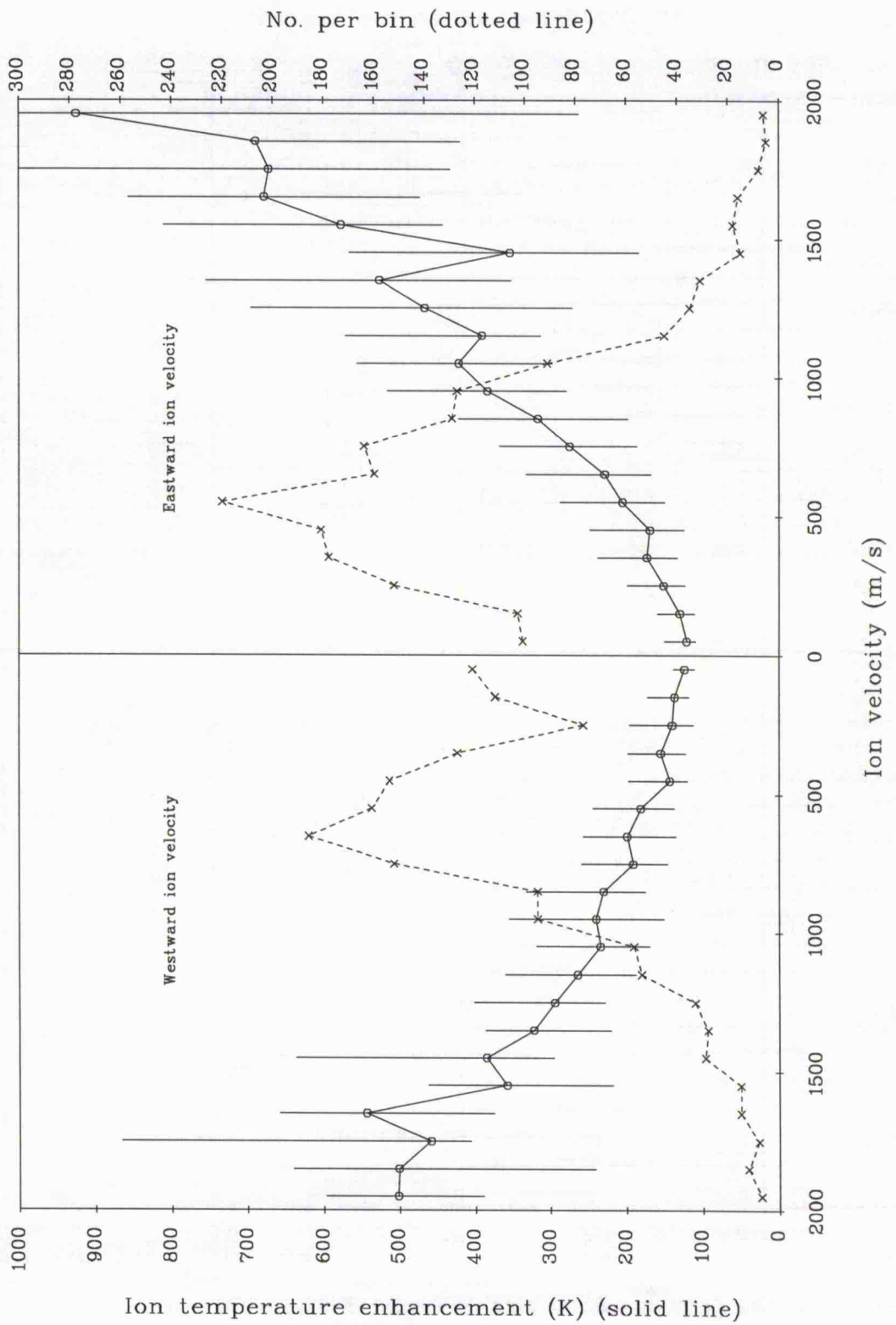


FIGURE 4.6: Temperature enhancement as a function of velocity

an ion velocity of  $1000 \text{ m s}^{-1}$  results in a median enhancement of around 250 K in the parallel ion temperature whereas an equivalent velocity in the dawn cell enhances the ion temperature by more than 400 K. For an ion velocity of  $1500 \text{ m s}^{-1}$ , the corresponding temperature enhancements are approximately 350 and 600 K in the dusk and dawn cells of the convection pattern, respectively. The results presented above are not directly comparable to those of *Baron and Wand (1983)*; the latter authors presented observations of ion temperature as a function of the zonal ion velocity from both the Chatanika and Millstone Hill incoherent scatter radars during two limited intervals. Observations from one of the intervals investigated by *Baron and Wand (1983)* are illustrated in figure 9 of chapter 2. For a zonal velocity of  $800 \text{ m s}^{-1}$ , the observations of *Baron and Wand (1983)* indicate an enhancement in the ion temperature over its unperturbed value of roughly 300 K for eastward zonal flow and around 600 K for westward flow, the unperturbed temperature taken as that at velocities around zero. In the present study corresponding values, assuming that the ion velocity is dominated by field-perpendicular zonal flows, a reasonable assumption at auroral latitudes, are nearer 200 and 300 K. It is most likely that the larger temperature enhancements seen by *Baron and Wand (1983)* result principally from the larger aspect angle of their observations, indeed the Chatanika beam was zonally directed which could result in enhancements in ion temperature double those expected in the field-parallel direction.

#### 4.4.2 Variation with interplanetary magnetic field orientation

The solar wind plasma and the interplanetary magnetic field (IMF) have been consistently monitored since 1963, by a series of spacecraft such as IMP-1 to 8, HEOS and ISEE-1 to 3. Hourly averages of the interplanetary magnetic field components, in addition to solar wind velocity and dynamic pressure measurements, are available during the intervals when the satellites were upstream of the bow shock. The IMF measurements covering the period of the present set of EISCAT observations were taken by the IMP-8 spacecraft. Although the proportion of each individual spacecraft orbit for which observations are available is highly variable, approximately half of the EISCAT data set employed in the current statistical study has associated IMF coverage. The response time of the ionosphere to variations in the interplanetary magnetic field ranges between some tens of minutes on the dayside to more than an hour on the nightside (*Todd et al., 1988; Lester et al., 1993*). It is, therefore, inappropriate to use observations of the interplanetary magnetic field at any higher time resolution than hourly averages in the present study, although IMF and solar wind data are available at up to 30 second resolution.

The present EISCAT field-parallel ion temperature and ion velocity observations have been classified according to the orientation of both the northward ( $B_z$ ) and eastward ( $B_y$ ) components of the IMF where these components are measured in the GSM (geocentric solar magnetic) coordinate system. Initial classification was according to the  $B_z$  component of the IMF. The upper two panels of figure 4.7 illustrate the diurnal distribution of ion

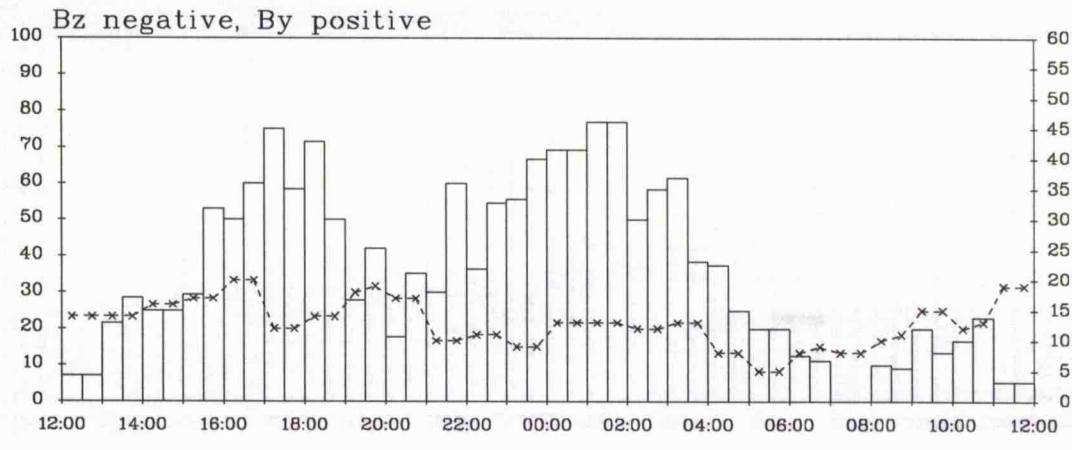
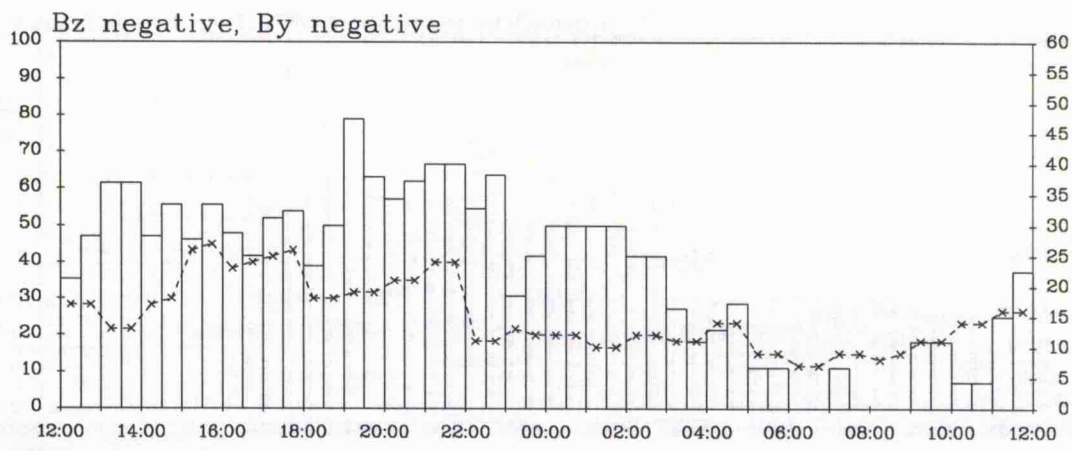
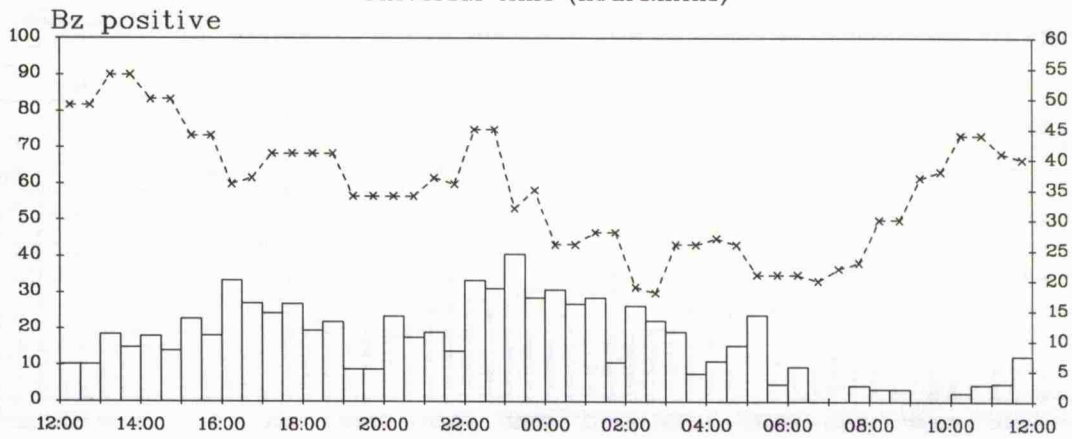
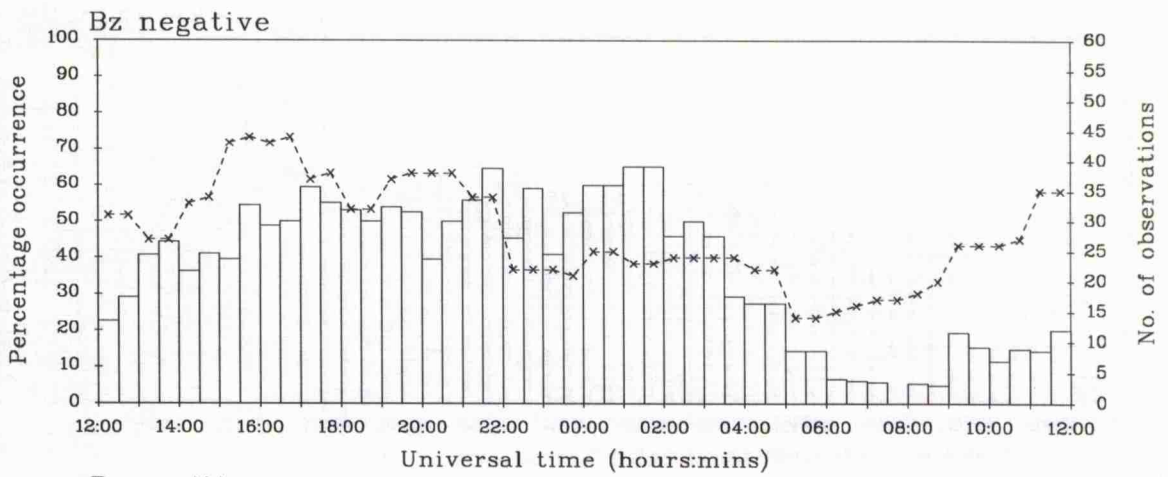


FIGURE 4.7: Variation of ion frictional heating with IMF

frictional heating observed by EISCAT for  $B_z$  negative (southward) and  $B_z$  positive (northward), irrespective of the orientation of the y component of the interplanetary magnetic field. As in previous figures of this type, the histograms represents the percentage occurrence of ion frictional heating and the line plots, the total number of observations, for each orientation of  $B_z$ .

For both orientations of  $B_z$ , the diurnal distribution of ion frictional heating exhibits a similar general form to that illustrated in figure 4.2, that is a broad and asymmetric distribution, centred in the midnight sector. At all universal times, however, the probability of occurrence of ion frictional heating is far greater for a southward orientation of  $B_z$  than for a northward  $B_z$ ; between 00:00 and 02:00 UT the percentage occurrence of frictional heating for  $B_z$  negative approaches 60% whereas for positive values of  $B_z$ , the corresponding figure is less than 30%. The minimum in the occurrence of frictional heating, corresponding to the general location of the night-time convection reversal, appears less clearly defined for the case of southward  $B_z$  than it is for northward  $B_z$ . During conditions of southward  $B_z$  both the size and duration of identified intervals of frictional heating (not illustrated) are also significantly greater than those for a northward z component of the interplanetary magnetic field; on the nightside the median enhancement in the field-parallel ion temperature for southward  $B_z$  generally exceeds that for northward  $B_z$  by more than 100 K and the median duration is almost doubled.

The dependence of high-latitude ionospheric convection on the orientation of the interplanetary magnetic field provides an explanation for these observations (*e.g. Friis-Christensen et al., 1985*). There is little doubt that the interplanetary magnetic field strongly influences magnetospheric and ionospheric convection although the exact processes involved in solar wind/magnetosphere/ionosphere coupling are not well determined. It is generally accepted that convection in the dayside ionosphere is driven by reconnection at the nose of the magnetosphere, the rate of which is highly dependant on the orientation of the z component of the IMF with a southward  $B_z$  required for reconnection at low magnetic latitudes. The resulting build-up of magnetic flux on the tailside leads to substorm expansion, which drives impulsive convection more confined to the nightside ionosphere. Viscous processes in the magnetosphere are also suggested to drive convection in the ionosphere, irrespective of the orientation of the z component of the IMF (*Axford and Hines, 1961*). Previous authors have, therefore, attributed ionospheric flows observed under conditions of northward  $B_z$  to viscous interaction. Recent research, however, indicates that enhanced convection on the nightside can persist for many hours after a northward turning of the z component of the IMF, driven by residual reconnection of open flux in the magnetotail, thus mimicking the effect of viscous interaction (*Lockwood and Cowley, 1992; Fox et al., 1994*). This interpretation complements the findings of *Wygant et al. (1983)* which revealed that the convection electric field reduces over about 9 hours after a northward turning of  $B_z$ . Overall, the pattern of ionospheric convection is, if anything, more complex under conditions of northward  $B_z$  than for southward  $B_z$  (*e.g.*

Cowley, 1982).

*Foster et al. (1986)*, as the foundation of an empirical model, constructed statistical patterns of high-latitude ionospheric convection based on ion velocity measurements by the Millstone Hill incoherent scatter radar, classified according to the orientation of the IMF using hourly averages of the latter. The authors found that the convection pattern greatly enhanced and expanded for negative values of  $B_z$ . Consequently, the occurrence of ion frictional heating would be expected to depend critically on the orientation of the  $z$  component of the IMF, with larger convection velocities, thus a greater percentage of ion frictional heating, expected for southward values of  $B_z$ .

The diurnal distributions of enhanced ion velocities observed by EISCAT, those exceeding  $500 \text{ m s}^{-1}$ , for both negative and positive  $z$  components of the IMF are illustrated in the upper panels of figure 4.8. As in figure 4.5, the ion velocity is further categorised according to its associated zonal component, to enable the location of the convection reversal to be more clearly determined. It is evident that the far greater proportion of frictional heating observed under conditions of southward  $B_z$  than when the  $z$  component of the IMF is oriented northward, is attributable to the higher occurrence of enhanced ion velocities during such intervals. As noted previously, the response time of ionospheric high-latitude convection after a southward turning of the  $z$  component of the IMF is some tens of minutes on the dayside to perhaps 90 minutes on the nightside. Moreover, even several hours after the IMF  $z$  component has turned northward, the effect of residual tail reconnection on nightside convection can still be significant. These factors may account for the relatively high occurrence of ion frictional heating when satellite observations indicate a northward  $B_z$  although, indeed it may be more appropriate to correlate the occurrence of frictional heating and enhanced ion flows, most of which are observed by EISCAT on the nightside, with IMF measurements from the previous hour. It is also interesting to note that for southward  $B_z$  the ion flow observed at EISCAT (albeit restricted to velocities exceeding  $500 \text{ m s}^{-1}$ ) is separated into two distinct regimes with respect to its zonal component whereas, under situations of northward  $B_z$ , the demarcation between eastward and westward zonal ion flow is not clearly defined and, indeed, the majority of enhanced flow has an associated eastward zonal component. This is, perhaps, a manifestation of a more complex convection pattern associated with northward  $B_z$  than the simple twin cell pattern which is associated with intervals of southward  $B_z$ .

Empirical models of ionospheric convection (*e.g. Reiff and Burch, 1985; Burch et al., 1985*) illustrate a strong skew imposed on the convection pattern by the eastward ( $y$ ) component of the IMF, reflecting asymmetries in magnetospheric convection dictated by  $B_y$ , particularly under conditions of southward  $B_z$  where convection is excited primarily by reconnection. These models are, however, based mainly on observations around noon. Further observational evidence for a  $B_y$  influence on ionospheric convection has been presented by such authors as *Rodger et al. (1984)*, *de la Beaujardière et al. (1986)* and *Burrage (1988)*, although the inferred details of the convection patterns vary from those

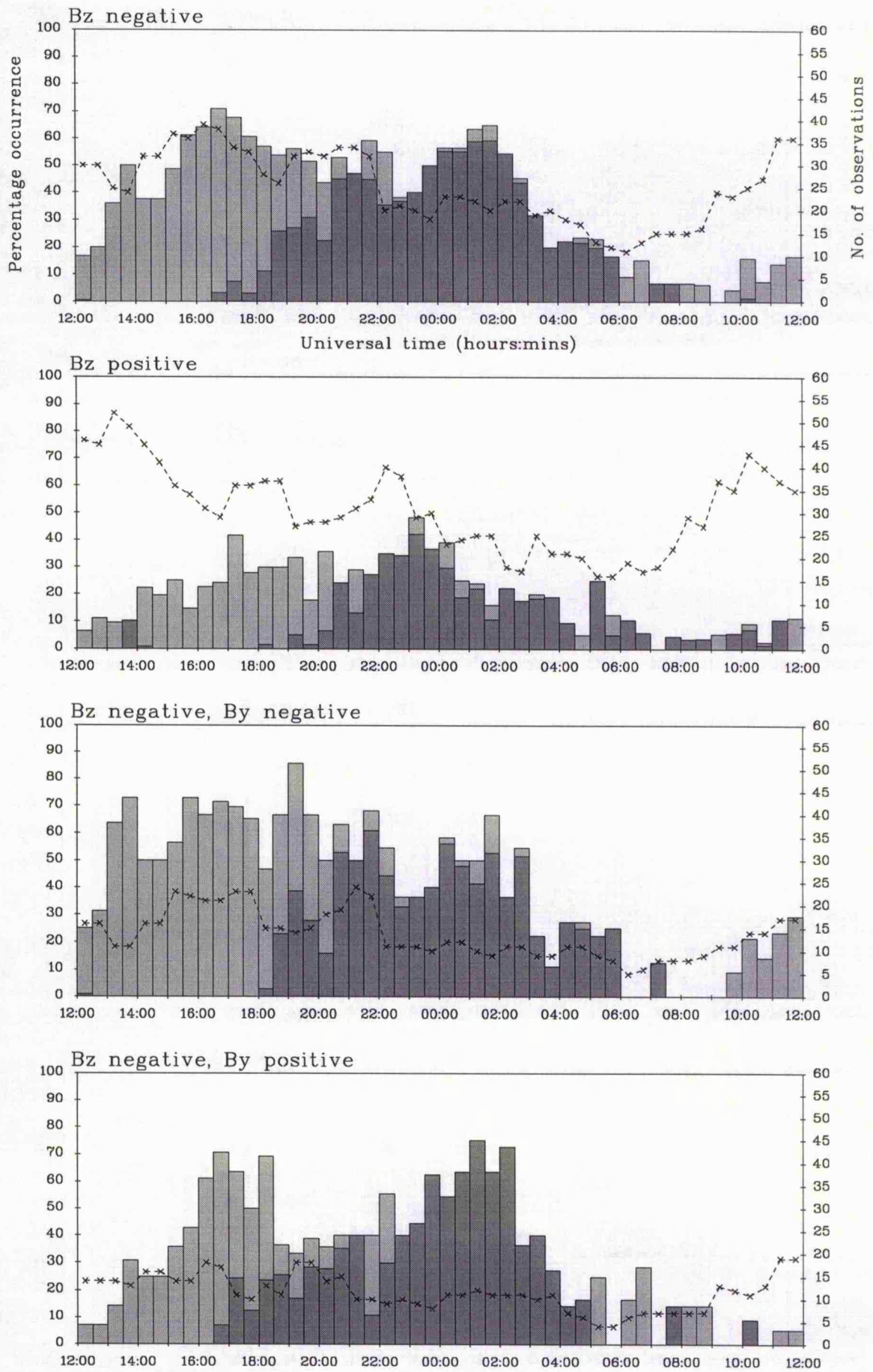


FIGURE 4.8: Variation of enhanced ion velocity with IMF

modelled, in particular with the observed patterns for  $B_y$  negative not simply being mirror images of the  $B_y$  positive patterns.

The diurnal distribution of ion frictional heating has been derived from the EISCAT field-parallel CP-1 and CP-2 observations at 312 km altitude for positive (eastward) and negative (westward) values of  $B_y$ , both under conditions of negative  $B_z$ . The lower two panels of figure 4.7 present the percentage occurrence of ion frictional heating with universal time for  $B_z$  negative with  $B_y$  negative and  $B_z$  negative with  $B_y$  positive. As in previous figures, the number of observations of each 30 minute bin are represented by a dotted line. Equivalent distributions of enhanced ion velocity are illustrated in the lower panels of figure 4.8. It is, however, only possible to draw speculative conclusions due to the low number of observations available.

The diurnal distribution of ion frictional heating appears to be very different for the two orientations of the  $y$  component of the interplanetary magnetic field, a difference which is clearly attributable to a corresponding difference between the occurrence distributions of enhanced ion velocities. For  $B_y$  negative the maximum occurrence of frictional heating of the F-region ions occurs around 20:00 UT, whereas, for  $B_y$  positive, this time corresponds to a minimum in the occurrence of ion frictional heating on the nightside. Moreover, for  $B_y$  negative there is a much higher percentage occurrence of ion frictional heating during the interval from 12:00 to 16:00 UT than for  $B_y$  positive and somewhat less frictional heating is observed around 00:00 UT. It must be reiterated that both distributions are derived from data taken during periods of negative  $B_z$ . It is not worthwhile to compare rigorously the distributions of enhanced ion velocity observed by EISCAT for both orientations of  $B_y$ , with observed and modelled convection patterns presented by previous authors. There is, however, a feature evident in the present observations that agrees well with statistical convection patterns derived from the SABRE coherent scatter radar measurements, presented by *Burrage (1988)*; this feature is the displacement in local time of the location of the nightside convection reversal between negative and positive values of  $B_y$ . For  $B_y$  negative, the location of the convection reversal, identified from figure 4.8, is situated close to 19:00 UT, with no observations of eastward velocity prior to 18:00 UT whereas, for positive values of  $B_y$ , the night-time reversal is displaced to an earlier local time by approximately an hour. This displacement is consistent with that observed by *Burrage (1988)* at the same geomagnetic latitude as the present observations, and supports the conclusions of *de la Beaujardière (1985)*, whose Sondrestromfjord incoherent scatter radar observations indicated that the effect of  $B_y$  is not limited to the noon hours. Present results are also consistent with those inferred from magnetometer measurements by *Rodger et al. (1984)*. The results of *Rodger et al. (1984)* indicate that, in the northern hemisphere, the position of the night-time convection reversal is at later local times for negative  $B_y$  than for positive  $B_y$  whereas, in the southern hemisphere, the converse is true.

#### 4.4.3 Variation with geomagnetic activity

Geomagnetic conditions reflect to some extent the magnitude and orientation of  $B_z$ , such that highly disturbed geomagnetic conditions correspond in general to large northward values of the IMF. More accurately, geomagnetic activity is a gauge of the energy input into the magnetosphere from the solar wind by the interaction of both magnetic fields and particles. Geomagnetic activity may be crudely characterised by  $K_p$  (Bartels, 1949), a 3 hourly planetary index derived from magnetometer measurements from eleven mid-latitude stations, 10 from the northern hemisphere and 1 from the southern hemisphere.  $K_p$ , a quasi-logarithmic index, is scaled from 0 to 9 with increments -, 0, +. Typical values of  $K_p$  are between 2 and 3, with storm time values approaching 7. Due to the non-uniform distribution of the contributing magnetometer stations, universal time variations are scaled out of the  $K_p$  index.

The variation of the diurnal distribution of ion frictional heating with geomagnetic activity, the latter categorised according to the  $K_p$  index, is illustrated in figure 4.9. Successive panels of this figure present the distribution of frictional heating for  $K_p \leq 1$ ,  $K_p = 2$ ,  $K_p = 3$  and  $K_p \geq 4$ . The total number of observations and the percentage occurrence of frictional heating at 312 km altitude for each range of  $K_p$  are presented, respectively, as line plots and histograms. Figure 4.10 presents corresponding distributions of enhanced F-region ion velocity for the ranges of  $K_p$  defined above.

The percentage occurrence of ion frictional heating exhibits a dramatic increase with increasing geomagnetic activity over all universal times; at around 20:00 UT, for example, the probability of observing ion frictional heating increases from less than 10% for  $K_p \leq 1$  to more than 70% for  $K_p \geq 4$ . Indeed for values of  $K_p$  in excess of 4, the occurrence of frictional heating observed around geomagnetic noon exceeds 30%. Although the double peaked form of the diurnal distribution is pronounced during moderate geomagnetic activity, under both highly disturbed and undisturbed conditions this feature becomes less well defined. For quiet conditions, this is due to the low incidence of frictional heating throughout the day. In addition to an increase in the occurrence of ion frictional heating, both the enhancement in the field-parallel ion temperature during identified intervals of ion frictional heating and the duration of these intervals tend to increase with increasing geomagnetic activity. The average enhancement in the parallel temperature for  $K_p \leq 1$  is typically half of its value for  $K_p \geq 4$ .

The marked dependence of ion frictional heating with geomagnetic activity is clearly attributable to a corresponding dependence of the ion velocity (see figure 4.10). With increasing  $K_p$  the occurrence of ion velocities in excess of  $500 \text{ m s}^{-1}$  increases significantly throughout the day. Indeed, the probability of observing high ion flows in any 30 minute bin exceeds 80% over much of the day for  $K_p \geq 4$ , corresponding to highly disturbed conditions. This intensification of convection is a well-known characteristic with increasing geomagnetic activity and is a feature of all empirical models (*e.g. Oliver et al., 1983; Holt et al., 1987*) as well as being observed in studies of individual intervals (*e.g. Alcayd  et al.,*

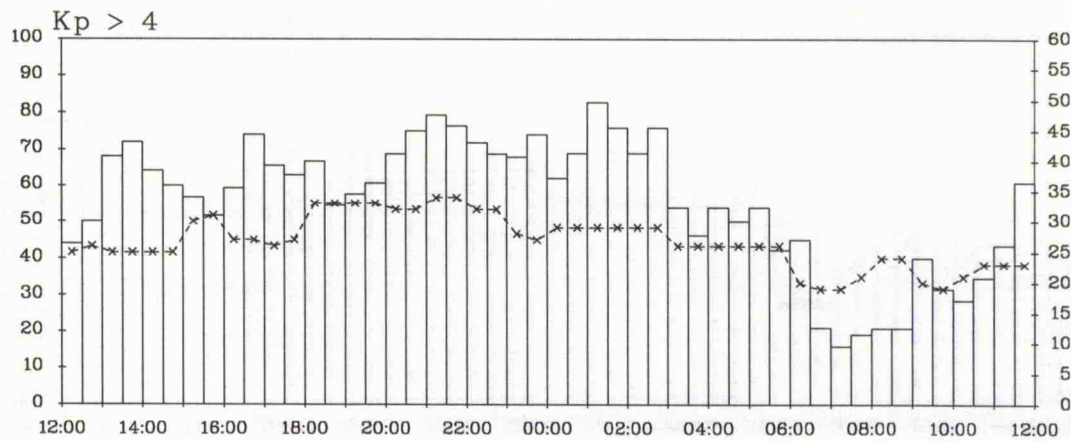
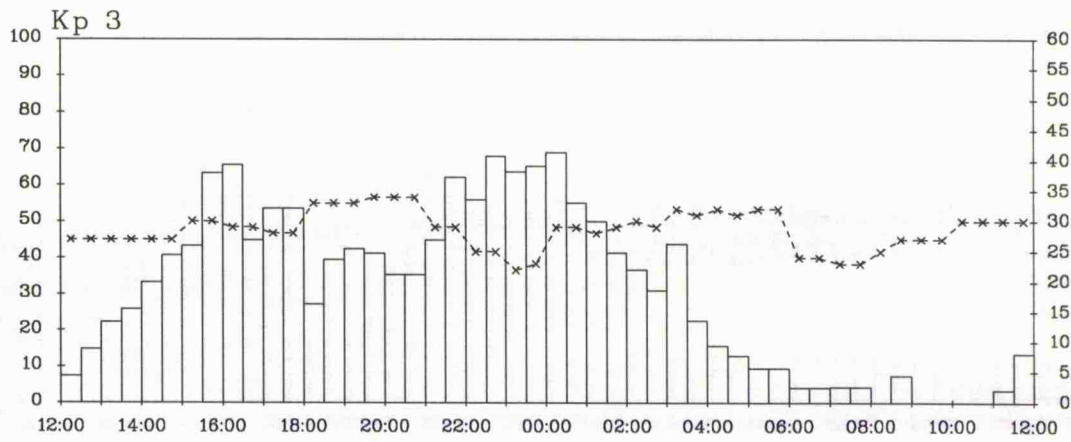
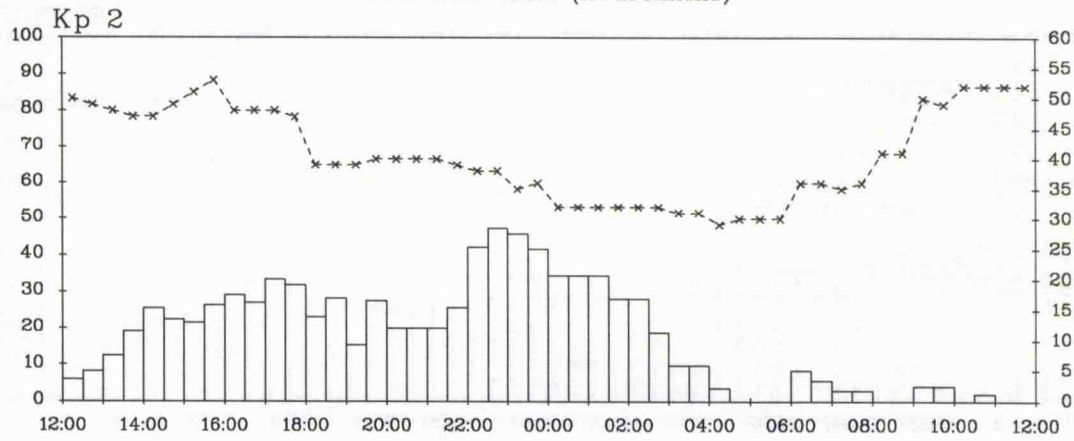
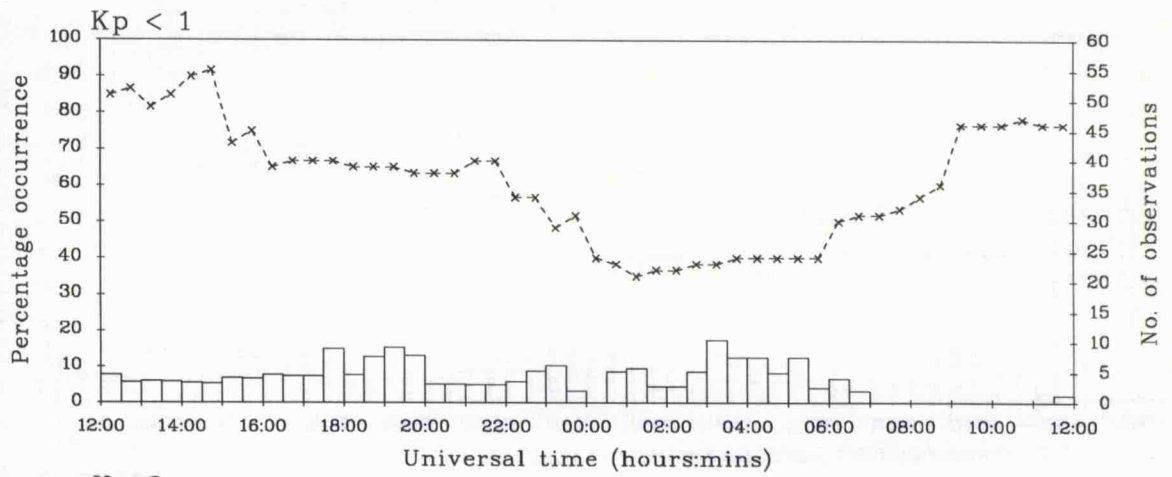


FIGURE 4.9: Variation of ion frictional heating with Kp

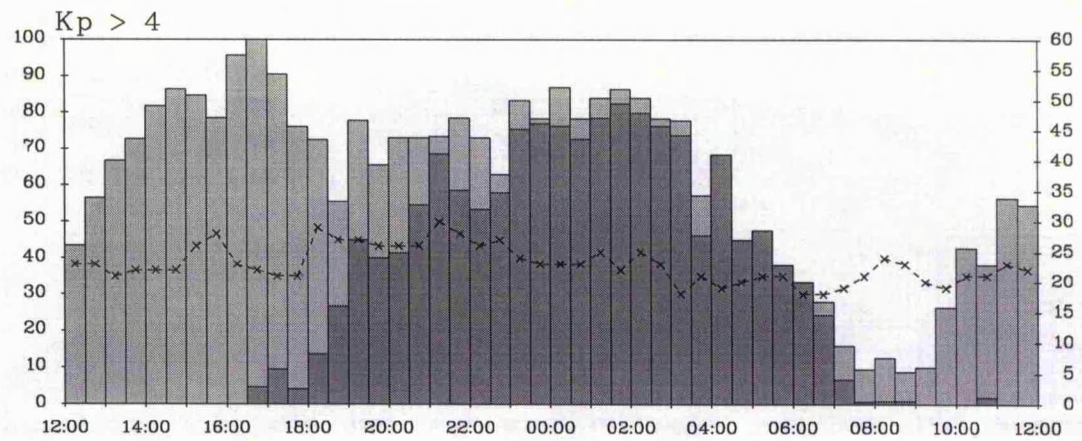
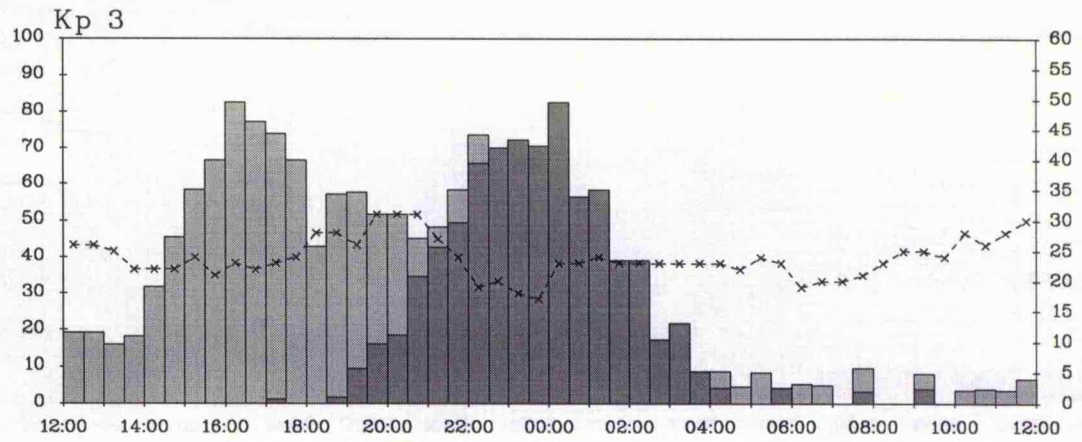
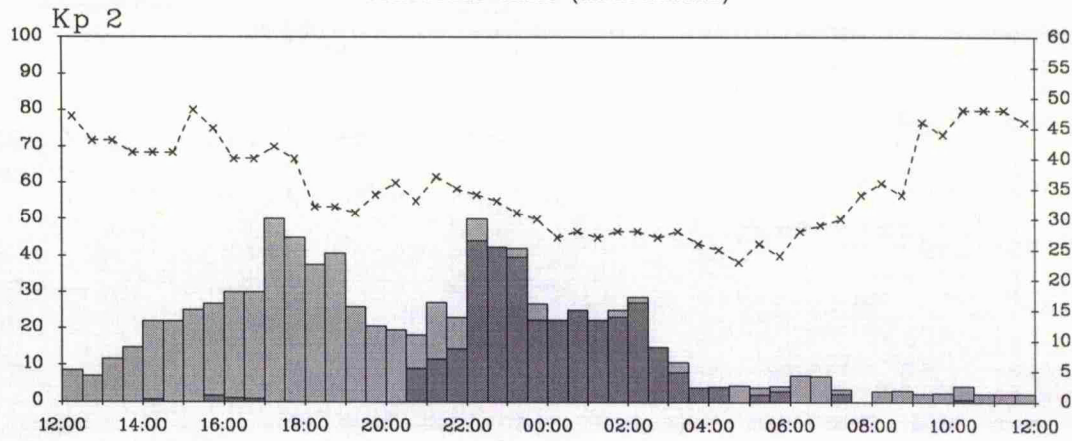
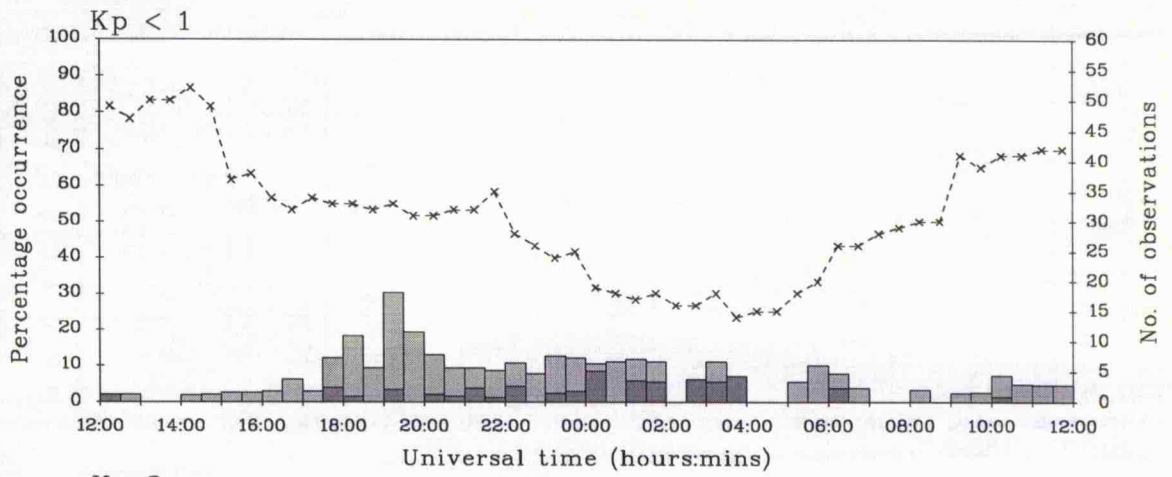


FIGURE 4.10: Variation of enhanced ion velocity with Kp

1986). This intensification is accompanied by the penetration of the convection pattern to lower magnetic latitudes. To some extent these results highlight the variation in the convection pattern with increasingly negative values of the z component of the interplanetary magnetic field, indeed reinforcing the results shown in the previous section.

Several authors have characterised the convection pattern as a function of  $K_p$ ; for example *Oliver et al. (1983)* derived, as the basis of an empirical model, averaged drift patterns of the F-region plasma between 60 and 75° invariant latitude as a function of  $K_p$  from incoherent scatter observations by the Millstone Hill radar taken during 1978. The work of *Senior et al. (1990)* is perhaps more applicable to the present study. *Senior et al. (1990)* constructed average convection patterns derived from a database of about 900 hours of EISCAT common programme 3 observations, taken between June, 1984 and November, 1987. As well as observing the intensification and extension of the convection pattern with increasing  $K_p$ , *Senior et al. (1990)* noted that the convection pattern rotated with increasing geomagnetic activity such that the average position of the nightside convection reversal moved to earlier local times. This had previously been suggested by the theoretical modelling of *Fontaine and Blanc (1983)* and was attributed by the authors to an increase, with increasing magnetic activity, of particle precipitation in the auroral zone. The results of *Senior et al. (1990)* indicated that, at the location of the radar, the centre of the convection reversal was displaced by some 2 hours; from 21:00 UT for  $K_p$  less than 2 to 19:00 for  $K_p$  in excess of 4. This time shift is indeed evident in the present study (see figure 4.10) and is of comparable value. It must be remembered that the y component of the IMF can induce similar asymmetries in the convection pattern (e.g. *de la Beaujardière et al., 1986; Burrage, 1988*), although any  $B_y$  effects should be averaged out, to a large extent, by the inclusion of a prolonged data set, as  $B_y$  is as likely negative as positive. *Senior et al. (1990)* also noted that under geomagnetically active conditions, larger flows arose in the evening convection cell than are observed in the morning cell. At the location of EISCAT, *Senior et al. (1990)* found that for  $K_p$  exceeding 4, the maximum of the northward component of the electric field (equivalent to westward flow) in the dusk sector was some 25% higher than the equivalent southward component (eastward flow). This result appears to be reproduced in the present study, for  $K_p \geq 4$  the occurrence probability of enhanced eastward flows is higher, although the relatively low number of observations under geomagnetically active conditions makes this assertion somewhat speculative.

#### 4.4.4 Variation with solar activity

The present set of EISCAT common programme observations extends over that part of solar cycle 22 characterised by a general increase in solar activity, from solar minimum between cycles 21 and 22, through the solar maximum around March 1990. The observations were loosely classed according to solar activity into those taken during solar minimum (1985 and 1986), solar maximum (1989 and 1990) and mid solar cycle (1987 and 1988). Figure 4.11 illustrates the diurnal distribution of ion frictional heating observed by

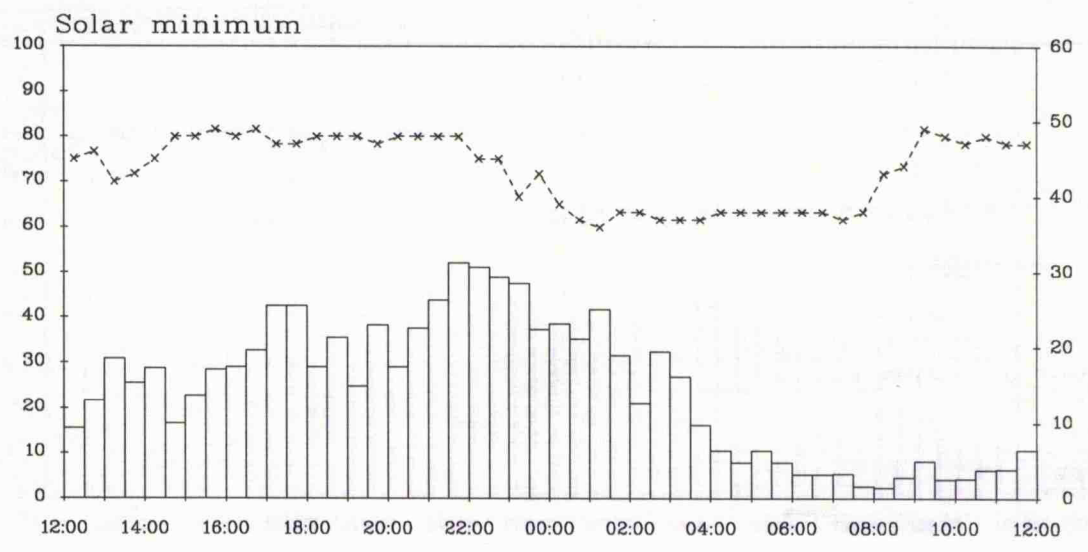
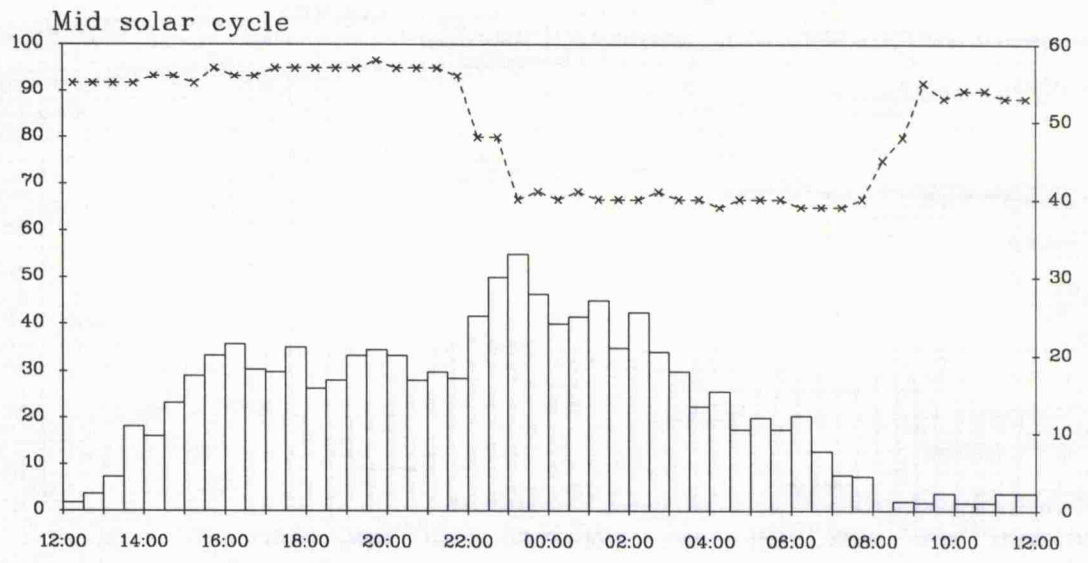
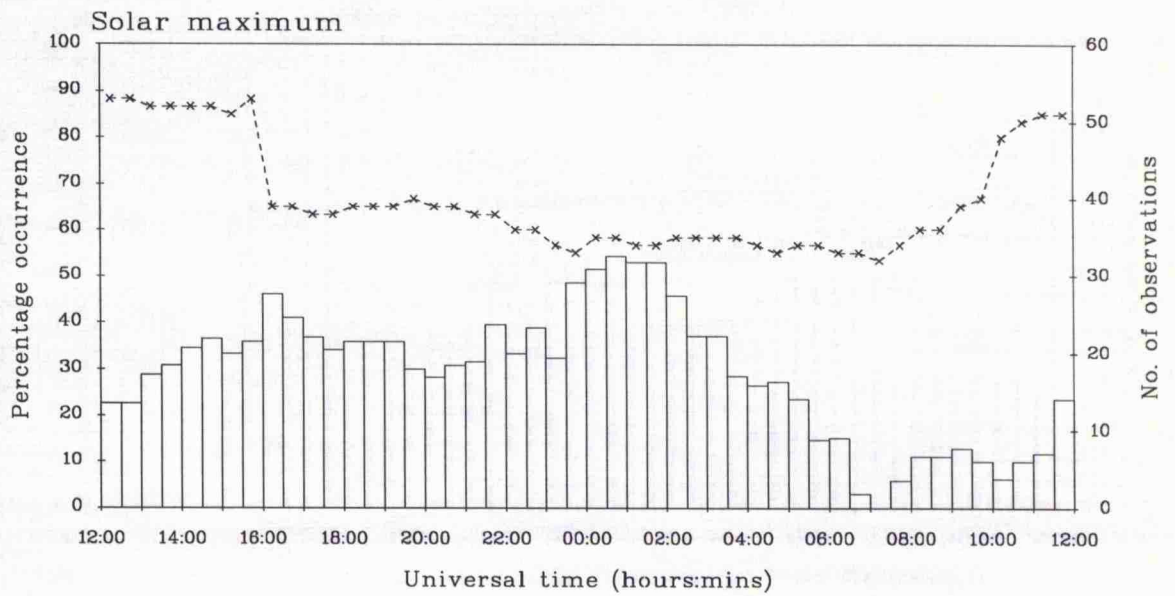


FIGURE 4.11: Solar cycle variation of ion frictional heating

EISCAT at 312 km altitude under solar minimum, mid solar cycle and solar maximum conditions, respectively. Again the histogram represents the percentage occurrence of ion frictional heating with universal time, and the superimposed line plot, the number of observations of each 30 minute bin. The latter varies between 40 and 60. Figure 4.12 presents equivalent distributions of enhanced ion velocities, those with a magnitude exceeding  $500 \text{ m s}^{-1}$ . Again velocities are further categorised in terms of the orientation of their associated zonal component.

It is instructive initially to consider the variation of the diurnal distribution of high ion flows during the solar cycle. It is evident from figure 4.12 that the occurrence probability of ion velocities exceeding  $500 \text{ m s}^{-1}$  in magnitude tends to increase markedly at all universal times with increasing solar activity; at 00:00 UT, for example, the percentage occurrence of enhanced ion velocity is around 40% for solar minimum, 50% during mid solar cycle, rising to almost 70% under solar maximum conditions. There is, however, no significant difference in the form of the distribution through the solar cycle. This trend can be explained with respect to the solar cycle variation of the geomagnetic activity. Magnetic activity on the earth tends to increase with increasing solar activity; the latter of which is characterised by an greater incidence of disturbances on the sun, such as solar flares and coronal holes. A study by *Hapgood et al. (1991)*, based on satellite observations taken over two complete solar cycles (numbers 20 and 21), revealed a distinct solar cycle variation in the IMF: the authors noted that the z component of the IMF tends to be of larger magnitude, and display a greater variance, at sunspot maximum, a factor which will contribute, at least in part, to a corresponding solar cycle variation in geomagnetic activity. The modal value of the  $K_p$  index during each of the two year intervals in the present data set corresponding to solar minimum, mid-solar cycle and solar maximum are 2o, 2+ and 3-, respectively. Although such an variation in  $K_p$  over the solar cycle may appear minimal, figure 4.10 illustrates the significant difference between the occurrence of enhanced F-region plasma flows for values of  $K_p$  around 3 and that for values of  $K_p$  around 2.

The diurnal distribution of ion frictional heating does not exhibit such a marked variation during the solar cycle as that observed in the ion velocities, although, on average, the occurrence of frictional heating does increase with ascending solar activity. Although not illustrated, the duration of identified intervals of ion frictional heating and the associated enhancement in the field-parallel ion temperature tend also to increase only slightly with increasing solar activity. It is suggested that the less pronounced increase in the occurrence of ion frictional heating with increasing solar activity than that observed in high ion flows, may be attributed to a solar cycle dependence of the response time of the neutral atmosphere to ion drag. The other major factors which govern ion frictional heating in the field-parallel direction, namely the mean neutral mass and the parallel ion temperature partition coefficient, would, conversely, tend to increase the parallel ion temperature enhancement with increasing solar activity for a given ion flow velocity; both of these quantities increase towards solar maximum in response to composition changes in the neutral atmosphere.

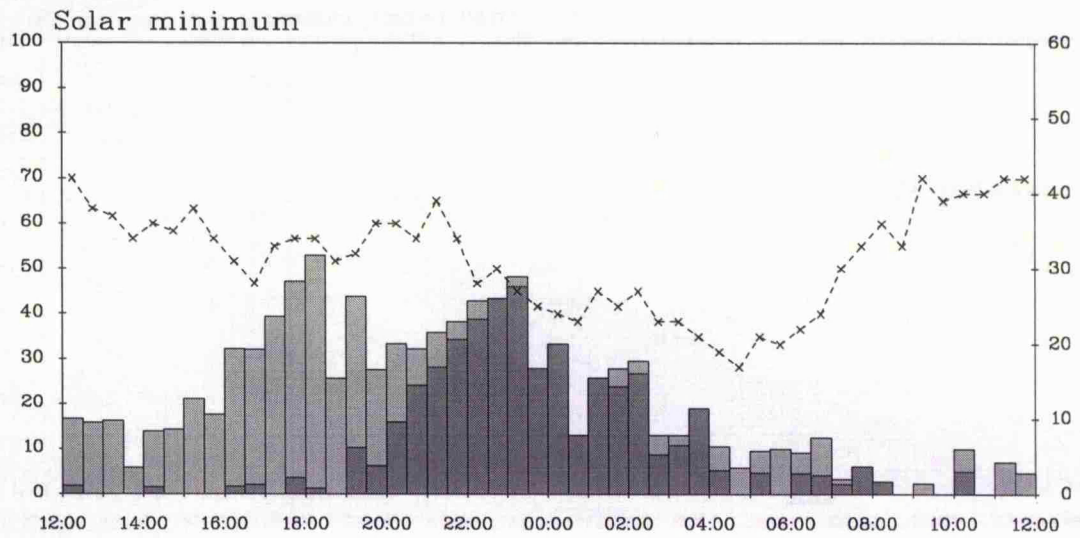
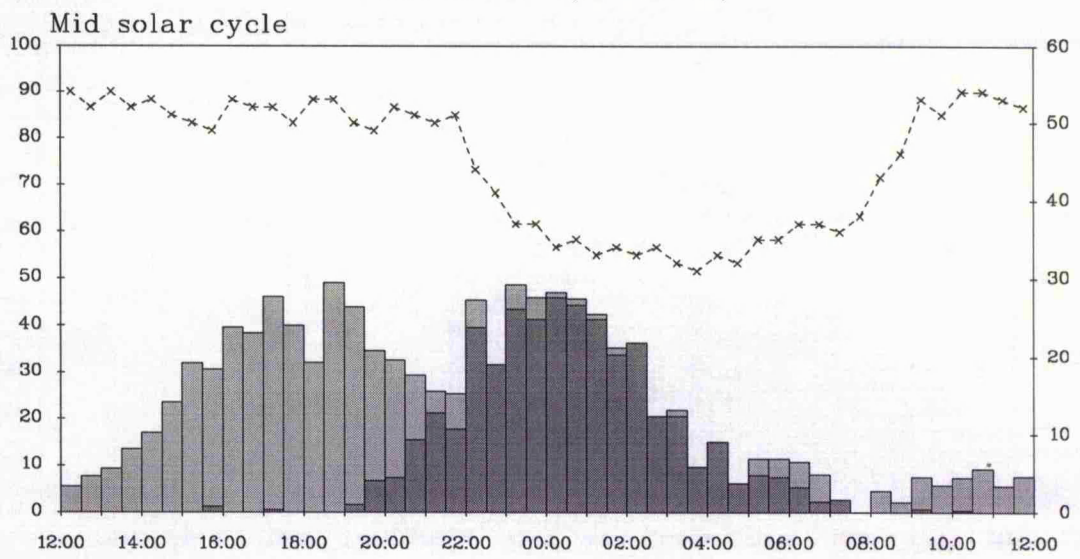
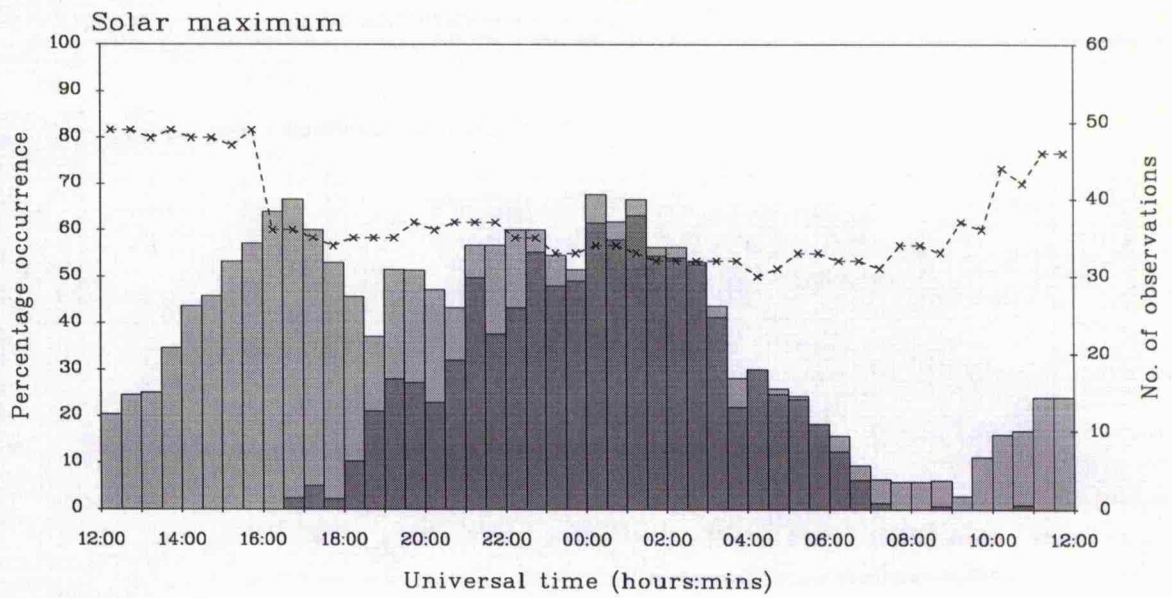


FIGURE 4.12: Solar cycle variation of enhanced ion velocity

The ionospheric plasma concentration exhibits, on average, an 11 year periodicity corresponding to the variation of solar emission in the X-radiation and ultraviolet wave bands. Between solar minimum and solar maximum, the electron density at F-region altitudes can increase by a factor exceeding three (*e.g. Davies, 1990*). The response time of the neutral atmosphere will, therefore, decrease with increasing solar activity, permitting the generation of larger neutral flows by ion drag: this will, to some degree, offset the effect of increased ion flows. Observational evidence supports the proposed explanation accounting for the far less pronounced increase in the occurrence of ion frictional heating with increasing solar activity than is observed in enhanced ion velocities. At solar minimum, an ion velocity of value  $1000 \text{ m s}^{-1}$  results in a median enhancement in the field-parallel ion temperature of some 500 K; under mid solar cycle and solar maximum conditions corresponding values are 400 K and 250 K, respectively. These observations highlight the significant influence of the electron density in determining, through ion drag, the extent of ion frictional heating through the solar cycle.

#### 4.4.5 Variation with season

In order to ascertain any seasonal dependence of ion frictional heating, the EISCAT observations were divided according to season, with the seasons defined as centred on the appropriate equinoxes and solstices. Successive panels of figure 4.13 illustrate the diurnal distribution of ion frictional heating observed by EISCAT during spring, summer, winter and autumn, respectively. Correspondingly, figure 4.14 illustrates the variation of the diurnal distribution of enhanced ion velocity with season.

Previous authors have suggested that the convection pattern in the high-latitude ionosphere varies seasonally. *Foster et al. (1986)* and *Holt et al. (1987)* investigated the seasonal variation of convection although they could not obtain a complete description of seasonal dependencies as their data, already subdivided according to IMF and  $K_p$ , was too sparse to draw any definitive conclusions. Later work by *de la Beaujardière et al. (1991)* concentrated purely on seasonal variations in convection. The authors present average patterns of ionospheric convection between  $67^\circ$  and  $82^\circ$  invariant latitude, derived for each season from observations taken between 1983 and 1988 by the Sondrestromfjord incoherent scatter radar. *de la Beaujardière et al. (1991)* suggested that a major factor effecting ionospheric convection on a seasonal basis is the semi-annual variation in geomagnetic activity. Geomagnetic conditions are most active at the equinoxes, a phenomenon proposed to result from a semi-annual variation in the effective southward component of the IMF caused by the seasonal variation in the Earth's dipole tilt angle (*Russell and McPherron, 1973*). Furthermore, *de la Beaujardière et al. (1991)* suggested that, as the Earth's dipole tilt angle changes, so does the relative position of the large-scale convection pattern, such that between summer and winter the pattern moves antisunward and also towards dawn.

It is helpful, initially, to ascertain if the observations indicate a seasonal dependence in enhanced F-region ion flow at the location of EISCAT. Figure 4.14 suggests that there is

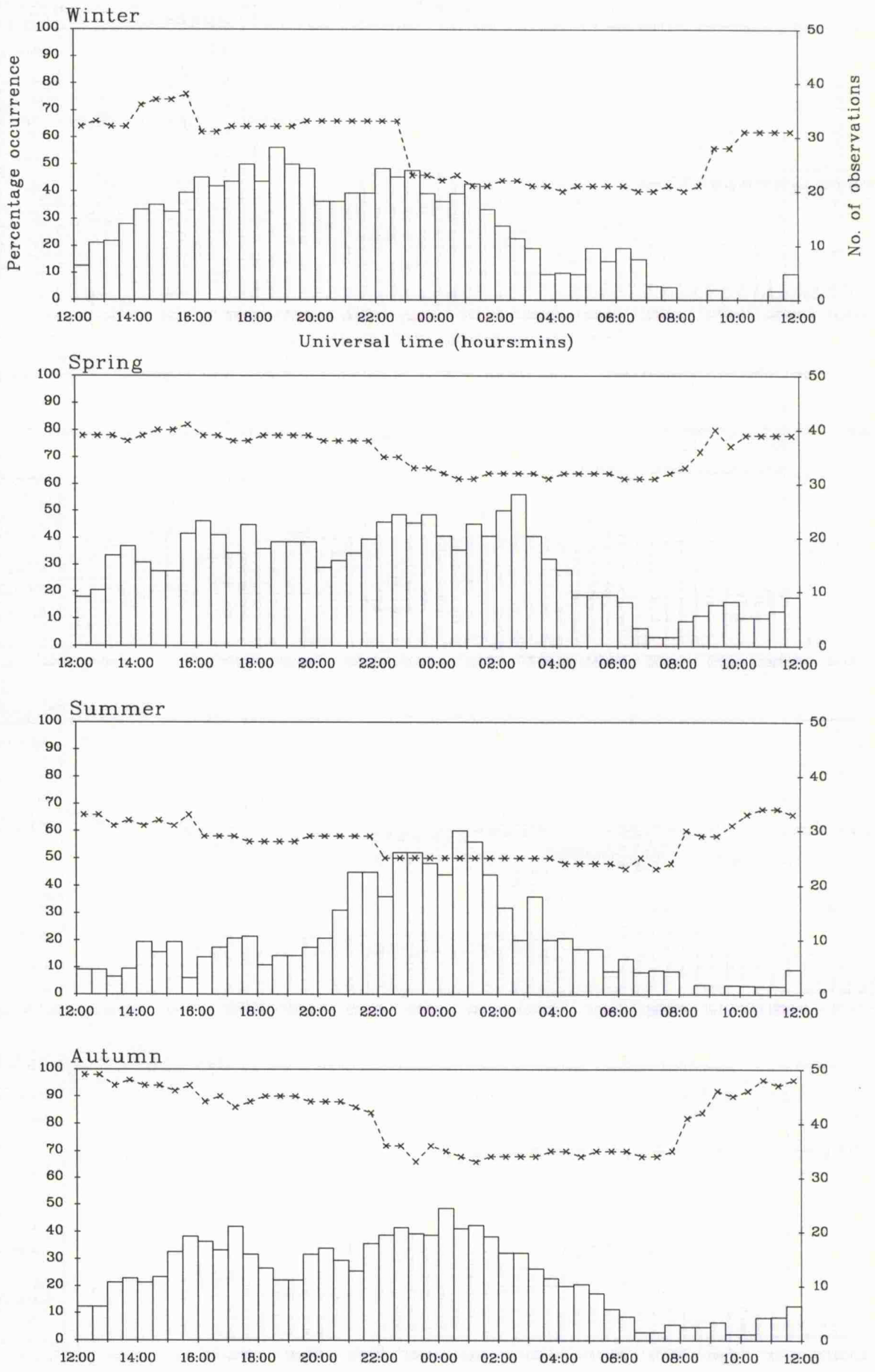


FIGURE 4.13: Seasonal variation of ion frictional heating

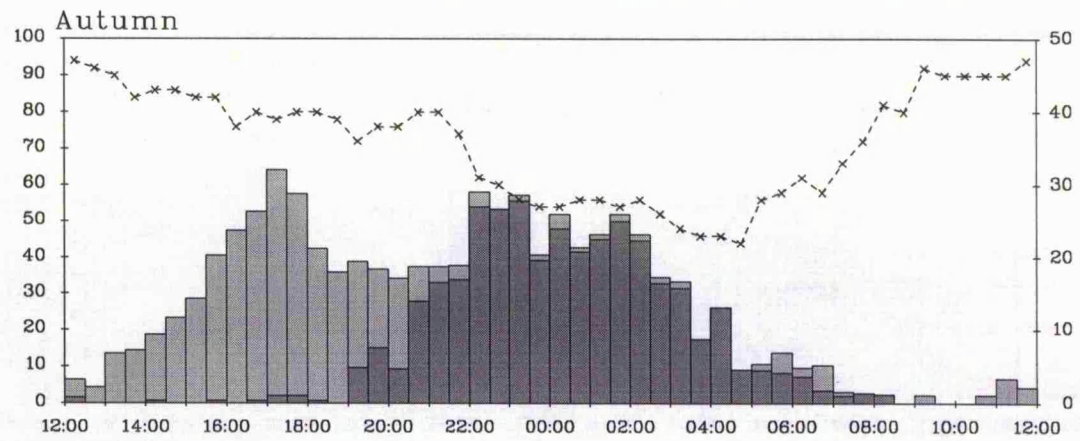
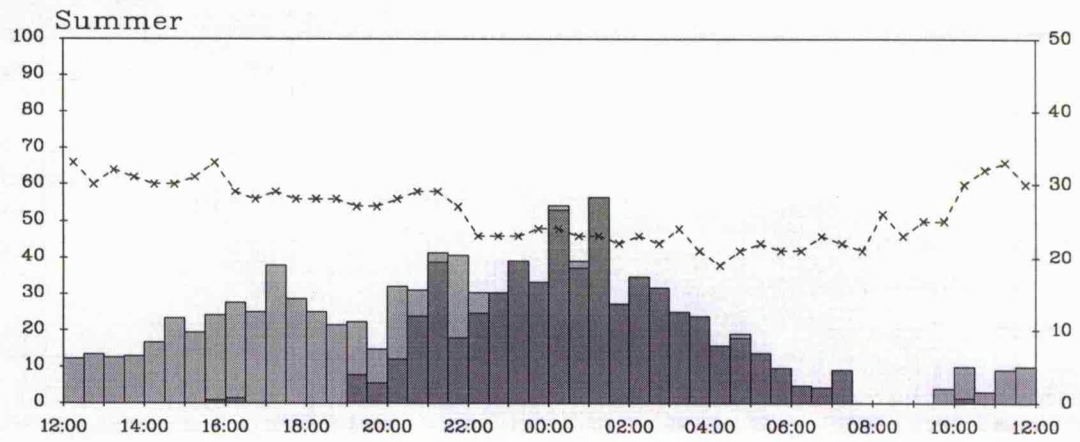
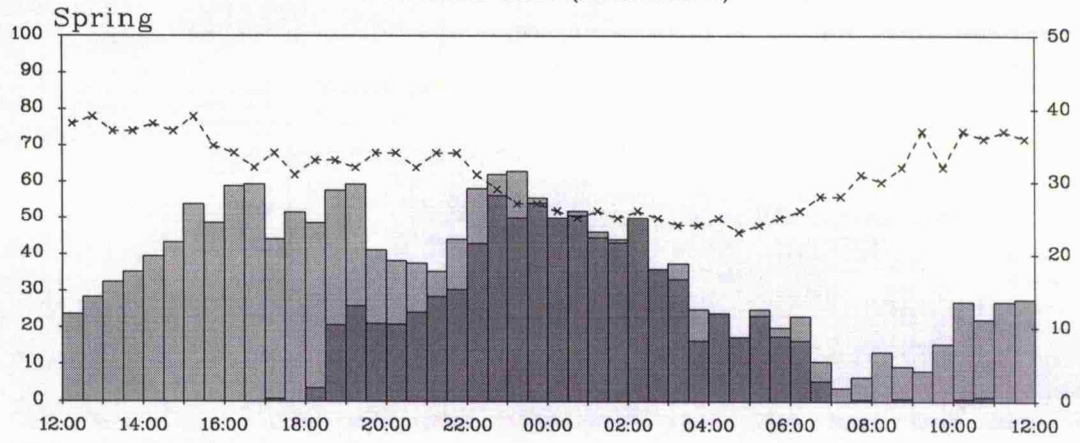
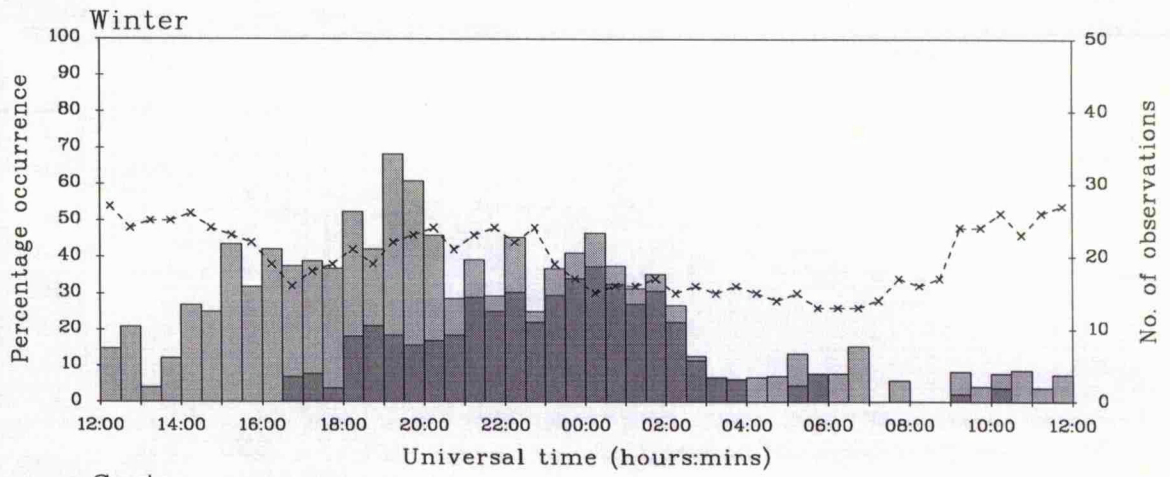


FIGURE 4.14: Seasonal variation of enhanced ion velocity

a increased occurrence of large ion flows at the equinoxes, particularly, in fact, in spring. This concurs with the assertion that geomagnetic activity is higher at the equinoxes and, indeed, over the years covered by the EISCAT data set, the modal value of  $K_p$  is 2o, 2+, 2- and 2+ for winter, summer, spring and autumn, respectively. As previously mentioned, with reference to the solar cycle variation of ion frictional heating, even such a small variation in  $K_p$ , is associated with large changes in the intensity and extent of the convection pattern. There is also evidence of an asymmetry in the convection pattern, at least at the location of the radar, between summer and winter: there is a preponderance of enhanced ion flow in the pre-midnight hours during the winter months and, conversely, in the dawn convection cell during summer. During spring and autumn, however, there is a roughly symmetric occurrence of large velocities in the dawn and dusk convection cells. These observations are consistent with those of *de la Beaujardière et al. (1991)*. At the lower latitude boundary of the field of view of the Sondrestromfjord incoherent scatter radar, equivalent to the geomagnetic location of the present observations, *de la Beaujardière et al. (1991)* noted that larger velocities tend to arise before midnight in winter and during the post-midnight hours in summer, attributable to dipole tilt effects on the position of the large-scale convection pattern.

The general shape of the diurnal distribution of ion frictional heating for each season is consistent with what would be anticipated from the corresponding distribution of enhanced ion velocity. During the equinoctial seasons, where there is a roughly symmetric occurrence of enhanced ion flows in the dawn and dusk sectors, the tendency for larger ion-neutral relative velocities to develop during the early morning hours (as discussed in section 4.4.1) introduces an asymmetry in the distribution of ion frictional heating between these two regimes. During summer, where the occurrence of enhanced velocities is less during the post-midnight hours, this asymmetry becomes more pronounced and in the winter months there is a slightly greater occurrence of ion frictional heating before midnight.

In the previous section, it was suggested that the change in electron density through the solar cycle has a marked effect on the occurrence of ion frictional heating. There is evidence that this is also true with regard to seasonal changes in electron density. On the nightside, where EISCAT observes the majority of intervals of ion frictional heating, the ionospheric electron density at F-region altitudes tends to be rather higher in summer than during the winter months, with intermediate values at the equinoctial seasons: the seasonal variation of electron density over Tromsø is discussed by *Farmer et al. (1990)*, who developed an empirical ionospheric model based on observations by the EISCAT radar. The enhancement in the field-parallel ion temperature for a given ion velocity tends, in general, to be higher in winter than in summer, consistent with the development of larger neutral winds through ion drag in the summer months, although the difference is not as pronounced as that observed over the solar cycle.

#### 4.5 Summary and Conclusions

The results of a statistical study of F-region ion frictional heating have been presented in this chapter. Over 3200 hours of field-aligned observations from the EISCAT common programmes CP-1 and CP-2, taken between 1985 and 1990, comprised the data set on which the investigation was based. The diurnal distribution of ion frictional heating observed by EISCAT over this six year interval, at 312 km altitude in the F-region, was constructed; the identification criterion for intervals of frictional heating was based on high-latitude observations by one of the Atmospheric Explorer satellites. The distribution of frictional heating exhibits a double peaked, although asymmetric, form centred around local magnetic midnight. This asymmetry results from the tendency for larger neutral winds to develop in the pre- as opposed to the post midnight sector. Furthermore, the dependence of the diurnal distribution of ion frictional heating on the orientation of the interplanetary magnetic field, geomagnetic activity, season and solar cycle has been investigated. A marked increase in the occurrence of ion frictional heating is noted with increasing geomagnetic activity and, moreover, for intervals where the z component of the interplanetary magnetic field is southward; both interpreted with respect to corresponding dependencies of ionospheric convection. Furthermore, the y component of the IMF, which is known to introduce asymmetries into the ionospheric convection pattern, effects markedly the shape of the distribution of ion frictional heating. A less pronounced increase in frictional heating with increasing solar activity is observed. The diurnal distribution of ion frictional heating exhibits a distinct seasonal variation, specifically with regard to the asymmetry in its form, attributable to a seasonal dependence of the ionospheric convection pattern.

## **Chapter 5**

### **Dayside ion frictional heating: EISCAT observations and comparison with model results**

#### **5.1 Introduction**

An extended period of intense dayside ion frictional heating was observed on 03 April 1992 with the UHF radar of the EISCAT facility during a run of the common programme CP-1-J. The elevated F-region ion temperature resulted from an enhancement in the ion drift velocity which steadily increased to a value in excess of  $2 \text{ km s}^{-1}$  during a 4 hour interval commencing at approximately 10 UT (12:15 MLT). The maximum enhancement in the field-parallel ion temperature, measured at 300 km altitude, exceeded 700 K. The electron concentration in the F-region was substantially depleted during the interval of ion frictional heating, which further resulted in an increase in the F-region electron temperature as the plasma was solar illuminated. This interval of ion frictional heating was unusual both in its prolonged duration and the local time of its occurrence. A zonal  $\mathbf{E} \times \mathbf{B}$  velocity signature, modelling that observed by EISCAT during the aforementioned interval, was imposed on the Sheffield University plasmasphere and ionosphere model (SUPIM). This chapter presents the EISCAT observations of ion frictional heating in the post-noon sector of 03 April 1992 and documents a comparison of these measurements with results from SUPIM, both without and with the adaptation of the model to include a calculated zonal component of the neutral wind.

#### **5.2 EISCAT CP-1-J observations of an interval of dayside ion frictional heating**

##### **5.2.1 EISCAT CP-1-J**

In EISCAT common programme 1, version J (CP-1-J) the transmitter beam at Tromsø is approximately aligned along the local magnetic field direction. The remote site radars perform an 8 position scan, intersecting the transmitter beam at 6 E-region altitudes and at a single F-region position, centred around 278 km, the last position being repeated twice within the scan. The duration of each scan is 10 minutes, with the dwell time in each position being approximately 1 minute. Remote site observations at the tristatic F-region altitude are, therefore, available every 5 minutes, whereas for a given E-region scan position, measurements are only available every 10 minutes. Four pulse schemes are transmitted: long pulse, alternating code and two power profiles. A long pulse scheme, with a pulse length of  $350 \mu\text{s}$ , yields an altitude resolution in the local magnetic field direction of some 22 km extending over 21 range gates centred from approximately 140 to 600 km altitude. The alternating code transmission scheme is employed for high resolution E-region observations. A 16 baud strong condition alternating code, using a baud length of  $21 \mu\text{s}$ , affords an altitude resolution of approximately 3.1 km between 86 and 270 km altitude. A

21  $\mu\text{s}$  power profile pulse scheme is sampled over the same range gates to enable a zero lag to be 'patched in' to the alternating code autocorrelation functions. A 40  $\mu\text{s}$  power profile scheme is also included for a slightly more coarse determination of raw E- and F-region electron density. Received signals are integrated over 5 seconds.

For the present study, observations from Tromsø have been post-integrated at a temporal resolution of 5 minutes and the remote site data, over the dwell time at each scan position. The signal-to-noise ratio of the F-region remote site and Tromsø long pulse observations employed in the present investigation are typically 20-30% and 100-300%, respectively.

### 5.2.2 Observations of an interval of dayside ion frictional heating

An extended run of the EISCAT CP-1-J experiment began at 16:00 UT on 30 March 1992 and continued until 16:00 UT on 03 April 1992. Figure 5.1 presents CP-1-J observations from 06:00 to 15:00 UT on 03 April. Panels a, c, d and f of figure 5.1 illustrate long pulse observations of F-region ion temperature, ion velocity, electron density and electron temperature, respectively, as a function of altitude from 150 to 550 km and as measured along the local magnetic field direction by the Tromsø UHF receiver. Positive field-parallel ion velocities are those towards the radar, i.e. down the field line. Panel b presents the two orthogonal components of the observed ion drift velocity relative to the local geomagnetic field at the F-region intersection altitude of 278 km, calculated by combining the ion velocity measured from long pulse transmission at each receiver site. The field-orthogonal zonal ion velocity component (shown in blue) is positive eastward and the meridional component (in red) is positive northward. Panel e of figure 5.1 illustrates CP-1-J alternating code measurements of electron density along the magnetic field direction through the E- and lower F-regions from 106 to 150 km altitude.

A prolonged interval of substantial F-region field-parallel ion temperature enhancement is observed in the post geomagnetic noon sector on 03 April 1992 (figure 5.1, panel a), prior to which the F-region ion temperature exhibits typical behaviour, increasing with altitude but varying little with time. The heating of the ion population is highly structured, with the field-parallel ion temperature increasing gradually after approximately 11:30 UT (corresponding to 13:45 MLT), then quite sharply at 12:00 UT and again just prior to 13:00 UT. At 13:20 UT a temporary reduction in the field-parallel ion temperature is observed, followed by another hour of intense ion heating before the temperature finally begins to reduce to its unperturbed value after 14:30 UT. The field-parallel ion temperature at 300 km altitude is enhanced above its ambient value by a maximum exceeding 700 K. The elevation of the F-region field-parallel ion temperature after 11:30 UT correlates with a zonal field-orthogonal ion drift velocity exceeding some 1000  $\text{m s}^{-1}$  (figure 5.1, panel b). The zonal component of the ion drift velocity steadily increases in a westward direction, over a four hour interval commencing at around 10:00 UT, to a maximum of around 2200  $\text{m s}^{-1}$ . The observed westward ion velocity corresponds to return, or sunward, flow on the

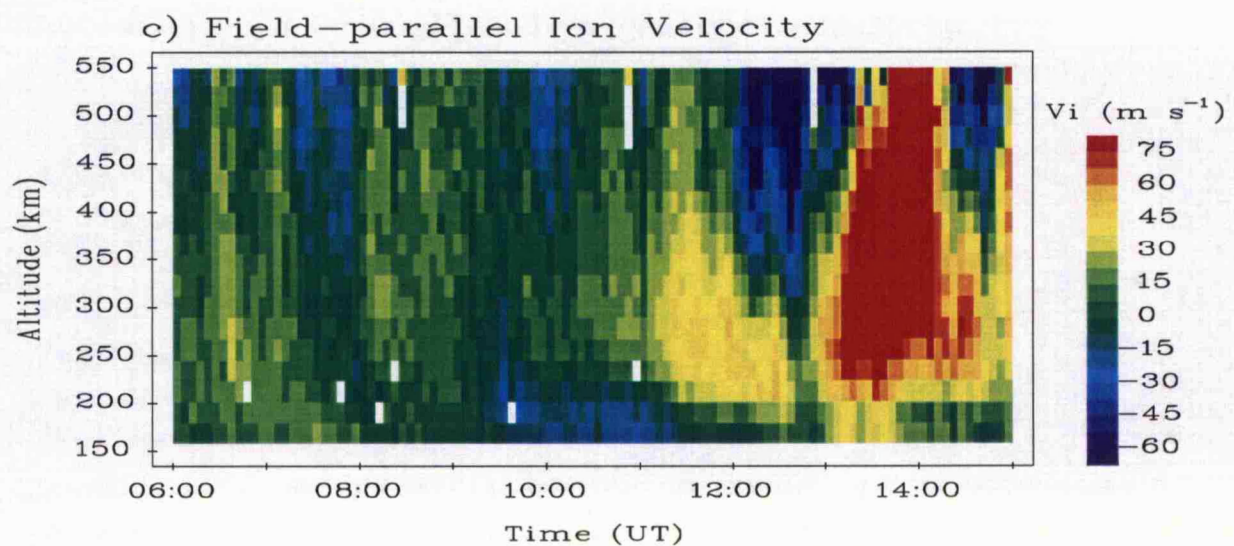
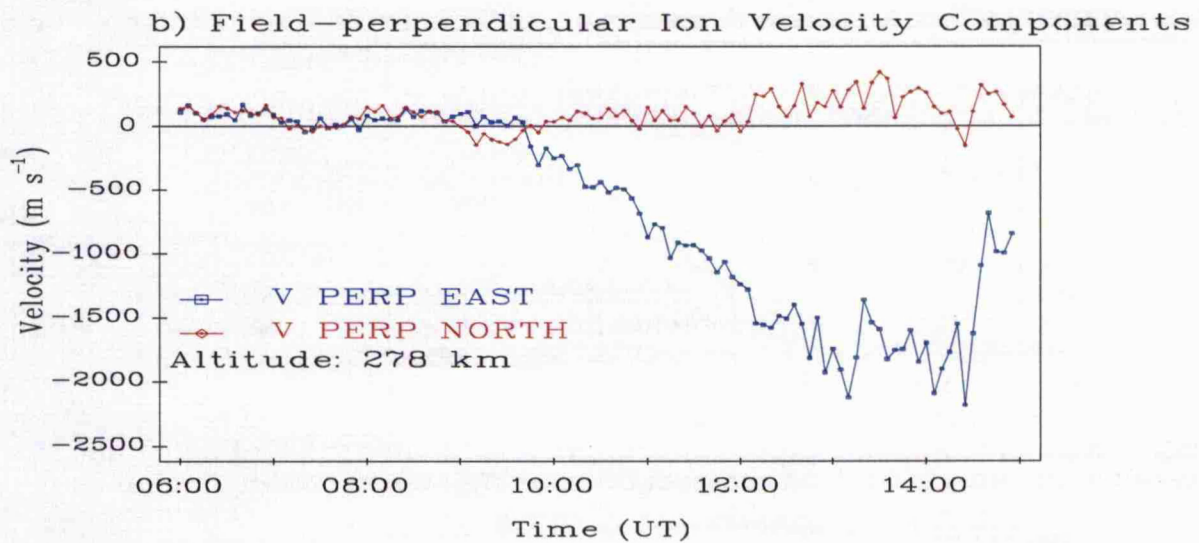
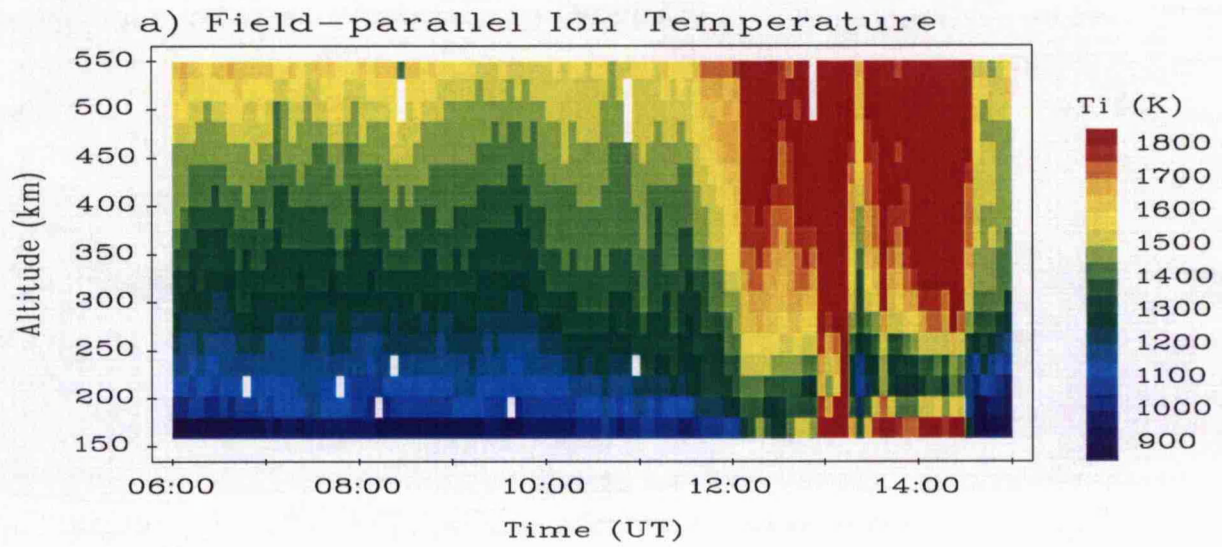
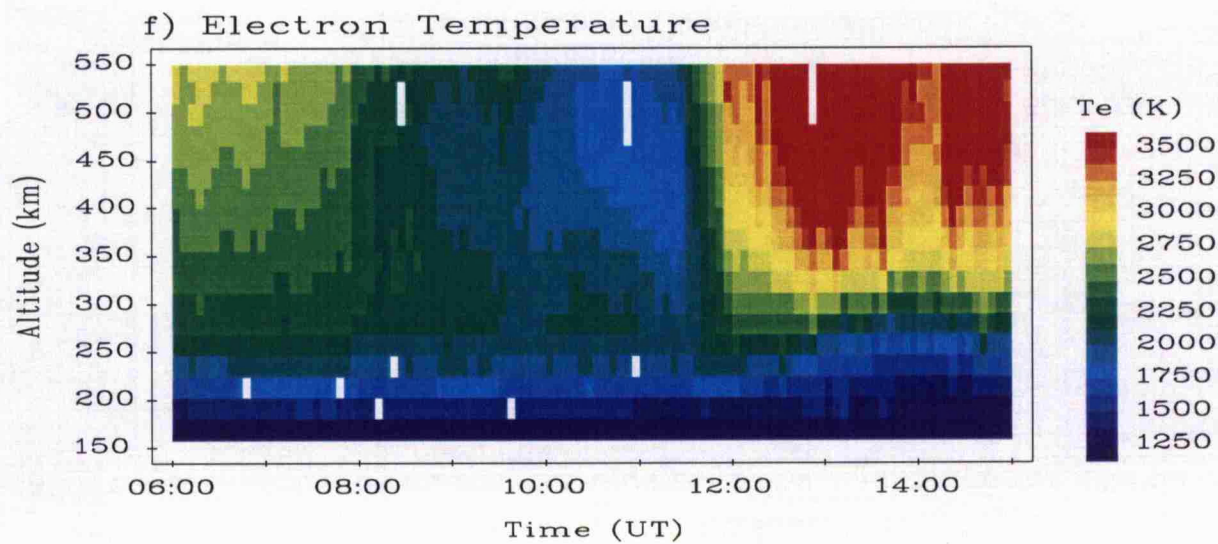
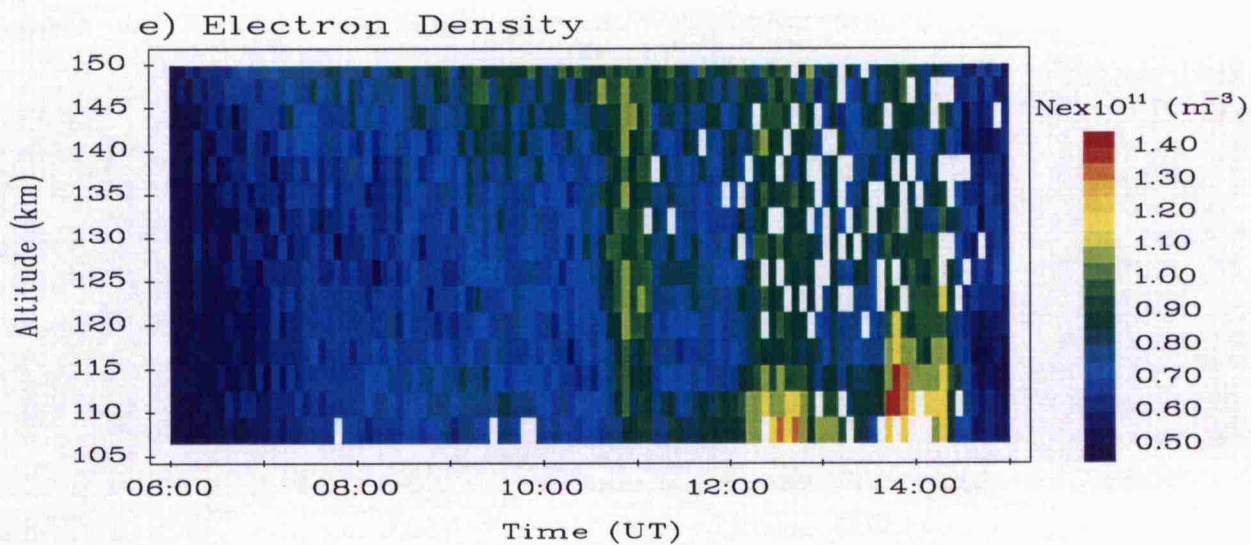
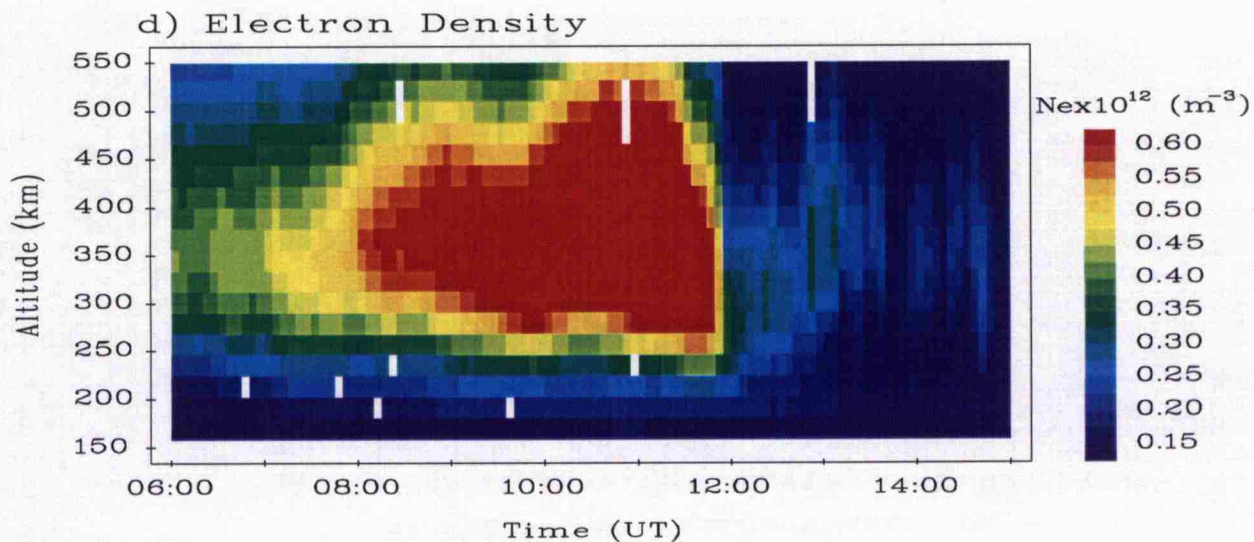


FIGURE 5.1: EISCAT CP-1-J observations for 3/4/1992



flanks of the convection pattern. The meridional component of the ion velocity remains comparatively low, less than  $500 \text{ m s}^{-1}$ , throughout the interval. The observed reduction in the field-parallel ion temperature shortly before 13:30 UT is coincident with a temporary decrease in the westward ion velocity. The simultaneous occurrence of enhanced ion temperatures and high ion drift velocities in the high-latitude F-region implies frictional heating of the ion population through contact with a stationary or slower moving neutral atmosphere. For the first 90 minutes of elevated zonal ion velocity, however, the ions undergo little field-parallel temperature enhancement. The subsequent interval of ion frictional heating is unusual in its prolonged nature, approximately 3 hours, and the local time of its occurrence, commencing around 11:30 UT (13:45 MLT), as compared with the results of the statistical study documented in the previous chapter which revealed a preponderance of frictional heating in the night-time sector, of typical duration less than 1 hour.

In EISCAT common programme analysis the ion temperature is derived assuming the ion thermal velocity distribution along the direction of observation is Maxwellian. Such analysis of incoherent scatter signals where the ion thermal velocity distribution is actually non-Maxwellian has been demonstrated theoretically to lead to an overestimate of the ion temperature and an underestimate of the electron temperature (*e.g. Suvanto et al., 1989b*). The errors induced in the derived temperatures through neglecting the non-Maxwellian nature of the velocity distribution, for the aspect angles and ion velocities involved in these data, are predicted to be less than some 2% (*Lathuillère and Hubert, 1989*). All of the incoherent scatter spectra for the Tromsø CP-1-J long pulse data presented in this chapter have been inspected by eye and there appear to be none which imply significant non-Maxwellian ion thermal velocity distributions along the direction of the magnetic field, although the incoherent scatter spectra from plasma with a non-Maxwellian ion thermal velocity distribution are not always visibly different from those from a plasma in which the velocity distribution is Maxwellian. Several of the spectra from the remote site receivers, which observe at larger aspect angles, do, however, indicate the possible existence of non-Maxwellian line-of-sight ion thermal velocity distributions during the highest ion flows.

Due to mechanisms highlighted in chapter 2, section 3.4 the molecular content of the ionosphere is enhanced during ion frictional heating, leading to the dominance of molecular ions up to altitudes which can, for intense events, exceed some 400 km. After about 12:00 UT during the observed interval of ion frictional heating there is a measured minimum in field-parallel ion temperature between approximately 170 km and 300 km altitude (figure 5.1, panel a). This minimum is, at least partially, due to an underestimate of the ion temperature as a consequence of an underestimate of the proportion of molecular ions within this region adopted in the standard composition model of the analysis routine. The underestimate of the field-parallel ion temperature yielded by the analysis routine is, moreover, accompanied by an underestimate of the analysed electron temperature. Furthermore, standard EISCAT analysis assumes that, for a multi-ion plasma, the line-of-

sight ion temperatures of all species are equal. The existence of a relative velocity between the ion and neutral populations, however, causes the atomic and molecular ion temperatures to diverge, with the greatest deviation being in the direction of the magnetic field (*Lathuillère and Hubert, 1989*). The ion temperature derived from incoherent scatter for a multi-ion plasma is not simply the weighted mean of the temperatures of the individual species present due to the non-linearity of the incoherent scatter spectrum.

Panel a of figure 5.2 contains time series, from 06:00 to 15:00 UT, of the ion temperature measured at each UHF receiver site at the F-region intersection altitude of 278 km. The ion temperatures measured by the receivers at Sodankylä, Kiruna and Tromsø are presented in red, green and blue respectively. The quoted error for the EISCAT measurements in this and successive figures is the combination of the fit error due to the analysis and the random error, the latter of which is calculated via the formulae of *du Castel and Vasseur (1972)*. The uncertainties associated with incoherent scatter observations have been discussed in more detail in chapter 3. The remote site ion temperatures, particularly those from the Sodankylä receiver which observes at a larger aspect angle than that at Kiruna, exhibit some evidence of the anisotropic nature of the F-region ion temperature with the ion temperature measured by the remote site receivers exceeding that measured at Tromsø over much of the interval of ion frictional heating: at the F-region intersection altitude of 278 km, the aspect angle of the mirror direction for the UHF receiver at Kiruna is about  $19^\circ$  compared with  $29^\circ$  for that at Sodankylä. The ion temperature measured at Sodankylä exceeds that measured by the Tromsø antenna by up to 300 K. Even during the undisturbed interval prior to the onset of ion frictional heating there is, however, a tendency for the ion temperature measured at Sodankylä to slightly exceed that measured at both of the other receiver sites, by several tens of Kelvin. At the F-region tristatic altitude an ion population dominated by  $O^+$  is assumed in the analysis. An increase in the proportion of molecular ions at this altitude, however, would result in an underestimate in the ion temperature measured at all receiver sites.

Figure 5.2, panel b presents time series, from 06:00 to 15:00 UT, of the field-perpendicular (green line) and field-parallel (blue line) components of ion temperature and the 3-dimensional ion temperature (red line) at 278 km altitude. These are calculated from the ion temperatures measured by the Tromsø and Sodankylä receivers by applying equations 2.14 and 2.15 in which the field-parallel ion temperature is that measured at Tromsø. The tendency for the ion temperature measured at Sodankylä to exceed that measured by the Tromsø receiver, and also that at Kiruna, even under undisturbed conditions results in the discrepancy between the field-parallel and field-perpendicular ion temperature components by some 200 K prior to the onset of frictional heating. During the interval of ion frictional heating, the perpendicular ion temperature at 278 km exceeds that parallel to the field by up to 1000 K although there are a small number of instances where the opposite is true, due to the Tromsø measurement of ion temperature exceeding that at Sodankylä. Again the parallel, perpendicular and 3-dimensional ion temperatures would be

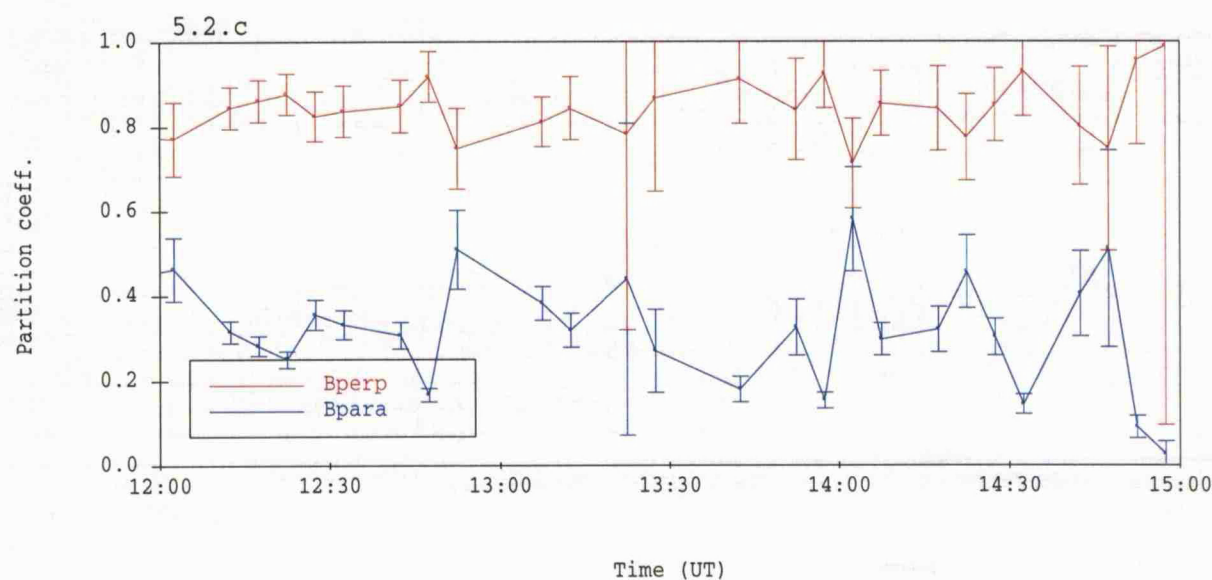
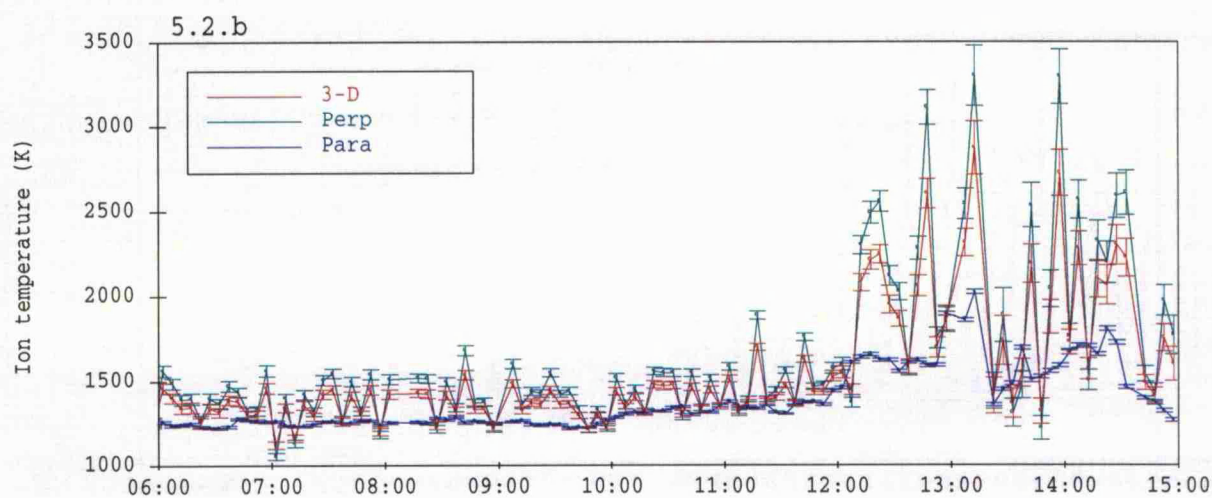
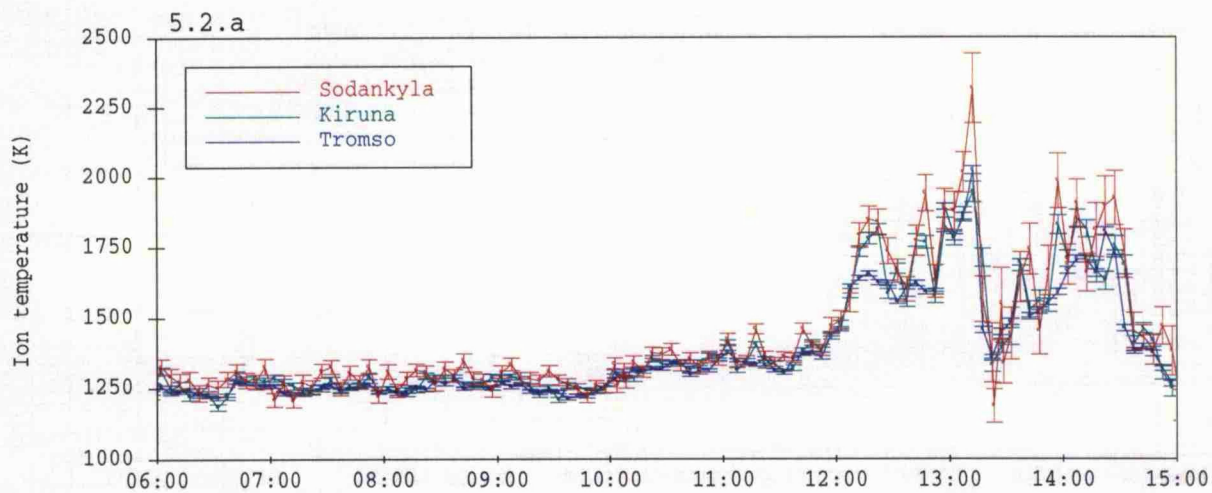


FIGURE 5.2: EISCAT CP-1-J long pulse ion temperature observations and ion temperature anisotropy

Altitude: 278 km

correspondingly affected by any underestimate in the ion temperatures measured at Tromsø and Sodankylä. Estimates of the field-perpendicular and 3-dimensional ion temperatures were also derived by combining the ion temperature measurements from Tromsø and Kiruna (not illustrated). Comparable results were obtained to those calculated using measurements of ion temperature from Tromsø and Kiruna, although with rather more variability as a consequence of the smaller scattering angle involved.

Equations 2.10, a and b, and 2.13 are employed, assigning a value of 1250 K to the unperturbed ion temperature, to calculate the field-perpendicular and field-parallel ion temperature partition coefficients,  $\beta_{\perp}$  and  $\beta_{\parallel}$ , at 278 km altitude. These quantities are plotted, in red and blue respectively, from 12:00 to 15:00 UT in panel c of figure 5.2. Instances where the Tromsø measurement of ion temperature exceeds that at Sodankylä, which would result in the calculated field-parallel ion temperature partition coefficient exceeding that perpendicular to the magnetic field, have been rejected. The derived values of the field-parallel partition coefficient at 278 km altitude tend to lie within the range 0.2 to 0.4 although any overestimate in the proportion of atomic oxygen ions in the analysis would cause an underestimate in the derived value of the field-parallel partition coefficient, and consequently an overestimate in the coefficient perpendicular to the magnetic field with such a method of calculation. Again, similar values of the partition coefficients were derived by combining ion temperature measurements from the receivers at Tromsø and Kiruna. The parallel partition coefficient expected due to  $O^+$ -O collisions (a mixture of resonant charge exchange and polarisation collisions) and pure polarisation interactions, the latter of which will arise not only due to the presence of molecular ions but due to  $O^+$  collisions with molecular neutrals, are 0.24 and 0.57 respectively (*Winkler et al., 1992*). These results imply a possible mixture of  $O^+$ -O and pure polarisation interactions, a similar conclusion to that noted by *McCrea et al. (1995)* from the examination of observations from the EISCAT special programme, SP-UK-BEAN.

In the daytime F-region, plasma tends to flow down the field lines at the location of EISCAT due to the action of the neutral wind, as is evident prior to the onset of frictional heating in panel c of figure 5.1. Through the interval of ion frictional heating, from approximately 11:30 UT, large field-parallel ion velocities are measured. During the early stages of the interval of ion frictional heating field-parallel plasma flow tends to be upwards (negative) in the topside ionosphere and downwards below a 'reversal altitude' which reduces from 400 to 300 km altitude over a 90 minute interval commencing at the onset of frictional heating. Around 12:30 UT, upward velocities of order  $100 \text{ m s}^{-1}$  are observed at 500 km altitude. As the interval progresses, the field-parallel plasma velocity becomes downwards at all altitudes, with a magnitude approaching  $150 \text{ m s}^{-1}$  at 300 km altitude, compared with quiet time flows of less than  $30 \text{ m s}^{-1}$ . The final twenty or so minutes of ion frictional heating are accompanied by upward plasma flow at altitudes above about 400 km. Such large field-aligned plasma flow results from enhanced ambipolar plasma diffusion due, in this case, to increased gradients in both ion and electron temperature (see later). The

flows will be modified by the ambient downward motion and any upward motion of the plasma caused by upwelling of the lower neutral atmosphere in response to Joule heating (see chapter 2, section 3.5).

A typical profile of F-region electron density (figure 5.1, panel d) is observed until approximately 11:30 UT. From this time, however, the electron density becomes substantially depleted at all altitudes above 170 km, for example, at 350 km, the electron density is reduced from  $1 \times 10^{12}$  to  $4 \times 10^{11} \text{ m}^{-3}$  by 11:50 UT. This depletion correlates with the onset of frictional heating of the F-region ion population. The depletion in F-region electron density during intervals of ion frictional heating is generally ascribed to a combination of two mechanisms; large field-aligned upward plasma velocities and enhanced recombination. As previously noted, rapid upflow of plasma, along the direction of the field-lines, is observed at all altitudes above about 300 km during the initial stages of ion frictional heating, which will contribute to the observed reduction in F-region electron density, particularly above this altitude. Enhanced recombination of the ionospheric plasma will account for much of the observed density depletion below about 300 km, due to the dominance of chemical loss processes at altitudes below the F-region peak (*Schunk et al., 1975*).

Panel e illustrates observations of electron density in the E- and lower F-regions derived from alternating code transmission. At altitudes below 106 km, the alternating code electron density is derived in standard analysis by assuming that the ion and electron temperatures are equal although, during intervals of large electric field the electron temperature in the E-region may be significantly enhanced by wave turbulent heating (*e.g. Schlegel and St-Maurice, 1981*). The alternating code electron density measurements derived below 106 km are, therefore, not presented. A typical altitude profile of electron density, through the E-region peak and bottomside of the F-region, is evident prior to the onset of ion frictional heating. During the interval of ion frictional heating, however, a slight enhancement in the E-region electron density is observed, increasing from some  $1.0 \times 10^{11}$  to  $1.5 \times 10^{11} \text{ m}^{-3}$  at 110 km altitude, directly correlating with the occurrence of enhanced F-region ion temperature. It is suggested that this increase in the E-region electron density is probably due to enhanced downward diffusion of F-region plasma along the magnetic field lines into this region rather than a result of auroral precipitation, a conjecture supported by several factors. The alternating code measurements of parallel ion velocity (not presented) illustrates a tendency for plasma to flow down the field line below 150 km altitude, with velocities of order  $50 \text{ m s}^{-1}$ , during the interval of ion frictional heating. This downflux of plasma would sustain such an increase in E-region electron density. Moreover, previous authors, including *McCrea et al. (1991)*, have concluded that precipitation of energetic particles into the auroral zone modifies the underlying convection electric field such that ion frictional heating tends to be suppressed.

Panel f of figure 1 presents measurements of F-region electron temperature. The observed minimum in the electron temperature around the F-region peak at local noon is

expected under conditions of medium or high solar activity, as noted by *Banks and Kockarts (1973)*. This is a consequence of the increased loss of electron energy to the F-region ions which varies as a square of the electron density. From about 11:30 UT the measured F-region electron temperature exhibits an increase at all altitudes above 250 km, correlating, again, with the onset of ion frictional heating. At 400 km altitude, the electron temperature increases to a maximum value exceeding 3500 K, compared with 2200 K at the same local time during undisturbed conditions two days previously. As has been mentioned, the electron temperature between some 170 and 300 km will be underestimated somewhat during the interval of ion frictional heating, the extent depending on that of ion composition modification. Auroral precipitation will result in an enhancement in the F-region electron temperature although, as noted previously, its occurrence is over this interval has been largely discounted. Moreover, such a large increase in electron temperature cannot be accounted for in terms of thermal energy transfer from the ion population, indeed the electron temperature greatly exceeds the ion temperature such that thermal energy exchange from the electrons to the ions will occur, although only to a very small degree.

It is therefore necessary to explain the increase in the electron temperature in terms of an alternative process; this process is most probably photoelectron heating (*e.g. Schunk and Nagy, 1978*). Energetic photoelectrons, the product of photo-ionisation of the neutral atmosphere, enter the ambient electron population thus raising its temperature. Indeed, it is this process that enhances the temperature of the electrons over that of the ions and neutrals in the unperturbed ionosphere. The interval of ion frictional heating was observed at the beginning of April and at the local time of the event the ionospheric plasma in the EISCAT field of view was sunlit. After approximately 11:30 UT, the F-region electron density was substantially depleted, although the neutral atmosphere would have been illuminated by a relatively constant photon flux leading to a similarly constant production of energetic photoelectrons. Thus, as the photoelectrons enter the significantly depleted thermal electron population, photoelectron heating would serve to increase the electron temperature far beyond that which would arise in undepleted plasma, where the ratio of photoelectrons to ambient thermal electrons would be much smaller. This effect is rarely seen with EISCAT, as, at the magnetic latitude of Tromsø, the occurrence of ion frictional heating is far greater before 04:00 and after 16:00 UT than between these hours (see chapter 4). Moreover, intervals of such duration as that of the present event are rarely observed, even in the nightside where the preponderance of frictional heating is much greater.

The occurrence of greatly enhanced F-region electron temperature persists after the F-region ions have ceased to be frictionally heated. It is suggested that this could be due to either the slower dissipation of the energy of the electron population compared with that of the ions or the maintenance of elevated electron temperatures by an external magnetospheric heat source.

The enhancement in F-region electron temperature will itself tend to modify the effects of ion frictional heating. The enhanced electron temperature reduces the rate of

dissociative recombination, as the coefficients of recombination vary inversely with electron temperature (*e.g. Torr and Torr, 1978*), thus acting to suppress the electron density depletion. In contrast, however, increased gradients in the electron temperature enhance the rate of ambipolar diffusion, yielding larger field-aligned flows and, hence, reducing the electron content. High electron temperatures, exceeding some 1500 K, enhance the vibrational temperature of the neutral molecules  $N_2$  and  $O_2$  (*Schunk and Nagy, 1978*). Vibrationally excited neutrals are thought to have a faster rate of reaction with  $O^+$  than the unexcited molecule. Thus for an enhanced electron temperature, the production of excited neutrals tends to reduce the electron content of the F-region, in addition to increasing the proportion of molecular ions.

This section has explained the observed behaviour of the F-region plasma during an interval of high ion drift in the dayside, and also highlights some of the problems inherent in the analysis of incoherent scatter under such conditions. In the following sections, the observations are compared with modelling results for the event from the Sheffield University model plasmasphere and ionosphere.

### **5.3 Modelling the interval of dayside ion frictional heating with the Sheffield University plasmasphere and ionosphere model (SUPIM)**

#### **5.3.1 SUPIM - An overview of the model**

The Sheffield University Plasmasphere and Ionosphere Model (SUPIM) is described in detail by *Bailey and Sellek (1990)*. In SUPIM, time-dependent equations of continuity and momentum for the molecular ions,  $N_2^+$ ,  $O_2^+$  and  $NO^+$ , and time-dependent equations of continuity, momentum and energy for the atomic ions,  $O^+$ ,  $H^+$  and  $He^+$ , and the electrons are solved along the axis of a closed magnetic flux tube from a base altitude in one hemisphere to the same altitude in the conjugate hemisphere. A centred axial dipole representation of the geomagnetic field is assumed. SUPIM outputs the concentration, temperature and field-aligned velocity for the electrons and each ion species at a discrete set of points along the magnetic field line. The model is an updated and enhanced version of that presented by *Bailey (1983)*. Enhancements to the earlier model were the inclusion of the equations of continuity and momentum for the  $He^+$ ,  $N_2^+$ ,  $O_2^+$  and  $NO^+$  ions, the zonal component of the  $\mathbf{E} \times \mathbf{B}$  drift velocity and frictional heating of the ions. Several of the atmospheric parameters were updated, the most important being improved estimates for the solar EUV fluxes and photo-ionisation cross-section, the inclusion of the MSIS-86 model thermosphere for temperature and concentrations of the neutral atmospheric constituents and the inclusion of the fully ionised 4-component plasma formulation for the ordinary and thermal diffusion coefficients.

SUPIM has recently been modified to take account of  $O^+$  temperature anisotropy relative to the geomagnetic field direction (*Moffett et al., 1993*). Account is taken of the partition of ion frictional heating into the  $O^+$  parallel and perpendicular distributions, using

values of the partition coefficient derived from the results given in table 2 of *Winkler et al. (1992)*. Ion-ion collisions, heat advection and conduction also enter naturally into the heat balance equations, without the need to adjust the frictional heating partition coefficients. Subsequent to the work documented in the present chapter, the model has been further modified to taken into account anisotropy of the  $\text{NO}^+$  population (*Jenkins et al., 1996a; 1996b*).

### 5.3.2 Modelling the interval of dayside ion frictional heating

Recently workers at the University of Sheffield have modelled the effects of large ion velocities on the nightside subauroral ionosphere, so called subauroral ion drift (SAID) events, using SUPIM (*Sellek et al., 1991; 1992; Moffett et al., 1991; 1992*). These studies also predict some of the ionospheric effects which are observed by EISCAT in the auroral zone during intervals of high ion flow, as pointed out by *Moffett et al. (1993)*. The interval of ion frictional heating observed by EISCAT in the afternoon sector of 03 April 1992 was modelled using SUPIM. The occurrence of elevated electron temperatures, in addition to the previously observed ionospheric response to large ion velocities, as occur on the nightside, makes this dayside interval particularly interesting to model.

For the present study all calculations were performed for the  $L = 6.3$  magnetic field line which intersects the Earth's surface near  $67^\circ$  latitude. For the model calculations  $F_{10.7}$  of  $160 \times 10^{-22} \text{ W m}^{-2} \text{ Hz}^{-1}$ ,  $A_p$  of 32 and a day number of 95 were chosen to represent solar and thermospheric conditions for 03 April 1992. The model was run at a temporal resolution of 5 minutes.

A base set of calculations was performed yielding data for a flux tube at local noon. Using these data as input an additional set of calculations was performed in which the flux tube was subjected to an imposed zonal  $\mathbf{ExB}$  drift with a signature simulating the zonal ion drift observed by EISCAT between 10:00 and 15:00 UT on 03 April. The field-orthogonal meridional ion velocity component remains comparatively low throughout this interval (see figure 1, panel b). Indeed, the maximum angle to the zonal made by the ion velocity vector barely exceeds  $10^\circ$ . Thus, the field-orthogonal ion velocity can be adequately modelled by considering solely its zonal component. Figure 5.3 illustrates the form of the zonal component of the  $\mathbf{ExB}$  drift input into the model at 278 km superposed upon the field-orthogonal zonal component of the ion velocity measured by EISCAT at the F-region intersection altitude of 278 km, in which negative velocities are those in the westward direction. In this and all successive figures, time series are presented as a function of elapsed time from 00:00 to 05:00 hours, where elapsed time is measured from the onset of applied  $\mathbf{ExB}$  drift to the modelled flux tube - 00:00 hours elapsed time corresponds to EISCAT observations at 10:00 UT. The variation with altitude of the  $\mathbf{ExB}$  drift applied to the flux tube reflects only the very small variation in the geomagnetic field strength. This is true to a very good approximation in the F-region, where the ion gyrofrequency greatly exceeds the ion-neutral collision frequency.

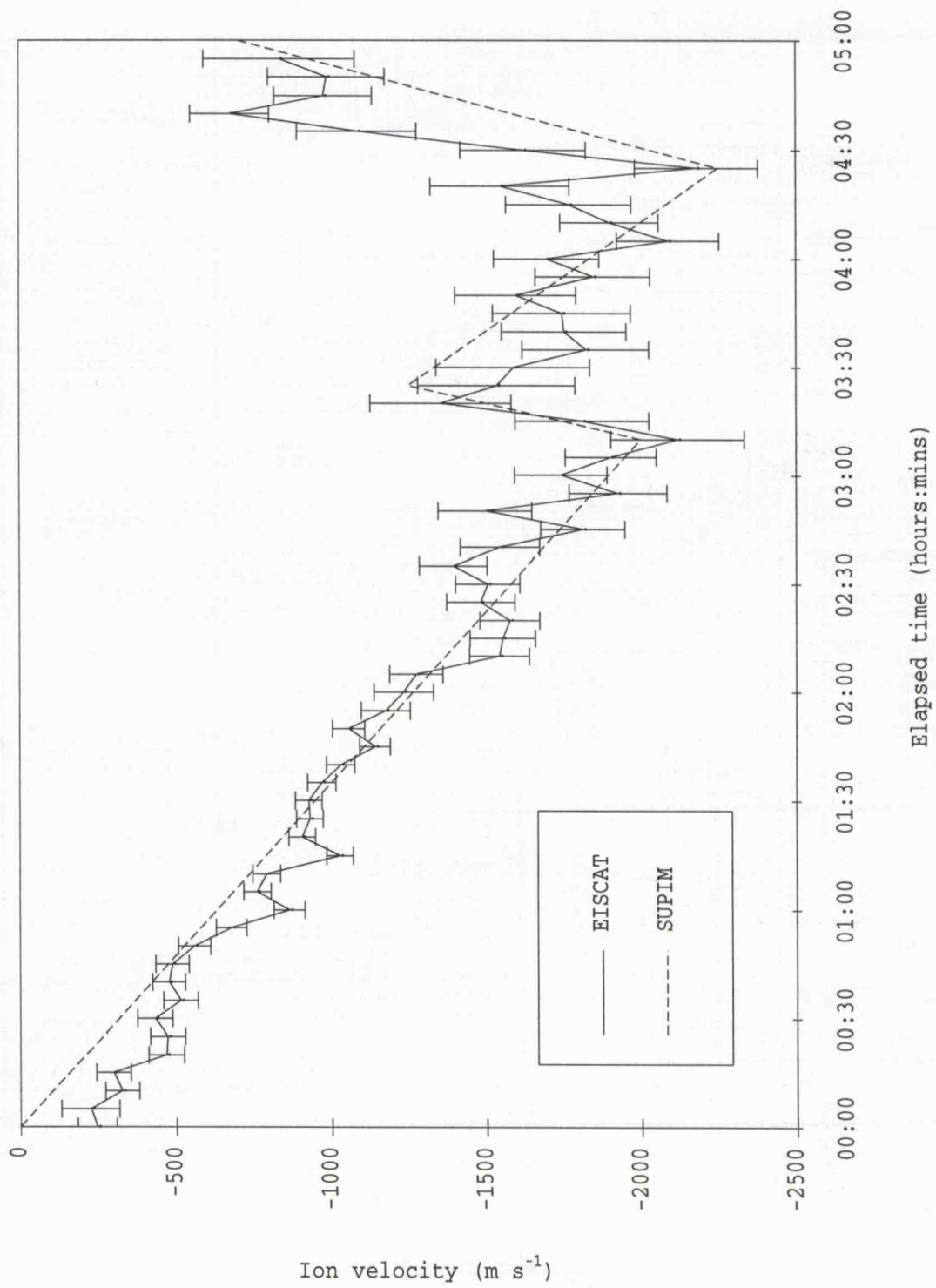


FIGURE 5.3: Observed and modelled zonal ion velocity component  
 Elapsed time of zero corresponds to 10:00 UT on 03/04/1992 in EISCAT data  
 Altitude: 278 km

The EISCAT ion temperature and field-aligned ion velocity measurements are compared to model results for  $O^+$ , although such a comparison is valid only over the altitude range for which  $O^+$  is the dominant ion species. During ion frictional heating the proportion of molecular ions in the F-region is enhanced, such that the altitude above which  $O^+$  dominates is increased. In the region where the ion composition is substantially modified the adoption of an invariant composition profile in EISCAT analysis results in underestimated ion and electron temperatures. Moreover, the single ion temperature derived would be a non-linear combination of  $O^+$  and molecular ion temperatures which diverge significantly in the presence of high ion-neutral relative flows, especially along the magnetic field direction where the molecular ion temperature can exceed that of  $O^+$  by several hundreds of Kelvin (*Lathuillère and Hubert, 1989*). At all altitudes above some 300 km it is assumed that throughout the interval of ion frictional heating  $O^+$  will remain the dominant ion species. This assumption is, in fact, consistent with model results presented later in the present chapter. The measured ion temperature, therefore, will approximate to the field-parallel  $O^+$  temperature. Above some 500 km, however, the EISCAT measurements become increasingly inaccurate due to a reduction in the signal-to-noise ratio.

The plasma packets observed over EISCAT will have experienced different past histories, depending on the convection pattern and production of ionisation. The EISCAT observations illustrate the behaviour of the ionosphere above the location of the radar but reveal little information about the more widespread spatial behaviour of the plasma or the time history of the observed plasma packets. The detailed inputs which determine the time history of flux tubes are poorly known. Large scale modelling relies on the adoption of a global convection pattern on which any comparison between observations and model results has been demonstrated to depend critically (*Quegan et al., 1988*). *Rasmussen et al. (1986)* employed simultaneous observations from both the Chatanika and Millstone Hill incoherent scatter radars to determine the input parameters for global modelling which still proved insufficient. The use of SUPIM as a single flux tube mode is, therefore, appropriate in the present context and, moreover, permits a higher temporal resolution that would be with practicable with a large scale model. However, it must be emphasised that the model calculations for a single flux tube of plasma are not aimed at performing a precise simulation of the EISCAT results. Conversely, the modelled plasma simply follows the zonal  $\mathbf{E} \times \mathbf{B}$  drift. No attempt is made to resolve the spatial and temporal behaviours of a parcel of plasma as it moves through the EISCAT field of view. Rather, the model results are used to support and elucidate the interpretations (made in section 5.2.2) of the observations of ion and electron temperatures; they also highlight the need to take account of ion temperature anisotropy and of acceleration of the neutral air due to relatively high dayside electron density and the extended nature of the interval of ion frictional heating. In view of these remarks, thermospheric conditions in the model were held at those for local noon.

### 5.3.3 Comparison of EISCAT observations with model results

For the reasons considered above, the comparison of the EISCAT measurements and the model results from SUPIM are principally confined to altitudes between 300 and 500 km. The fluctuations in the observations over short time scales, due to rapid variations in the field-orthogonal zonal ion velocity will not be reproduced in the model results, as the zonal component of the  $\mathbf{E} \times \mathbf{B}$  drift applied to the model is a smoothed function of the observed velocity. EISCAT Tromsø CP-1-J long pulse measurements of field-parallel ion temperature, field-parallel ion velocity, electron density and electron temperature at 300, 400 and 500 km altitude with model predictions for these parameters from SUPIM (in which the neutral wind has been set to zero) are illustrated in figures 5.4, 5.7, 5.8 and 5.9, respectively. Figure 5.5 presents the 3-dimensional, field-perpendicular and field-parallel  $O^+$  temperature output by the model at the above altitudes, and figure 5.10, the modelled ion composition. EISCAT measurements of ion temperature anisotropy can only be calculated at the intersection altitude of 278 km, and, together with model predictions of anisotropy at this altitude, are depicted in figure 5.6.

**Ion temperature** The lower, middle and upper panels of figure 5.4 illustrate time series of measured field-parallel ion temperature (solid line) with associated error and modelled field-parallel  $O^+$  temperature (dashed line) from 00:00 to 05:00 hours elapsed time at 300, 400 and 500 km altitude, respectively. The dotted line in this and successive figures, showing SUPIM results for a non-zero neutral wind, will be referred to in a later section. At 00:00 hours elapsed time, the modelled and measured field-parallel temperature at all altitudes under comparison differ by less than 200 K, with the measured temperatures exceeding those from the model. Both initial profiles show an increase in temperature with altitude. Until approximately one hour elapsed time the observed field-parallel ion temperature at all altitudes exceeds the modelled field-parallel  $O^+$  temperature. Thereafter, the modelled temperature remains consistently higher than that observed. The modelled field-parallel  $O^+$  temperature at all altitudes echoes the double peaked form of the zonal  $\mathbf{E} \times \mathbf{B}$  drift velocity imposed on SUPIM, attaining a maximum at 04:30 hours elapsed time. The observed temperature similarly exhibits a double peaked appearance, with the two maxima coinciding temporally with those yielded by the model, although, in contrast with the predicted behaviour, the maximum enhancement occurs in conjunction with the first peak in zonal velocity. Unlike the theoretical field-parallel  $O^+$  temperature predicted by the model, which steadily increases from 00:00 hours elapsed time, the observed ion temperature shows little or no enhancement above its unperturbed level at any altitude for the first 1.5 hours after the onset of elevated ion velocity. The enhancement in the observed field-parallel ion temperature above its unperturbed value increases with altitude between 300 and 500 km, in concurrence with the predicted behaviour, although the observations exhibit a more pronounced altitude dependence.

The predicted field-parallel temperature enhancement far exceeds that measured with EISCAT, the difference between the two becoming progressively larger as the interval

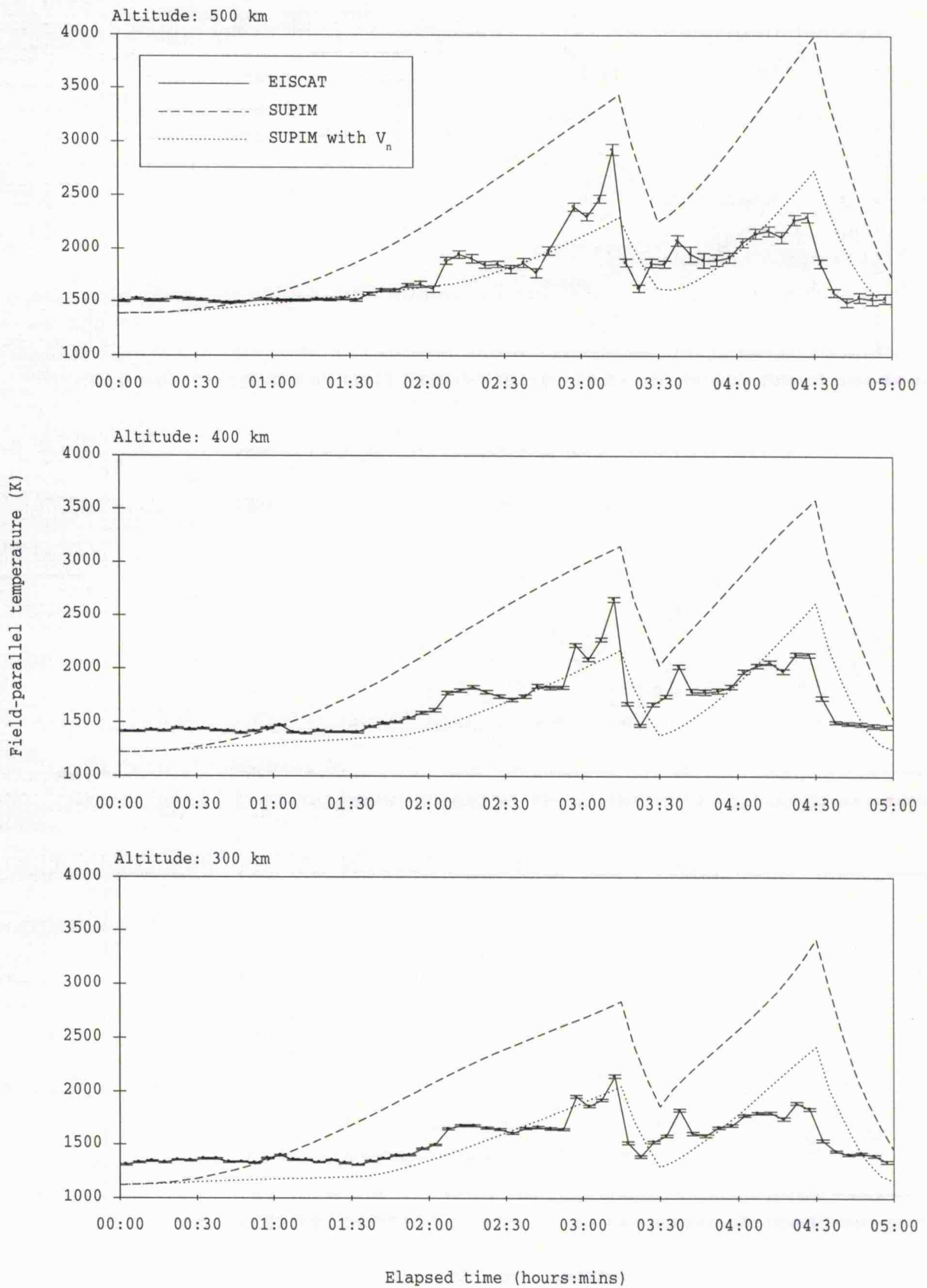


FIGURE 5.4: Observed and modelled field-parallel ion temperature

proceeds. The model predicts far more heating during the interval of enhanced zonal flow than is observed; for example, at an elapsed time of 03:15, the predicted enhancement in the field-parallel temperature above its ambient value at 400 km exceeds that observed by some 500 K, increasing to 1500 K at 04:30 hours. A possible mechanism to account for this discrepancy is detailed later.

Figure 5.5 presents time series of the 3-dimensional  $O^+$  temperature (solid line), field-parallel  $O^+$  temperature (dashed line) and field-perpendicular  $O^+$  temperature (dotted line) output by SUPIM from 00:00 to 05:00 hours elapsed time at 300, 400 and 500 km altitude. The  $O^+$  temperature output by SUPIM is initially isotropic, but with the onset of an  $\mathbf{E} \times \mathbf{B}$  drift the field-parallel and field-perpendicular  $O^+$  temperature diverge at all altitudes, the extent of anisotropy increasing with the  $\mathbf{E} \times \mathbf{B}$  drift velocity. The degree of anisotropy in the  $O^+$  temperature reduces with altitude, a consequence of stabilising effect of ion-ion and ion-electron collisions on the  $O^+$  thermal velocity distribution, as discussed by, for example, *McCrea et al. (1993)*.

The enhancement in the 3-dimensional ion temperature declines with altitude as a consequence of the decrease in frictional heating with altitude. This decrease in ion frictional heating with altitude is due to a combination of a decreasing mean neutral mass and increased heat loss by the processes of convection and advection. In contrast, however, to the behaviour of the 3-dimensional  $O^+$  temperature, the enhancement in the field-parallel  $O^+$  temperature increases with altitude within the altitude range 300 to 500 km, as noted also in the observations; this is a consequence of energy transfer due to ion-ion collisions between the field-perpendicular ion population and that parallel to the magnetic field.

The observed field-parallel, field-perpendicular and 3-dimensional ion temperatures, with associated error, at the intersection altitude of 278 km are presented as solid lines in figure 5.6 (see section 5.2.2 and panel b of figure 2). The model predictions of the parallel, perpendicular and 3-dimensional  $O^+$  temperature at this altitude are superposed (dashed lines). At this altitude, significant modification of the ion composition could occur such that a comparison between measurements and model results may be slightly misleading. A comparison of observed and predicted field-parallel ion temperatures at 278 km altitude is very similar to that discussed previously for 300 km, in that SUPIM severely overestimates the amount of heating of the ion population parallel to the magnetic field. The ion temperature at the F-region tristatic altitude would be more severely underestimated than at 300 km due to the shortcomings inherent in a constant composition profile analysis method and, in addition, its comparison with the  $O^+$  temperature would, of course, become less valid due to the increased proportion of molecular ions. The systematic difference in even quiet time ion temperatures measured at Sodankylä and Tromsø yields the apparent anisotropy in the observed ion temperature at elapsed time 00:00 hours, which is not predicted by the model. As with the comparison of field-parallel ion temperatures, the observed field-perpendicular ion temperature is initially higher than is predicted, but after an hour, the opposite becomes true and remains consistently so over the remainder of the

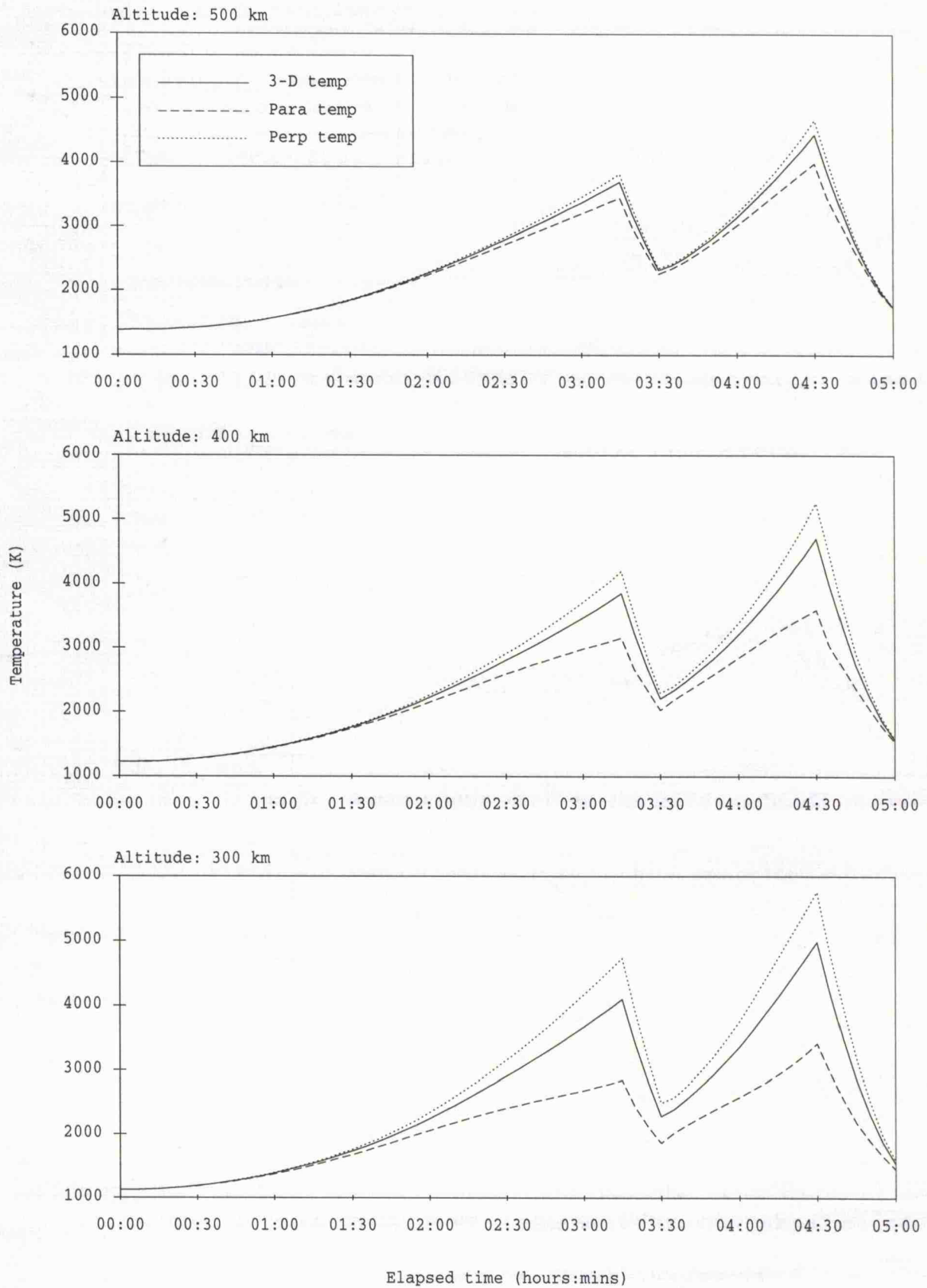


FIGURE 5.5: Modelled parallel, perpendicular and 3-D  $O^+$  temperature

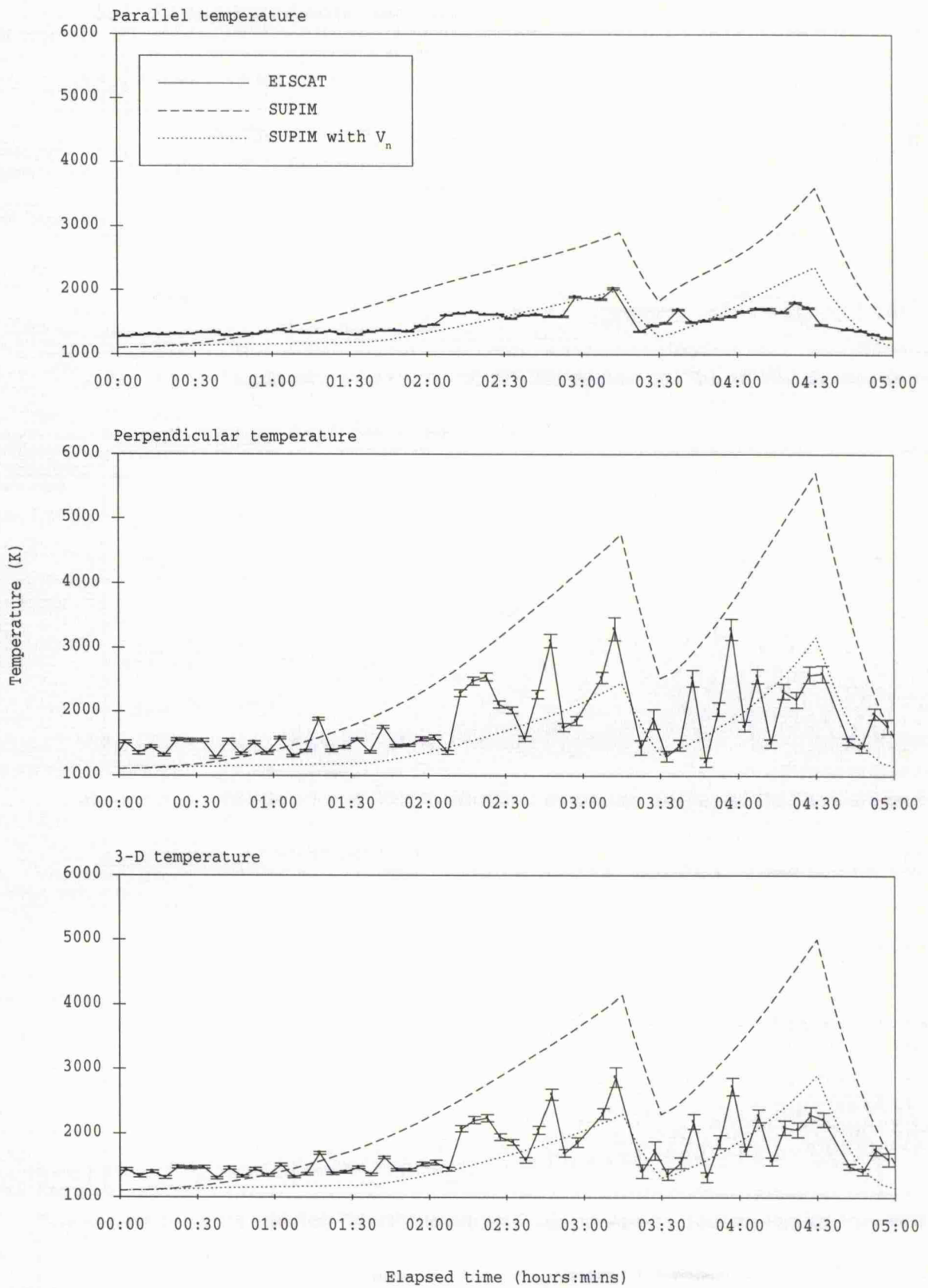


FIGURE 5.6: Observed and modelled parallel, perpendicular and 3-D ion temperature

Altitude: 278 km

interval. The observed field-perpendicular ion heating at 278 km, and the 3-dimensional ion temperature increase, is highly overestimated in the model results.

**Ion velocity** Time series of measured field-parallel ion velocity with associated error (solid line) and modelled field-parallel O<sup>+</sup> velocity (dashed line) at 300, 400 and 500 km altitude are presented in figure 5.7. In this figure positive velocities represent those down the field line. Initial ion velocities, both observed and predicted, are under 30 m s<sup>-1</sup> magnitude at all altitudes and are downwards at altitudes below some 410 km in the model results and 350 km in the observations. At 300 km altitude, both predicted and observed field-parallel ion velocities remain almost consistently downwards throughout the interval. The measured and modelled ion velocities at this altitude do, however, appear to be somewhat out of phase, with the predicted field-aligned O<sup>+</sup> velocity increasing in magnitude when the observed ion velocity reduces, and vice versa. The largest observed ion flows, some 150 m s<sup>-1</sup> down the field line at 03:30 elapsed time, are more than double those predicted, which are more or less constant at 50 m s<sup>-1</sup> after 02:00 hours elapsed time. At an altitude of 400 km, the initial predicted and observed field-parallel flows are oppositely directed, downwards and upwards respectively. The modelled field-parallel O<sup>+</sup> velocity remains downward or close to zero throughout the interval whereas ion upflows of some 50 m s<sup>-1</sup> magnitude are observed between 02:00 (coincident with the onset of substantial ion temperature enhancement) and 03:00 hours elapsed time. Downward ion flows approaching 200 m s<sup>-1</sup> at 03:30 hours elapsed time are observed at this altitude compared with predicted downwards velocities of no more than 40 m s<sup>-1</sup>. At 500 km altitude, both modelled and measured field-parallel ion velocities are initially upwards, although, after about 15 minutes, observations indicate downward ion velocities, consistent with those at lower altitudes. The observations illustrate large field-parallel ion upflows from around 02:00 hours elapsed time, followed by a temporary reversal to give return ion flow some one hour later. Although reversals in the direction of the modelled field-parallel O<sup>+</sup> velocity are apparent, these are somewhat out of phase with those observed, and, as at lower altitudes, the parallel flows observed are far greater in magnitude than those modelled. When the zonal ion velocity reduces towards the end of the interval, ion downflow is again apparent in both observations and model results.

Although the observations and model predictions of field-aligned ion velocity exhibit some similar general features, they are not particularly consistent, particularly in flow magnitude. This discrepancy could be due, at least in part, to the modification of field-aligned ion flow by the neutral wind, both ambient and caused by Joule expansion of the lower thermosphere, neither of which are considered in the model.

**Electron density** Figure 5.8 illustrates time series of measured electron density with associated error (solid line) and modelled electron density (dashed line). The discrepancy between the initial measured and modelled electron density profiles principally results from the displacement by some 100 km between the observed and model altitude of the F-region peak. The altitude of the observed F-region peak in electron density, around 370 km,

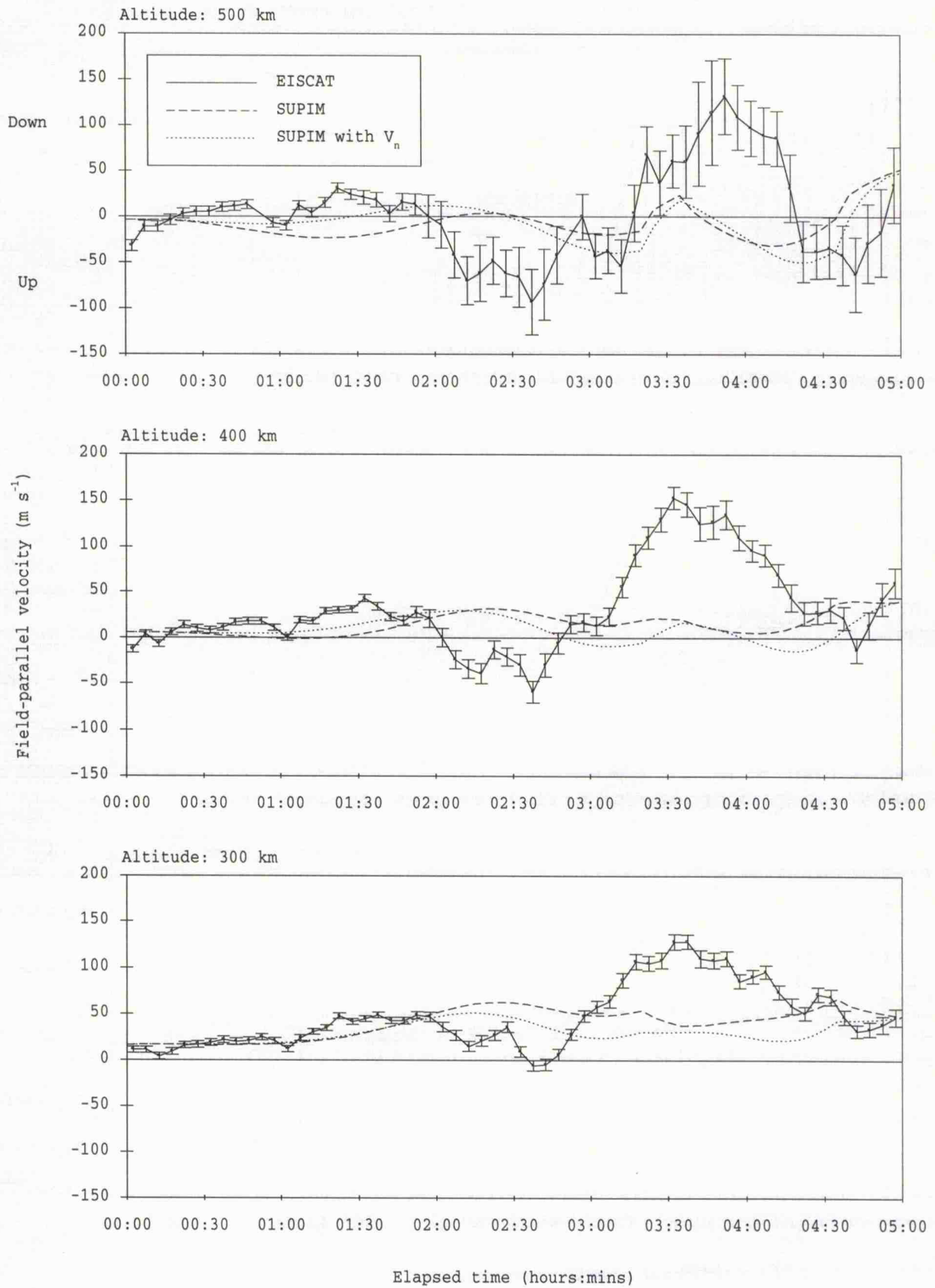


FIGURE 5.7: Observed and modelled field-parallel ion velocity

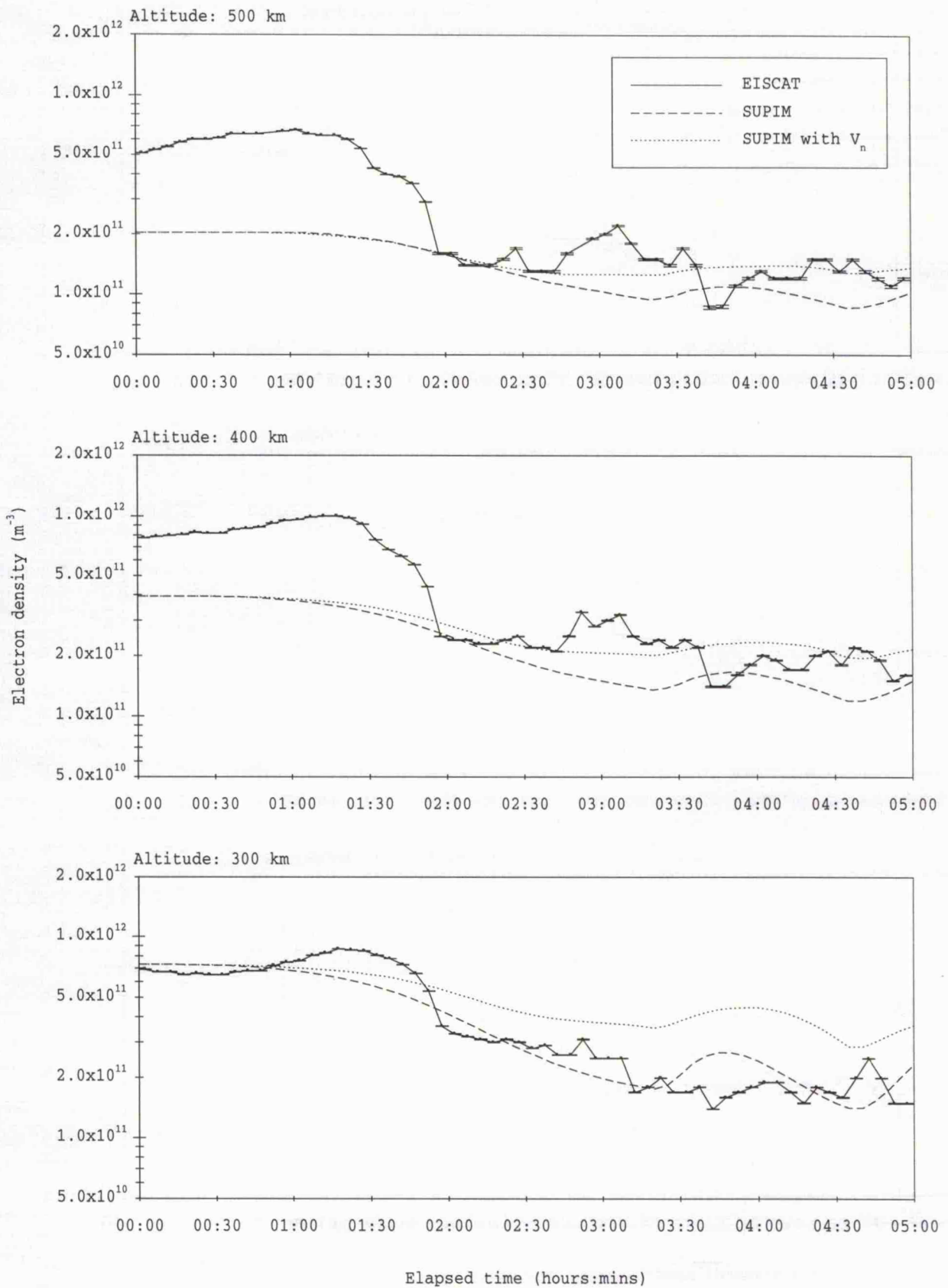


FIGURE 5.8: Observed and modelled electron density

exceeds that modelled although the peak electron densities are similar. This makes a quantitative comparison between the extent of the observed and predicted electron density depletion in response to enhanced plasma flow rather more difficult. This discrepancy between the observed and modelled peak electron height is tolerated in the comparison, since the observed rapid depletion in electron density in the early stages of the event may be a spatial rather than a temporal feature.

Both model results and observations show the depletion in the electron density which, for the reasons explained in the previous section, accompanies frictional heating. The predicted and observed electron concentrations responses exhibit the variation expected from study of their respective ion temperatures, the predicted electron density reducing smoothly from 00:00, the measured electron density depleting rapidly around 01:45 hours elapsed time although this latter feature may well be spatial rather than temporal. The increase in the modelled electron density at all heights, starting at 03:15 hours, corresponds to the central minimum in the imposed zonal  $\mathbf{ExB}$  drift.

**Electron temperature** Time series of electron temperature, both measured, with associated error, (solid line) and modelled (dashed line), are shown in figure 5.9 from 00:00 to 05:00 hours elapsed time at 300, 400 and 500 km altitude. The initial modelled electron temperature increases with altitude in this region whereas the observations illustrate a minimum in electron temperature around some 430 km altitude, resulting in a discrepancy between the initial measured and modelled electron temperature profiles, especially at 300 km. During conditions of medium and high solar activity, the electron temperature tends to minimise around the F-region peak. For the model data the altitude range from 300 to 500 km lies above the electron temperature minimum so that the initial temperature tends to increase with height whereas, in the observations, this altitude range straddles this minimum, accounting for the decrease and then increase in electron temperature with altitude. Thus, the difference in the modelled and observed initial electron temperature profiles is attributable to some degree to the difference between the initial predicted and observed electron density profiles.

The predicted and observed electron temperatures mirror the variation expected to result from the variation in the corresponding electron density, the predicted electron temperature increasing smoothly from 00:00, the measured electron temperature doing so rapidly at 01:30 hours elapsed time. The predicted elevation in electron temperature from its initial value, throughout the period of high ion drift, is greater than that observed for altitudes below about 400 km whereas, above that altitude, the reverse tends to be true. The feature of enhanced electron temperatures in the model results confirms the assertion that the observed electron temperature enhancement is not a consequence of auroral precipitation as this is not included in the model.

**Ion composition** Time series of the proportion of the total ion density constituted by  $\text{O}_2^+$ ,  $\text{O}^+$  and  $\text{NO}^+$  predicted by the model are presented as full, dashed and dotted lines respectively in figure 5.10. Between the altitudes of 300 and 500 km throughout the entire

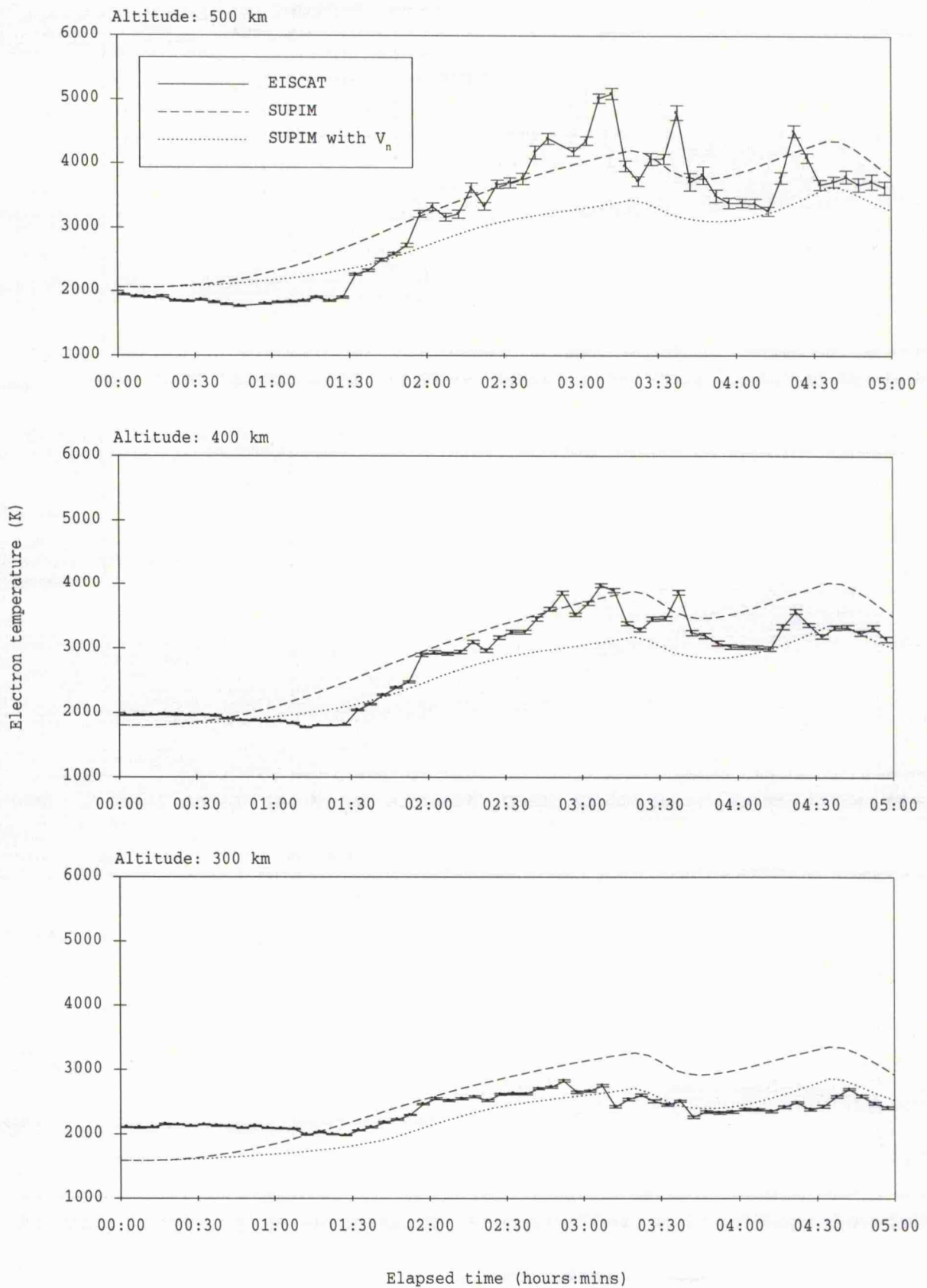


FIGURE 5.9: Observed and modelled electron temperature

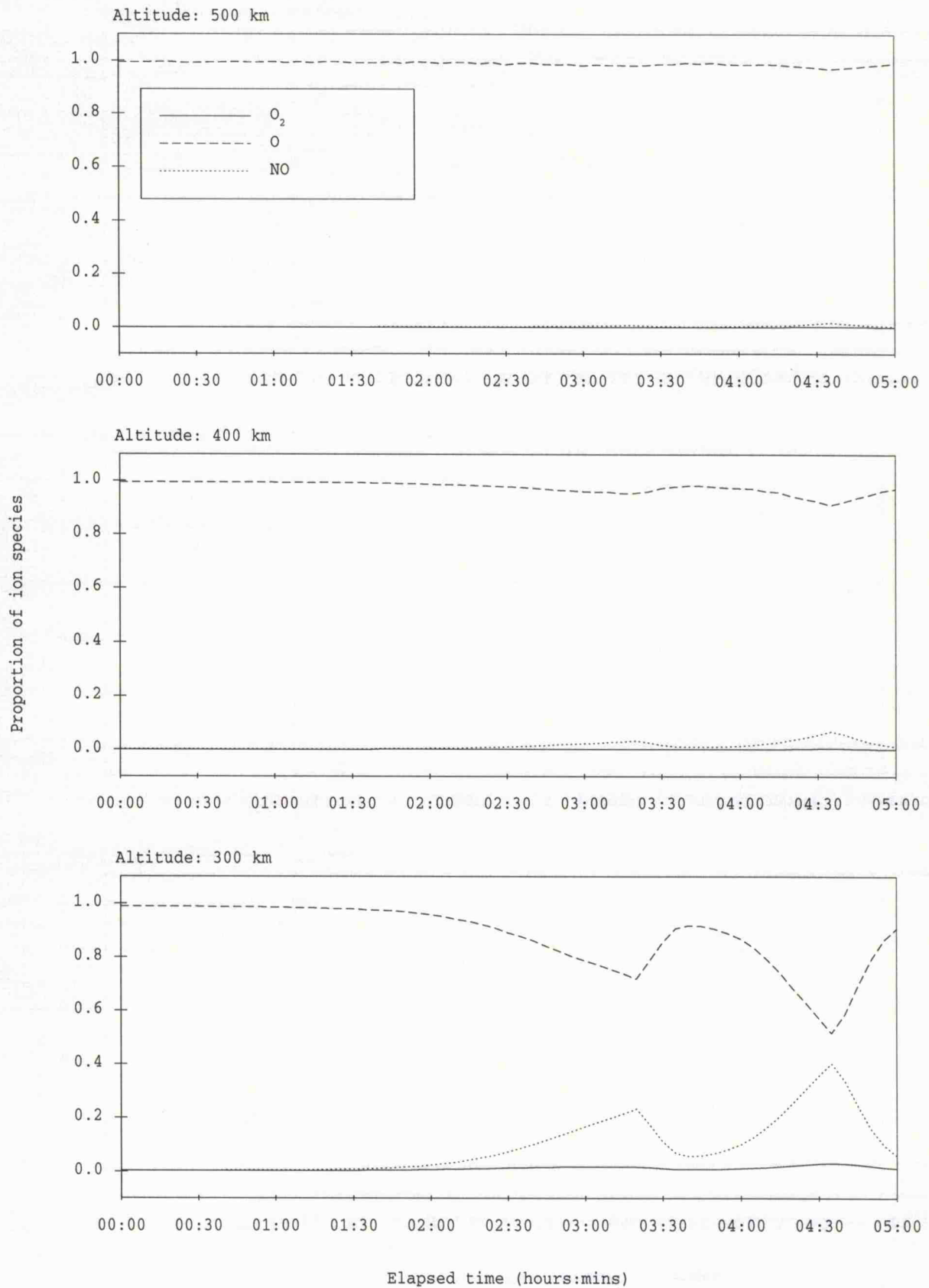


FIGURE 5.10: Modelled ion composition

interval, the three aforementioned ions comprise over 98% of the total modelled ion density with  $H^+$ ,  $He^+$  and  $N_2^+$  constituting the remainder. Over this altitude range 100%  $O^+$  is assumed in the ion composition model for EISCAT analysis. Between 300 and 500 km altitude,  $O^+$  is predicted to comprise over 99% of the initial ion density constituted by  $O_2^+$ ,  $O^+$  and  $NO^+$ . The proportion of molecular ions, particularly  $NO^+$ , increases at all altitudes with the imposition of a zonal  $E \times B$  signature, correlating with the predicted response of the ion temperature. The increase in the proportion of  $O_2^+$  and  $NO^+$  at higher altitudes occurs to a far lesser degree than at low altitudes, increasing to only 2% at 500 km altitude compared to nearly 40% at 300 km altitude at 04:30 hours elapsed time: at the intermediate height of 400 km, the maximum proportion of these molecular ions comprises less than 10%. At 278 km altitude, the proportion of molecular ions increases to almost half of the total ion population. If the actual ion composition was modified to such an extent, at 278 and 300 km altitude the ion and electron temperatures output by EISCAT analysis would be underestimated by a factor of roughly 1.5. Therefore, a comparison of observations and the model results for  $O^+$  at these altitudes would be severely compromised by the predicted presence of a significant proportion of molecular ions. This factor could account, at least partially, for the discrepancy between the observed ion temperatures and the modelled  $O^+$  temperatures at 278 and 300 km altitude but not at 400 or 500 km, where the increase in the proportion of molecular ions is negligible, up to a maximum of less than 10% of the total composition. Thus, there must be an additional factor necessary to explain the discrepancy between modelled and measured ion temperatures.

To summarise the initial model/observations comparison, the modelled  $O^+$  temperature enhancement both parallel and perpendicular to the field far exceeds the observed ion temperature enhancement, whereas the modelled electron density and electron temperature responses are in general agreement with those observed given the initial discrepancy in the electron density profiles. The observed field-parallel ion velocity is significantly underestimated in the predictions. One possible reason for the overestimate in predicted ion heating is that the neutral wind term in the modelling is set to zero. Over prolonged intervals of ion frictional heating, the neutral wind may become significant due to ion drag (see chapter 2, section 3.3), particularly on the dayside where the plasma density, even though highly depleted, tends to remain higher than on the nightside. The acceleration of the neutral wind tends to suppress frictional heating, and does so particularly at lower altitudes (see later) which would account for the larger gradient in the observed ion temperature enhancement with altitude than is predicted. Neglecting the neutral wind in the model would also account for the difference between the predicted and observed field-parallel ion temperature enhancement tending to increase with elapsed time because the neutral velocity progressively approaches that of the ions.

#### 5.3.4 Inclusion of a calculated neutral wind in SUPIM

A simplified momentum equation for the neutral gas, neglecting horizontal viscosity,

is given by equation 2.16 (e.g. *Baron and Wand, 1983*). The Sheffield University plasmasphere and ionosphere model was amended to include a calculated field-orthogonal zonal component of neutral wind generated using equation 2.16, although neglecting the terms describing the Coriolis force and pressure gradients. Initially the neutral atmosphere was assumed to be stationary. Observations from ground-based and satellite Fabry-Perot interferometers indicate neutral wind velocities up to several hundred  $\text{m s}^{-1}$  but rarely exceeding  $1000 \text{ m s}^{-1}$  (*D. Rees, private communication*). Theoretical work (*Fuller-Rowell, 1985; Walterscheid and Lyons, 1989; 1992*) has shown that, under conditions of strong convective forcing, parcels of neutral air tend to escape from strong zonal forcing by also moving meridionally: thus the acquired zonal neutral wind velocity is limited. Consequently, in the investigation of the effect of the neutral wind, the zonal neutral velocity was constrained to a maximum of  $700 \text{ m s}^{-1}$ . Further analysis documented in chapter 6 indicate that, during this interval, the zonal neutral wind at F-region altitudes does appear to be constrained to values around  $700 \text{ m s}^{-1}$ , although perhaps the best justification for applying this limit comes from the success it has in modelling the ion temperature.

Figure 5.11 illustrates time series of calculated field-orthogonal zonal neutral wind from 00:00 to 05:00 hours elapsed time at 300 (solid line), 400 (dashed line) and 500 km (dotted line). Negative velocities are those in the westward direction. The upper limit for the zonal neutral drift speed of  $700 \text{ m s}^{-1}$  is attained between approximately 01:40 to 02:20 hours elapsed time depending on altitude. The neutral wind is, consequently, constrained to this limit over much of the 5 hours interval.

### 5.3.5 Comparison of EISCAT observations with results of the amended model

Time series of the modelled field-parallel  $\text{O}^+$  temperature, field-parallel  $\text{O}^+$  velocity, electron temperature and electron density with SUPIM including a non-zero zonal component of neutral wind at 300, 400 and 500 km altitude are illustrated in dotted lines in figures 5.4, 5.7 and 5.8 and 5.9, respectively, in addition to the EISCAT long pulse observations (solid line) and model results from SUPIM with a neutral wind set at zero (dashed line) of those plasma parameters. Figure 5.12 and figure 5.13 present predicted  $\text{O}^+$  temperature anisotropy and ion composition results at the above altitudes, equivalent to those in figures 5.5 and 5.10, from the model with the inclusion of a non-zero zonal neutral wind component. Figure 5.6 presents modelled  $\text{O}^+$  temperature anisotropy at 278 km altitude again both with (dotted line) and without (dashed line) an included neutral wind, and EISCAT observations of ion temperature anisotropy at this altitude. All figures range from 00:00 to 05:00 hours elapsed time.

**Ion temperature** From figure 5.4 it is evident that the inclusion of a calculated field-orthogonal component of zonal neutral wind in SUPIM results in a decrease in the predicted enhancement in field-parallel  $\text{O}^+$  temperature at all altitudes throughout the duration of imposed drift. The modelled field-parallel  $\text{O}^+$  temperature demonstrates a far better

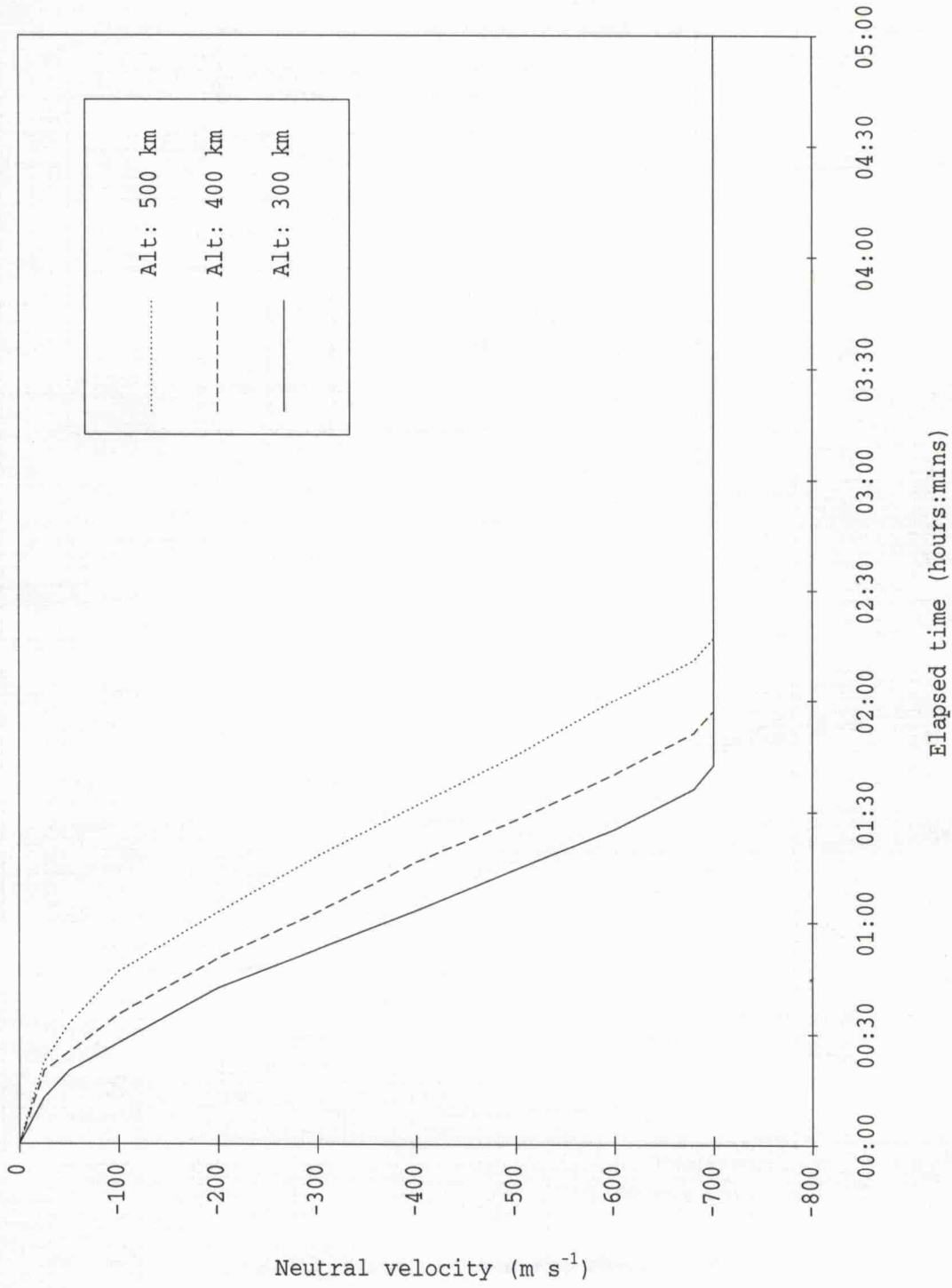


FIGURE 5.11: Calculated zonal neutral wind component

agreement with the observations of field-parallel ion temperature than is predicted from the model run in which no neutral wind is included. The field-parallel ion temperature enhancement is slightly underestimated by the predictions at 400 and 500 km altitude, until an elapsed time of 04:00 hours, after which the model field-parallel O<sup>+</sup> temperature enhancement exceeds that observed. At 300 km altitude, however, the enhancement in the modelled temperature above its initial value remains almost consistently higher than that observed. The overestimate in the predicted field-parallel temperature enhancement, particularly after 04:00 hour elapsed time, implies that the zonal component of the neutral wind may actually attain higher values than the quoted limit of 700 m s<sup>-1</sup>.

The modelled 3-dimensional, field-parallel and field-perpendicular O<sup>+</sup> temperatures in figure 5.12 from SUPIM with included zonal neutral wind at 300, 400 and 500 km altitude are compared to those in figure 5.5 for SUPIM with a neutral wind set at zero. The O<sup>+</sup> temperature departs from isotropy in both cases, although the extent of this departure is reduced at all altitudes in the case where the neutral wind has been included. The inclusion of a field-orthogonal zonal neutral wind component reduces the ion-neutral relative velocity, on which the degree of anisotropy depends. The degree of anisotropy is thus reduced preferentially at lower altitudes where the zonal component of the neutral wind is larger, until around 02:30 hour elapsed time.

The predictions of O<sup>+</sup> temperature anisotropy at 278 km altitude from the model with an included zonal component of neutral wind are illustrated in figure 5.6 (dotted line). These results are, in general, in better agreement with the observations of anisotropic ion temperatures at this altitude than those from the model with no neutral wind (dashed line).

**Ion velocity** A comparison between the observed field-parallel ion velocity and the modelled field-parallel O<sup>+</sup> velocity is not improved by the introduction of a zonal neutral wind into the SUPIM calculations (see figure 5.7). The predicted flow magnitude, already an underestimate of that observed, is further reduced at low altitudes, although at 500 km the introduction of a zonal neutral wind tends to enhance field-aligned O<sup>+</sup> flows. Although the field-perpendicular zonal component of the neutral wind is included in the model, the meridional neutral wind, which is not considered, will have a large effect on the behaviour of field-aligned plasma flow. A northward meridional neutral wind of some 600 m s<sup>-1</sup> could force downward field-aligned flows of the order of the maximum observed values. Indeed, the justification for limiting the zonal component of the neutral wind to a maximum of 700 m s<sup>-1</sup> is that its meridional component will become enhanced under such strong convective forcing.

**Electron density** The effect of a zonal neutral wind on the modelled electron density, as seen from figure 5.8 is to reduce the predicted depletion in electron concentration at all altitudes throughout the interval of imposed  $\mathbf{E} \times \mathbf{B}$  drift. The inclusion of a neutral wind appears to degrade the model/measurement comparison slightly, particularly at lower altitudes, although the difference between the initial electron density profiles makes the comparison of measured and modelled electron density less applicable.

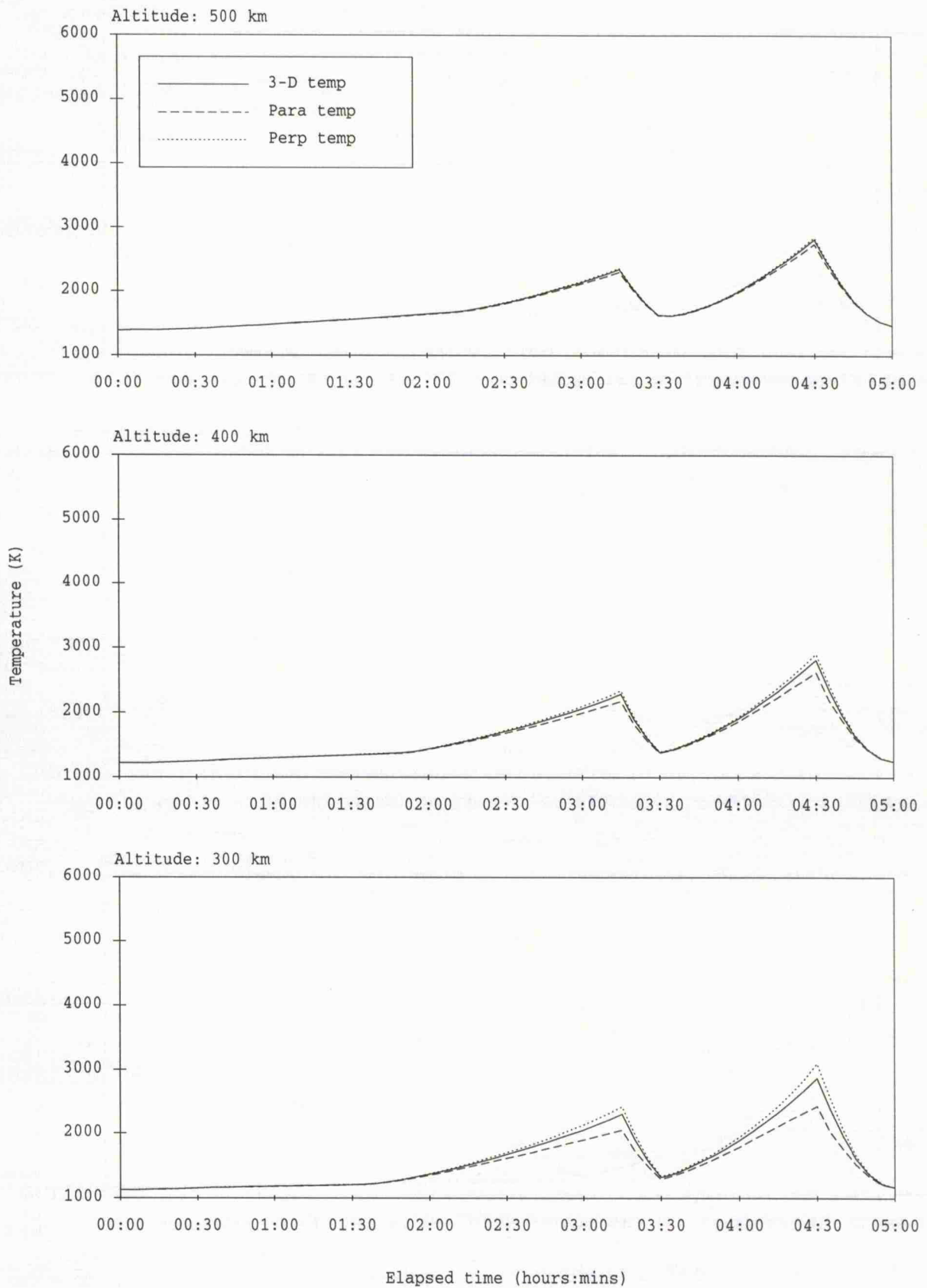


FIGURE 5.12: Modelled parallel, perpendicular and 3-D  $O^+$  temperature  
 SUPIM with  $V_n$

**Electron temperature** Time series of modelled electron temperature, with SUPIM including neutral wind, are presented in figure 5.9. The inclusion of the calculated zonal component of the neutral wind reduces the enhancement in the modelled electron temperature at all altitudes and at all elapsed times compared to that computed without neutral dynamics. Again, the difference in the initial height profile of electron temperature makes a comparison somewhat difficult, but at 300 km altitude the inclusion of a neutral wind serves to reduce the predicted electron temperature enhancement such that it becomes closer to what is observed. At the higher altitudes, however, its inclusion causes the predicted electron temperature enhancement to be less than that measured.

**Ion composition** Predictions of ion composition from SUPIM with the inclusion of a zonal neutral wind (figure 5.13) are compared to those without (figure 5.10). With the introduction of a zonal component of the neutral wind, the enhancement in the proportion of the molecular ions,  $\text{NO}^+$  and  $\text{O}_2^+$  is greatly reduced at all altitudes under consideration. This is most apparent at 300 km altitude where the percentage of these molecular ions increases to only 5% of the ion population compared to nearly 40% with no neutral wind. If this is indeed the case, then EISCAT measurements of ion and electron temperature at this altitude would be only marginally underestimated by considering an ionosphere of solely  $\text{O}^+$  and, furthermore, the comparison of observations and modelled parameters for  $\text{O}^+$  would remain valid to a great degree. Indeed, even at 278 km altitude, the tristatic F-region altitude, the percentage of molecular ions increases to less than 15% with the inclusion of a neutral wind into the model (not illustrated).

In summary, the inclusion of a non-zero neutral wind in SUPIM reduces the  $\text{O}^+$  temperature to values much closer to the ion temperatures observed by EISCAT and also increases confidence in the comparison, especially at the lower altitudes under study. At the same time the comparison of the other parameters is not severely affected.

#### 5.4 Summary and conclusions

A prolonged interval of intense F-region ion frictional heating was observed by EISCAT in the post noon sector of 03 April 1992, correlating with an enhanced field-orthogonal westward component of the ion velocity. The interval was atypical of frictional heating both in its extended duration and the local time of its occurrence. In addition to the typical consequences of ion frictional heating - anisotropic ion temperatures, large field-aligned flows and electron density reduction - an enhancement in the F-region electron temperature was observed. This enhancement resulted from solar illumination of the depleted electron population.

EISCAT observations for this period were compared to predictions from SUPIM in which the neutral wind was set to zero. Although both exhibited similar general trends in field-parallel ion temperature, field-parallel ion velocity, electron density and electron temperature, the extent of the observed ion heating was substantially overestimated in the model results. It was proposed that the omission of a neutral wind from the model, which,

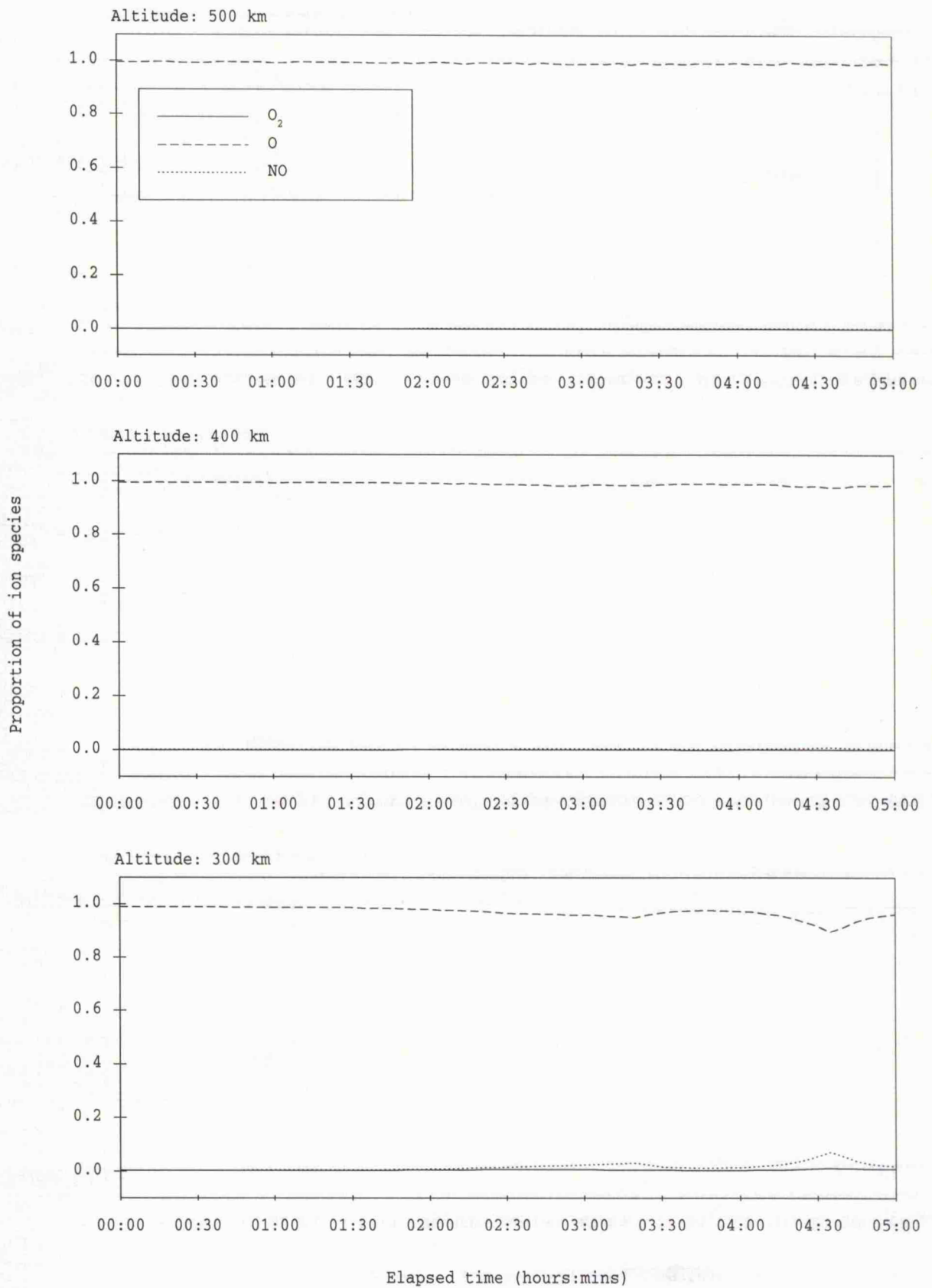


FIGURE 5.13: Modelled ion composition

SUPIM with  $V_n$

for such a prolonged interval of high ion velocity on the dayside, would be greatly enhanced as a consequence of ion drag, may contribute to the discrepancy. The adaptation of SUPIM to include a calculated field-orthogonal zonal component of neutral wind reduced the modelled field-parallel ion temperatures nearer to those values observed, thereby confirming the importance of neutral dynamics in determining the extent of ion frictional heating. Indeed, the ability to include the effects of a calculated non-zero neutral wind makes the model much more effective when seeking to understand the behaviour of the Earth's ionosphere during intervals of ion frictional heating.

## Chapter 6

### E-region ion-neutral coupling during intervals of enhanced electric field

#### 6.1 Introduction

A prolonged run of the EISCAT UHF common programme CP-1-J commenced at 16:00 UT on 30 March 1992 and continued until 16:00 UT on 03 April 1992. The CP-1-J observations revealed an extended interval, post local geomagnetic noon on 03 April 1992, during which the F-region ion velocity orthogonal to the geomagnetic field was significantly enhanced, to values exceeding  $2 \text{ km s}^{-1}$  corresponding to a perpendicular electric field of some  $100 \text{ mV m}^{-1}$ . The response of the ionospheric F-region to this prolonged interval of enhanced ion drift is discussed in some detail in the previous chapter as is, moreover, a comparison of the parameters measured by EISCAT CP-1-J during this interval with results from SUPIM - the Sheffield University plasmasphere and ionosphere model. In the present chapter, however, observations from the post magnetic noon sector of 03 April 1992 are used to illustrate a method by which estimates of the E-region ion-neutral collision frequency may be derived during such intervals of enhanced perpendicular electric field.

From both the rotation of the ion velocity vector and the reduction in the ion velocity magnitude with respect to that in the ionospheric F-region during the interval of enhanced electric field, independent estimates of the ratio of the ion-neutral collision frequency to the ion gyrofrequency, the so-called normalised ion-neutral collision frequency, are made at the CP-1-J E-region tristatic altitudes. Initial calculations assume that, at E-region altitudes, the neutral atmosphere remains stationary. Furthermore, from the ion velocity measurements, the extent of frictional heating of the ion population at both the F-region and E-region tristatic altitudes is predicted from a solution of the simplified ion energy balance equation. The difference between the predicted and observed enhancements in field-parallel ion temperature is attributed to thermospheric motion and, hence, used to derive first order estimates of the neutral wind. The E-region estimates of the neutral wind are subsequently employed to calculate revised estimates of the normalised ion-neutral collision frequency whereas the neutral wind derived in the F-region is compared to modelled values presented in the previous chapter.

#### 6.2 A new method for the estimation of the normalised ion-neutral collision frequency during intervals of enhanced electric field

Various authors have attempted to derive estimates of the ion-neutral collision frequency from observations by incoherent scatter radar. Many, including *Wand and Perkins (1968)*, *Salah et al. (1975)*, *Wand (1976)*, *Wickwar et al. (1981)*, *Lathuillère et al. (1983b)*, *Flå et al. (1985)* and *Huuskonen et al. (1986)*, retrieved the collision frequency directly from the returned signal through a spectral fitting technique, or equivalently from the ACF. The influence of frequent ion-neutral collisions at E-region altitudes on the

incoherent scatter spectrum (*e.g. Hagfors and Brokelman, 1971*) is discussed in section 2.2 of chapter 3 and is, moreover, illustrated in figure 8 of that chapter. Generally, in fitting for the collision frequency, the ion and electron temperatures are assumed equal, thus restricting fitting of this type to altitudes below some 110 km and low electric field values, although *Schlegel et al. (1980)* successfully managed to fit simultaneously for ion temperature, electron temperature and ion-neutral collision frequency from incoherent scatter observations by the Chatanika radar.

An alternative method of determining the ion-neutral collision frequency from incoherent scatter observations was adopted by *Nygrén et al. (1987)*, although a similar method had previously been proposed by *Kohl et al. (1985)*. *Huuskonen et al. (1984)* and *Nygrén et al. (1984)* present expressions describing the relationship between the vertical ion velocity for various orientations of the ionospheric electric field. From these relationships, *Nygrén et al. (1987)* estimated the ion-neutral collision frequency from EISCAT observations to altitudes approaching 140 km. For the altitude range over which the ion-neutral collision frequency could be determined from the conventional fitting technique, both methods produced comparable values which agreed in general with estimates based on the CIRA (1972) reference model atmosphere. In their method for the determination of the ion-neutral collision frequency, *Nygrén et al. (1987)* assumed that the neutral wind at E-region altitudes was negligible although the authors did suggest an approach by which their method could be adapted to account for motion of the neutral atmosphere.

In the present chapter, a further method for calculating the ion-neutral collision frequency at E-region altitudes from the ion velocity is established; indeed this technique permits the derivation of two independent estimates of the collision frequency. The theoretical foundation of this method is outlined below.

An expression describing the ion drift in the frame of reference of the neutral atmosphere resulting from an externally imposed perpendicular electric field,  $\mathbf{E}$ , is given by equation 2 of chapter 3. As this relationship, a solution of the simplified ion momentum equation, provides the basis of the present work it is reiterated below.

$$\mathbf{v}_i - \mathbf{v}_n = \frac{1}{1 + (\mathbf{v}_{in}/\Omega_i)^2} \left[ \frac{\mathbf{E}_{eff} \times \mathbf{B}}{B^2} + \frac{\mathbf{v}_{in} \cdot \mathbf{E}_{eff}}{\Omega_i B} \right] \quad (6.1)$$

The effective electric field  $\mathbf{E}_{eff}$ , the electric field in the frame of reference of the thermosphere, is related to the applied electric field  $\mathbf{E}$  via the following expression

$$\mathbf{E}_{eff} = \mathbf{E} + \mathbf{v}_n \times \mathbf{B} \quad (6.2)$$

All other parameters have been defined in previous chapters. In such a simplification, relative ion-neutral motion is restricted to the plane perpendicular to the geomagnetic field, implying an absence of effects driving field-aligned ion flow such as parallel electric fields. The effective electric field will vary with altitude, in response to any corresponding variation

in the neutral wind.

An increase in the ratio of the ion-neutral collision frequency to the ion gyrofrequency, also termed the normalised ion-neutral collision frequency (*Nygrén et al., 1987*), characteristic of decreasing altitude, will result in the progressive rotation of the ion-neutral relative velocity vector in the field-perpendicular plane from the  $\mathbf{E}_{\text{eff}} \times \mathbf{B}$  direction towards the direction of the effective electric field  $\mathbf{E}_{\text{eff}}$ . Furthermore, a reduction in the magnitude of the relative ion-neutral velocity is also predicted with increasing normalised ion-neutral collision frequency. With increasing ion-neutral collision frequency, the ion velocity tends towards the neutral velocity such that in the lower E-region the ion population is collisionally constrained to move with the neutral atmosphere. In the F-region, where ion-neutral collisions are infrequent, the ionospheric plasma is constrained to move only along the magnetic field direction in the absence of an applied perpendicular electric field. In the presence of such a field, however, the F-region ions move, in the frame of reference of the geomagnetic field, approximately with the  $\mathbf{E} \times \mathbf{B}$  in the field-perpendicular direction such that

$$\mathbf{v}_i = \frac{\mathbf{E} \times \mathbf{B}}{B^2} \quad (6.3)$$

It follows from equation 6.1 that it is theoretically possible to determine the normalised ion-neutral collision frequency, at an altitude in the E-region where collisions have a significant effect on ion dynamics, independently from both the rotation of the differential ion-neutral velocity vector in the plane perpendicular to the magnetic field from the  $\mathbf{E}_{\text{eff}} \times \mathbf{B}$  direction at that altitude and from the reduction in the magnitude of the field-perpendicular ion-neutral relative velocity from that of  $\mathbf{E}_{\text{eff}} \times \mathbf{B}$ .

The normalised ion-neutral collision frequency at a given altitude can be derived from the angle of rotation of the direction of relative ion-neutral flow at that altitude from the  $\mathbf{E}_{\text{eff}} \times \mathbf{B}$  direction at that altitude using the simple relationship stated below, where  $\Phi$  represents the angle of each vector from a reference direction in the field-perpendicular plane.

$$\frac{V_{\text{in}}}{\Omega_i} = \tan(\Phi[\mathbf{E}_{\text{eff}} \times \mathbf{B}] - \Phi[\mathbf{v}_i - \mathbf{v}_n]) \quad (6.4)$$

Moreover, the normalised ion-neutral collision frequency at a particular altitude can be calculated from the reduction in the magnitude of the ion-neutral relative velocity from that of  $\mathbf{E}_{\text{eff}} \times \mathbf{B}$ , the latter of which is expressed by the ratio  $E_{\text{eff}}/B$ , via the expression

$$\left(\frac{V_{\text{in}}}{\Omega_i}\right)^2 = \left(\frac{(E_{\text{eff}}/B)^2}{|\mathbf{v}_i - \mathbf{v}_n|^2}\right) - 1 \quad (6.5)$$

If the neutral wind can be regarded as negligible at the altitudes where the ion-neutral

collision frequency is to be determined, equation 6.1 can be simplified thus

$$\mathbf{v}_i = \frac{1}{1 + (\nu_{in}/\Omega_i)^2} \left[ \frac{\mathbf{E} \times \mathbf{B}}{B^2} + \frac{\nu_{in}}{\Omega_i} \frac{\mathbf{E}}{B} \right] \quad (6.6)$$

If the neutral atmosphere is considered stationary, it is therefore possible to determine the normalised ion-neutral collision frequency at any given altitude in the E-region from both the rotation of the ion velocity vector from the  $\mathbf{E} \times \mathbf{B}$  direction at that altitude and from the reduction in the magnitude of the ion velocity from that of  $\mathbf{E} \times \mathbf{B}$ , the latter of which is expressed by the ratio  $E/B$ . Under this simplifying assumption, the solutions of equation 6.1, in terms of the normalised ion-neutral collision frequency, can be written in the form of expressions 6.7 and 6.8 below.

$$\frac{\nu_{in}}{\Omega_i} = \tan(\Phi[\mathbf{E} \times \mathbf{B}] - \Phi[\mathbf{v}_i]) \quad (6.7)$$

$$\left( \frac{\nu_{in}}{\Omega_i} \right)^2 = \left( \frac{(E/B)^2}{\nu_i^2} \right) - 1 \quad (6.8)$$

As mentioned previously, in the F-region, where ion-neutral collisions are infrequent, the ions move approximately with the  $\mathbf{E} \times \mathbf{B}$  drift. Thus, providing the geomagnetic field  $\mathbf{B}$  can be assumed invariant with altitude between the E-region and the F-region, the F-region ion velocity can be employed in equations 6.7 and 6.8 to determine the normalised ion-neutral collision frequency: this assumption is further discussed in section 3.3 of the present chapter. If the neutral atmosphere is assumed stationary, equation 6.7 can, therefore, be used to determine the normalised ion-neutral collision frequency at an altitude where ion-neutral collisions are significant from the rotation of the field-perpendicular ion velocity,  $\mathbf{v}_i$ , at that altitude from the direction of the F-region ion flow, the latter representative of  $\mathbf{E} \times \mathbf{B}$ . Moreover, equation 6.8 can be used to determine the normalised ion-neutral collision frequency from the reduction in the magnitude of the ion velocity from that in the F-region.

As previously noted, *Nygrén et al. (1987)* assumed that the neutral wind at E-region altitudes was negligible in their method for the determination of the ion-neutral collision frequency although the authors did propose an approach by which their method could be amended to account for neutral motion given an estimate of the horizontal component of the neutral wind.

In order to calculate the ratio of the ion-neutral collision frequency to the ion gyrofrequency at a given altitude in the E-region via the above method, it is necessary to have measurements of the field-perpendicular ion vector velocity at that altitude and a corresponding measurement of the F-region drift, preferably on the same field line so that no assumptions about the spatial extent of variations in the electric field are necessary. Several versions of the field-aligned EISCAT UHF common programme 1, including CP-1-

I and CP-1-J, make both E-region and F-region tristatic common volume measurements and would therefore be appropriate for such a study. Additionally, this technique, similar to that of Nygrén *et al.* (1987), relies on the presence of enhanced ionospheric electric fields. Consequently, the extended interval of CP-1-J in the post-noon sector of 3 April 1992 during which the perpendicular ion velocity magnitude is enhanced to values approaching  $2.5 \text{ km s}^{-1}$  has been selected as a suitable data set on which to perform such a study. In fact, as demonstrated later in this chapter, these data particularly highlight the need to account for the neutral wind in the calculation of the ion-neutral collision frequency by this method.

### **6.3 Derivation of the normalised ion-neutral collision frequency from EISCAT CP-1-J observations**

#### **6.3.1 Experimental arrangement**

The experimental arrangement and transmission schemes of version J of the EISCAT UHF common programme CP-1, CP-1-J, are reviewed in detail in section 2.1 of the chapter 5. In addition to the F-region tristatic intersection volume, centred around an altitude of 278 km, the remote site receiver beams intersect the transmitter beam at 6 altitudes in the E-region: 91, 96, 101, 109, 117 and 125 km. Observations from each of the E-region tristatic positions are available every 10 minutes and from the F-region common intersection volume, every 5 minutes, with the dwell time of the remote site receivers in each position being approximately 60 seconds.

#### **6.3.2 EISCAT CP-1-J observations of E- and F-region ion velocity**

The observing geometry of the CP-1-J experiment enables the vector ion velocity to be determined at six E-region altitudes in addition to the F-region altitude of 278 km, by combining the ion velocity measurements at those altitudes from each receiver site. Figure 6.1 illustrates both the field-perpendicular zonal (full line, positive eastward) and field-perpendicular meridional (dotted line, positive northward) components of the vector ion velocity, with associated errors, at 278, 125, 117 and 109 km altitude between 10:00 and 15:00 UT on 03 April 1992. The quoted errors include uncertainties due to the analysis and the random error (*du Castel and Vasseur, 1972*). Ion velocity components are presented only where the signal-to-noise measurement at each of the three UHF receiver sites employed in their calculation exceeds a threshold of 2%. Measurements of the field-orthogonal ion velocity from the three lower E-region tristatic altitudes, 91, 96 and 101 km, are not presented as many of the incoherent scatter signals returned from those altitudes were not sufficiently well determined for analysis and many of those from which an ion velocity estimate could be derived were of low signal-to-noise ratio: a consequence of the low electron density at these altitudes. The ion velocity components calculated at 278 km altitude were derived from long pulse transmission. At the E-region tristatic altitudes, however, the remote site observations are from the reception of long pulse signals whereas

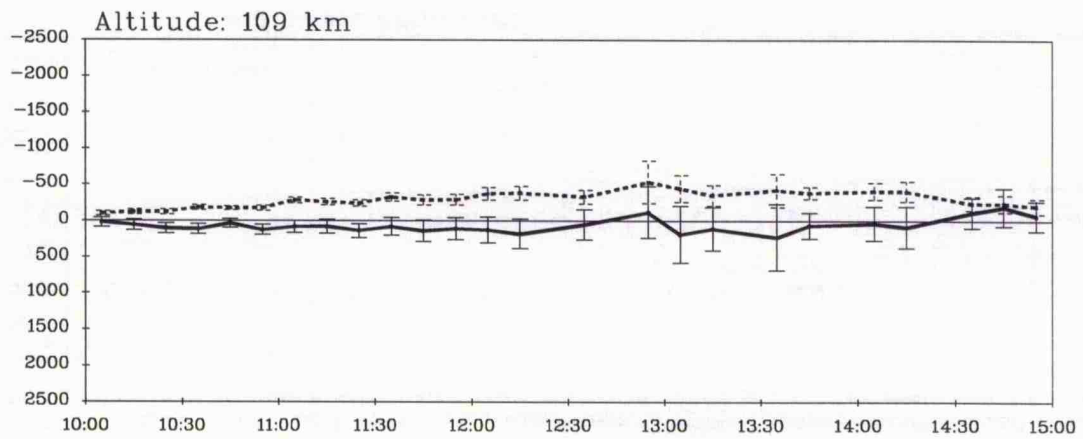
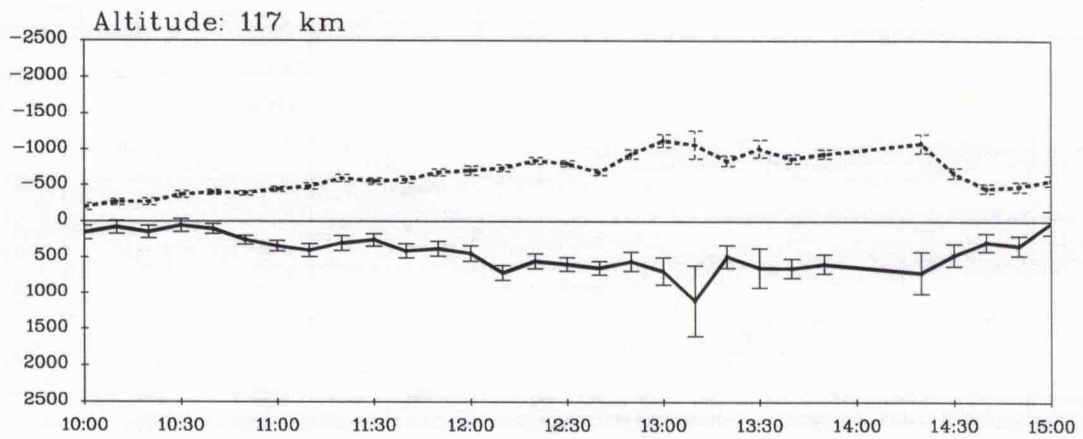
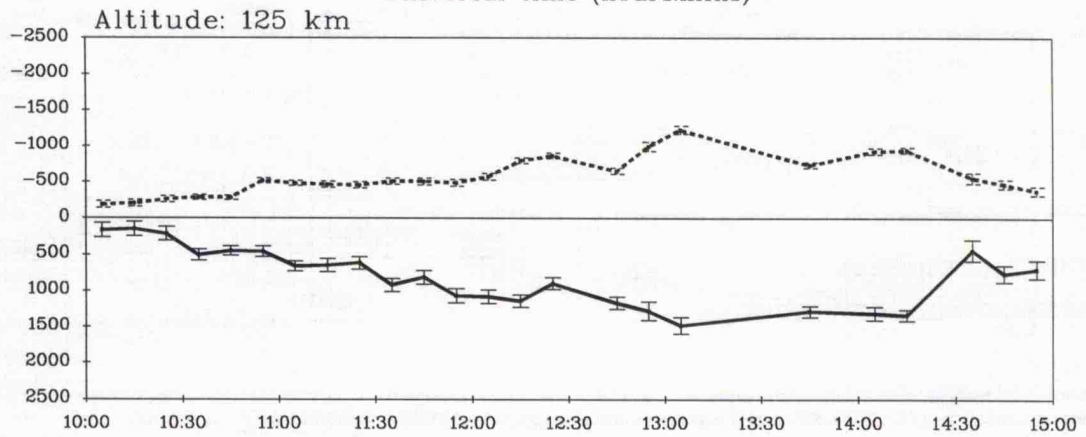
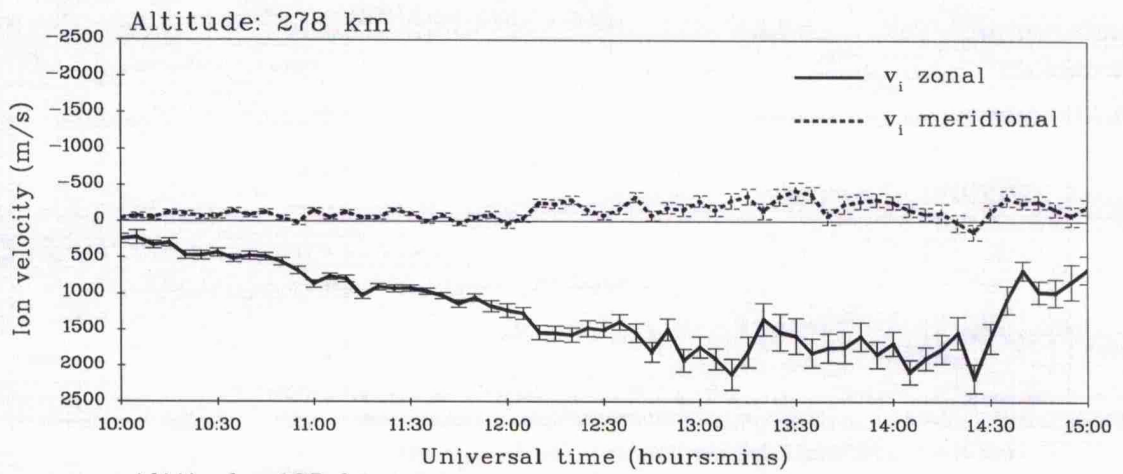


FIGURE 6.1: EISCAT ion velocity measurements from 03 April 1992

the observations from Tromsø were derived from the transmission of alternating codes.

At the F-region tristatic altitude of 278 km, the field-perpendicular zonal component of the ion velocity increases to a maximum approaching  $2500 \text{ m s}^{-1}$  in a westward direction whereas the meridional component remains comparatively low throughout the interval, less than  $400 \text{ m s}^{-1}$ . The zonal component of the ion velocity remains consistently westward at 278 km altitude, whereas the meridional ion velocity, although predominantly directed northward, undergoes several reversals in direction. At 125 km altitude, the magnitude of the zonal component of the ion velocity is reduced with respect to that at 278 km, attaining a maximum value of around  $1500 \text{ m s}^{-1}$ . Conversely, the field-perpendicular meridional ion velocity component at 125 km altitude greatly exceeds that at the F-region tristatic altitude and remains consistently northward throughout the interval. Whereas at 278 km altitude the field-perpendicular zonal component of the ion velocity greatly exceeds the corresponding meridional component, at 125 km altitude the meridional ion velocity component is not significantly less than the zonal velocity component. At 117 km, the zonal ion velocity component is generally lower than that observed at 125 km whereas the magnitude of the meridional component is comparable at these two E-region intersection altitudes. In contrast to the behaviour observed at higher altitudes, at 117 km the magnitude of the meridional component of the ion velocity exceeds that of the zonal component over much of the interval. At 109 km altitude, neither of the field-perpendicular components of the ion velocity attain values in excess of  $500 \text{ m s}^{-1}$ , however, the meridional ion velocity is significantly greater than the corresponding zonal component. Moreover, the zonal ion velocity component at 109 km does not remain consistently westward as is observed at higher altitudes; short-lived instances of eastward zonal flows are evident slightly prior to 13:00 UT and between 14:30 and 15:00 UT. The field-perpendicular ion velocity components determined from observations at 101, 96 and 91 km altitude, respectively, (not presented) tend, also, to exhibit a progressive reduction in magnitude with decreasing altitude, although the variability in the measurements is great.

The behaviour of the individual field-perpendicular ion velocity components implies both a progressive rotation in the orientation of the ion velocity vector in the field-orthogonal plane, from zonal to meridional, and a reduction in the velocity magnitude with decreasing altitude, effects which are more clearly demonstrated in figure 6.2. Figure 6.2 presents the field-orthogonal ion velocity magnitude (upper panel) and the angle from meridional northward of the field-orthogonal ion velocity vector (lower panel) with associated error estimates, at the altitudes of 278, 125, 117 and 109 km over the same time interval as the previous figure, between 10:00 and 15:00 UT on 03 April 1992. In the lower panel of figure 6.2, positive angles indicate eastward zonal ion velocities and negative angles represent westward directed zonal flow.

At 278 km altitude, the ion velocity vector is directed at an angle of between  $10$  and  $20^\circ$  to the field-orthogonal westward direction, and its magnitude increases from an initial value of  $250 \text{ m s}^{-1}$  at 10:00 UT to approximately  $2250 \text{ m s}^{-1}$ . The short periods during

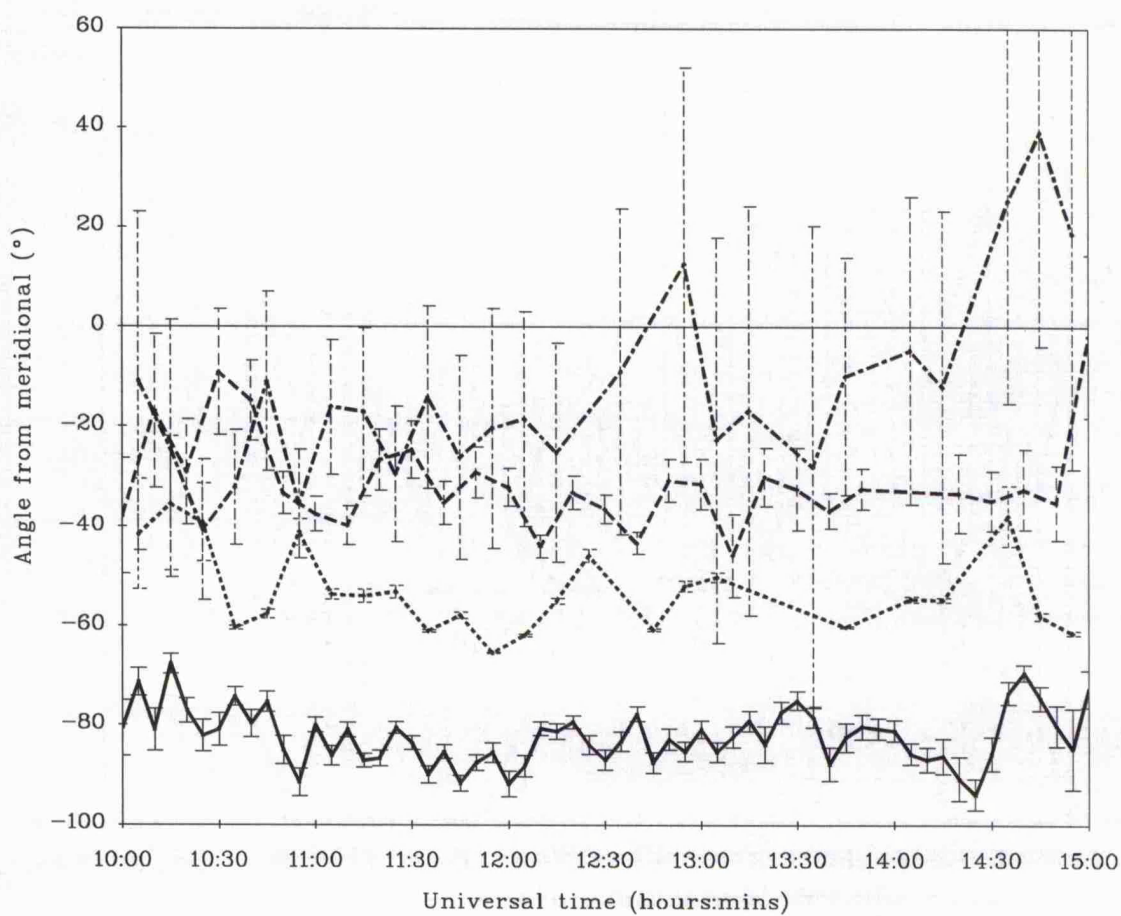
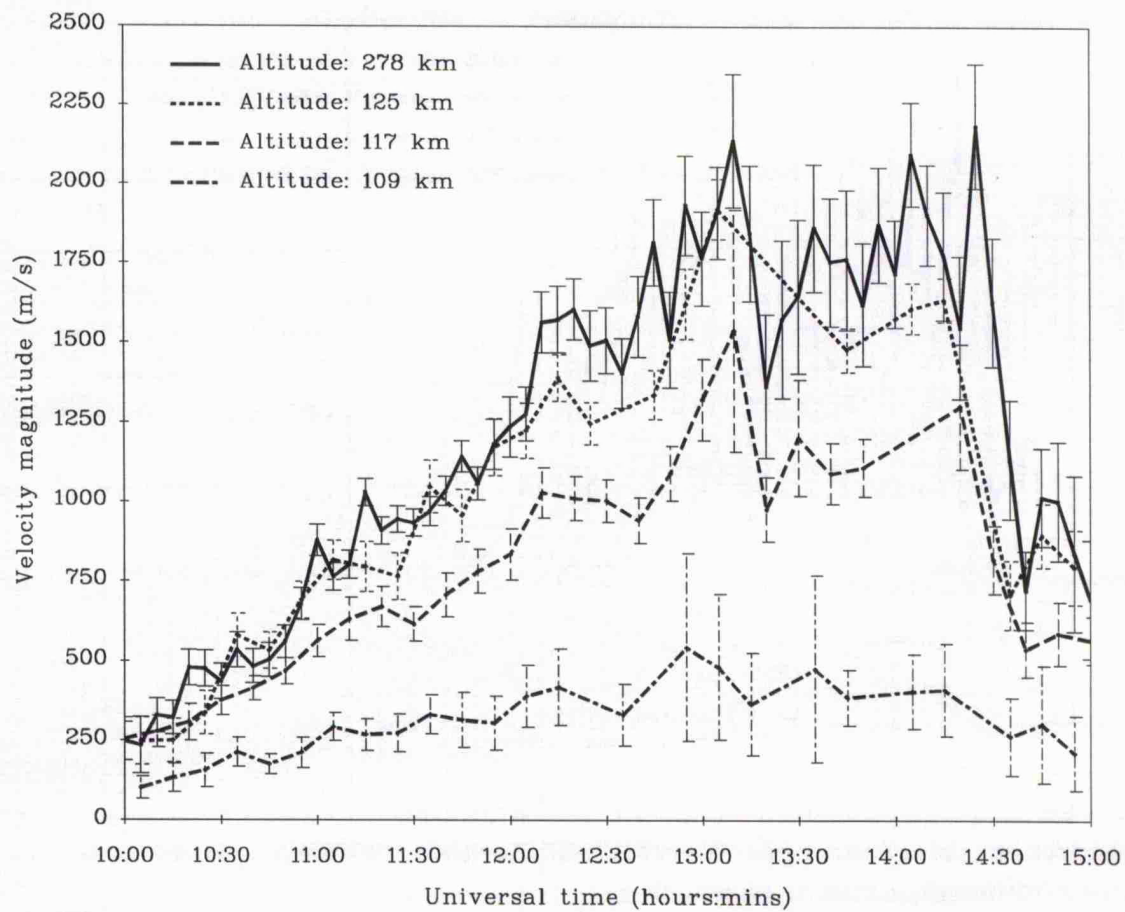


FIGURE 6.2: Ion velocity magnitude and direction

which meridional flow at the F-region tristatic altitude was southward (see figure 6.1) are represented by angles of less than  $-90^\circ$ . At an altitude of 125 km the field-orthogonal ion velocity magnitude is slightly reduced with respect to that at 278 km over much of the 5 hour interval, typically by some 10%. The ion velocity vector, however, has been significantly rotated towards the meridional northward direction, by an angle approaching  $30^\circ$ . The magnitude of the ion velocity at 117 km altitude attains a maximum of approximately  $1500 \text{ m s}^{-1}$  at 13:00 UT; the velocity vector is rotated from that at an altitude of 125 km by about  $20^\circ$ . At 109 km altitude the orthogonal ion velocity magnitude is reduced to less than one fifth of its value at the F-region tristatic altitude and is rotated by some  $60^\circ$  from the direction of the F-region ion velocity.

Both the rotation in the field-perpendicular ion velocity observed by EISCAT during the above interval, from a near geomagnetic zonal westward direction towards the meridional north with decreasing altitude and the reduction in the magnitude of the ion velocity from that measured at F-region altitudes, illustrate the effect of increasing collisional coupling with the neutral atmosphere on the motion of the ion population. Indeed, the sense of rotation of the ion velocity is consistent with what would be anticipated given the direction of the F-region flows: westward F-region ion flows indicate a northward applied electric field. However, it must be realised that in the presence of an applied electric field, a progressive rotation in the observed perpendicular ion velocity and reduction in the velocity magnitude with decreasing altitude will not necessarily be observed. With increasing ion-neutral collision frequency there is certainly a progressive rotation of the relative ion-neutral velocity vector from the direction of  $\mathbf{E}_{\text{eff}} \times \mathbf{B}$  to that of  $\mathbf{E}_{\text{eff}}$ , but this does not necessarily imply that the ion velocity will be observed to progressively rotate, as the effective electric field, or more specifically the neutral wind, varies with altitude. Similarly, the ion velocity magnitude will not necessarily be observed to progressively reduce with decreasing altitude.

### 6.3.3 Derivation of the normalised ion-neutral collision frequency

The ratio of the ion-neutral collision frequency to the ion gyrofrequency, the normalised ion-neutral collision frequency, has been derived at the three highest CP-1-J E-region intersection altitudes, 109, 117 and 125 km altitude during the interval of enhanced electric field in the post-noon sector on 03 April 1995. In the initial calculations of the normalised collision frequency the neutral wind at all altitudes is assumed to be negligible, thus expressions 6.7 and 6.8 are employed. The validity of this assumption is discussed later, particularly with reference to the present observations; indeed first order estimates of the neutral wind are derived and employed to calculate revised estimates of normalised collision frequency. Independent estimates of the normalised ion-neutral collision frequency during this interval have been derived from the rotation of the observed ion velocity vector at each of the E-region altitudes from the direction of the observed F-region ion velocity at 278 km, representative of that of  $\mathbf{E} \times \mathbf{B}$ , and from the reduction in the velocity magnitude from that observed at 278 km altitude, the latter is expressed by the ratio  $E/B$ . As mentioned

previously, in assuming that the F-region ion velocity measurements are representative of  $\mathbf{E} \times \mathbf{B}$  in the E-region, the geomagnetic field must be assumed to be approximately equal in both its magnitude and direction between the F-region tristatic altitude and the E-region altitudes of interest. Calculations of the IGRF model of the geomagnetic field at the position of EISCAT indicate that between the F-region and the E-region the magnitude and direction of the magnetic field vary by less than 5% and  $1^\circ$ , respectively; the resultant effect on the derived value of the normalised ion-neutral collision frequencies would be less than 5%.

Figure 6.3 presents time series of normalised ion-neutral collision frequency, with associated errors, at 125 (upper panel), 117 (central panel) and 109 km altitude (lower panel) from 10:00 to 15:00 UT on 03 April 1992 derived from the EISCAT CP-1-J observations of the rotation of the ion velocity vector (full line) and the reduction in the velocity magnitude (dashed line) from those measured at the F-region altitude of 278 km. Additionally, modelled values of the normalised collision frequency at each of the above altitudes are illustrated by a dotted line. The normalised ion-neutral collision frequency is modelled at the CP-1-J tristatic E-region altitudes using the MSIS-86 model thermosphere (*Hedin, 1987*) and the IGRF model, appropriate to the above date and the geographic location of EISCAT. The ion-neutral collision frequency is modelled for an ion population comprising  $\text{NO}^+$  and a neutral atmosphere comprising  $\text{O}_2$ ,  $\text{N}_2$  and  $\text{O}$ , with the neutral densities being taken from the MSIS-86 atmospheric model. The collisions of  $\text{NO}^+$  with all aforementioned neutral species are non-resonant interactions, combining long range polarisation attraction and short-range repulsion, and, unlike resonant charge exchange interactions in which an ion collides with its parent neutral, such polarisation type collisions are not dependant on the effective temperature which varies with electric field. The ion-neutral collision frequency is calculated using tabulated values of the collision coefficients presented by *Schunk and Nagy (1980)* such that

$$v_{\text{in}} = 4.34 \times 10^{-16} N_{[\text{N}_2]} + 4.28 \times 10^{-16} N_{[\text{O}_2]} + 2.44 \times 10^{-16} N_{[\text{O}]} \quad (6.6)$$

where the collision coefficients are quoted in units of  $\text{m}^{-3} \text{s}^{-1}$  (*Schunk and Walker, 1973*).

The ion gyrofrequency is calculated, again for  $\text{NO}^+$  ions, from the IGRF model of the geomagnetic field via the standard equation (2.5), quoted in section 2 of chapter 2. At E-region altitudes, analysis of EISCAT autocorrelation functions assumes a composition of 100% molecular ions with a mean relative molecular mass of 30.5, equivalent to an ion population comprising 75%  $\text{NO}^+$  and 25%  $\text{O}_2^+$ , although in modelling the normalised ion-neutral collision frequency an ion gas comprising totally  $\text{NO}^+$  is assumed. However, even in the extreme case where 100%  $\text{O}_2^+$  is assumed, the modelled collision to gyrofrequency ratios are almost identical to those calculated assuming solely  $\text{NO}^+$ . The variation with time of the modelled values of normalised ion-neutral collision frequency over the five hour interval, albeit small, results primarily from the variation with universal time of the densities of the neutral species yielded by the MSIS-86 model. The discontinuity in the modelled

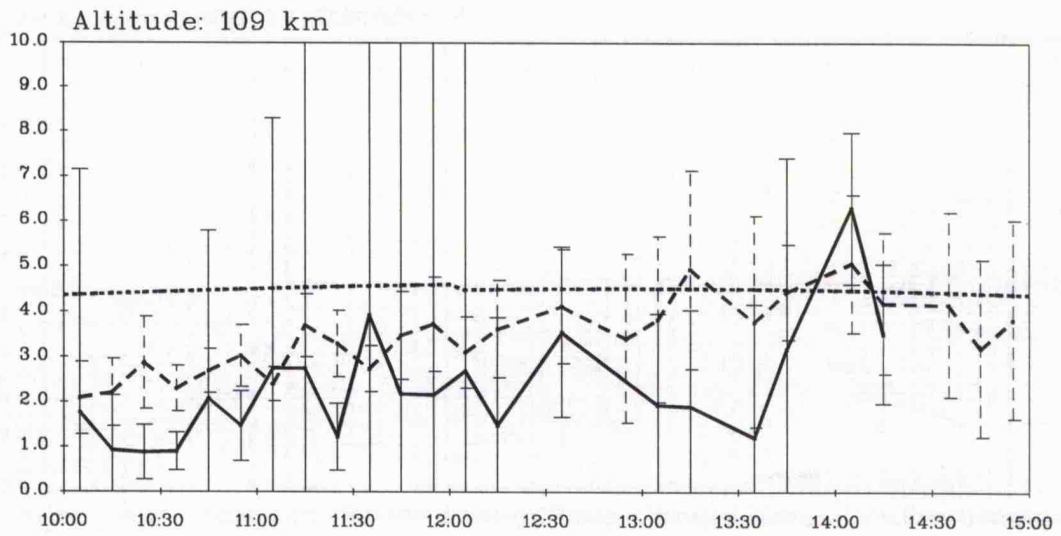
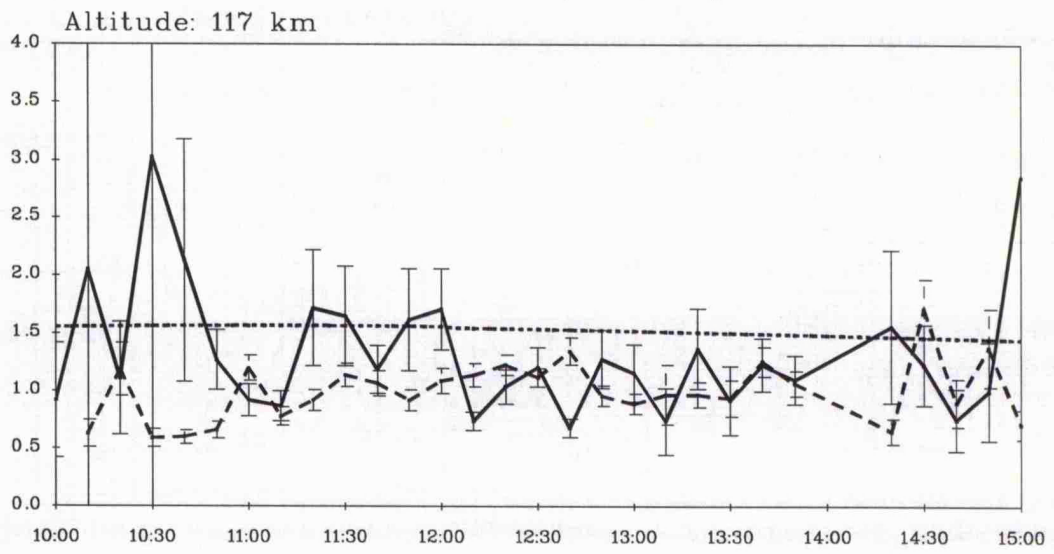
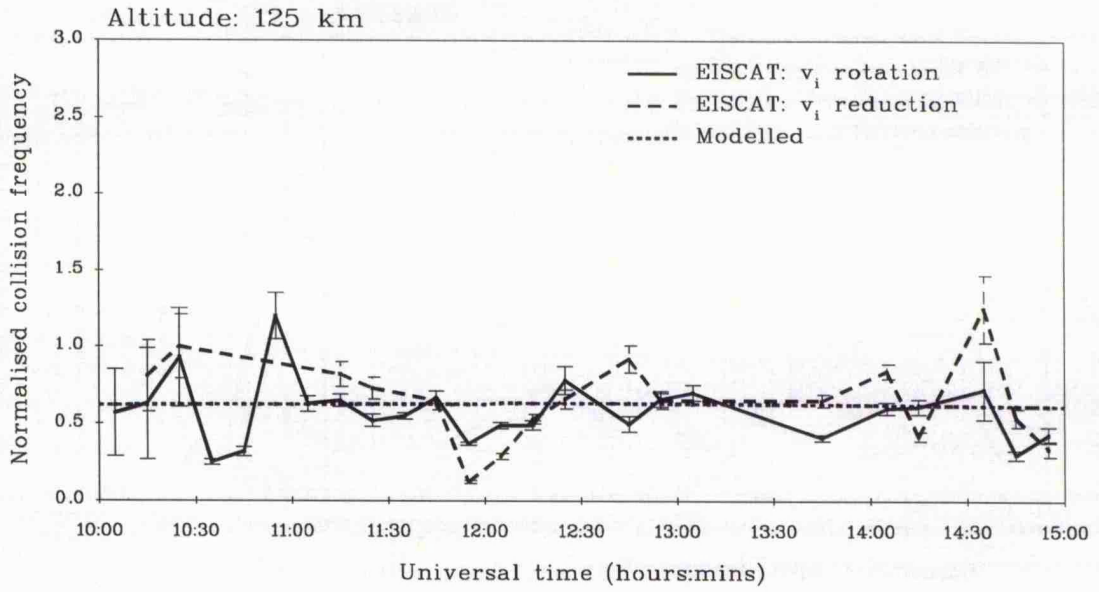


FIGURE 6.3: Modelled and calculated normalised collision frequency

values at 12:00 UT is a consequence of the parameterisation of MSIS-86 by  $A_p$ , a three hourly index.

At 125 km altitude, the values of normalised collision frequency derived from the EISCAT observations of both ion velocity rotation and reduction in velocity magnitude are similar, although rather variable, and are comparable to those predicted. At the tristatic altitude of 117 km, the derived values of the normalised ion-neutral collision frequency remain comparable, but generally less, than the modelled values. At 109 km altitude, the tendency for the modelled ratio to exceed those derived from the EISCAT observations continues, but, it is noticeable that the value of the normalised collision frequency derived from the rotation of the ion velocity is, in general, significantly less than that derived from the observations of the reduction of the ion velocity magnitude. Furthermore, at this altitude, the derived values of normalised collision frequency demonstrate a gradual increase with time through the interval. At altitudes below 109 km the modelled values of normalised collision frequency (not shown) tend also to exceed those derived from the EISCAT measurements, although the latter are highly variable. The altitude at which the modelled normalised collision frequency is of value unity is approximately 119 km, compared with 117 km for the ratio derived from the EISCAT ion velocity observations. The mean and standard deviation of normalised collision frequency derived from EISCAT observations of ion velocity rotation and reduction, and modelled using the MSIS-86 and IGRF models, are given in table 6.1 below.

Normalised ion-neutral collision frequency						
Altitude (km)	Velocity rotation		Velocity reduction		Modelled	
	mean	st. dev.	mean	st. dev.	mean	st. dev.
125	0.6	0.1	0.6	0.3	0.63	0.01
117	1.2	0.5	1.1	0.2	1.53	0.03
109	2.7	1.2	3.7	0.7	4.49	0.06

**TABLE 6.1:** Derived and modelled normalised ion-neutral collision frequencies.

Larger electric fields enable more accurate determination of the normalised ion-neutral collision frequency; the mean values and associated standard deviations of the normalised ion-neutral collision frequencies quoted above are therefore calculated from those estimates of normalised collision frequency derived between 11:00 and 14:30 UT, corresponding to an electric field exceeding  $35 \text{ mV m}^{-1}$  in magnitude. Moreover, it should be noted that the rotation in the ion velocity vector is likely to provide a more accurate estimate of the

normalised ion-neutral collision frequency at higher altitudes in the E-region, as changes in the orientation of the velocity vector with normalised collision frequency are more pronounced for small values of the latter. At 125 km altitude, the ion velocity magnitude is comparable to that in the F-region, indeed sometimes it exceeds that at 278 km altitude in which case an estimate of the collision frequency is not possible, whereas in direction, it is significantly rotated (see figure 6.2). This normalised ion-neutral collision frequency could therefore theoretically be derived from the rotation in the ion velocity at higher altitudes than 125 km given measurements of the ion velocity at these altitudes: for a normalised ion-neutral collision frequency of 0.2, appropriate to an altitude approaching 140 km, ion velocity vector would be rotated by some  $10^\circ$ . Conversely, at lower altitudes the reduction in the magnitude of the ion velocity is more pronounced, the ion velocity magnitude exhibits a significant reduction between 117 and 109 km altitude, from a maximum exceeding  $1500 \text{ m s}^{-1}$  to less than  $500 \text{ m s}^{-1}$ .

Several previous authors have compared incoherent scatter measurements of the ion-neutral collision frequency with those predicted from atmospheric models. Measurements of the collision frequency from the Arecibo radar, presented by *Wand and Perkins (1968)*, compared favourably with those from the CIRA (1965) model thermosphere. Similarly, both *Wickwar et al. (1981)* and *Lathuillère et al. (1983b)* found that measurements of the collision frequency from the Chatanika incoherent scatter radar were consistent with modelled values derived from the JACCHIA (1971) model. *St-Maurice et al. (1981)* compared ion-neutral collision frequencies calculated from the CIRA (1972) atmospheric model with those measured by the Chatanika radar (*Schlegel et al., 1980*). The authors stated that in order for the modelled collision frequencies to agree with those observed, the density of each neutral species from CIRA (1972) at E-region altitudes had to be scaled down by a factor of 1.36, although this value was calculated for an altitude of 94 km at which the Chatanika observations of the ion-neutral collision frequency was most accurately determined. Although *Nygrén et al. (1987)* obtained general agreement between ion-neutral collision frequencies derived from EISCAT observations and results from the CIRA (1972) model atmosphere, at altitudes above 120 km the derived values tended to be more than those modelled whereas below 110 km the converse appeared to be true, thus implying that the measured scale height of the neutral number density was less than predicted by the model. The results presented here are consistent with those of both *Nygrén et al. (1987)* and *St-Maurice et al. (1981)*, suggesting that the modelled neutral densities at lower E-region altitudes could be overestimated.

A rigorous comparison of these results with previous measurements of ion-neutral collision frequency is not included. Rather, the intention of this chapter is to demonstrate an alternative method to that of *Nygrén et al. (1987)* by which the normalised ion-neutral collision frequency can be derived from EISCAT observations of ion velocity under conditions of enhanced electric fields - conditions under which the derivation of the ion-neutral collision frequency by a standard fitting technique is generally unsuccessful. It is, at

this juncture, informative to point out the relative merits and disadvantages of this method over that of *Nygrén et al. (1987)*. These authors employed previously derived functional relationships between the electric field and the vertical ion velocity to derive the ion-neutral collision frequency during a EISCAT UHF special programme run in which the transmitter was pointed vertically and the remote sites remained at a single F-region tristatic volume. One distinct advantage of their method is that simultaneous electric field and E-region vertical ion velocity measurements were thus available whereas, for the present method, the remote site radars must scan between the F-region and the E-region intersection volume of interest and over this time - of order several minutes - the ionosphere must be assumed static. Thus, the present method is inappropriate under situations of rapidly varying electric fields associated with substorm activity as observed by, for example, *Williams et al. (1990a)*. Moreover, the method of *Nygrén et al. (1987)* generates height profiles of collision frequency. The major advantage of the technique documented above is that it enables two simultaneous estimates of the collision frequency to be derived for any estimate of the E-region ion velocity. Both this method, and that of *Nygrén et al. (1987)*, enable the collision frequency to be derived to higher altitudes than by conventional fitting, although in the present study this is limited by the geometry of the experiment, under situations of enhanced electric fields where conventional fitting is inappropriate.

#### 6.3.4 Estimation of the neutral wind

Recently, a number of authors have attempted to derive estimates of the E-region neutral wind from EISCAT observations of ion velocity (*e.g. Virdi et al., 1986; Williams and Virdi, 1989; Kunitake and Schlegel, 1991; Virdi and Williams, 1993; Brekke et al., 1994*). These studies have mainly been in relation to the investigation of tidal oscillations in the lower thermosphere, and were thus restricted to relatively undisturbed conditions. In most of these studies the authors assumed, following the work of *Brekke et al. (1974)*, that, during such quiet conditions, the ion motion in the E-region was principally governed by that of the neutral atmosphere such that measurements of the ion velocity could be used as a monitor of neutral velocities provided a small correction for the effect of the electric field was introduced. The approach adopted by these authors is essentially the antithesis of that adopted in the present study; the correction employed to negate the effect of electric fields assumed modelled values of the normalised ion-neutral collision frequency. In the present study, first-order estimates of the E-region neutral wind are derived by an alternative method, from a simplified ion energy balance equation.

Figure 6.4 presents the EISCAT CP-1-J observations of the field-parallel ion temperature between 108 and 150 km altitude from 10:00 to 15:00 UT on 03 April 1992, derived from alternating code transmission. At altitudes below 108 km the ion and electron temperatures are not fitted independently, rather, analysis proceeds by assuming that the temperatures of the ion and electron populations are equal. Data gaps arise where the incoherent scatter autocorrelation functions are not sufficiently well determined for analysis

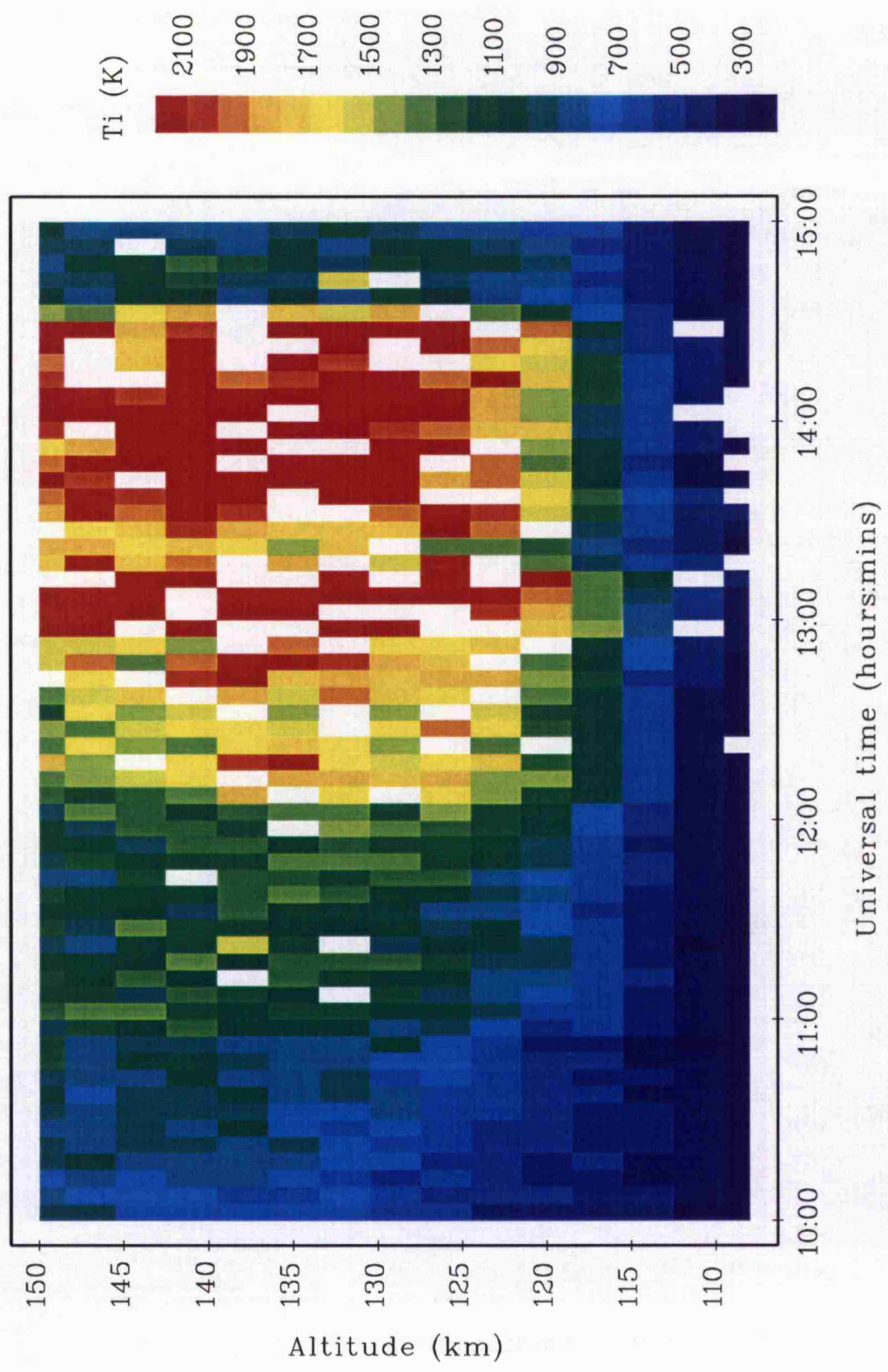


FIGURE 6.4: Alternating code parallel ion temperature

to yield the ionospheric parameters. The heating of the ion population commences at around 11:30 UT and is highly structured; F-region observations of field-parallel observations from this interval are illustrated in panel a of figure 5.1.

The problems inherent in the derivation of ion temperatures by analysis of the returned incoherent scatter signal during intervals of high ion flow velocities have been discussed extensively in previous chapters. In the direction parallel to the magnetic field, uncertainties in the derived ion temperature principally result from the adoption of a time invariant ion composition model. An increase in the proportion of molecular ions above that assumed in the analysis can result in the significant underestimate in the values of ion temperature yielded by the analysis. The ion composition profile adopted for standard EISCAT analysis (illustrated in figure 3.17), however, already assumes an ion population totally comprising of molecular species below an altitude of 150 km.

The 13 moment ion energy balance equation (equation 2.1) may be significantly simplified on application to a realistic ionosphere in the presence of large electric fields. Under such conditions, the energy balance equation may be expressed in the form quoted in equation 2.6, which represents the ion energy balance equation for a thermosphere comprising a number of neutral species. Equation 2.6 may be solved with respect to ion temperature, appropriate to the field-parallel ion population (*e.g. St-Maurice and Schunk, 1977*).

$$T_{\parallel} - T_{eq} = \frac{\langle m_n \rangle}{2k_B} \beta_{\parallel} (\mathbf{v}_i - \mathbf{v}_n)^2 \quad (6.9)$$

The ambient, or equilibrium ion temperature,  $T_{eq}$ , defined as the ion temperature in the absence of strong frictional heating, is equivalent to the sum of the neutral temperature and a small contribution to the ion temperature due to electron-ion thermal energy exchange. The term on the left hand side, thus represents the steady state enhancement in the field-parallel ion temperature in response to ion frictional heating; such steady state conditions are attained in a characteristic time which is the inverse of the ion-neutral collision frequency. Equation 6.9 is more accurately applicable at F-region altitudes, for the reasons discussed in chapter 2, however even at 109 km altitude frictional heating of the ion population is significant thus the above equation is still considered appropriate.

Predictions of the enhancement in the field-parallel ion temperature at the three E-region tristatic altitudes of 109, 117 and 125 km altitude were derived from the observed ion velocity magnitudes at those altitudes from the simplified form of the ion energy balance equation given above, assuming a stationary thermosphere. The average neutral mass,  $\langle m_n \rangle$ , has been calculated from equation 2.9 for an ion population comprising  $\text{NO}^+$  and the neutral species being  $\text{O}_2$ ,  $\text{N}_2$  and  $\text{O}$  with their densities being taken from MSIS-86 thermospheric model. The expressions for the collision frequencies of the polarisation interactions between these ion and neutral species are those quoted in the review of *Schunk and Nagy (1980)*. The field-parallel ion temperature partition coefficient,  $\beta_{\parallel}$ , is evaluated

employing equation 2.11a, again appropriate to the molecular ion species  $\text{NO}^+$ . In the calculation of the parallel temperature partition coefficient, it is necessary to adopt a value for  $\alpha_{\text{in}}$ , a numerical constant which is the ratio of generalised transport cross sections involved in the momentum transfer collision frequency. *St-Maurice and Schunk (1977)* presents values of  $\alpha_{\text{in}}$  for various collision mechanism and ranges of energy in table 1. This value adopted for  $\alpha_{\text{in}}$  is taken from table 1 of *St-Maurice and Schunk (1977)* for polarisation collisions of type B; this value was adopted by those authors for all non-resonant ion-neutral interactions. Values of  $\beta_{\parallel}$  estimated from the above equation, with neutral densities, again, taken from MSIS-86, range between some 0.53 and 0.55 which are comparable with theoretical values derived by *St-Maurice and Schunk (1977)* for  $\text{NO}^+$ - $\text{N}_2$  interactions and estimates from EISCAT observations by *Lathuillère et al. (1991)*.

Similarly, the field-parallel ion temperature enhancement is predicted at 300 km, from the CP-1-J velocity measurement at the F-region tristatic altitude of 278 km. Predictions are performed at 300 km rather than 278 km for reasons explained later in the current section. An ion population comprising  $\text{O}^+$  and the atmospheric constituents  $\text{O}_2$ ,  $\text{N}_2$  and  $\text{O}$  are assumed; the densities of the thermospheric gases again taken from the MSIS-86 thermospheric model. Although collisions between atomic oxygen ions and molecular neutrals constitute a non-resonant polarisation-type ion-neutral interaction in which the collision frequency is simply a product of the collision coefficient for that interaction and the density of the neutral species involved (*Schunk and Nagy, 1980*), a more complex interaction takes place between ionic atomic oxygen and its parent neutral species. For  $\text{O}^+$ - $\text{O}$  collisions, in addition to a polarisation type interaction, resonant charge exchange, a energy dependant interaction, can occur and will dominate the collision frequency over 235 K, where that temperature represents the average of the ion and neutral temperatures.

The precise values of the collision frequencies which should be used in aeronomical calculations are somewhat uncertain, particularly in the case of  $\text{O}^+$ - $\text{O}$  interactions as discussed, for example, by *Burnside et al. (1993)*. It is now generally accepted that the early theoretical formulations, derived by *Dalgarno (1964)*, *Banks (1966)* and *Schunk and Walker (1973)*, underestimate the resonant charge exchange collision frequency between  $\text{O}^+$  and  $\text{O}$ , although the factor by which the  $\text{O}^+$ - $\text{O}$  collision frequency is underestimated is still a subject of considerable debate. Experimental work by *Burnside et al. (1987)*, *Christie (1990)*, *Sipler et al. (1991)* and *Buonsanto et al. (1992)* indicates that, for resonant charge exchange collisions between  $\text{O}^+$  and  $\text{O}$ , the collision frequency may be underestimated by a factor approaching 2. Other recently published work has, however, indicated that a factor of around 1.2 is perhaps more appropriate, this work includes the experimental studies reported by *Davis (1993)* and *Davis et al. (1995)* and the theoretical work of *Stallcop et al. (1992)* and *Pesnell et al. (1993)*. *Salah (1993)* attempted to reconcile previous results in order to recommend a standard collision frequency; the author suggested that the  $\text{O}^+$ - $\text{O}$  resonant charge exchange collision frequency of *Banks (1966)*, as quoted in the review of *Schunk and Nagy (1980)*, should be multiplied by a coefficient of 1.7; *Salah (1993)* dubbed

this the ‘Burnside factor’. In the present work, in view of the comments of *Salah (1993)*, the expression for the O<sup>+</sup>-O collision frequency is amended accordingly.

For the polarisation collisions between O<sup>+</sup> and the neutral molecular species present, a value for  $\alpha_{in}$  of 0.95 is adopted in the calculation of the field-parallel ion partition coefficient, corresponding to polarisation collision model B proposed by *St-Maurice and Schunk (1977)*. For the resonant charge exchange interactions between O<sup>+</sup> and atomic oxygen, the choice of an appropriate value is less straightforward (*McCrea et al., 1993*). *St-Maurice and Schunk (1977)* stated that their model A cross-section ratio was the most appropriate to resonant charge exchange collisions, applicable to ion temperatures below 2500 K. More recent results, from the Monte-Carlo type simulations of *Winkler et al. (1992)* have indicated that a more suitable value of  $\alpha_{in}$  would be 0.25 rather than the value of 0.45 corresponding to resonant charge exchange model A of *St-Maurice and Schunk (1977)* (*McCrea et al., 1993*). Therefore, following the work of *McCrea et al. (1993)*, the ratio of the collision cross sections for O<sup>+</sup>-O collisions adopted for the evaluation of the parallel partition coefficient is taken as 0.25. An overestimate of the neutral densities produced by MSIS-86, indicated in the previous section, will not effect the calculation of the average neutral mass and the field-parallel ion temperature partition coefficients provided the relative proportions of the neutral species are correct.

The field-parallel ion temperature enhancement predicted from CP-1-J measurements of the ion velocity at 109, 117, 125 km altitude in the E-region and at 300 km altitude in the F-region between 10:00 and 15:00 on 03 April 1992 are compared to those observed. To define an observed enhancement in the parallel ion temperature it is necessary to define an unperturbed ion temperature at each altitude. Ion temperature exhibits only a slight diurnal variation, and the modal value over an extended quiet interval is an adequate representation of its unperturbed value (*McCrea et al., 1991*). Therefore, as in the statistical study of ion frictional heating documented in chapter 4, the unperturbed ion temperature is defined as the modal parallel ion temperature, calculated from its distribution over the 03 April 1992.

Figure 6.5 presents time series of the observed (full line) and expected (dashed line) field-parallel ion temperature enhancement at 300, 125, 117 and 109 altitude from 10:00 to 15:00 UT on 03 April 1992. Uncertainties in these parameters are also indicated. The CP-1-J observations of ion temperature enhancement are illustrated for the range gate centred at an altitude of 300 km in preference to those at the tristatic F-region altitude of 278 km. Results of the modelling work documented in chapter 5 indicate that the production of molecular ions at 300 km altitude during this interval of ion frictional heating is negligible; the proportion of molecular ions, principally NO<sup>+</sup>, increases to a values of less than 5%, whereas at the F-region tristatic intersection altitude the proportion of molecular ions increases to almost 15% of the total ion concentration. Thus at 300 km altitude, the field-parallel ion temperature yielded by analysis is less likely to be significantly underestimated by the adoption of a constant ion composition model in standard EISCAT analysis.

The maximum observed enhancement in the field-parallel ion temperature decreases

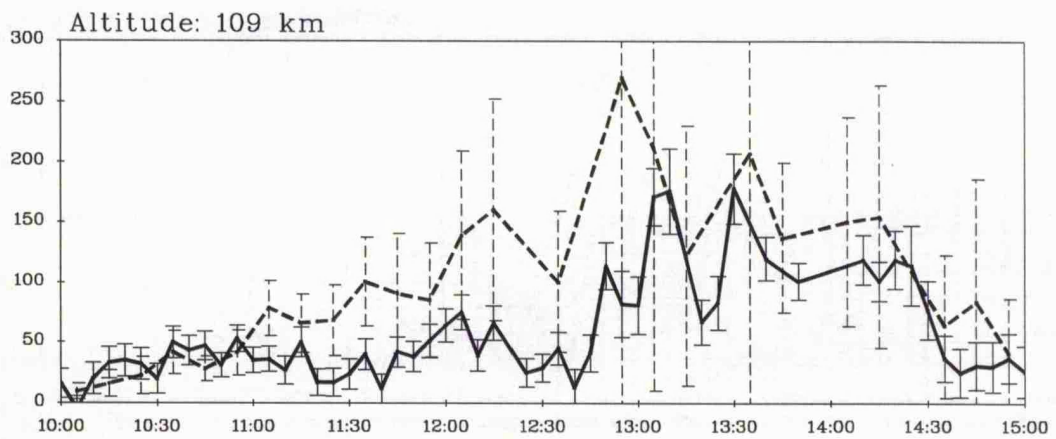
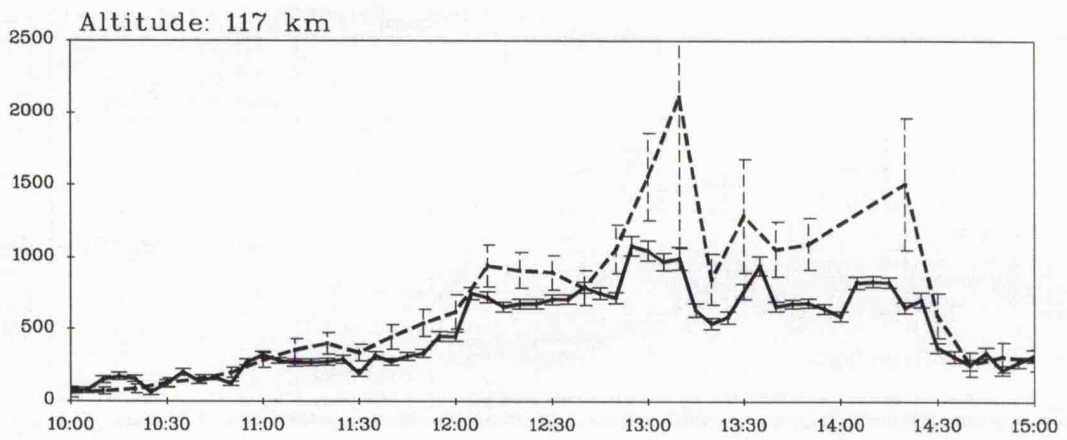
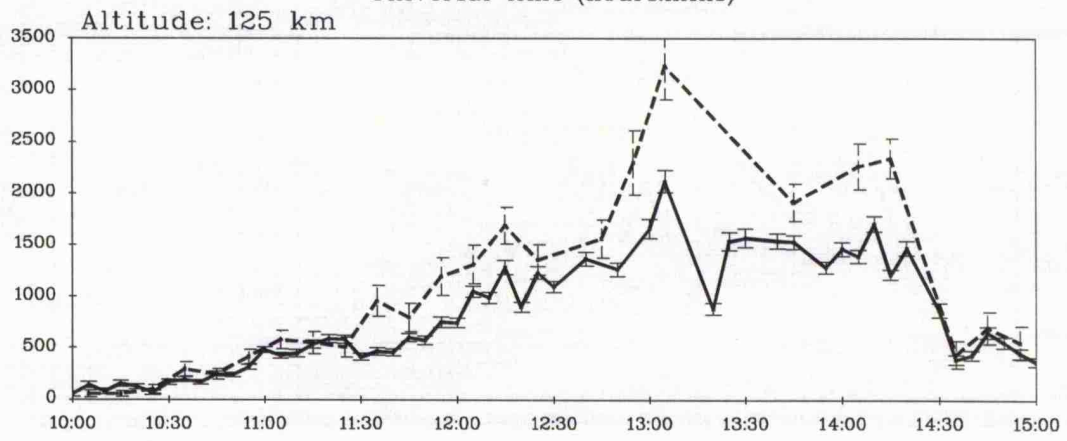
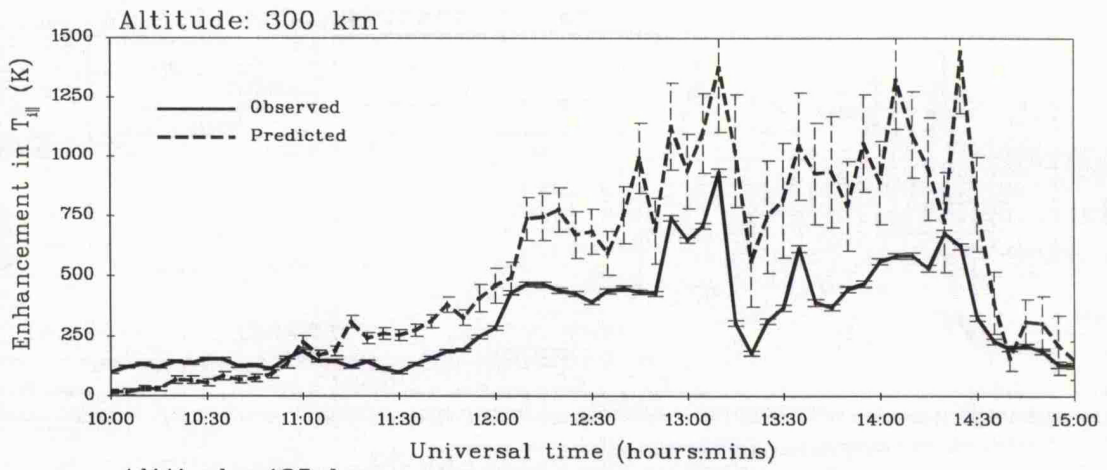


FIGURE 6.5: Observed and predicted ion temperature enhancement

from approximately 2000 K at 125 km to 200 K at 109 km altitude, a consequence of the reduction in the ion-neutral velocity in response to increased collisional coupling between the two populations. At all three altitudes under consideration the predicted enhancement generally exceeds that observed, by as much as 1000 K. This could be a consequence of neglecting the neutral velocity term in modelling the field-parallel ion temperature enhancement. The existence of a neutral wind due to ion drag would reduce the ion-neutral velocity difference, thus suppressing ion frictional heating, especially over such an extended period of enhanced ion flow. An additional mechanism has been suggested to heat the ions at E-region altitudes. *McBride et al. (1972)* argue that turbulent heating of the E-region ions by the modified two-stream instability will occur during intervals of large electric field in a process analogous to electron turbulent heating (*e.g. Schlegel and St-Maurice, 1981*). Theoretical calculations by *St-Maurice et al. (1981)* suggest that ion turbulent heating can attain a maximum of 50% of the frictional heating rate however the authors demonstrated that such heating would peak at an altitude of less than 100 km.

If the difference between the observed and expected field-parallel ion temperature enhancements is attributed to the effect of a neutral wind in the same direction as the ion motion, a first order approximation of the neutral wind can be calculated, using a rearranged form of equation 6.9. The assumption that the ion and neutral flows are in the same direction implies that the ion drag term constitutes the dominant term in the neutral momentum balance equation. The time constant for the response of the neutral atmosphere to ion drag is given by the neutral-ion collision frequency, which is inversely proportional to the plasma density (*Baron and Wand, 1983*). Electron densities observed by EISCAT during this interval are presented in figure 1 of chapter 5 and at E-region altitudes are typically  $1.0 \times 10^{11}$ , yielding a response time constant of only 6 hours. The relatively high E-region electron density during this interval suggests that ion drag will constitute a significant force on the thermosphere not only in the F-region but also at E-region altitudes. If, in fact, the neutral wind is not in the same direction as the ion flow, due to the significance of other terms in the neutral momentum balance equation such as the Coriolis force, this assumption would produce the minimum value of the neutral wind magnitude required to reduce the predicted field-parallel ion temperature enhancement to that observed.

Figure 6.6 presents time series of the derived neutral wind velocity, with associated errors, at 300, 125, 117 and 109 km altitude from 10:00 to 15:00 UT on 03 April 1992. Positive velocities indicate those where the neutral velocity is in the same sense as the ion velocity at that altitude. Where the predicted value of the field-parallel ion temperature does not exceed that observed by EISCAT, the value of the neutral wind is negative, implying motion of the neutral atmosphere in an opposite direction to that of the ion flow. The derived neutral wind at all altitudes tends to increase with time, consistent with an ion drag effect over a long period of frictional heating. Furthermore, the neutral wind tends to decrease with decreasing altitude between 125 and 109 km altitude, also consistent with the response of the neutrals to ion drag, the time constant of which is inversely proportional to

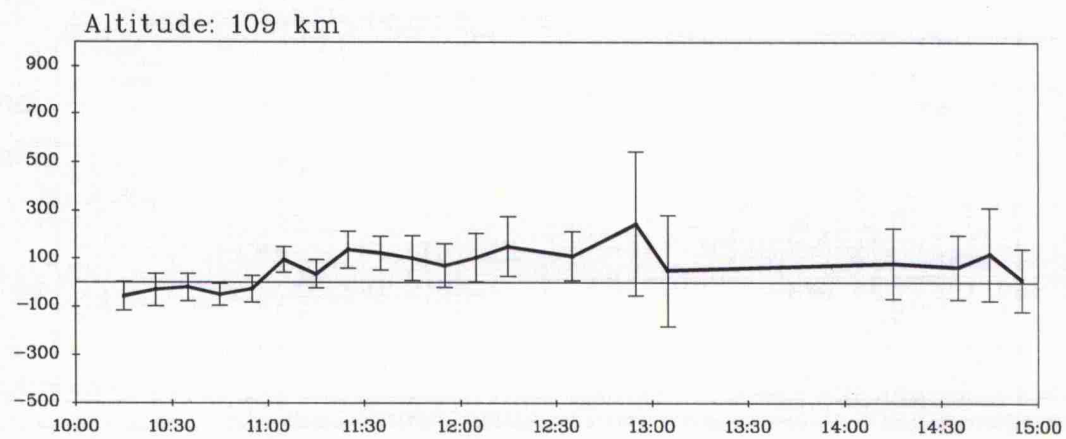
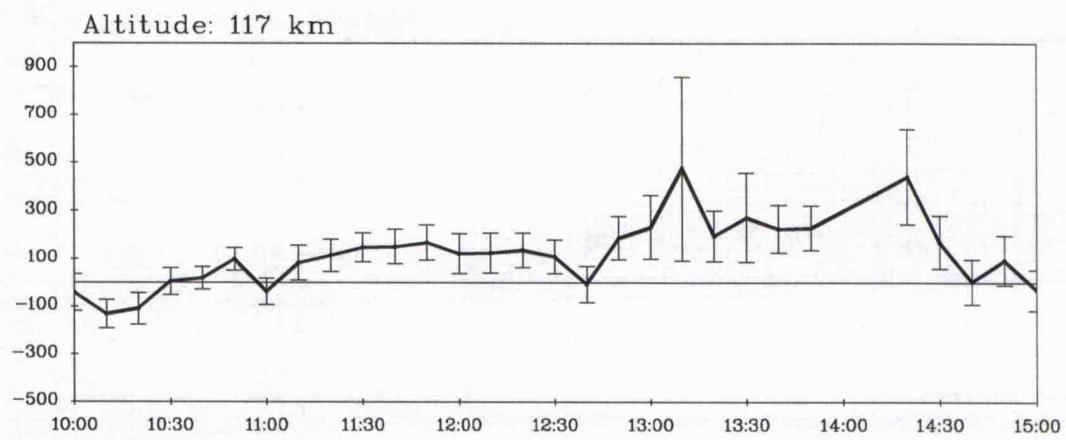
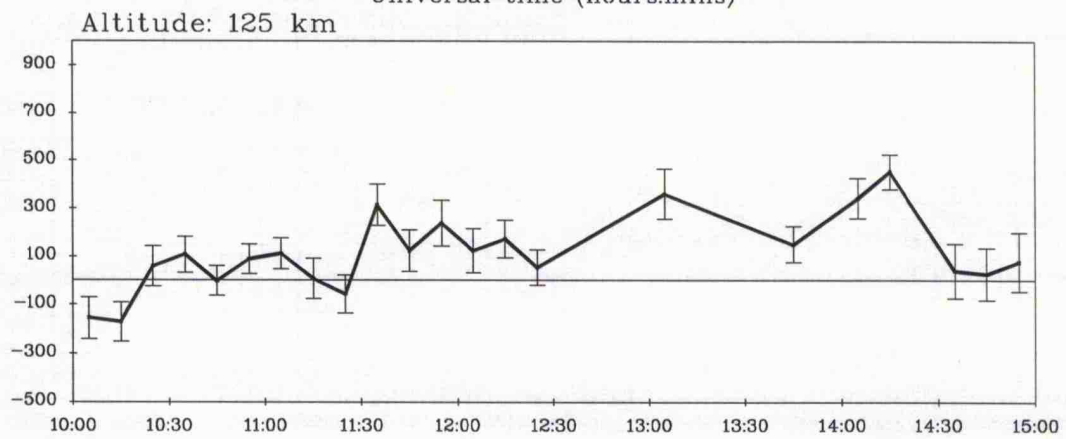
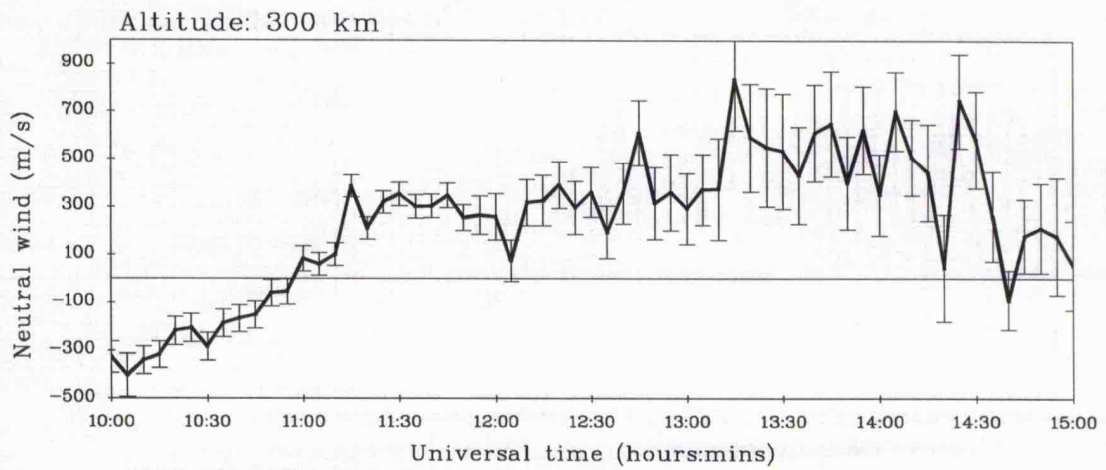


FIGURE 6.6: Predicted neutral wind

the plasma density which tends to decrease with altitude within that altitude range. Estimates of the E-region neutral wind prior to the onset of large electric fields are not inconsistent with those determined by previous authors under quiet conditions. For example, *Kunitake and Schlegel (1991)* deduced equatorward neutral winds of around  $80 \text{ m s}^{-1}$  at 109 km at around 10:00 UT; at this altitude the results presented here illustrate southward neutral flow (ion flow is northward) of similar magnitude. A thorough comparison of the neutral wind with values quoted by previous authors is not appropriate, as the neutral winds are assumed parallel to the ion flow: rather, first-order estimates of the neutral wind are deduced in order to correct the values of the normalised ion-neutral collision frequency derived in the previous section.

The F-region neutral wind derived from the difference between the predicted and observed field-parallel ion temperature at 300 km may be compared with that illustrated in figure 11 of chapter 5. Figure 5.11 illustrates the modelled field-perpendicular zonal component of the neutral velocity between 00:00 and 05:00 hours elapsed time, corresponding to the interval 10:00 to 15:00 UT on the 03 April 1992, calculated from a simplified form of the neutral momentum equation containing ion drag and vertical viscosity terms. In figure 5.11, negative values indicate a westward zonal component of the neutral velocity. In the present figure positive values indicate essentially westward neutral flows, flows in the same direction as the ion motion at 300 km. The initial modelled zonal neutral wind was set to zero, whereas the F-region neutral wind magnitude derived from the disparity between the observed and predicted enhancement in the field-parallel ion temperature exceeds  $300 \text{ m s}^{-1}$ . The modelled neutral velocity magnitude was artificially constrained in magnitude to a maximum of  $700 \text{ m s}^{-1}$ , for the reasons discussed in section 5 of chapter 5. This is reinforced by the present results in which the F-region neutral wind attains a limiting value around  $800 \text{ m s}^{-1}$ .

### 6.3.5 Revised estimate of the normalised collision frequency

For such a prolonged interval of enhanced ion velocity on the dayside as observed post-noon on 03 April 1995, the neutral wind becomes significant. For less extended intervals of enhanced ion flow or those on the nightside where the electron density is lower, ion drag would have a far less pronounced effect on the lower thermosphere. The results highlighted in the previous section indicate that the assumption adopted in the calculation of the normalised collision frequency in section 3.3 of this chapter, that the neutral wind is negligible, is not necessarily valid under all circumstances. Expressions 6.7 and 6.8 were employed in that section to derive two independent estimates of the ratio of the ion-neutral collision frequency to the ion gyrofrequency from the rotation of the ion velocity vector and reduction in the velocity magnitude from that observed in the F-region. In the present section, the normalised collision frequency is calculated by equations 6.4 and 6.5, incorporating the E-region neutral winds derived in the previous section. The calculated neutral winds derived in the E-region are themselves first order estimates, assuming neutral

flows parallel to the direction of the ion velocity. Moreover, the calculation of the neutral wind, or more specifically the field-parallel ion temperature partition coefficient and mean neutral mass, itself requires modelled values of the ion-neutral collision frequency: this introduces an inconsistency, as the neutral wind is subsequently being used to derived corrected values of the normalised collision frequency. The inclusion of the neutral wind is, however, not intended to provide definitive results, rather to gauge a general effect of a neutral wind on calculations of the normalised collision frequency by this method.

Figure 6.7 presents a time series of the revised estimate of the normalised ion-neutral collision frequency at 125 (upper panel), 117 (central panel) and 109 km (lower panel) altitude from 10:00 to 15:00 UT on 03 April 1992, derived from the rotation of the relative ion-neutral velocity vector from the direction of  $\mathbf{E}_{\text{eff}} \times \mathbf{B}$  (solid line). For comparison, the estimate of the normalised collision frequency calculated from the rotation of the ion velocity vector from the  $\mathbf{E} \times \mathbf{B}$  direction is included (dashed line) as are the modelled values (dotted line). As the neutral wind is assumed to flow in the direction of the E-region ions, the direction of relative ion-neutral flow will be the same as that of the observed ion velocity: the effective electric field will, however, be oriented in a different direction to the imposed electric field. Figure 6.8 illustrates a corresponding time series of the revised estimate of the normalised ion-neutral collision frequency derived from the reduction in magnitude of the relative ion-neutral velocity from that of  $\mathbf{E}_{\text{eff}} \times \mathbf{B}$  (solid line). Again, values of the normalised collision frequency derived assuming a stationary thermosphere and modelled values are also included, represented by dashed and dotted lines, respectively.

The mean and standard deviation of normalised collision frequency, calculated between 11:00 and 14:30 UT, derived from EISCAT observations of the rotation in the ion-neutral difference velocity and reduction in its magnitude are presented in table 6.2 below.

Normalised ion-neutral collision frequency				
Altitude (km)	Velocity rotation		Velocity reduction	
	mean	st. dev.	mean	st. dev.
125	0.7	0.2	0.7	0.3
117	1.6	0.7	1.3	0.5
109	3.3	1.2	4.9	0.9

**TABLE 6.2:** Derived normalised ion-neutral collision frequencies, derived assuming a non-zero E-region neutral wind.

At all altitudes, the normalised ion-neutral collision frequency derived with the inclusion of a

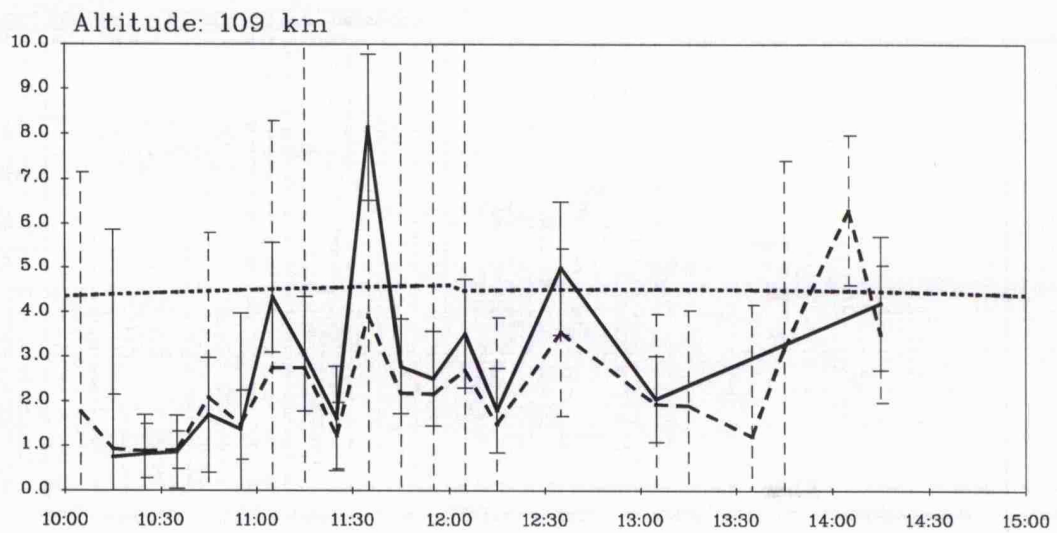
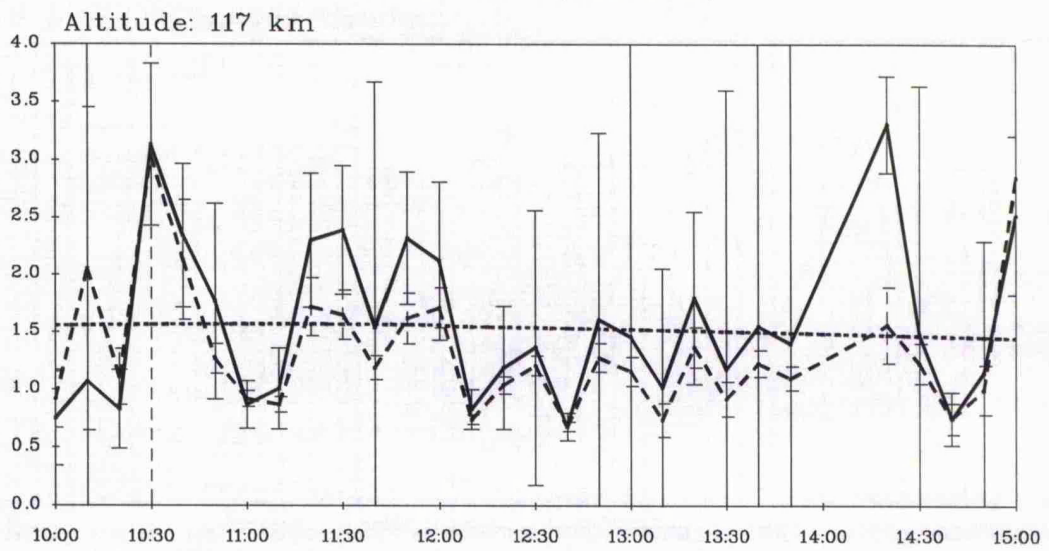
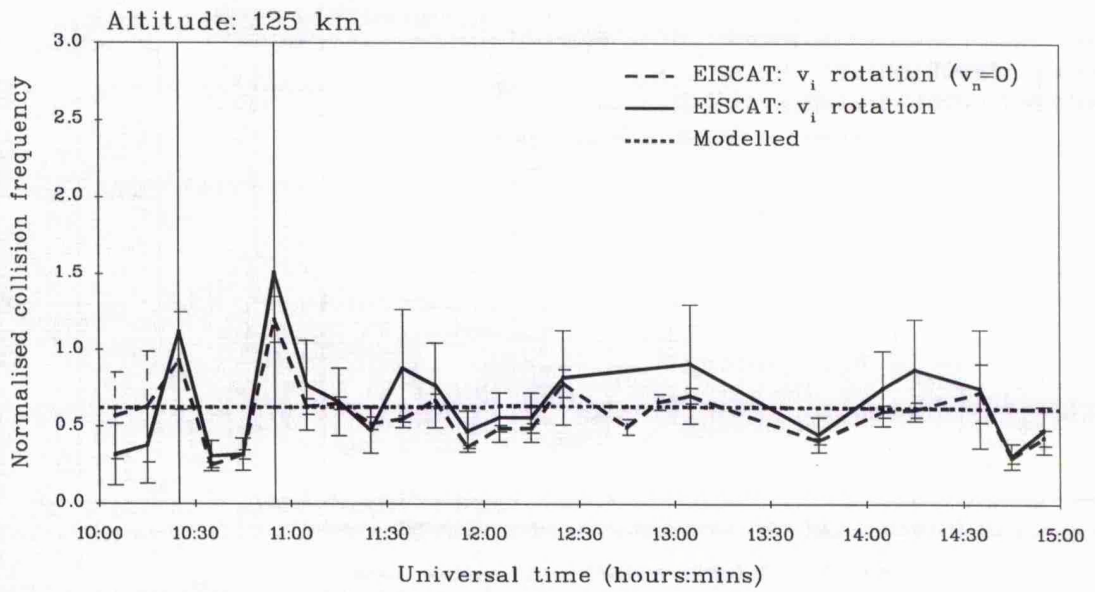


FIGURE 6.7: Modelled and calculated normalised collision frequency

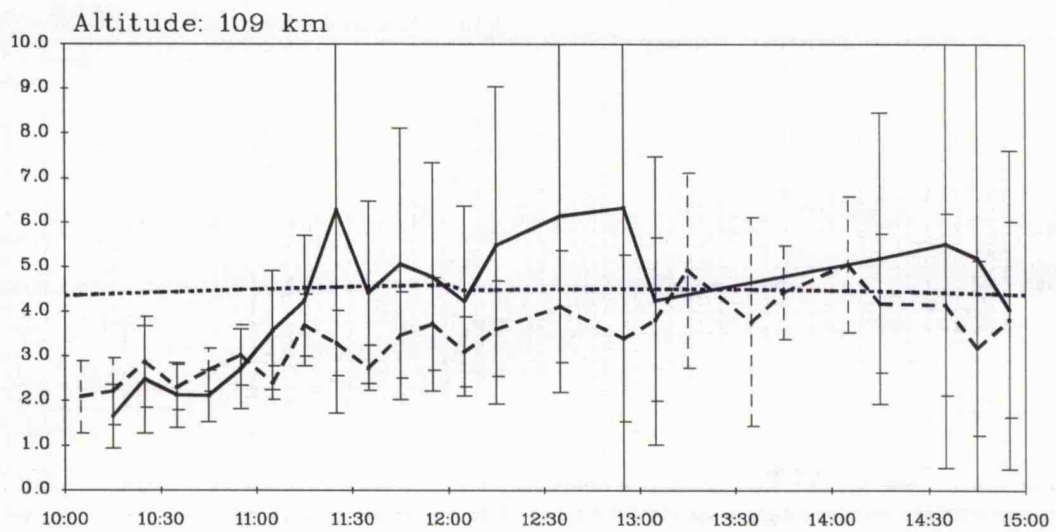
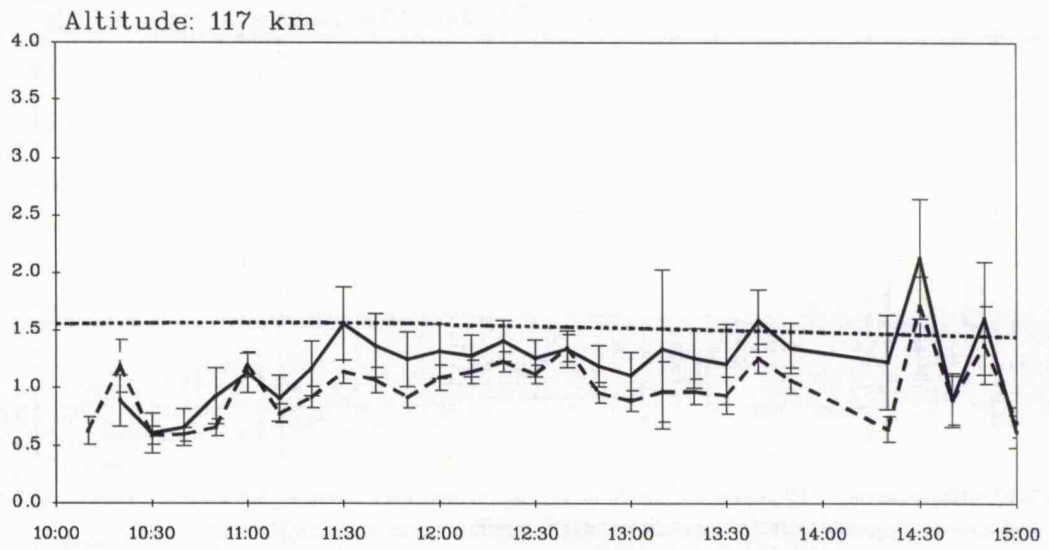
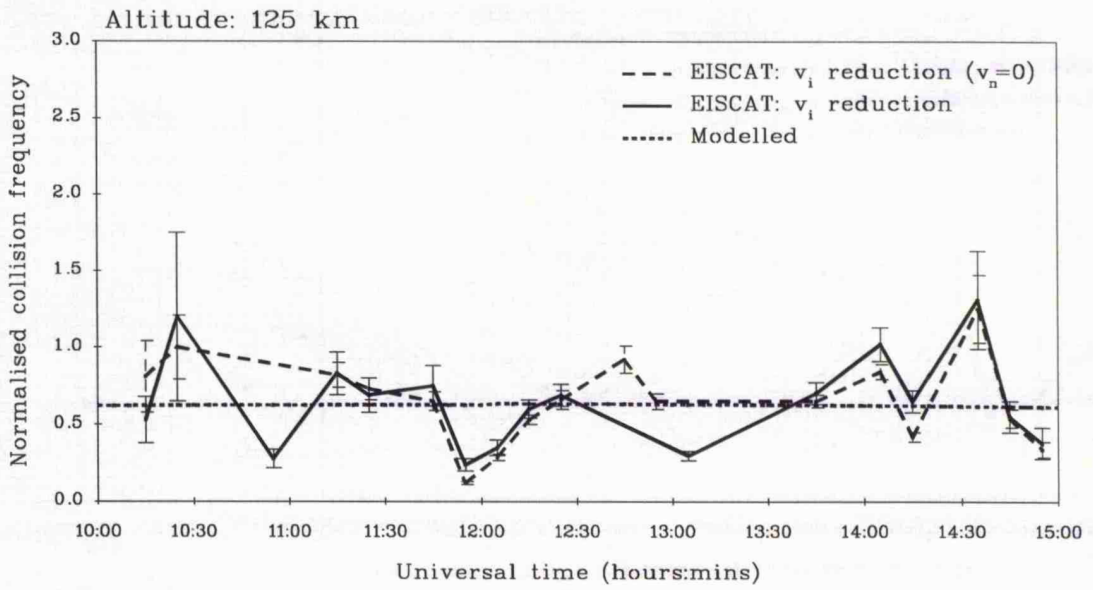


FIGURE 6.8: Modelled and calculated normalised collision frequency

first-order estimate of the neutral wind tends to be greater than that derived ignoring thermospheric flow; it is noticeable, however, the converse tends to be true when the neutral flow is oppositely directed to that of the ions. Although the inclusion of a neutral wind does tend to increase the estimates of the normalised collision frequency towards the modelled values, the difference in the derived values of the normalised ion-neutral collision frequency introduced with the inclusion of a non-zero neutral wind is generally less than the estimated error in the normalised collision frequency. The inclusion of the derived neutral wind term does not appear to have a significant effect on the values of the normalised ion-neutral collision frequency, although the difference between the results does relate to the effect of assuming that the neutral wind is in the same direction as the ion flow.

#### **6.4 Summary and conclusions**

EISCAT CP-1-J observations on 03 April 1992, revealed an extended interval during which the perpendicular electric field was significantly enhanced, to values in excess of  $100 \text{ mV m}^{-1}$ . From both the rotation of the ion velocity vector and reduction in the velocity magnitude with decreasing altitude during the interval, estimates of the ratio of the ion-neutral collision frequency to ion gyrofrequency were made at the CP-1-J E-region tristatic altitudes, which were compared to predictions based on the MSIS-86 thermospheric model and IGRF model of the geomagnetic field. The discrepancy between the modelled normalised collision frequency and that derived from the EISCAT observations at lower E-region altitudes is attributed to an overestimate of the neutral densities produced by MSIS-86, in accord with previous authors.

Furthermore, from the ion velocity measurements during this interval, the extent of frictional heating of the ion population at the E-region tristatic altitudes was derived from a simplified form of the ion energy balance equation. The predicted enhancement in the field-parallel ion temperature was compared to those observed, and, by attributing the discrepancy to thermospheric motion in response to an ion drag force on the neutral atmosphere, first order estimates of the neutral wind velocity were obtained. These thermospheric flows, the values of which are not inconsistent with previous measurements, were further employed to derive revised estimates of the normalised collision frequency. Their inclusion, however, is not particularly significant at the altitudes under consideration.

## Chapter 7

### Summary and further work

#### 7.1 Introduction

Ion frictional heating constitutes a highly significant mechanism whereby magnetospheric energy, originating in the solar wind, may be deposited into the high-latitude ionosphere and ultimately the neutral atmosphere. This thesis documents a study of ion frictional heating in the high-latitude ionosphere, based principally on observations by the UHF radar of the European incoherent scatter (EISCAT) facility situated in Northern Scandinavia. Incoherent scatter is possibly the single most important technique for ground based remote sensing of the ionosphere and upper atmosphere and the EISCAT facility boasts the most sophisticated incoherent scatter radars in operation. A review of ion frictional heating is presented in chapter 2 of this thesis, incoherent scatter and the EISCAT facility are detailed in chapter 3.

This chapter summarises the work presented in the thesis; the principal findings gleaned from the analysis are highlighted and their relevance is noted. Furthermore, some suggestions for proposed future work are presented, work which both continues and extends that documented and, in addition, some ideas for new work given the wealth of recently constructed experimental facilities such as CUTLASS and the EISCAT Svalbard radar (ESR).

#### 7.2 Summary of the principal results

**Chapter 4: Statistical study of ion frictional heating** The results of a statistical study of ion frictional heating in the high-latitude F-region were presented in chapter 4. The investigation was based on in excess of 3200 hours of field-aligned common programme observations taken by the UHF system of the EISCAT radar facility between January 1995 and December 1990. The objective of the statistical study was to extend the previous study of *McCrea et al. (1991)* in which the authors derived the diurnal distribution of ion frictional heating from observations taken over a two year interval at solar minimum. The enlargement of the database enabled ion frictional heating to be further characterised according to various solar and geophysical parameters. The criterion adopted for the identification of ion frictional heating was that of *McCrea et al. (1991)*, which was based on a selection criterion derived by *St-Maurice and Hanson (1982)* for the study of high-latitude F-region ion temperature observations by the Atmospheric Explorer-C satellite.

The diurnal distribution of ion frictional heating was established, and exhibited a double peaked, although asymmetric, form centred around local magnetic midnight. The asymmetry was attributed to the tendency for larger neutral winds to develop in the pre-midnight sector than after magnetic midnight, ion frictional heating is preferentially suppressed during the pre-midnight hours. Furthermore, the occurrence of ion frictional heating was found to increase markedly with increasing geomagnetic activity, the latter

characterised according to  $K_p$ , and, moreover, under conditions of a southward  $z$  component of the interplanetary magnetic field (IMF). Observations also indicated a  $B_y$  influence on the shape of the distribution of frictional heating. The dependence of ion frictional heating on geomagnetic activity and the orientation of the IMF was clearly attributable to a corresponding dependence observed in ionospheric convection. Similarly, the seasonal dependence of ion frictional heating reflected, to a large degree, the seasonal variation of the high-latitude convection pattern. Although a significant increase in the occurrence of enhanced ion velocities was evident with increasing solar activity, the corresponding increase in ion frictional heating was far less pronounced, probably attributable due to a solar cycle variation of the response time of the neutral atmosphere to ion drag.

**Chapter 5: Dayside ion frictional heating: EISCAT observations and comparison with model results** An extended interval of intense ion frictional heating was observed by the EISCAT UHF radar in the post geomagnetic noon sector on 03 April 1993. Frictional heating of the F-region ions correlated with an enhancement in the field-perpendicular westward flow to a value exceeding  $2 \text{ km s}^{-1}$  over a four hour period commencing at approximately 10 UT. This interval of frictional heating is atypical of those characterised in chapter 4, both in its prolonged duration and in the local time of its occurrence. Moreover, solar illumination of the depleted F-region plasma resulted in a simultaneous enhancement in the electron temperature, a feature not generally associated with intervals of ion frictional heating observed by EISCAT, the majority of which occur on the nightside. This interval was described in detail in chapter 5, and, moreover, compared with model results.

A zonal ion velocity signature, modelling that observed by EISCAT during the aforementioned interval, was imposed on the Sheffield University plasmasphere and ionosphere model (SUPIM). The predicted response of the ionospheric F-region to the imposition of an extended interval of enhanced ion flow, specifically the occurrence of large field-aligned plasma flows, depletion in F-region electron concentration and the development of anisotropic ion temperatures, concurred with the radar observations. Moreover, the enhancement in the F-region electron temperature observed by EISCAT was also evident in the model results. Although observed trends in the F-region field-parallel ion temperature were reproduced by the model, the model results substantially overestimated the extent of ion frictional heating. It was proposed that this discrepancy was due, at least in part, to the omission of atmospheric motion from SUPIM. Such a prolonged interval of enhanced ion velocity on the dayside would, it was suggested, induce large neutral flows in response to ion drag. Indeed, when a modelled zonal neutral wind was introduced, the ion temperatures reduced to values comparable with those observed. This result confirms the importance of neutral dynamics in determining the extent of ion frictional heating in the high-latitude ionosphere. Indeed, the ability to include the effects of local thermospheric

winds enhances the effectiveness of the model, particularly for studies of this type.

**Chapter 6: E-region ion-neutral coupling during intervals of enhanced electric field.** The response of the high-latitude ion population to an enhanced electric field depends greatly on altitude. More specifically it is the altitude variation of the ratio of the ion-neutral collision frequency to the ion gyrofrequency, the so-called normalised collision frequency, which determines the dynamics of the ions and this further governs ion energetics. With decreasing altitude, as collisions between the ion and neutral populations become significant, the ion motion progressively rotates in the plane perpendicular to the magnetic field towards the direction of the electric field. Moreover, the magnitude of the ion flow speed reduces with increasing ion-neutral collisional coupling.

In chapter 6 a new method was introduced by which estimates of the normalised ion-neutral collision frequency in the E-region could be derived from both the rotation in the ion velocity vector and the reduction in the velocity magnitude with respect to the ion velocity at F-region altitudes. Indeed, this method provides a means by which the normalised collision frequency can be derived from EISCAT observations of ion velocity under conditions of enhanced electric fields - conditions under which the derivation of the ion-neutral collision frequency by a standard fitting technique is generally unsuccessful. The validity of this approach was demonstrated using EISCAT UHF common programme observations from the prolonged interval of enhanced electric field post local geomagnetic noon on 03 April 1992 (see chapter 5). Values of the normalised ion-neutral collision frequency derived via this technique were compared with predictions based on the IGRF model of the geomagnetic field and the MSIS-86 thermospheric model. Although comparable in value to the model results, the estimates of the normalised ion-neutral collision frequency tended, in general, to be lower, a discrepancy attributed to an overestimate in the neutral densities output by the MSIS-86 model atmosphere. In the initial calculations, a stationary neutral atmosphere at E-region altitudes was assumed. The approach was subsequently amended such that estimates of the E-region neutral wind, deduced from the EISCAT observations via a simplified form of the ion energy balance equation, could be incorporated. Results indicate that the inclusion of the neutral wind does not have a significant effect in the determination of the normalised ion-neutral collision frequencies by this method.

### 7.3 Suggestions for future work

It is anticipated that much of the future work related to that in this thesis will incorporate observations by the EISCAT Svalbard radar (ESR). The location of the ESR, several hundred miles north of the Norwegian mainland, makes it ideal for the study of the ionospheric polar cap and the cusp/cleft region of the magnetosphere. Moreover, the extended spatial coverage of the CUTLASS facility, comprising two HF coherent radars, one at Hankasalmi in Finland and the other at Pykkvibær in Iceland, will enable observations by EISCAT and the ESR to be placed in context with respect to large scale convection features. The CUTLASS radar system constitutes an integral part of the

SuperDARN network of HF radars which cover almost  $180^\circ$  in longitude in the northern hemisphere and includes conjugate Antarctic stations (*e.g. Greenwald et al., 1995*). SuperDARN observations provide a means by which ionospheric convection can be mapped over much of the high-latitude ionosphere.

Although the work documented in this thesis can be extended by the introduction of complementary data sets from different experimental facilities, the observations comprising the basis of this work, particularly those by the UHF radar of the EISCAT facility, must also be fully exploited; most importantly, the method for the determination of the normalised ion-neutral collision frequency should be tested on a far more extensive set of data. It is also necessary that the statistical study of ion frictional heating be extended to include all available observations so that its dependence particularly on season and the IMF  $B_y$  can be more accurately determined. Moreover, observations spanning an entire solar cycle could highlight possible differences between ascending and descending solar activity.

The transmission of alternating code pulse schemes in EISCAT UHF experiments over the last several years provides a database of high quality observations at E-region altitudes, with an altitude resolution of several kilometres. Such observations are ideal for studying electron turbulent heating, a process which, like ion frictional heating, is a manifestation of electrodynamic coupling between the magnetosphere and ionosphere. In the E-region, where the ions are, to some extent, collisionally constrained to move with the neutral atmosphere but the electrons are still magnetised, perpendicular electric fields set up currents. When the electric current exceeds a threshold determined by the local ion-acoustic speed, plasma instabilities are generated. The instability, a modified two-stream instability known as the Farley-Buneman instability (*Farley, 1963; Buneman, 1963*), heats the electrons by wave drag, a process analogous to frictional heating between particles. Observations of electron turbulent heating from the Chatanika incoherent scatter radar were presented by *Schlegel and St-Maurice (1981)*; indeed these authors first attributed such enhancements in E-region electron temperature to heating by unstable waves in the presence of enhanced convection electric fields. Turbulent heating of the electron population was subsequently identified in special programme observations by the EISCAT UHF radar (*e.g. Williams et al., 1990a; 1992*). The routine transmission of alternating codes in EISCAT common programme experiments since 1992 facilitates the study of electron turbulent heating on a statistical basis, indeed preliminary analysis suggests that turbulent heating constitutes as systematic a heating effect on the E-region electrons as frictional heating of the F-region ions.

In conclusion, the work presented in this thesis emphasises the significant effect that electric fields, which originate through the coupling of the terrestrial and solar environments, have on the dynamics and energetics of the ionosphere and thermosphere system at high-latitudes. The recent deployment of a variety of new experimental facilities, both ground and space based, provides an unprecedented opportunity to further the understanding of the complex chain of interactions governing solar-terrestrial relations.

## References

- AIKIO A.T., H.J. OPGENOORTH, M.A.L. PERSSON AND K.U. KAILA (1993) Ground-based measurements of an arc-associated electric field. *J. Atmos. Terr. Phys.* **55**, 797.
- ALBRITTON D.L., I. DOTAN, W. LINDINGER, M. McFARLAND, J. TELLINGHUISEN AND F.C. FEHSENFELD (1977) Effects of ion speed distributions in flow-drift tube studies on ion-neutral reactions. *J. Chem. Phys.* **66**, 410.
- ALCAYDÉ D. AND J. FONTANARI (1986) Neutral temperature and winds from EISCAT CP-3 observations. *J. Atmos. Terr. Phys.* **48**, 931.
- ALCAYDÉ D., P. BAUER AND J. FONTANARI (1984) Dynamical coupling of the auroral F-region ionosphere and thermosphere: Case studies. *J. Atmos. Terr. Phys.* **46**, 625.
- ALCAYDÉ D., G. CAUDAL AND J. FONTANARI (1986) Convection electric fields and electrostatic potential over  $61^\circ < \Lambda < 72^\circ$  invariant latitude observed with the European incoherent scatter facility: 1. Initial results. *J. Geophys. Res.* **91**, 233.
- AXFORD W.I. AND C.O. HINES (1961) A unifying theory of high-latitude geophysical phenomena and geomagnetic storms. *Can. J. Phys.* **39**, 1433.
- BAILEY G.J. (1983) The effect of a meridional ExB drift on the thermal plasma at L = 1.4. *Planet. Space Sci.* **31**, 389.
- BAILEY G.J. AND R. SELLEK (1990) A mathematical model of the Earth's plasmasphere and its application in a study of He<sup>+</sup> at L = 3. *Ann. Geophys.* **8**, 171.
- BANKS P.M. (1966) Collision frequency and energy transfer: Ions. *Planet. Space Sci.* **14**, 1105.
- BANKS P.M. (1967) Ion temperature in the upper atmosphere. *J. Geophys. Res.* **72**, 3365.
- BANKS P.M. (1980) "Energy sources of the high-latitude upper atmosphere." in *Exploration of the polar upper atmosphere*, D. Reidel Publishing Company, Dordrecht, 113.
- BANKS P.M. AND G. KOCKARTS (1973) *Aeronomy*. Academic Press, New York.
- BARAKAT A.R. AND R.W. SCHUNK (1983) O<sup>+</sup> ions in the polar wind. *J. Geophys. Res.* **88**, 7887.
- BARAKAT A.R., R.W. SCHUNK AND J.-P. ST-MAURICE (1983) Monte Carlo calculations of the O<sup>+</sup> velocity distribution in the auroral ionosphere. *J. Geophys. Res.* **88**,

3237.

BARON M.J. AND R.H. WAND (1983) F-region ion temperature enhancements resulting from Joule heating. *J. Geophys. Res.* **88**, 4114.

BARTELS J. (1949) The standardised index,  $K_s$  and the planetary index,  $K_p$ . *Int. Union Geod. Geophys. IATME Bull.*, 97.

BATES H.F. (1973) Atmospheric expansion through Joule heating by horizontal electric fields. *Planet. Space Sci.* **21**, 2073, 1973.

BATES H.F. (1974) Atmospheric expansion from Joule heating. *Planet. Space Sci.* **22**, 925.

BEYNON W.J.G. AND P.J.S. WILLIAMS (1978) Incoherent scatter of radio waves from the ionosphere. *Rep. Prog. Phys.* **41**, 909.

BLOCK L.P. AND C.-G. FÄLTHAMMAR (1968) Effects of field-aligned currents on the structure of the ionosphere. *J. Geophys. Res.* **73**, 4807.

BOWLES K.L. (1958) Observations of vertical incidence scatter from the ionosphere at 41 Mc/sec. *Phys. Rev. Lett.* **1**, 454.

BOWLES K.L. (1963) Measuring plasma density in the magnetosphere. *Science* **139**, 389.

BREKKE A., R.J. DOUPNIK AND P.M. BANKS (1974) Observations of neutral winds in the auroral E-region during the magnetospheric storm of August 3-9, 1972. *J. Geophys. Res.* **79**, 2448.

BREKKE A., S. NOZAWA AND T. SPARR (1994) Studies of the E-region neutral wind in the quiet auroral ionosphere. *J. Geophys. Res.* **99**, 8801.

BRINTON H.C. (1975) *In-situ* measurements of plasma drift velocity and enhanced  $\text{NO}^+$  in the auroral electrojet by the Bennett spectrometer on AE-C. *Geophys. Res. Lett.* **2**, 243.

BRINTON H.C., J.M. GREBOWSKY AND L.H. BRACE (1978) The high-latitude winter F-region at 300 km: Thermal plasma observations from AE-C. *J. Geophys. Res.* **83**, 4767.

BUNEMAN O. (1963) Excitation of field-aligned sound waves by electron streams. *Phys. Rev. Lett.* **10**, 285.

BUONSANTO M.J., Y.K. TUNG AND D.P. SIPLER (1992) Neutral atomic oxygen density from nighttime radar and optical wind measurements at Millstone Hill. *J. Geophys. Res.* **97**, 8673.

BURCH J.L., P.H. REIFF, J.D. MENIETTI, R.A. HEELIS, W.B. HANSON, S.D.

- SHAWHAN, E.G. SHELLEY, M. SUGIURA, D.R. WEIMER AND J.D. WINNINGHAM (1985) IMF By-dependent plasma flow and Birkeland currents in the dayside magnetosphere: 1. Dynamics Explorer observations. *J. Geophys. Res.* **90**, 1577.
- BURNSIDE R.G., C.A. TEPLEY AND V.B. WICKWAR (1987) The O<sup>+</sup>-O collision cross-section: Can it be inferred from aeronomical measurements? *Ann. Geophys.* **5**, 343.
- BURRAGE M.D. (1988) Radar studies of high latitude convection flows. PhD Thesis, University of Leicester, UK.
- CAHILL L.J., R.L. ARNOLDY, AND W.W.L. TAYLOR (1980) Rocket observations at the northern edge of the eastward electrojet. *J. Geophys. Res.* **85**, 3407.
- CHRISTIE M. (1990) A comparison of optically measured and radar derived horizontal neutral winds. MSc Thesis, Utah State University, USA.
- COLE K.D. (1961) On solar wind generation of polar geomagnetic disturbances. *Geophys. J. R. Astron. Soc.* **6**, 103.
- COLE K.D. (1962) Joule heating of the upper atmosphere. *Aust. J. Phys.* **15**, 223.
- COLE K.D. (1971) Atmospheric excitation and ionisation by ions in strong auroral and man-made electric fields. *J. Atmos. Terr. Phys.* **33**, 1241.
- COWLEY S.W.H. (1982) The causes of convection in the Earth's magnetosphere: A review of developments during the IMS. *Rev. Geophys. Space Phys.* **20**, 531.
- CROWLEY G., N.M. WADE, J.A. WALDOCK, T.R. ROBINSON AND T.B. JONES (1985) High time-resolution observations of periodic frictional heating associated with a Pc5 micropulsation. *Nature* **316**, 528.
- DALGARNO A. (1964) Ambipolar diffusion in the F-region. *J. Atmos. Terr. Phys.* **26**, 989.
- DAVIES K. (1990) *Ionospheric radio*. Peter Peregrinus Ltd., London.
- DAVIS C.J. (1993) The interaction between the thermosphere and ionosphere at high-latitudes. PhD Thesis, University of Southampton, UK.
- DAVIS C.J., A.D. FARMER AND A. ARULIAH (1995) An optimised method for calculating the O<sup>+</sup>-O collision parameter from aeronomical measurements. *Ann. Geophys.* **13**, 541.
- DE LA BEAUJARDIÈRE O., R.R. VONDRAK AND M.J. BARON (1977) Radar observations of electric fields and currents associated with auroral arcs. *J. Geophys. Res.* **82**, 5051.
- DE LA BEAUJARDIÈRE O., R.R. VONDRAK, R.A. HEELIS, W.B. HANSON AND

R.A. HOFFMAN (1981) Auroral arc electrodynamic parameters measured by AE-C and the Chatanika radar. *J. Geophys. Res.* **86**, 4671.

DE LA BEAUJARDIÈRE O., V.B. WICKWAR AND J.H. KING (1986) "Sondrestrom radar observations of the effect of the IMF  $B_y$  component on polar cap convection." in *Solar wind-magnetosphere coupling*, Terra Scientific Publishing Company, Tokyo, 595.

DE LA BEAUJARDIÈRE O., D. ALCAYDÉ, J. FONTANARI AND C. LEGER (1991) Seasonal dependence of high-latitude electric fields. *J. Geophys. Res.* **96**, 5723.

DOUGHERTY J.P. AND D.T. FARLEY (1963) A theory of incoherent scattering of radio waves by a plasma: 3. Scattering in a partly ionised gas. *J. Geophys. Res.* **66**, 5473.

DU CASTEL F. AND G. VASSEUR (1972) Evaluation des performances d'un sondeur ionosphérique à diffusion incohérent. *Ann. Telecommun.* **27**, 239.

DU CASTEL F., H. CARRU, M. PETIT AND P. WALDTEUFEL (1966) Le sondeur ionosphérique à diffusion du CNET. *L'Onde Élec.* **46**, 1.

DUNGEY J.W. (1961) Interplanetary magnetic field and the auroral zones. *Phys. Rev. Lett.* **6**, 47.

EVANS J.V. (1969) Theory and practice of ionosphere study by Thomson scatter radar. *Proc. IEEE* **57**, 496.

EVANS J.V. (1971) Observations of F-region vertical velocities at Millstone Hill: 1. Evidence for drifts due to expansion, contraction and winds. *Radio Sci.* **6**, 609.

FABRY C. (1928) *C. r. hebdomadaire des séances Acad. Sci., Paris* **187**, 777.

FARLEY D.T. (1963) A plasma instability resulting in field-aligned irregularities. *J. Geophys. Res.* **68**, 6083.

FARLEY D.T. (1969) Incoherent scatter correlation function measurements. *Radio Sci.* **4**, 935.

FARLEY D.T. (1972) Multiple-pulse incoherent scatter correlation function measurements. *Radio Sci.* **7**, 661.

FARMER A.D., M. LOCKWOOD, T.J. FULLER-ROWELL, K. SUVANTO AND U.P. LØVHAUG (1988) Model predictions of the occurrence of non-Maxwellian plasmas and analysis of their effects on EISCAT data. *J. Atmos. Terr. Phys.* **50**, 487.

FARMER A.D., T.J. FULLER-ROWELL AND S. QUEGAN (1990) Comparing numerical simulations of the high-latitude ionosphere to an empirical mean model based on EISCAT data. *Adv. Space Res.* **10**, 143.

FEDDER J.A. AND P.M. BANKS (1972) Convection electric fields and polar

thermospheric winds. *J. Geophys. Res.* **77**, 2328.

FEJER J. (1960) Scattering of radio waves by an ionised gas in thermal equilibrium, *J. Geophys. Res.* **65**, 2635.

FELDSTEIN Y.I. AND Y.I. GALPERIN (1985) The auroral luminosity structure in the high-latitude upper atmosphere: Its dynamics and relationship to large scale structure of the Earth's magnetosphere. *Rev. Geophys.* **23**, 217.

FLÄ T, S. KIRKWOOD AND K. SCHLEGEL (1985) Collision frequency measurements in the high-latitude E-region with EISCAT. *Radio Sci.* **20**, 785.

FOLKESTAD K., T. HAGFORS AND S. WESTERLUND (1983) EISCAT: An updated description of technical characteristics and operational capabilities. *Radio Sci.* **18**, 867.

FONTAINE D. AND M. BLANC (1983) A theoretical approach to the morphology and dynamics of diffuse auroral zones. *J. Geophys. Res.* **88**, 7171.

FOSTER J.C., J.M. HOLT, R.G. MUSGROVE AND D.S. EVANS (1986) "Solar wind dependencies of high-latitude convection and precipitation." in *Solar wind-magnetosphere coupling*, Terra Scientific Publishing Company, Tokyo, 477.

FOX N.J., M. LOCKWOOD, S.W.H. COWLEY, M.P. FREEMAN, E. FRIIS-CHRISTENSEN, D.K. MILLING, M. PINNOCK AND G.D. REEVES (1994) EISCAT observations of unusual flows in the morning sector associated with weak substorm activity. *Ann. Geophys.* **12**, 541.

FRIIS-CHRISTENSEN E., Y. KAMIDE, A.D. RICHMOND AND S. MATSUSHITA (1985) Interplanetary magnetic field control of high-latitude electric fields and currents determined from Greenland magnetometer data. *J. Geophys. Res.* **90**, 1325.

FULLER-ROWELL T.J. (1984) A two-dimensional, high-resolution, nested-grid model of the thermosphere: 1. Neutral response to an electric field spike. *J. Geophys. Res.* **89**, 2971.

FULLER-ROWELL T.J. (1985) A two-dimensional, high-resolution, nested-grid model of the thermosphere: 2. Response of the thermosphere to narrow and broad electrodynamic features. *J. Geophys. Res.* **90**, 6567.

GLATTHOR N. (1993) NO<sup>+</sup> enhancement in the auroral F-region during ion frictional heating events, found in EISCAT CP-1 data. *J. Atmos. Terr. Phys.* **55**, 1417.

GLATTHOR N. AND R. HERNÁNDEZ (1990) Temperature anisotropy of drifting ions in the auroral F-region observed by EISCAT. *J. Atmos. Terr. Phys.* **52**, 545.

GORDON W.E. (1958) Incoherent scattering of radio waves by free electrons with applications to space exploration by radar. *Proc. IRE* **46**, 1824.

- GORDON W.E. (1964) Arecibo ionospheric observatory. *Science* **146**, 26.
- GOSLING J.T., J.R. ASBRIDGE, S.J. BAME AND W.C. FELDMAN (1976) Solar wind speed variations, 1962-1974. *J. Geophys. Res.* **81**, 5061.
- GOSLING J.T., J.R. ASBRIDGE, S.J. BAME AND W.C. FELDMAN (1978) Solar wind stream interfaces. *J. Geophys. Res.* **83**, 1401.
- GREENWALD R.A., K.B. BAKER, J.R. DUDENEY, M. PINNOCK, T.B. JONES, E.C. THOMAS, J.-C. VILLAIN, J.-C. CERISIER, C. SENIOR, C. HANUISE, R.D. HUNSUCKER, G. SOFKO, J. KOEHLER, E. NIELSEN, R. PELLINEN, A.D.M. WALKER, N. SATO AND H. YAMAGISHI (1995) DARN/SUPERDARN: A global view of the dynamics of high-latitude convection. *Space Science Rev.* **71**, 761.
- HAGFORS T. (1961) Density fluctuations in a plasma in a magnetic field with applications to the ionosphere. *J. Geophys. Res.* **66**, 1699.
- HAGFORS T. AND R.A. BROKELMAN (1971) A theory of collision dominated fluctuations in a plasma with applications to incoherent scattering. *Phys. Fluids* **14**, 1143.
- HAGFORS T., P.S. KILDAL, H.J. KÄRCHER, B. LIESENKÖTTER AND G. SCHROER (1982) VHF parabolic cylinder antenna for incoherent scatter radar research. *Radio Sci.* **17**, 1607.
- HÄGGSTRÖM I. AND P.N. COLLIS (1990) Ion composition changes during F-region density depletions in the presence of electric fields at auroral latitudes. *J. Atmos. Terr. Phys.* **52**, 519.
- HAPGOOD M.A., M. LOCKWOOD, G.A. BOWE, D.M. WILLIS AND Y.K. TULUNAY (1991) Variability of the interplanetary medium at 1 a.u. over 24 years: 1963-1986. *Planet. Space Sci.* **39**, 411.
- HARGREAVES J.K. (1979) *The upper atmosphere and solar-terrestrial relations*. Von Nostrand Reinhold Publishing Company, New York.
- HARRIS K.K., G.W. SHARP AND W.C. KNUDSEN (1967) Ion temperature and relative ion composition measurements from a low-altitude polar orbiting satellite. *J. Geophys. Res.* **72**, 5939.
- HEDIN A.E. MSIS-86 thermospheric model (1987) *J. Geophys. Res.* **92**, 4649.
- HEY J.S., J.B.G. ROBERTS, G.N. TAYLOR AND C.D. WATKINS (1968) High power radar for ionospheric research. *Nature* **220**, 865.
- HOLT J.M., R.H. WAND, J.V. EVANS AND W.L. OLIVER (1987) Empirical models for the plasma convection at high latitudes from Millstone Hill observations. *J. Geophys. Res.* **92**, 203.

HUBERT D. (1982) Auroral ion velocity distribution function: The Boltzmann model revisited. *Planet. Space Sci.* **30**, 1137.

HUBERT D. (1983) Auroral ion velocity distribution function: Generalized polynomial solution of Boltzmann's equation. *Planet. Space Sci.* **31**, 119.

HUBERT D. (1984) Auroral ion distribution function of the E region. *Planet. Space Sci.* **32**, 1061.

HUBERT D. AND E. KINZELIN (1992) Atomic and molecular ion temperatures and ion temperature anisotropy in the auroral F-region in the presence of large electric fields. *J. Geophys. Res.* **97** 4053.

HUUSKONEN A., T. NYGRÉN, L. JALONEN, AND J. OKSMAN (1984) The effect of electric field-induced vertical convection on the precipitation E-layer. *J. Atmos. Terr. Phys.* **46**, 927.

HUUSKONEN A., T. NYGRÉN, L. JALONEN, T. TURUNEN AND J. SILÉN (1986) High resolution EISCAT observations of the ion-neutral collision frequency in the lower E-region. *J. Atmos. Terr. Phys.* **48**, 827.

JENKINS B., R.J. MOFFETT, J.A. DAVIES AND M. LESTER (1996a) A nightside ion-neutral frictional heating event: Ion composition and O<sup>+</sup> and NO<sup>+</sup> temperature anisotropy. *Adv. Space Res.* **18**, 57.

JENKINS B., R.J. MOFFETT, J.A. DAVIES AND M. LESTER (1996b) Nightside ion frictional heating: Atomic and molecular ion temperature anisotropy and ion composition changes. *J. Atmos. Terr. Phys.*, in press.

JONES G.O.L., P.J.S. WILLIAMS, K.J. WINSER, M. LOCKWOOD AND K. SUVANTO (1988) Large plasma velocities along the magnetic field line in the auroral zone. *Nature* **336**, 231.

KEATING J.G., F.J. MULLIGAN, D.B. DOYLE, K.J. WINSER AND M. LOCKWOOD (1990) A statistical study of large field-aligned flows of thermal ions at high-latitudes. *Planet. Space Sci.* **38**, 1187.

KELLY J.D. AND V.B. WICKWAR (1981) Radar measurements of high-latitude ion composition between 140 and 300 km altitude. *J. Geophys. Res.* **86**, 7617.

KILLEEN T.L., P.B. HAYS, G.R. CARIGNAN, R.A. HEELIS, W.B. HANSON, N.W. SPENCER AND L.H. BRACE (1984) Ion-neutral coupling in the high-latitude F-region: Evaluation of ion heating terms from Dynamics Explorer-2. *J. Geophys. Res.* **89**, 7495.

KNUDSEN W.C. AND G.W. SHARP (1967) Ion temperatures measured around a dawn-dusk auroral zone satellite orbit. *J. Geophys. Res.* **72**, 1061.

KOHL H., H. LÜHR AND J. OTTEN (1985) "Altitude and latitude scan in the ionosphere

during a substorm compared with magnetometer recordings" presented at the Second EISCAT International Workshop, Aberystwyth.

KUNITAKE M. AND K. SCHLEGEL (1991) Neutral winds in the lower thermosphere at high latitudes from five years of EISCAT data. *Ann. Geophys.* **9**, 143.

LA HOZ C. (1982) EISCAT meetings 82/7.

LANCHESTER B.S., K. KAILA AND I.W. McCREA (1996) Relationship between large horizontal electric fields and auroral arc elements. *J. Geophys. Res.* **101**, 5075.

LATHUILLÈRE C. (1987) Ion composition response to auroral energy inputs in the lower F-region. *Ann. Geophys.* **5**, 449.

LATHUILLÈRE C. AND A. BREKKE (1985) Ion compositions in the auroral ionosphere as observed by EISCAT. *Ann. Geophys.* **3**, 557.

LATHUILLÈRE C. AND D. HUBERT (1989) Ion composition and ion temperature anisotropy in periods of high electric fields from incoherent scatter observations. *Ann. Geophys.* **7**, 285.

LATHUILLÈRE C., G. LEJEUNE AND W. KOFMAN (1983a) Direct measurement of ion composition with EISCAT in the high-latitude F1-region. *Radio Sci.* **18**, 887.

LATHUILLÈRE C., V.B. WICKWAR AND W. KOFMAN (1983b) Incoherent scatter measurements of ion-neutral collision frequencies and temperatures in the lower thermosphere of the auroral region. *J. Geophys. Res.* **88**, 137.

LATHUILLÈRE C., D. HUBERT, C. LA HOZ AND W. KOFMAN (1991) Evidence of anisotropic temperatures of molecular ions in the auroral ionosphere. *Geophys. Res. Lett.* **18**, 163.

LEADABRAND R.L., M.J. BARON, J. PETRICEKS AND H.F. BATES (1972) Chatanika, Alaska, auroral-zone incoherent scatter facility. *Radio Sci.* **7**, 747.

LEHTINEN M.S. AND I. HÄGGSTRÖM (1987) A new modulation principal for incoherent scatter measurements. *Radio Sci.* **22**, 625.

LESTER, M., O. DE LA BEAUJARDIÈRE, J.C. FOSTER, M.P. FREEMAN, H. LÜHR, J.M. RUOHONIEMI, W. SWIDER (1993) The response of the large scale ionospheric convection pattern to changes in the IMF and substorms: Results from the SUNDIAL 1987 campaign. *Ann. Geophys.* **11**, 556.

LEWIS R.V., P.J.S. WILLIAMS, G.O.L. JONES, H.J. OPGENOORTH AND M.A.L. PERSSON (1994) The electrodynamics of a drifting auroral arc. *Ann. Geophys.* **12**, 478.

LOCKWOOD M. (1982) Thermal ion outflows in the topside auroral ionosphere and the effects of low-altitude transverse acceleration. *Planet. Space Sci.* **30**, 595.

LOCKWOOD M. (1991) Review paper: The excitation of ionospheric convection. *J. Atmos. Terr. Phys.* **53**, 177.

LOCKWOOD M. AND S.W.H. COWLEY (1992) "Ionospheric convection and the substorm cycle." in *Substorms 1: Proceedings of the first international conference on substorms*, European Space Agency Publications, Nordwijk, 99.

LOCKWOOD M. AND T.J. FULLER-ROWELL (1987a) The modelled occurrence of non-thermal plasma in the ionospheric F-region and the possible consequences for ion outflow into the magnetosphere. *Geophys. Res. Lett.* **14**, 371.

LOCKWOOD M. AND T.J. FULLER-ROWELL (1987b) Correction to "The modelled occurrence of non-thermal plasma in the ionospheric F-region and the possible consequences for ion outflow into the magnetosphere". *Geophys. Res. Lett.* **14**, 581.

LOCKWOOD M., B.J. BROMAGE, R.B. HORNE, J.-P. ST-MAURICE, D.M. WILLIS AND S.W.H. COWLEY (1987) Non-Maxwellian ion velocity distributions observed using EISCAT. *Geophys. Res. Lett.* **14**, 111.

LOCKWOOD M., K. SUVANTO, J.-P. ST-MAURICE, K. KIKUCHI, B.J.I. BROMAGE, D.M. WILLIS, S.R. CROTHERS, H. TODD AND S.W.H. COWLEY (1988) Scattered power from non-thermal F-region plasma observed by EISCAT: Evidence for coherent echoes? *J. Atmos. Terr. Phys.* **50**, 467.

LOCKWOOD M., I.W. McCREA, G.H. MILLWARD, R.J. MOFFETT AND H. RISHBETH (1993) EISCAT observations of ion composition and temperature anisotropy in the high-latitude F-region. *J. Atmos. Terr. Phys.* **55**, 895.

LØVHAUG U.P. AND T. FLÅ (1986) Ion temperature anisotropy in the auroral F-region as measured with EISCAT. *J. Atmos. Terr. Phys.* **48**, 959.

MAEHLUM B.N., T.L. HANSEN, A. BREKKE, K. FOLKESTADT AND O. HOLT (1984) Preliminary results from a study of the F-region heating during an intense aurora observed by EISCAT. *J. Atmos. Terr. Phys.* **46**, 619.

MARKLUND G. (1984) Auroral arc classification scheme based on the observed arc-associated electric field pattern. *Planet. Space Sci.* **32**, 193.

MARKLUND G., I. SANDAHL AND H.J. OPGENOORTH (1982) A study of the dynamics of a discrete auroral arc. *Planet. Space Sci.* **30**, 179.

McBRIDE J.B., E. OTT, J.P. BORIS AND J.H. ORENS (1972) Theory and simulation of turbulent heating by the modified two-stream instability. *Phys. Fluids* **15**, 2367.

McCREA I.W. (1989) Radar observations of high-energy deposition and dissipation in the high-latitude ionosphere. PhD Thesis, University of Leicester, UK.

McCREA I.W., M. LESTER, T.R. ROBINSON, N.M. WADE AND T.B. JONES (1991)

On the identification and occurrence of ion frictional heating events in the high-latitude ionosphere. *J. Atmos. Terr. Phys.* **53**, 587.

McCREA I.W., M. LESTER, T.R. ROBINSON, J.-P. ST-MAURICE, N.M. WADE AND T.B. JONES (1993) Derivation of the ion temperature partition coefficient  $\beta_{||}$  from the study of ion frictional heating events. *J. Geophys. Res.* **98**, 15701.

McCREA I.W., G.O.L. JONES AND M. LESTER (1995) The BEAN experiment - An EISCAT study of ion temperature anisotropies. *Ann. Geophys.* **13**, 177.

McFARLAND M., D.L. ALBRITON, F.C. FEHSENFELD, E.E. FERGUSON AND A.L. SCHMELTEKOPF (1973) Flow-drift technique for ion mobility and ion-molecule reaction rate constant measurements: 2. Positive ion reactions of  $N^+$ ,  $O^+$  and  $NO^+$  with  $N_2$  from thermal to  $\sim 2$  eV. *J. Chem. Phys.* **59**, 6620.

McPHERRON R.L. (1979) Magnetospheric substorms. *Rev. Geophys. Space Phys.* **17**, 657.

MOFFETT R.J. AND S. QUEGAN (1983) The mid-latitude trough in the electron concentration of the ionospheric F-layer: A review of observations and modelling. *J. Atmos. Terr. Phys.* **45**, 315.

MOFFETT R.J., R. SELLEK AND G.J. BAILEY (1991) The behaviour of  $H^+$  and  $He^+$  ions in the topside ionosphere during a short-lived subauroral ion drift. *Planet. Space Sci.* **39**, 1209.

MOFFETT R.J., R.A. HEELIS, R. SELLEK AND G.J. BAILEY (1992) The temporal evolution of the ionospheric signatures of subauroral ion drifts. *Planet. Space Sci.* **40**, 663.

MOFFETT R.J., B. JENKINS AND G.J. BAILEY (1993) A modelling study of anisotropic ion temperatures generated in the F-layer by subauroral ion drifts. *Ann. Geophys.* **11**, 1051.

MOORCROFT D.R. (1964) On the determination of temperature and ionic composition by electron backscattering from the ionosphere and magnetosphere. *J. Geophys. Res.* **69**, 955.

MOORCROFT D.R. AND K. SCHLEGEL (1988) Evidence for non-Maxwellian ion velocity distributions in the F-region. *J. Atmos. Terr. Phys.* **50**, 455.

MURDIN J. (1979) Errors in incoherent scatter radar measurements. EISCAT technical note 79/16.

NYGRÉN T., L. JALONEN, J. OKSMAN AND T. TURUNEN (1984) The role of electric field and neutral wind direction in the formation of sporadic E-layers. *J. Atmos. Terr. Phys.* **46**, 373.

NYGRÉN T., L. JALONEN AND A. HUUSKONEN (1987) A new method of measuring

the ion-neutral collision frequency using incoherent scatter radar. *Planet. Space Sci.* **35**, 337.

OLIVER W.L., J.M. HOLT, R.H. WAND AND J.V. EVANS (1983) Millstone hill incoherent scatter observations of auroral convection over  $60^\circ < \Lambda < 75^\circ$ : 3. Average patterns versus  $K_p$ . *J. Geophys. Res.* **88**, 5505.

OLIVER W.L., S. FUKAO, T. SATO, T. TSUDA, S. KATO, I. KIMURA, A. ITO, T. SARYOU AND T. ARAKI (1988) Ionospheric incoherent scatter measurements with the MU radar: Observations of F-region electrodynamic. *J. Geomag. Geoelec.* **40**, 963.

OPGENOORTH H.J., I. HÄGGSTRÖM, P.J.S. WILLIAMS AND G.O.L. JONES (1990) Regions of strongly enhanced perpendicular electric fields adjacent to auroral arcs. *J. Atmos. Terr. Phys.* **52**, 449.

PERRAUT S., A. BREKKE, M. BARON AND D. HUBERT (1984) EISCAT measurements of ion temperatures which indicate non-isotropic ion velocity distributions. *J. Atmos. Terr. Phys.* **46**, 531.

PESNELL W.D., K. OMIÐVAR AND W.R. HOEGY (1993) Momentum transfer collision frequency of  $O^+-O$ . *Geophys. Res. Lett.* **20**, 1343.

QUEGAN S., G.J. BAILEY, R.J. MOFFETT, R.A. HEELIS, T.J. FULLER-ROWELL, D. REES AND R.W. SPIRO (1982) A theoretical study of the distribution of ionisation in the high-latitude ionosphere and the plasmasphere: First results on the mid-latitude trough and the light-ion trough. *J. Atmos. Terr. Phys.* **44**, 619.

QUEGAN S., R.S. GILL AND M. LOCKWOOD (1988) Comparisons between EISCAT observations and model calculations of the high-latitude ionosphere. *J. Atmos. Terr. Phys.* **50**, 1057.

RAITT W.J., U. VON ZAHN AND P. CHRISTOPHERSON (1975) A comparison of thermospheric neutral gas heating and related energetic plasma phenomena at high-latitudes during geomagnetic disturbances. *J. Geophys. Res.* **80**, 2277.

RAMAN R.S.V., J.-P. ST-MAURICE AND R.S.B. ONG (1981) Incoherent scattering of radar waves in the auroral ionosphere. *J. Geophys. Res.* **86**, 4751.

RASMUSSEN C.E., R.W. SCHUNK, J.J. SOJKA, V.B. WICKWAR, O. DE LA BEAUJARDIÈRE, J. FOSTER, J. HOLT, D.S. EVANS AND E. NIELSEN (1986) Comparison of simultaneous Chatanika and Millstone Hill observations with ionospheric model predictions. *J. Geophys. Res.* **91**, 6986.

RATCLIFFE J.A. (1972) *An introduction to the ionosphere and magnetosphere*. Cambridge University Press.

REES M.H. (1989) *Physics and chemistry of the upper atmosphere*. Cambridge

University Press.

REES M.H. AND J.C.G. WALKER (1968) Ion and electron heating by auroral electric fields. *Ann. Geophys.* **24**, 193.

REIFF P.H. AND J.L. BURCH (1985) By-dependent plasma flow and Birkeland currents in the dayside magnetosphere: 2. A global model for northward and southward IMF. *J. Geophys. Res.* **90**, 1595.

RICHMOND A.D. (1982) "Thermospheric dynamics and electrodynamics." in *Solar-terrestrial physics*, D. Reidel Publishing Company, Dordrecht, 523.

RISHBETH H. (1972) Thermospheric winds and the F-region: A review. *J. Atmos. Terr. Phys.* **34**, 1.

RISHBETH H. (1988) Basic physics of the ionosphere: A tutorial review. *J. Inst. Elect. Rad. Eng.* **58**, 207, 1988.

RISHBETH H. AND W.B. HANSON (1974) A comment on plasma pile-up in the F region. *J. Atmos. Terr. Phys.* **36**, 703.

RISHBETH H. AND P.J.S. WILLIAMS (1985) The EISCAT ionospheric radar: The system and its early results. *Q. J. R. Astr. Soc.* **26**, 478.

ROBLE R.G. AND R.E. DICKINSON (1972) Time-dependent behaviour of a stable auroral red arc excited by an electric field. *Planet. Space Sci.* **20**, 591.

RODGER A.S., S.W.H. COWLEY, M.J. BROWN, M. PINNOCK AND D.A. SIMMONS (1984) Dawn-dusk ( $\gamma$ ) component of the interplanetary magnetic field and the local time of the Harang continuity. *Planet. Space Sci.* **32**, 1021.

RODGER A.S., R.J. MOFFETT AND S. QUEGAN (1992) The role of ion drift in the formation of ionisation troughs in the mid- and high-latitude ionosphere - A review. *J. Atmos. Terr. Phys.* **54**, 1.

RÖTTGER J. (1991) "Incoherent scatter observations of the auroral ionosphere with the EISCAT radar facility." in *Auroral Physics*, Cambridge University Press, 419.

RUSSEL C.T. AND R.L. McPHERRON (1973) Semiannual variation of geomagnetic activity. *J. Geophys. Res.* **78**, 92.

SALAH J.E., J.V. EVANS AND R.H. WAND (1975) E-region measurements at Millstone Hill. *J. Atmos. Terr. Phys.* **37**, 461.

SALAH J.E. (1993) Interim standard for the ion-neutral atomic oxygen collision frequency. *Geophys. Res. Lett.* **20**, 1543.

SATO T., I. ATSUO, W.L. OLIVER, S. FUKOA, T. TSUDA, S. KATO AND I.

- KIMURA (1989) Ionospheric incoherent scatter measurements with the middle and upper atmosphere radar: Techniques and capability. *Radio Sci.* **24**, 85.
- SCHLEGEL K., H. KOHL AND K. RINNERT (1980) Temperatures and collision frequency in the polar-E region measured with the incoherent scatter technique. *J. Geophys. Res.* **85**, 710.
- SCHLEGEL K. AND J.-P ST-MAURICE (1981) Anomalous heating of the polar E-region by unstable plasma waves: 1. Observations. *J. Geophys. Res.* **86**, 1447.
- SCHMELTEKOPF A.L., E.E. FERGUSON AND F.C. FEHSENFELD (1968) Afterglow studies of the reactions  $\text{He}^+$ ,  $\text{He}(2^3\text{S})$  and  $\text{O}^+$  with vibrationally excited  $\text{N}_2$ . *J. Chem. Phys.* **48**, 2966.
- SCHUNK R.W. (1975) Transport equations for aeronomy. *Planet. Space Sci.* **23**, 437.
- SCHUNK R.W. (1977) Mathematical structure of transport equations for multispecies flows. *Rev. Geophys. Space Phys.* **15**, 429.
- SCHUNK R.W. (1983) "The terrestrial ionosphere." in *Solar-terrestrial physics*, D. Reidel Publishing Company, Dordrecht, 609.
- SCHUNK R.W. AND A.F. NAGY (1978) Electron temperatures in the F-region of the ionosphere: Theory and observations. *Rev. Geophys. Space Phys.* **16**, 355.
- SCHUNK R.W. AND A.F. NAGY (1980) Ionospheres of terrestrial planets. *Rev. Geophys. Space Phys.* **18**, 813.
- SCHUNK R.W. AND J.J. SOJKA (1982a) Ion temperature variations in the daytime high-latitude F-region. *J. Geophys. Res.* **87**, 5169.
- SCHUNK R.W. AND J.J. SOJKA (1982b) Ionospheric hot spot at high-latitudes. *Geophys. Res. Lett.* **9**, 1045.
- SCHUNK R.W. AND J.C.G. WALKER (1972) Ion velocity distributions in the auroral ionosphere. *Planet. Space Sci.* **20**, 2175.
- SCHUNK R.W. AND J.C.G. WALKER (1973) Theoretical ion densities in the lower ionosphere. *Planet. Space Sci.* **21**, 1875.
- SCHUNK R.W., W.J. RAITT AND P.M. BANKS (1975) Effect of electric fields on the daytime high-latitude E- and F-regions. *J. Geophys. Res.* **80**, 3121.
- SELLEK R., G.J. BAILEY, R.J. MOFFETT, R.A. HEELIS AND P.C. ANDERSON (1991) Effects of large zonal plasma drifts on the subauroral ionosphere. *J. Atmos. Terr. Phys.* **53**, 557.
- SELLEK R., R.J. MOFFETT AND G.J. BAILEY (1992) Effects of rapid zonal plasma

flow in the mid-latitude ionosphere: Modulation of the field-aligned plasma flow by neutral air upwelling. *Adv. Space Res.* **12**, 171.

SENIOR C., D. FONTAINE, G. CAUDAL, D. ALCAYDÉ AND J. FONTANARI (1990) Convection electric fields and electrostatic potential over  $61^\circ < \Lambda < 72^\circ$  invariant latitude observed with the European incoherent scatter facility: 2. Statistical results. *Ann. Geophys.* **8**, 257.

SHANNON C.E. (1948) A mathematical theory of communication. *Bell systems technical journal*, 379.

SIPLER D.P., M.E. HAGAN, M.E. ZIPF AND M.A. BIONDI (1991) Combined optical and radar wind measurements in the F region over Millstone Hill. *J. Geophys. Res.* **96**, 21255.

SOJKA J.J. AND R.W. SCHUNK (1984) A theoretical F-region study of ion compositional and temperature variations in response to magnetospheric storm inputs. *J. Geophys. Res.* **89**, 2348.

SOJKA J.J. AND R.W. SCHUNK (1989) Theoretical study of the seasonal behaviour of the global ionosphere at solar maximum. *J. Geophys. Res.* **94**, 6739.

ST-MAURICE J.-P. AND W.B. HANSON (1982) Ion frictional heating at high-latitudes and its possible use for *in situ* determination of neutral thermospheric winds and temperatures. *J. Geophys. Res.* **87**, 7580.

ST-MAURICE J.-P. AND W.B. HANSON (1984) A statistical study of F-region ion temperatures at high-latitudes based on Atmospheric Explorer-C data. *J. Geophys. Res.* **89**, 987.

ST-MAURICE J.-P. AND R.W. SCHUNK (1973) Auroral ion velocity distributions using a relaxation model. *Planet. Space Sci.* **21**, 1115.

ST-MAURICE J.-P. AND R.W. SCHUNK (1974) Behaviour of ion velocity distributions for a simple collisional model. *Planet. Space Sci.* **22**, 1.

ST-MAURICE J.-P. AND R.W. SCHUNK (1977) Auroral ion velocity distributions for a polarization collision model. *Planet. Space Sci.* **25**, 243.

ST-MAURICE J.-P. AND R.W. SCHUNK (1979) Ion velocity distributions in the high-latitude ionosphere. *Rev. Geophys. Space Phys.* **17**, 99.

ST-MAURICE J.-P. AND D.G. TORR (1978) Nonthermal rate coefficients in the ionosphere: The reactions of  $O^+$  with  $N_2$ ,  $O_2$  and  $NO$ . *J. Geophys. Res.* **83**, 969.

ST-MAURICE J.-P., W.B. HANSON AND J.C.G. WALKER (1976) Retarding potential analyzer measurement of the effect of ion-neutral collisions on the ion velocity distribution in the auroral ionosphere. *J. Geophys. Res.* **81**, 5438.

ST-MAURICE J.-P., K. SCHLEGEL AND P.M. BANKS (1981) Anomalous heating of the polar E-region by unstable plasma waves: 2. Theory. *J. Geophys. Res.* **86**, 1453.

STALLCOP J.R., H. PARTRIDGE AND E. LEVIN (1991) Resonance charge transfer, transport cross-sections and collision integrals for N<sup>+</sup> and O<sup>+</sup> interactions. *J. Chem. Phys.* **95**, 6429.

STUBBE P. AND S. CHANDRA (1971) Ionospheric warming by neutral winds. *Planet. Space Sci.* **19**, 731.

SUVANTO K., M. LOCKWOOD AND T.J. FULLER-ROWELL (1989a) The influence of anisotropic F-region ion velocity distributions on ionospheric ion outflows into the magnetosphere. *J. Geophys. Res.* **94**, 1347.

SUVANTO K., M. LOCKWOOD, K.J. WINNER, B.J.I. BROMAGE AND A.D. FARMER (1989b) Analysis of incoherent scatter radar data from non-thermal F-region plasma. *J. Atmos. Terr. Phys.* **51**, 483.

SWIFT D.W. (1975) The effect of electric fields and ion-neutral collisions on Thomson scatter spectra. *J. Geophys. Res.* **80**, 4380.

TERESHCHENKO V.D., E.D. TERESHCHENKO AND H. KOHL (1991) The incoherent scattering of radio waves in a non-Maxwellian plasma: The effects of Coulomb collisions. *J. Geophys. Res.* **96**, 17591.

THOMSON J.J. (1906) *Conduction of electricity through gases*. Cambridge University Press.

TIMOFEEV E.E., M.K. VALLINKOSKI, T.V. KOZELOVA, A.G. YAHNIN AND R.J. PELLINEN (1987) Systematics of arc-associated electric fields and currents as inferred from radar backscatter measurements. *J. Geophys.* **61**, 122.

TODD H., S.W.H. COWLEY, M. LOCKWOOD, D.M. WILLIS, AND H. LÜHR (1988) Response time of the high-latitude dayside ionosphere to sudden changes in the north-south component of the IMF. *Planet. Space Sci.* **36**, 1415.

TORR M.R., J.-P. ST-MAURICE AND D.G. TORR (1977) The rate coefficient for the O<sup>+</sup>+N<sub>2</sub> reaction in the ionosphere. *J. Geophys. Res.* **82**, 3287.

TORR D.G. AND M.R. TORR (1978) Chemistry of the thermosphere and ionosphere. *J. Atmos. Terr. Phys.* **41**, 797.

TURUNEN T. (1986) GEN-SYSTEM - A new experimental philosophy for EISCAT radars. *J. Atmos. Terr. Phys.* **48**, 777.

UNGSTRUP E, D.M. KLUMPAR AND W.J. HEIKKILA (1979) Heating of ions to superthermal energies in the topside ionosphere by electrostatic ion cyclotron waves. *J. Geophys. Res.* **84**, 4289.

- VILLANTE U. (1975) Some remarks on the structure of the distant neutral sheet. *Planet. Space Sci.* **23**, 723, 1975.
- VIRDI T.S. AND P.J.S. WILLIAMS (1993) Altitude variations in the amplitude and phase of tidal oscillations at high-latitude. *J. Atmos. Terr. Phys.* **55**, 697.
- VIRDI T.S., G.O.L. JONES AND P.J.S. WILLIAMS (1986) EISCAT observations of the E-region semidiurnal tide. *Nature* **324**, 354.
- WALTERSCHEID R.L. AND L.R. LYONS (1989) The neutral E-region zonal winds during intense postmidnight diffuse aurora: Response to observed particle fluxes. *J. Geophys. Res.* **94**, 3703.
- WALTERSCHEID R.L. AND L.R. LYONS (1992) The neutral circulation in the vicinity of a stable auroral arc. *J. Geophys. Res.* **97**, 19489.
- WAND R.H. (1976) Semidiurnal tide in the E-region from incoherent scatter measurements at Arecibo. *Radio Sci.* **11**, 641.
- WAND R.H. AND F.H. PERKINS (1968) Radar Thomson scatter observations of temperature and ion-neutral collision frequency in the E-region. *J. Geophys. Res.* **78**, 6370.
- WATKINS B.J. AND P.M. BANKS (1974) A preliminary study of high-latitude thermospheric temperatures from incoherent scatter radar observations. *J. Geophys. Res.* **79**, 5307.
- WEISS L.A., P.H. REIFF, J.J. MOSES, R.A. HEELIS AND B.D. MOORE (1992) "Energy dissipation in substorms." in *Substorms 1: Proceedings of the first international conference on substorms*, European Space Agency Publications, Nordwijk, 309.
- WICKWAR V.B., C. LATHUILLÈRE, W. KOFMAN AND G. LEJEUNE (1981) Elevated electron temperatures in the auroral E-layer measured with the Chatanika radar. *J. Geophys. Res.* **86**, 4721.
- WILLIAMS P.J.S. AND A.R. JAIN (1986) Observations of the high-latitude trough using EISCAT. *J. Atmos. Terr. Phys.* **48**, 423, 1986.
- WILLIAMS P.J.S. AND T.S. VIRDI (1989) EISCAT observations of tidal modes in the lower ionosphere. *J. Atmos. Terr. Phys.* **51**, 569.
- WILLIAMS P.J.S., T.S. VIRDI, S.W.H. COWLEY AND M. LESTER (1990a) Short-lived bursts of plasma velocity in the auroral zone: 1. Observational evidence from radar measurements. *J. Atmos. Terr. Phys.* **52**, 421.
- WILLIAMS P.J.S., G.O.L. JONES, B. JONES, H. OPGENOORTH AND I. HAGGSTROM (1990b) High-resolution measurements of magnetospheric electric fields. *J. Atmos. Terr. Phys.* **52**, 439.

- WILLIAMS P.J.S., B. JONES AND G.O.L. JONES (1992) The measured relationship between electric field strength and electron temperature in the auroral E-region. *J. Atmos. Terr. Phys.* **54**, 741.
- WINKLER E., J.-P. ST-MAURICE AND A.R. BARAKAT (1992) Results from improved Monte Carlo calculations of auroral ion velocity distributions. *J. Geophys. Res.* **97**, 8399.
- WINSER K.J., G.O.L. JONES AND P.J.S. WILLIAMS (1986) A quantitative study of the high-latitude ionospheric trough using EISCAT's common programmes. *J. Atmos. Terr. Phys.* **48**, 893.
- WINSER K.J., M. LOCKWOOD AND G.O.L. JONES (1987) Non-thermal plasma observations using EISCAT: Aspect angle dependence. *Geophys. Res. Lett.* **14**, 957.
- WINSER K.J., G.O.L. JONES AND P.J.S. WILLIAMS (1988a) Variations in field-aligned plasma velocity with altitude and latitude in the auroral zone: EISCAT observations and the physical interpretation. *Phys. Script.* **37**, 640.
- WINSER K.J., G.O.L. JONES AND P.J.S. WILLIAMS (1988b) Large field-aligned velocities observed by EISCAT. *J. Atmos. Terr. Phys.* **50**, 379.
- WINSER K.J., G.O.L. JONES, P.J.S. WILLIAMS AND M. LOCKWOOD (1989) Observations of large field-aligned flows of thermal plasma in the auroral ionosphere. *Adv. Space Res.* **9**, 57.
- WINSER K.J., M. LOCKWOOD, G.O.L. JONES, H. RISHBETH AND M.G. ASHFORD (1990) Measuring ion temperatures and studying the ion energy balance in the high-latitude ionosphere. *J. Atmos. Terr. Phys.* **52**, 501.
- WU S.T. AND K.D. COLE (1976) Transient thermospheric heating and movement caused by an auroral electric field. *Planet. Space Sci.* **24**, 727.
- WYGANT J.R., R.B. TORBERT AND F.S. MOZER (1983) Comparison of S3-2 polar cap potential drops with the interplanetary magnetic field and models of magnetopause reconnection. *J. Geophys. Res.* **88**, 5727.
- YAU A.W., B.A. WHALEN, A.G. McNAMARA, P.J. KELLOGG AND W. BERNSTEIN (1983) Particle and wave observations of low-altitude ionospheric ion acceleration events. *J. Geophys. Res.* **88**, 341.